

Antarctic Meteorites XXXI

Papers presented to the
Thirty-first Symposium
on Antarctic Meteorites



June 5-7, 2007

NATIONAL INSTITUTE OF POLAR RESEARCH

TOKYO

国立極地研究所

Tuesday, June 5, 2007

0900–1200 **Registration** **Auditorium (6th Floor)**

Oral sessions will be held in the auditorium, 6th floor of the Main Building

** denotes speaker*

0925–0930 **Fujii Y.** (Director-General, NIPR)
Opening Address

Chairs: Noguchi T. and Tomiyama T.

| | | |
|-----------|--|-----|
| 0930–0945 | Choi B.-G.* , Lee J. I., Yoo H., Park J., Jang N., Kim O. J. and Garrod S. Report on the first Korean Antarctic Meteorite Expedition to Martin Hills, Nash Hills, Pirrit Hills and Thiel Mountains | 9 |
| 0945–1000 | Miao B.* , Lin Y. and Wang D. The petrology and origin of new ureilites found in Grove Mountains, Antarctica | 50 |
| 1000–1015 | Noguchi T.* , Nakamura T., Aoki T., Toh S., Imae N., Iwata N. and Tottuki Micrometeorite Curation Team Discovery of a chondritic porous interplanetary dust particle among Antarctic micrometeorites | 78 |
| 1015–1030 | Niihara T.* , Imae N. and Kojima H. Petrography of Yamato-791088, a heavily shocked H chondrite | 73 |
| 1030–1045 | Kimura M.* , Fukuda H., Suzuki A. and Ohtani E. Unique high-pressure phase assemblage in a heavily shocked L6 chondrite, NWA 4719 | 39 |
| 1045–1100 | Aoki T.* , Nakamuta Y. and Toh S. Dislocation densities of olivine crystals structurally strained in variable degrees from a shocked chondrite | 1 |
| 1100–1115 | Nishioka I.* , Funaki M. and Venkata Rao K. Paleomagnetic study of basalts from Lonar impact crater | 77 |
| 1115–1130 | Weihaupt J. G. and Rice A.* Suggestions of multiple meteoroid impact in Antarctica: How do we sort it out ? | 103 |
| 1130–1230 | —Lunch— | |
| 1230–1245 | Nakamuta Y.* Carbon minerals in the highly shocked Goalpara ureilite | 69 |
| 1245–1300 | Yamaguchi A.* , Barrat J. A., Greenwood R. C., Bohn M., Cotten J., Benoit M. and Franchi I. A. The Stannern trend eucrites: Contamination of main group eucritic magmas by crustal partial melts | 105 |

| | | |
|-----------|--|----|
| 1300–1315 | Tomiyama T.* , Bizzarro M. , Huss G. R. and Krot A. N. ²⁶ Mg deficit dating for differentiation in pallasite parent bodies | 99 |
| 1315–1330 | Honda M.* , Nagao K. and Nagai H. Irradiation history of Gibeon iron meteorite | 28 |

Chairs: Fagan T. J. and Arai T.

| | | |
|-----------|--|----|
| 1330–1345 | Takeda H.* , Yazawa Y. , Arai T. , Yamaguchi A. , Saito M. , Ishii T. , Otsuki M. and Kanamori H. Feldspathic lunar meteorites from the farside and production of their lunar simulants | 95 |
| 1345–1400 | Arai T.* , Takeda H. , Yamaguchi A. and Ohtake M. Dhofar 489 et al. as ground truth of the lunar farside crust | 3 |
| 1400–1415 | Fagan T. J.* Formation of symplectic inclusions by direct quenching of a high-FeO/ (FeO+MgO) silicate liquid on the Moon | 15 |
| 1415–1430 | Terada K.* , Sasaki Y. , Anand M. , Joy K. H. and Sano Y. U-Pb systematics of phosphates in lunar basaltic regolith breccia, MET 01210 | 97 |
| 1430–1445 | Nyquist L. E.* , Shih C.-Y. and Reese Y. D. Lunar crust/mantle formation intervals | 80 |
| 1445–1515 | —Coffee Break— | |
| 1515–1530 | Hiroi T.* , Nimura T. , Ueda Y. , Sasaki S. and Pieters C. M. How much of the S-type asteroids are made of ordinary chondrite materials, and why are they so highly space-weathered ? | 25 |
| 1530–1545 | Ozima M.* , Yin Q.-Z. , Podosek F. and Miura Yayoi Comparative study of near- and far-side lunar soils: Toward the understanding early evolution of the Earth | 86 |

—Special Talk (I)—

Chair: Kimura M.

| | | |
|-----------|---|----|
| 1545–1645 | Grossman J. N.* , Brearley A. J. , Kimura M. and Weisberg M. K. Advances in the characterization and classification of the least-metamorphosed chondrites | 19 |
| 1700–1900 | Welcome Party (6th Floor) | |

Wednesday, June 6, 2007

Chairs: Righter K. and Mikouchi T.

| | | |
|-----------|--|----|
| 0930–0945 | Mikouchi T.* and Kurihara T. Y000027, Y000047 and Y000097: Mineralogy and petrology of paired Yamato 00 lherzolitic shergottites | 52 |
| 0945–1000 | Imae N.* and Ikeda Y. Petrography of new lherzolitic shergottites of Yamato (Y) 000027, Y000047, and Y000097: Main lithologies and shock veins | 32 |
| 1000–1015 | Ikeda Y.* and Imae N. Magmatic inclusions in new lherzolitic shergottites, Y000027, Y000047, and Y000097 | 30 |
| 1015–1030 | Shirai N.* and Ebihara M. Chemical composition of lherzolitic shergottites Yamato 000097 | 91 |
| 1030–1045 | Misawa K.*, Shih C.-Y., Reese Y. and Nyquist L. E. Rb-Sr and Sm-Nd isotopic studies of lherzolitic shergottite Yamato 000097 | 54 |
| 1045–1100 | Nagao K.*, Park J. and Choi H. Noble gases of the Yamato 000027 and Yamato 000097 lherzolitic shergottites | 62 |
| 1100–1115 | Hoffmann V., Torii M. and Funaki M.* Yamato 000097 magnetic signature and comparison with other lherzolitic shergottites: Preliminary results | 26 |
| 1115–1130 | Righter K.* Early differentiation of Mars: Constraints from siderophile elements and oxygen fugacity | 89 |
| 1130–1145 | McKay G.*, Le L. and Mikouchi T. Al, Ti, and Cr: Complex zoning in synthetic and natural nakhlite pyroxenes | 48 |
| 1145–1300 | —Lunch— | |

Chairs: Nakamura-Messenger K. and Okazaki R.

| | | |
|-----------|---|----|
| 1300–1315 | Suzuki A.*, Nakashima S. and Nakamura T. Infrared and Raman spectroscopy of Antarctic micrometeorites | 93 |
| 1315–1330 | Okazaki R.* and Nakamura T. Noble-gas and oxygen isotopes and REE abundances of Antarctic micrometeorites | 83 |
| 1330–1345 | Kusuno H.*, Fukuoka T., Kojima H. and Matsuzaki H. Determination of ²⁶ Al content for Antarctic meteorites using AMS | 43 |
| 1345–1400 | Kitajima F.* and Nakamura T. A micro-Raman study on thermal histories of carbonaceous matter in carbonaceous chondrites | 41 |

| | | |
|-----------|--|-----|
| 1400–1415 | Keller L. P.* and Messenger S. Amorphous silicates in primitive solar system materials | 35 |
| 1415–1430 | Nakamura-Messenger K.*, Messenger S., Keller L. P., Clemett S. J. and Zolensky M. E. Organic globules in the Tagish Lake CI2 and Bells CM2 carbonaceous chondrites | 67 |
| 1430–1445 | Oba Y. and Naraoka H.* Isotopic variations of macromolecular organic matter from CM chondrites during hydrous pyrolysis | 82 |
| 1445–1515 | —Coffee Break— | |
| 1515–1530 | Uesugi M.* and Uesugi K. Observation of the radius of compound chondrules in meteorite chips | 101 |
| 1530–1545 | Miura H.*, Nakamoto T. and Doi M. Shock-wave heating model for chondrule formation: Conditions to reproduce chondrule shapes | 56 |
| 1545–1600 | Nakashima D.*, Ott U., Hoppe P. and El Goresy A. Search for extinct ³⁶ Cl: Vigarano CAIs and the Pink Angel from Allende | 71 |
| 1600–1615 | Jull A.J.T.*, Biddulph D. L., McHargue L. R., Zahn D., Burr G. S., Kim K. J. and Bland P. A. Measurements of ¹⁴ C, ¹⁰ Be and ¹²⁹ I in meteorites and applications | 107 |

—Special Talk (II)—

Chair: Yoneda S.

| | | |
|-----------|--|----|
| 1615–1715 | Ebel D. S.*, Kita N., Ushikubo T. and Weisberg M. K. Microtomographic, petrologic and isotopic observations of the accretion histories of chondrules | 13 |
|-----------|--|----|

Thursday, June 7, 2007

Chairs: Gucsik A. and Imae N.

| | | |
|-----------|---|----|
| 0930-0945 | Gucsik A.* , Protheroe Jr. W. J., Stirling J. A.R., Ninagawa K., Nishido H., Okumura T., Matsuda N., Bérczi Sz., Nagy Sz., Kereszturi A. and Hargitai H. | 21 |
| | Cathodoluminescence imaging and spectral analyses of phosphates in the Martian meteorites: A review | |
| 0945-1000 | Kayama M. , Gucsik A.*, Matsuda N., Nishido H. and Ninagawa K. | 34 |
| | Cathodoluminescence spectral study of alkali feldspar and plagioclase in Yamato Martian nakhlite meteorites | |
| 1000-1015 | Matsuda N.* , Nishido H., Gucsik A., Ninagawa K., Okumura T. and Kayama M. | 47 |
| | Cathodoluminescence, micro-Raman and infrared studies of silica minerals in nakhlite from Antarctica | |
| 1015-1030 | Nagy Sz.* , Józsa S., Gucsik A., Bérczi Sz., Ninagawa K., Nishido H. and Veres M. | 65 |
| | Optical and Raman spectroscopical properties of the shocked olivines from ALHA 77005 sample | |
| 1030-1045 | Okumura T.* , Gucsik A., Nishido H., Ninagawa K. and Sakamoto M. | 85 |
| | Cathodoluminescence and micro-Raman analyses of planar deformation features in shocked quartz from impact craters | |
| 1045-1100 | Kereszturi A.* | 37 |
| | Distribution and occurrence of liquid water on Mars from the analysis of valley network structure | |
| 1100-1115 | Bérczi Sz.* , Pócs T., Horváth A., Gánti T., Kereszturi A., Sik A. and Szathmáry E. | 7 |
| | Possibility of transient liquid water on the dark subpolar dune fields of Mars | |
| 1115-1130 | Miura Yasunori* | 58 |
| | Detailed analytical scanning electron micrography of carbon-bearing materials at the Barringer meteorite crater in U.S.A. | |

Poster Session

| | |
|---|----|
| Bérczi Sz., Gucsik A., Hargitai H., Kereszturi A. and Nagy Sz. | 5 |
| Martian and “terrestrial” shergottites: Comparison of the Iherzolite (inclusion), olivin-phyric basalt and alkaline basalts rocks | |
| Hargitai H. I. | 23 |
| Meteorites in education | |
| Miura Yasunori | 60 |
| FE-ASEM observation of impact spherules with carbon, Fe, and Ni on KT geological boundary: Proposed model of various impacts among rocks, atmosphere and ocean on earth | |
| Nagy Sz., Gucsik A., Józsa S., Bérczi Sz., Ninagawa K. and Nishido H. | 64 |
| Planar microstructures on the shock-induced deformation twins in clinopyroxene from the aubrite Allan Hills 78113 | |
| Ninagawa K., Kuyama T., Imae N. and Kojima H. | 75 |
| Thermoluminescence study of Japanese Antarctic meteorites X | |

Abstract only

| | |
|--|----|
| Das J. P. and Murty S.V.S. | 11 |
| Search for precompaction irradiation records in chondrules | |
| Goswami J. N., Mishra R. and Rudraswami N. G. | 17 |
| Al-Mg and Fe-Ni isotope records in UOCs belonging to low petrologic grades | |
| Marakushev A. A., Zinovieva N. G. and Granovsky L. B. | 45 |
| Three genetic types of ultrahigh-pressure minerals in meteorites | |

ABSTRACTS

Dislocation densities of olivine crystals structurally strained in variable degrees from a shocked chondrite. T. Aoki¹, Y. Nakamuta² and S. Toh³, ¹Department of Earth and Planetary Sciences, Graduate School of Sciences, Kyushu University, Hakozaki 6-10-1, Fukuoka, 812-8581, Japan, (tomotaro@geo.kyushu-u.ac.jp), ²Kyushu University Museum, Kyushu University, Hakozaki 6-10-1, Fukuoka, 812-8581, Japan, ³ Research Laboratory for High Voltage Electron Microscopy, Kyushu University, Hakozaki 6-10-1, Fukuoka, 812-8581, Japan.

Introduction

Most meteorites were subjected to shock metamorphism in some degrees. Estimation of the degree of shock is important in order to know the evolution processes of materials in a planet and also in the solar system. Uchizono *et al.* [1] found based on shock experiments that the lattice strains of olivine crystals, being obtained from broadening of reflections in an X-ray diffraction pattern, correlate proportionally to shock pressures loaded on them. Their result suggests that the lattice strain can be used as an index to estimate quantitatively shock pressures under which meteorites were shocked. However, structural mechanism which causes the lattice strain is not well known. In this study, we observed small olivine crystals from a Naryilco chondrite by transmission electron microscopy (TEM) after estimating their lattice strains by an X-ray method using a Gandolfi camera.

Sample and Experiments

Naryilco chondrite is a moderately shocked chondrite, being composed of breccias of various sizes and shock veins. Shock stage of this meteorite is S4 based on Stöffler *et al.* [2]. Eighteen single crystals of olivine, being less than 100 μm in size, were taken out from a Naryilco specimen for XRD analyses using a Gandolfi camera after analyzing chemical compositions with an electron probe micro-analyzer (EPMA). The accelerating voltage and specimen current for the EPMA analyses are 15 kV and 1.0×10^{-8} A, respectively. Cr and V were used as a target and a filter for the XRD analyses, and the anode voltage and current were 40 kV and 34 mA, respectively. Precise peak positions and breadths of the each diffraction line were determined by using a profile-fitting technique [3]. The lattice strains of olivine crystals were determined from a coefficient between β and $\tan\theta$ according to the equation, $\beta = 4e \tan\theta$ [4], where β , e and θ are integral breadth of each diffraction line, lattice strain of the crystal and a half of diffraction angle of each diffraction line, respectively. Selected four samples from the eighteen crystals were fabricated to about 200 nm thick by a focused ion beam (FIB) method together with a San Carlos olivine as a standard for the TEM observation. (JEM-200CX at Kyushu University HVEM Laboratory). The accelerating voltage for the FIB milling is 30 kV.

Results and Discussions

The lattice strains of eighteen olivine crystals were determined as the result of XRD analyses using a Gandolfi camera and shown in Table 1. The lattice strains of olivine crystals range from 0.075 % to 0.278 %. Samples 1, 5, 6 and 17 were used for TEM observation.

The San Carlos olivine shows homogeneous contrast with no textures under bright and dark field conditions in TEM observations, suggesting that fabrication by a FIB causes no or very few damages even on surface of a sample. Dark field images of samples 1, 5, 6 and 17 are shown in Figure 1. As can be seen in Figure 1, the number and the form of dislocations vary among samples showing various lattice strains. Sample 1 shows small number of linear dislocations mostly directed to [001]. Sample 5 shows medium number of linear dislocations mainly directed to [001] and low-angle grain boundary. Sample 6 also shows medium number of dislocations, but in which two distinct directions were observed, one of which directs to [001] but the other is not known. Sample 17 shows large number of curved, interconnected dislocations nearly directed to [001].

Dislocation densities in samples 1, 5, 6 and 17 were measured in dark field images using 002, 062, 02 $\bar{1}$ and 002 diffractions, respectively, in which samples satisfy no extinction conditions. The dislocation densities of samples 1, 5 and 6 were estimated by dividing the number of dislocations by the area of samples, and that of sample 17 were estimated by dividing the total length of dislocations by the volume, because dislocations of sample 17 are connected to each other. The obtained dislocation densities are 2×10^8 , 32×10^8 , 26×10^8 and 208×10^8 cm^{-2} for samples 1, 5, 6 and 17, respectively. The results suggest a linear correlation between lattice strains and common logarithms of dislocation densities of samples and reveal that the lattice strain obtained by an XRD method corresponds to the density of dislocations observed by TEM (Figure 2).

Acknowledgement

We thank Prof. Noriyuki Kuwano at Art, Science and Technology Center for Cooperative Research, Kyushu University, who gave us many helpful advices on this study. And special acknowledgement is made to Dr. Harini Sosiati at the Research Laboratory for High Voltage Electron Microscopy,

Kyushu University, who helped us to fabricate samples by FIB milling.

References

[1] Uchizono *et al.* (1999) *Mineralogical J.*, 21(1), 15-23. [2] Stöfler *et al.* (1991) *Geochimica et Cosmochimica Acta*, 55, 3845-3867. [3] Nakamuta Y. (1994) *Zeolite*, 11(4), 171-179. [4] Wilson A.J.C. (1962) *X-Ray Optics*, 6-28.

Table 1. Lattice strains of eighteen olivine crystals and San Carlos olivine obtained by XRD analyses using a Gandolfi camera.

| Sample | Lattice strain (%) |
|--------|--------------------|
| SC | 0.030(01) |
| 1 | 0.075(04) |
| 2 | 0.121(09) |
| 3 | 0.131(07) |
| 4 | 0.155(06) |
| 5 | 0.164(12) |
| 6 | 0.170(09) |
| 7 | 0.170(10) |
| 8 | 0.170(10) |
| 9 | 0.188(15) |
| 10 | 0.190(10) |
| 11 | 0.192(09) |
| 12 | 0.193(16) |
| 13 | 0.200(10) |
| 14 | 0.205(14) |
| 15 | 0.212(09) |
| 16 | 0.236(14) |
| 17 | 0.250(18) |
| 18 | 0.278(14) |

The standard deviations of the lattice strains are in the parentheses. SC means San Carlos olivine.

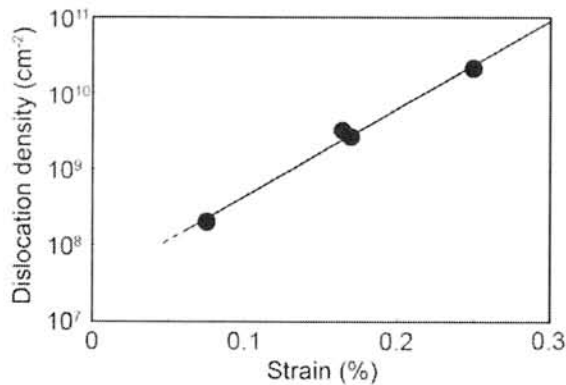


Figure 2. Plots of dislocation densities versus lattice strains for samples 1, 5, 6 and 17. The vertical axis is logarithmic.

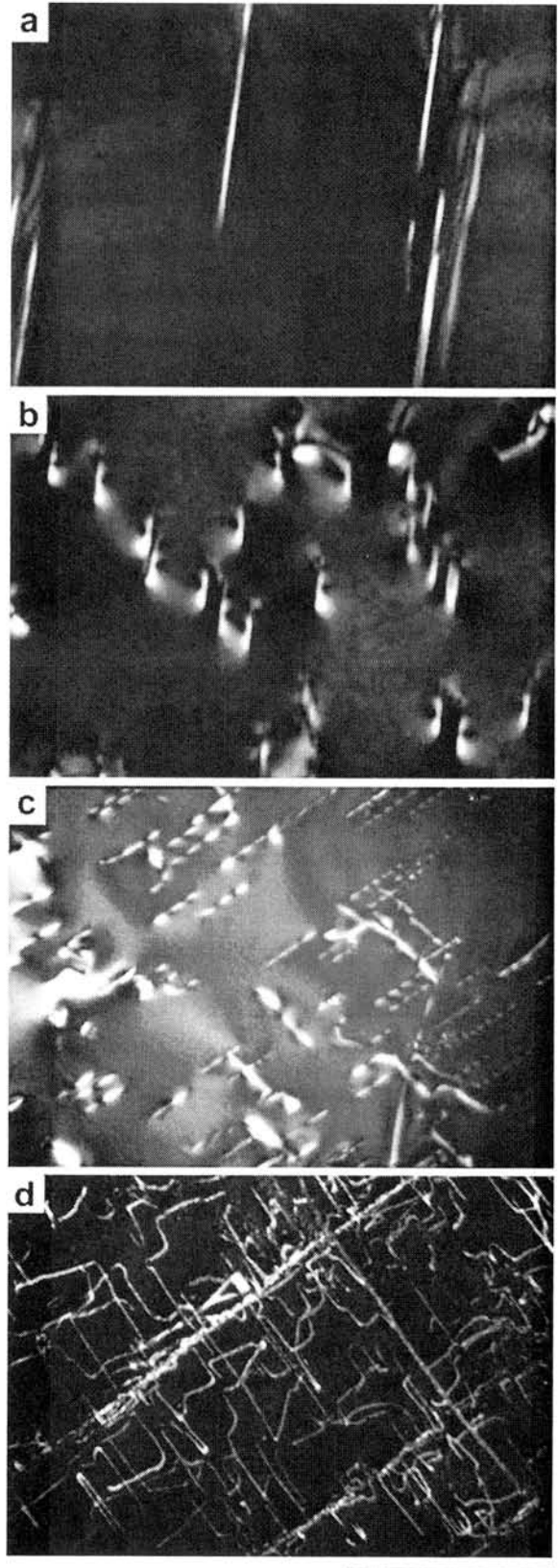


Figure 1. Dark field images of four samples of olivine. Figure a, b, c and d are the images of samples 1, 2, 3 and 4, respectively. The horizontal bar at lower right of the photographs shows 1μm in length.

Dhofar 489 et al. as ground truth of the lunar farside crust. T. Arai¹, H. Takeda², A. Yamaguchi¹, and M. Ohtake³. ¹Antarctic Meteorite Research Center, National Institute of Polar Research, Kaga, Itabashi, Tokyo 173-8515, Japan (tomoko@nipr.ac.jp), ²Dept. of Earth & Planetary Science, The University of Tokyo, Hongo, Tokyo 113-0033, Japan, ³Planetary Science Department, Japan Aerospace Exploration Agency (JAXA), 3-1-1 Yoshinodai, Sagami-hara, 229-8510, Japan.

Introduction: Models of the lunar crustal evolution in the Apollo era have been continuously updated with data from post-Apollo orbital satellites and lunar meteorites. Lunar meteorites randomly sampling the Moon, serve as ground truth of unexplored regions. Dhofar 489 is a crystalline matrix anorthositic breccia including clasts of magnesian anorthosites (MAN) and a spinel troctolite (ST) and is the most depleted in Th, FeO, and REE [1]. Based on the global elemental mapping data of Th and FeO [e.g. 2-4], the derivation from the farside highland is highly likely. The extremely old ³⁹Ar-⁴⁰Ar age (4.23 Ga) [1], which is in stark contrast with those of most Apollo highland samples with much younger ages (~3.8–4.0 Ga) [e.g. 5], also supports the farside origin. Another fourteen meteorites (Dhofar 303, 305, 306, 307, 309, 310, 311, 730, 731, 908, 909, 911, 950, and 1085) have been proposed to be paired with Dhofar 489 based on the compositional similarity [6]. Preliminary study of Dhofar 309 showed that a wide range of variations in texture, mineral composition, and modal abundance relative to those in Dhofar 489 [1]. This result suggests the mineralogical and petrologic diversity within the suite of this impact melt. Here, we presented further result of mineralogical and petrologic studies of Dhofar 309 in combination with Dhofar 489, to understand the compositional and textural variety of the impact-melt rocks and to discuss the lithologies of the farside crust, and the origin of the asymmetry in the nearside-farside crust compositions.

Sample and method: Mineralogical analyses were done by electron probe microanalyzer (EPMA) at the Ocean Research Institute of Univ. of Toyo (JEOL 733 and 8900) and National Institute of Polar Research (JEOL 8200).

Dhofar 309 vs. 489 in petrology & mineralogy: Dhofar 309 exhibits a distinct texture from Dhofar 489. It consists of clasts of magnesian anorthosite (MAN) and fine-grained crystalline rocks with troctolitic composition, embedded in the devitrified matrix (Fig. 1). The latter clasts are angular-shaped and include angular plagioclase fragments of up to 1 mm across. The coarse grain size of the incorporated plagioclase infers the probable origin of the MAN. While fine-grained (10-50 μ m across) olivines in these clasts are sub-rounded, plagioclases are lath-shaped. The overall texture indicates that they are an annealed impact-melt rock (IM). In contrast, Dhofar 489 includes the clasts of the MAN and anorthositic spinel troctolite (ST) with poikilitic olivines of a few to 500 μ m across [1]. Such a coarse-grained troctolite clast is not present in Dhofar 309. While the matrix of Dhofar 309 is fairly uniform, that of Dhofar 489 is extremely heterogeneous. The differences in constituent clast types and textures of clasts and matrix observed in these paired meteorites reflect the diversity in the cooling / annealing episode of the impact melt and the local heterogeneity within this impact-melt suite.

The MAN clast of Dhofar 309 consists of >90 vol% plagioclase with olivine plus extremely minor pyroxene. This mode of occurrence is comparable with that of Dhofar 489 with 96.5 vol% plagioclase [7]. Twin lamellae of plagioclase are commonly present in the MAN clasts of Dhofar 489 and 309, which is indicative of igneous nature. Note that the modal abundance of the IM clasts in Dhofar 309 is roughly similar to that of the ST clast in Dhofar 489 (Table 1), which suggests that the precursor of the IM clast should have similar bulk composition to the ST and could be the ST itself. Accordingly, the lack of the ST clast in Dhofar 309 can be interpreted that the some of ST was fused and mixed into the impact melt, ended up with the IM.

Interestingly, the abundance of pyroxene in the IM clast of Dhofar 309 is greater than that of ST clast of Dhofar 489 (Table 1). The pyroxene of > 10 vol% in the IM clast should stem from neither the MAN nor ST, but from some other rock type bearing pyroxene. Modal abundance of the fine-grained crystalline impact-melt matrix of Dhofar 489 shows the derivation from the mixture of the ST and MAN (Table 1). As in the case of IM clast, the higher abundance (8-9 vol%) of pyroxene in the Dhofar 489 matrix suggests the presence of the precursor rock with pyroxene. Yet, clasts of pyroxene-bearing rocks have not been found either in Dhofar 489 or 309.

Plagioclase compositions of the MAN, IM, and matrix in Dhofar 309 (An_{95-97}) are all similar to those in Dhofar 489 (An_{94-98}). Olivine compositions in Dhofar 309 show bimodal distribution for the MAN and IM, as well as for those of Dhofar 489 (Fig. 2). The overall olivine composition of Dhofar 309 is slightly more Mg-rich than those of Dhofar 489 (Fig. 2). Pyroxene compositions of Dhofar 309 are close to those of Dhofar 489. The ratios of Cr/(Cr+Al) and Fe/(Fe+Mg) of the spinels in Dhofar 309 show analogous, but slightly greater distribution than those in Dhofar 489. The more magnesian compositions of olivine in the MAN of Dhofar 309 compared with those of Dhofar 489 can be interpreted in the following scenario. Since olivine in the MAN apparently crystallized from trapped melts within the plagioclase cumulates, small amounts of crystallizing olivine evolved the liquid, generating more Fe-rich olivines. Thus, the MAN in Dhofar 309 probably represents the earlier crystallization product from the parent magma than that in Dhofar 489.

Olivines in the clasts of ST, MAN, IM, and matrix in Dhofar 309 and 489 are all brown-colored, despite of their Mg-rich composition. The brown color is rare in the igneous Mg-rich olivine unlike fayalite. The uniform presence of the brown olivines in the different rock types, grain sizes, and shapes should not be due to terrestrial weathering, but impact metamorphism.

Rock types of the farside crust: The bimodal mg# distribution and differences in the modal abundance of the MAN and ST clasts in Dhofar 489 [1], and of the

MAN and IM in Dhofar 309 indicate that at least two distinct rock types exist in the farside crust represented by Dhofar 489 et al. meteorites. The highly anorthositic compositions, relatively coarse grain sizes and extremely low abundances in incompatible trace elements (ITEs) of the MAN and ST [1] imply that they formed as cumulates from a common differentiation magma body. Higher modal abundance of plagioclase and lower mg# in the MAN relative to those in the ST imply that the ST was an earlier crystallizing product in the differentiation. If the ST is a primary product of the magma ocean, it was generated at the depth of a few tens of km, which is an estimated burial depth from the phase stability [1], and the MAN possibly crystallized at the comparable or more likely shallower depth.

There should be another rock type with pyroxene, likely norite, inferred from the higher abundance of pyroxene in the IM clast of Dhofar 309 and the impact-melt matrix of Dhofar 489. The IM clasts were derived from mixture of ST and the third rock type, though clasts of pyroxene-bearing rocks have not been found so far. Nevertheless, the pyroxene is probably not a dominant phase in the farside highland as suggested by the global mineral maps [8], and the MAN and ST is likely representative of the farside crust. Norites distributed in and around the South Pole-Aitken (SPA) basin of the farside [8] might be linked with the missing pyroxene-bearing rock. Olivine-bearing anorthositic rocks widely distributed across the farside crust [8] further implies that the MAN and ST should not be generated from a local intrusion, but from a large, at least semi-hemispheric scale of large magma ocean.

Global crustal evolution inferred from the asymmetric crust compositions: The modal abundance of IM clast of Dhofar 309 and crystalline impact-melt matrix of Dhofar 489 well matches with the acknowledged bulk composition of the global crust (75-90 vol% plagioclase) [6, 9]. This coincidence shows that Dhofar 489 et al. meteorites represent the average mode of occurrence of the lunar crust.

While the modal abundance of plagioclase in the MAN is comparable to that of the nearside ferroan anorthosite (FAN), the Fo value in the MAN greatly exceeds that in the FAN (Fig. 3). However, both the MAN (Dhofar 489) and FAN (60025) show comparably low Th content (<0.1 ppm) [1]. These data do not rule out the possible co-magmatic origin of the FAN and the

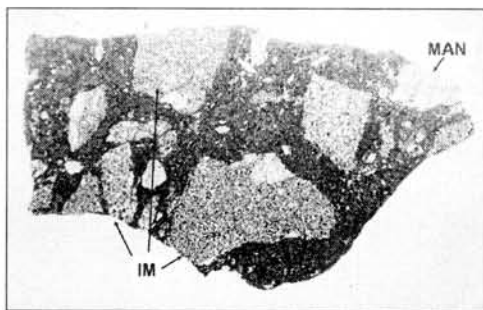


Fig.1. Photomicrograph of Dhofar 309 thin section. Angular clasts of crystalline impact-melt rocks (IM) and a clast of magnesian anorthosite (MAN) embedded in dark devitrified matrix. FOV 1.3 cm.

Table 1. Modal abundance (vol%).

| | D309 IM | D489 ST | D489 matrix |
|-------------|------------|------------|----------------|
| Plagioclase | 67.0 | 72.0 | 81.4 |
| Olivine | 23.0 | 25.0 | 10.0 |
| Pyroxene | 10.7 | 2.7 | 8.6 |
| Spinel | 0.5 | 0.3 | - |

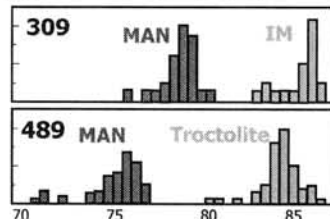


Fig. 2. Olivine compositions (Fo) of Dhofar 309 and 489.

MAN. In contrast, the ST can not be petrogenetically related to Apollo troctolites with general enrichment of incompatible trace elements. [e.g. 10].

Combined mineral maps [8, 11] and mg# distribution of the global feldspathic crust [12] show that the nearside highland is Fe-rich with orthopyroxene, while the farside highland is Mg-rich with olivine. These orbital data are consistent with the ground truth (Dhofar 489 et al. MAN for farside highland and Apollo FAN for nearside highland). The asymmetry of the mineralogical and chemical compositions in the global crust can be explained by differentiation of a single magma ocean as a result of a common liquid line of descent in forsterite-anorthite-silica system. In general, magmatic differentiation produces the normal cumulate sequence of dunite → troctolite → norite with decrease in mg#, and floated anorthosite in the later stage. The order of crystallization infers the crust formation of the farside (Mg-rich troctolite, (norite), and anorthosite) preceded that of the nearside (Fe-rich anorthosite). This implication is consistent with the ITEs concentration on the nearside as denoted by Procellarum KREEP terrane (PKT) [13], which is interpreted as the last dreg of the magma ocean [14-16]. Although it seems likely that the farside crust formed at earlier stage of the magma ocean crystallization than the nearside, the origin and the mechanism to generate the asymmetry can not be defined until acquisition of mode of occurrence and mg# of the globe-wide crust.

- References:** [1] Takeda H. et al. (2006) *EPSL*, **247**, 171-184. [2] Lawrence D. J. et al. (2003) *JGR*, **108(E9)**, 5102. [3] Lucey P. G. et al. (2000) *JGR*, **105**, 20377-20386. [4] Gillis J. J. B. et al. (2004) *GCA* **63**, 3791-3805. [5] Tera F. et al. (1974) *EPSL*, **22**, 1-22. [6] Korotev R. L. et al. (2006) *GCA*, **70**, 5935-5956. [7] Arai T. et al. (2007) *EPS*, submitted. [8] Lucey P. G. (2004) *GRL*, **31**, L08701. [9] Warren P. H. (2004) *The Moon In Meteorites, Comets, and Planets*. [10] Papike et al. (1998) *Lunar samples, In Planetary Materials, Reviews in Mineralogy and Geochemistry* **36**. [11] Hawke B. R. et al. (2003) *JGR* **108(E6)**, 5050. [12] Lucey P. G. and Cahill J. (2006) *LPS XXXVII*, #1660. [13] Jolliff B. L. et al. (2000) *JGR* **105**, 4197-4216. [14] Haskin L. A. (1998) *JGR* **103**, 1679-1689. [15] Wieczorek M. A. and Phillips R. J. (2000) *JGR* **105**, 20417-20420. [16] Korotev R. L. (2000) *JGR*, **105**, 4317-4346.

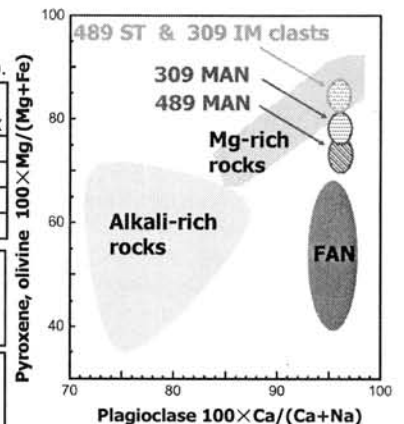


Fig. 3. MAN vs. FAN in a plot of plagioclase (An) vs. olivine, pyroxene (mg#) compositions.

MARTIAN AND "TERRESTRIAL" SHERGOTTITES: COMPARISON OF THE LHERZOLITE (INCLUSION), OLIVINE-PHYRIC BASALT AND ALKALINE BASALTS ROCKS. Sz. Bérczi¹, A. Gucsik², H. Hargitai³, A. Kereszturi³, Sz. Nagy³, ¹Eötvös University, Institute of Physics, Dept. Materials Physics, H-1117 Budapest, Pázmány Péter sétány 1/c., Hungary; (berczisani@ludens.elte.hu), ²Max Planck Institute for Chemistry, Department of Geochemistry, Becherweg 27, D-55128, Mainz, Germany, (gucsik@mpch-mainz.mpg.de), ³Eötvös Loránd University, Institute of Geography and Geology, H-1117 Budapest, Pázmány Péter sétány 1/c., Hungary.

Introduction: Because of the genetic, petrographic and geochemical similarities between shergottites and terrestrial basalts containing mantle xenolith rocks we may study several parallel effects on the "terrestrial shergottites" and Martian shergottites. The Martian shergottites form three main subgroups: the basaltic-shergottites (i.e. Shergotty itself), the picritic-shergottites or olivine-phyric shergottites (i.e. Northwest Africa 1068) and the lherzolitic or peridotitic shergottites (i.e. ALHA-77005). The three groups of shergottites have formation ages between 170 and 500 Mys. The corresponding terrestrial counterparts (here we studied those from Szentbékállá, North-Balaton Mountains, Hungary) are the host basalt, which is sometimes olivine-phyric, some of its inclusions (lherzolite, wehrlite, websterite and harzburgite). Such basalts also can be found in the North-Balaton Highland vicinity basaltic region and in Little Hungarian Plain and Tapolca Basin basalts.

The study of Martian meteorites is the main joint program of the HAS-JSPS group from Okayama University, Japan and of Eötvös University, Budapest and West Hungary University, Sopron, Hungary. In this framework we plan to carry out shergottite comparisons focused this paper on.

Hungarian Terrestrial "shergottites": the Szentbékállá series

Several basalt volcanic units in the North-Balaton Mountains, in the Little Hungarian Plain and other parts of the Carpathian Basin (Nógrád-Gömör Mts, Persány Mountains in Transylvania, Romania) contain mantle xenoliths. We selected the Szentbékállá locality as example counterparts for shergottites. Mantle xenoliths were collected and studied from the Szentbékállá basalt tuff and also from other basalts and tuffs of the North-Balaton Mountains region [1, 2]. Mantle xenoliths specimens, however, from Kapolcs, Szigliget, and Sitke were also studied.

Two types of lherzolites are the main ultramafic inclusion types in Szentbékállá: exhausted lherzolites with smaller grains size and protogranular lherzolites with lightly exhausted REE content. The first group is more harzburgitic in mineral composition because olivine and orthopyroxene are their main mineral constituents. The second – protogranular – group is composed of the four main mineral phases of the lherzolites: olivine, orthopyroxene, clinopyroxene and spinel. The exhausted lherzolites group is a good petrographic analog to the peridotitic-(lherzolitic)-shergottites, because they are similar to these harzburgitic-lherzolitic rocks. The series contains basalts with large olivine xenocrysts, too. These rocks are good mineralogical counterparts of the olivine-phyric shergottites also containing large olivine xenocrysts.

In this study the following specimens were our samples: Progran, Average-Lherzolite, Wehrlite and Spinel-pyroxenite. (A Dunite and a Layered-Lherzolite sample were also included from the xenoliths.) The host basalt samples of Szentbékállá, Szigliget and Kapolcs were also studied. INAA, electron microprobe and

petrographic microscopic studies were carried out on the samples.

We measured the REE content of the various xenolith types, of separated mineral components of the average lherzolite and the spinel-pyroxenite and of host basalts or tuffs.

Geochemical model for origin of Martian shergottites: Considering REE geochemistry of Martian shergottites Warren and Bridges [3] suggested a classification to the three subgroups. In this model the degree of assimilation of the crust components distinct those magmas coming from Martian mantle. This model is similar to that we proposed in 1984 for the Szentbékállá series of inclusions. When the Martian basaltic partial melts leave their source regions they exhaust it in some geochemical components, mainly REEs. According to the exhausting level they defined strongly (S), median (M) and lightly (L) exhausted shergottites. The S-shergottites are represented by QUE94201, the M-shergottites are by ALHA77005, and the L-shergottites by Shergotty and Zagami. (Although the L-shergottites can be also derived from the S-shergottites so, that uprising lava assimilated crust components with large REE content.)

Suggested source regions for olivine-phyric shergottites: The MER rovers discovered that a shergottite type may exist in the form of surface boulders along the trip way of Spirit in Gusev crater. McSween reported on the 36th LPSC that the olivine rich Martian basalts may be the counterparts of the olivine-phyric shergottites on the basis of the Pancam textural images, the miniTES and Mössbauer spectrometer data [4]. The olivines (phenocrysts) occur in visible sized porphyric form as (25 %) textural component of rocks Humphrey, Adirondack, and Mazatzal in the Gusev-crater. The Fe/Mg ratio of these olivines was also similar to that of olivine-phyric shergottites. Because of the spectral similarities of these rocks to the southern terra rocks on Mars, Spirit MER Team suggested that mainly such basalt that is the olivine-phyric shergottite forms the Noachian terra. According to Irving et al. (2005) the Tharsis Volcano Mountains are the sources of the olivine-phyric basalts.

Discussion of "Terrestrial" shergottites:

Peridotite is the basic component of both terrestrial and Martian mantle. From these mantles partial melts are separated and pour on the surface or crystallize in the upper crust. Basaltic or picritic lavas penetrate through the upper mantle and crust. Along their way they assimilate or loose some components. At the same time these lavas may convey fragments of the layers penetrated and the broken boulders are embedded as xenoliths in the host rocks. This transporting mechanism makes it possible to collect xenoliths samples of deeper layers of upper mantle, too.

The various xenoliths represent different formation mechanisms. On the basis of mineral composition and REE abundance pattern in the Szentbékállá series it is

possible to sketch the formation history of various xenolith types. On the basis of INAA REE measurements the petrologic genetics of the Progran, the Average-Lherzolite, the Wehrlite, the Spinel-pyroxenite (and the Dunite and the Layered-Lherzolite sample) were derived. Three main factors have affected the REE abundances of these ultramafic inclusions, also as shown for Martian shergottites by Warren and Bridges.

Sometimes, melt separates totally from its parental environment. In those localities, where it had been retained, the REE concentration increased. After separation, the REE concentration decreased exhausting the source region both in main minerals of partial melting, and REE elements in the whole parental region. In localities, where partial melts crystallized, the rock has elevated REE concentration. Finally, assimilation of components from the penetrated rocks may also change liquid composition [6].

The Szentbékállá series of ultramafic inclusions can be arranged according to these processes. The highest REE abundances characterize those samples which have originated by separation of the melt from the parental environment. Both basalt lavas poured onto surface and Spinel-pyroxenite samples crystallized in depths has such high REE abundances. The second group of samples consists of xenoliths which retained more (i.e. Layered lherzolites) or less (Wehrlite) of their lherzolitic composition in spite of the fact that more partial melts had accumulated – and later crystallized – in them, as compared those which had separated from them partially.

These factors are: partial melting from the mantle source, partial separation of the melted liquids from the source environment and assimilation on their way from mantle source to the surface.

REE almost totally partition into the melt during the partial melting process. The high REE concentrations originated in this way are transported with the melt. If the melt separates from the source region, moves away and crystallizes, the degree of partial melting is inversely related to the degree of partial melting [5].

The third group of mantle xenoliths consists of lherzolitic inclusions which in some degree has depleted

in components (as REE) which had gone into partial melts. The Average lherzolite, the Dunite sample may belong to this group. Probably the Progran sample is the less exhausted one among xenolith inclusions of Szentbékállá.

Summary:

Comparative studies between the “terrestrial shergottites” and Martian shergottites will give new dataset about the processes which formed Martian genetic sequence of igneous shergottite type rocks. During the studies of Martian meteorites in the joint program of the HAS-JSPS group from Okayama, Japan and Budapest-Sopron, Hungary will focus on this work in the next two years.

Acknowledgments: Thanks for HAS-JSPS/104 Fund for supporting our work.

References: [1] Bérczi Sz., Bérczi J. (1986): REE Content in the Szentbékállá Series of Peridotite Inclusions. *Acta Mineralogica et Petrologica Szeged*. XXVIII. p.61-74, [2] Sz. Bérczi, S. Hegyi, Gy. Hudoba, S. Józsa, Gy. Szakmány (2006): Planetary analog materials studies: Martian shergottites and their counterparts from the Szentbékállá series of mantle lherzolite inclusions and the host basalts in Hungary. XXXVII LPSC, #1122, LPI, Houston. [3] Warren, P. H., Bridges, J. C. (2005): Geochemical Subclassification of Shergottites and the Crustal Assimilation Model. 36th LPSC, #2098. LPI, Houston; [4] McSween, H. Y., Jr., Milam, K. A. (2005): Comparison of Olivine-rich Martian Basalts and Olivine-Phyric Shergottites. 36th LPSC, #1202. LPI, Houston; [5] Ringwood, A. E. (1975): Some aspects of the minor element chemistry of lunar mare basalts. *The Moon*. 12. 127-157. [6] Bérczi Sz. (1991): *Kristályoktól Bolygótestekig*. 210. old. Akadémiai Kiadó, Budapest.

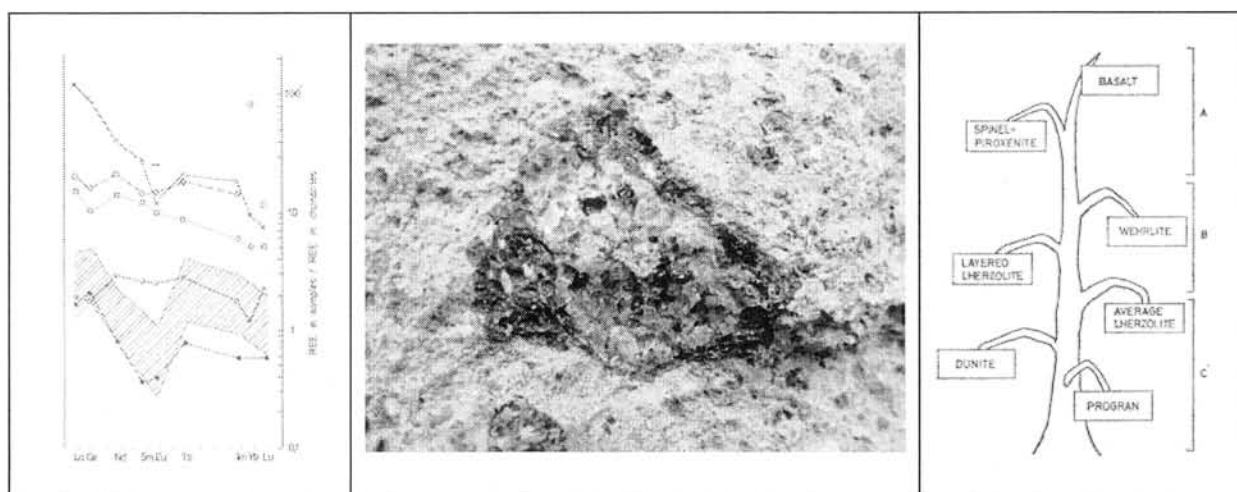


Fig. 1. Chondrite normalized REE abundances in the members of the Szentbékállá ultramafic inclusions. X – basalt, ŷ – wehrlite, □ – spinel-pyroxenite, ● – dunite, ○ – layered lherzolite.

Fig. 2. A basalt tuff with lherzolite xenolith ultramafic inclusion from Szentbékállá, North-Balaton region, Hungary.

Fig. 3. Arrangement of the Szentbékállá series of ultramafic inclusions according to separation of the melt from the parental environment, enrichment and exhausted nature of their REE abundances.

Possibility of transient liquid water on the dark subpolar dune fields of Mars. Sz. Bérczi (1,2), T. Pócs (1), A. Horváth (1,3), Gánti T.(1), A. Kereszturi (1,4), A. Sik (1,4), E. Szathmáry (1,5), (1) Collegium Budapest (Institute for Advanced Study), H-1014 Budapest, Szentháromság tér 2. Hungary, (2) Eötvös University, Inst. of Physics, Cosmic Mat. Sp. Res. Gr. H-1117 Budapest, Pázmány 1/a. Hungary, (3) Konkoly Observatory, H-1525 Budapest Pf. 67. Hungary, (4) Eötvös University, Dept. Physical Geography, H-1117 Budapest, Pázmány 1/c. Hungary, (5) Eötvös University, Dept. of Plant Taxonomy and Ecology, H-1117 Budapest, Pázmány 1/c. Hungary (bercziszeni@ludens.elte.hu)

1. Introduction: MGS, MEX, MRO images of the South Polar region of Mars revealed a wide range of defrosting phenomena. Studies of MOC, HRSC, HiRISE, MOLA and TES datasets made it possible for us to distinguish various transient phenomena: fans, Dalmatian spot, seepages and spiders. Some of these formations were interpreted alternatively by “dry-cold” and “wet” models. Here we compare and unify some of the models in order to explain a complex process in which dark spots are the source of linear “seepages-like” slope streaks in some dark dune fields.

2. Observations: In late winter or at early spring, growing dark structures appear on seasonal CO₂ ice cover. Some of them are diffuse and fan-shaped, while others are circular and confined slope streaks emanates from them [1].

The observed characteristics of the analyzed features are: (1) low albedo markings on the seasonal frost-covered surface where the albedo values are between 0.1 and 0.15 [2,3], (2) from winter to spring they grow in size and disappear with the disappearance of seasonal surface frost early summer, (3) occurrence on dark mantled terrain or on intracrater dark dune fields, (4) they show internal structures with a darker central part, surrounded by a lighter, outer ring, (5) their diameters are between a dozen and some hundred meters, (6) yearly reoccurrence of features in the analyzed sites is between 50-65%.

Besides morphometric analysis, the surface temperature was also investigated around these features. In connection with the changes in TES temperature records, two stages can be distinguished in the evolution of the phenomenon: 1. while the surface temperature is around 150 K, diffuse fans emanate from the dark features, 2. after the surface temperature starts to rise considerably (to about 200-240 K and more), the CO₂ ice cover becomes thinner and on the dune slopes sharp-edged, dark seepage-like structures can be observed.

3. Interpretation:

3.1. Kieffer's cold-dry model: Christensen et al. [4] interpreted the appearance and temporal development of some kinds of spots and fans by CO₂ defrosting and outburst. Outbursts are produced by the CO₂ jets in their model [5], according to which the early spring sunshine penetrates into the CO₂ ice and becomes absorbed at the bottom. There the absorbed solar heat increases the temperature and at the sublimation point of the CO₂, gas phase appears. The high-

pressure gas erupts from below the dry ice layer and releases itself into the atmosphere. During this jet activity the flowing gas drags fine dust particles from below the CO₂ ice. The stream of the outpouring gas jet may be modified by the winds which divert the stream of its way up and deposits dust in the direction of the wind. As a result, on the top if the ice fan-shaped tails are forming. These fans of dark material covering on the frosted surface witness both out bursting gas and wind affecting its pathway.

3.2. Wet model for the seepage-like structures: Confined, sharp edged spots and streaks are present when CO₂ only partly covers the surface or does not exist at all, suggesting a layered structure of the seasonal frost: thin H₂O ice below the thicker CO₂ ice [6]. We observed the appearance of streaks at some dark spots. They started from circular spots and followed descending direction. Our suggestion was that such streaks may be formed by the seepage of liquid water/brine below the thin ice crust. The atmospheric pressure on the observed dunes is too low (varies in a year between 4.6 and 5.5 mbar) for pure liquid water. But below the ice cover, dense brine may be liquid ephemerally. The formation of the descending streaks may also be the result of a moving fluid, moving wetted grains or even moving front of phase change.

4. Combined model: We propose a new model that incorporates both the Kieffer CO₂ jet [7] and DDS-seepage [8] models. The important stages of events in this synthetic model are the following: 1. During autumn the temperature decreases and first H₂O, later CO₂ freezes onto the surface forming a layered structure. 2. In springtime the sunshine causes the outburst of CO₂ gas jets (forming the fans), and the disappearance of the upper CO₂ layer there (forming dark spots). 3. As spring advances the stronger insolation absorbed by the dune surfaces warms up the dune grains at the localities where earlier the gas jets formed a hole in the CO₂ ice. In this stage a very thin ephemeral water layer may form on the grain surfaces, below the water ice, and between the liquid and the roofing solid ice thin water vapor layer may also appear. During this period the liquid layer itself, or the lubricated grains may seep down, or even the front of the phase change may move downward – forming the slope structures. 4. By the end of spring the surface ice disappears but between the grains ice or liquid water may still be present in some mm depth for a very brief period of time. 5. In the last phase all the near-surface H₂O is sublimated or evaporated.

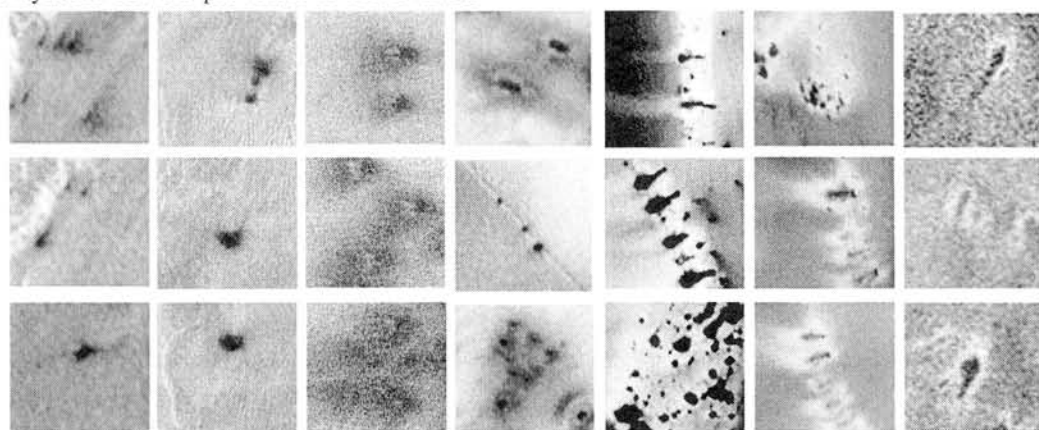
This synthetic model explains better the sequence of observational phenomena than either the dry gas jet or the wet seepage model could have done alone. Of course, there are still open questions: Why do early spots without fans exist? Can the water vapor and water ice insulate the liquid phase and from the cold air sufficiently? What is the possible composition of the seeping brines that can stay liquid at the low temperature?

5. Astrobiological outlook: Strongly bonded adsorbed water [9] may form thin veneer on the Martian surface. Solid-state greenhouse effect [10] may also increase the temperature, but the possible values are unknown. The heat insulator capacity of the thin water ice layer and the duration of the liquid phase is also unknown. The decreasing volume of the melting ice may produce a thin water vapor layer between the liquid water and the covering water ice, providing even lower heat conductivity for the full system. The possible presence of ephemeral near/surface seasonal liquid water on Mars is of high importance for any kind of possible life [5,11,12], but unfortunately the available data are not sufficient for a firm conclusion yet.

6. Acknowledgment: Authors thank the HRSC team for their support, and NASA and Malin Space Science Systems for the provision of MGS MOC

images. The ESA ECS-project No. 98004 is highly acknowledged.

7. References: [1] Horváth, A.; Kereszturi, A.; Bérczi, Sz.; Sik, A.; Pócs, T.; Gesztesi, A.; Gánti, T. Szathmáry, E. (2005) 36th LPSC, #1128. [2] Edgett, K. S. & Parker, T. J. (1998). 29th LPSC #1338. [3] Edgett, K.S., Supulver, K.D., Malin, M.C. (2000) 31th LPSC #4041. [4] Christensen, P. R., Kieffer, H. H., Titus, T. N. (2005) *AGU Fall Meeting*, #P23C-04. [5] Kieffer H.H., Christensen P.R., Timothy T.N. (2006) *Nature* 442. 793-796. [6] Gánti, T., Horváth, A., Bérczi, Sz., Gesztesi, A., Szathmáry E. (2003) *Origins of Life and Evolution of the Biosphere* 33: pp. 515-557. [7] Kieffer H.H., Christensen P.R., Timothy T.N. (2006) *Nature* 442. 793-796. [8] Horváth, A., Kereszturi, Á., Bérczi, Sz., Sik, A., Pócs, T., Gesztesi, A., Gánti, T., Szathmáry, E. (2005) 34th LPSC #1128. [9] Möhlmann D. (2004) *Icarus* 168, 318-323. [10] Kaufmann E., Kömle N., Kargl G. (2004) COSPAR04-A-02226. [11] Horvath A., Gánti T., Gesztesi A., Bérczi Sz., Szathmáry E. (2001) 32th LPSC, #1543. [12] Prieto-Ballesteros P.O., Fernandez-Remolar D.C., Rodríguez-Manfredi J.A. Selsis F., Manrubia S.C. (2006) *Astrobiology* 6. 651-667.



E0302386 1 M0300279 2 M0301512 3 M0302972 4 M0800984 5 M0807911 6 M0902370 7
 LS=152.51 LS=163.63 LS=167,51 LS=171.43 LS=218.37 LS=235.06 LS=241.20

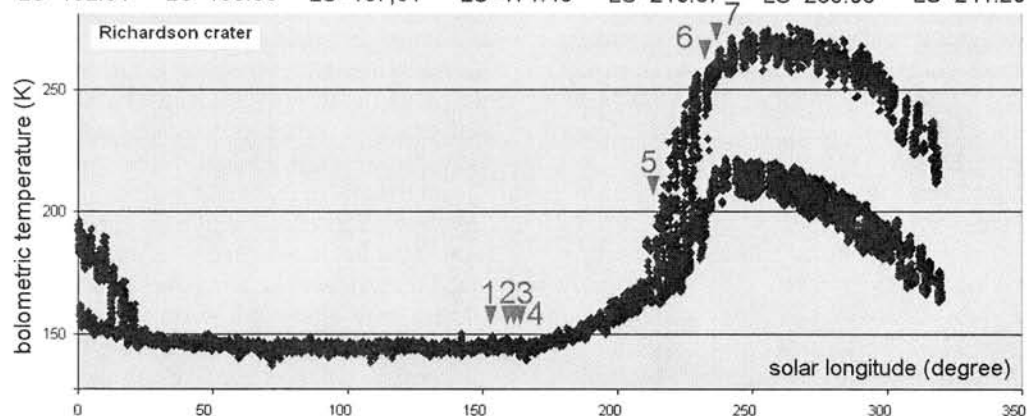


Figure: The correlation between TES bolometric temperatures (below) and spot morphology (top, where subsets are 300x300 m); 1,2,3,4 mark the first; 5,6,7 the second phase of spot development

Report on the first Korean Antarctic Meteorite Expedition to Martin Hills, Nash Hills, Pirrit Hills and Thiel Mountains. B.-G. Choi¹, J. I. Lee², H. Yoo³, J. Park⁴, N. Jang⁵, O. J. Kim¹ and S. Garrod⁶, ¹Dept. of Earth Science Education, Seoul National University, Seoul, Korea, ²Korea Polar Research Institute, Songdo-dong 7-50, Incheon, Korea, ³Susak-dong 108-803, Seoul, Korea, ⁴Shinyoung-dong 179-10, Seoul, Korea, ⁵Chungok-dong 851, Donghae, Korea, ⁶1 Riverside Cottages, Sedgwick, Cumbria, UK.

Abstract:

In January 2007, the first Korea Expedition for Antarctic meteorites (KOREAMET) conducted a search for meteorites on the blue ice fields at Martin Hills, Nash Hill, Pirrit Hills and Thiel Mountains. Total seven members were participated in the program including three scientists, two mountaineers, one Camera man and a guide. No meteorite was found in Martin, Nash and Pirrit Hills, and five new Antarctic meteorites were recovered at Moulton Escarpment, Thiel Mountains.

Martin Hills and Pirrit Hills:

The Martin Hills (82°00'S, 88°00'W) and Pirrit Hills (81°09'S, 85°05'W), West Antarctica have been searched for meteorites by [1] and one meteorite was found in each area. Since signs of ice melting, in the form of regelation portholes, were present at both sites and only two meteorites were recovered after a few days of expedition, [1] concluded that these sites are not ideal for meteorite recovery.

Between 10 and 23 January 2007, we spent 5 and 4 working days on the blue ice fields at Martin Hills and Pirrit Hills, respectively. We also visited Nash Hills (81°50'S, 89°10'W) that is near the Martin Hills and searched for meteorites for about 5 hours.

No meteorite was found in these areas. As noticed by [1], we also observed many regelation portholes on the blue ice fields in these areas. We made the same conclusion with [1] that the Martin, Nash and Pirrit Hills are not ideal places for meteorite hunting.

Thiel Mountains:

The blue ice fields on the Thiel Mountains, located near the western end of the Transantarctic Mountains, are well known for meteorite accumulation: total 61 meteorites including Thiel Mountains pallasite have been recovered from these areas by previous expeditions [2, 3].

We flew from the Patriot Hills using Twin-otter and spent 7 hours on the blue ice fields at Moulton Escarpment, Thiel Mountains (85°10'S, 94°33'W; Fig. 1) and found five meteorites. Masses of the meteorites vary from 193 to 432 gram: total mass is 1,395 gram. All of them are surrounded by fusion crust either completely or partially. According to their surface texture and magnetic susceptibilities [4], four of them may be ordinary chondrites (magnetic susceptibility = 64 to 147 x 10⁻³ SI unit; Fig. 2) and

one is more metal-rich (magnetic susceptibility = 217 x 10⁻³ SI unit).



Fig. 1. Aerial photo of Moulton Escarpment that KOREAMET visited.



Fig. 2. One of ordinary chondrites found in Moulton Escarpment by KOREAMET. The bottom is magnetic susceptibility (MS) meter showing that the meteorite is relatively high in MS and probably H-group.

Transportation and laboratory treatments:

The meteorites were put into Teflon bags and then vacuum sealed with plastic bags. They were contained in frozen container and transported to Korea by ship. The meteorites arrived at the lab on 24, April 2007. The bags were opened in Globe box filled with high purity N₂ gas in the laboratory. Now we are preparing samples for petrological study and oxygen isotope measurements. The results will be reported at the symposium.

Acknowledgements: We thank Ralph P. Harvey, Kevin Richter, Hideyasu Kojima, Bingkui Miao and Luigi Folco for useful discussions when we designed the expedition. We are also grateful to members of Antarctic Logistics and Expeditions for their help during the expedition. This work was supported by KOPRI PROJECT PE07020 (P.I., Lee) and KOSEF R01-2006-000-10522-0 (P.I., Choi).

References:

[1] Lee P. et al. (1999) *Lunar Planet. Sci.* 30, 2046. [2] Grossman J. N. (1994) *Meteoritics*, 29,100-143. [3] Russel S. S. et al. (2002) *Meteorit. Planet. Sci.*, 37, A157-A184. [4] Folco L. et al. (2006) *Meteorit. Planet. Sci.*, 41, 343-353.

Search for precompaction irradiation records in chondrules. J P Das and S. V. S. Murty, Physical Research Laboratory, Ahmedabad 380009 India.

Introduction:

Chondrules are some of the earliest formed silicate spherules in the solar system; by flash heating and rapid cooling. It is fairly established that chondrules are nebular products, were floating in the interplanetary space for some time before becoming part of their parent body, and are thus likely to have been exposed to the galactic cosmic rays as well as radiations from early Sun. These precompaction irradiations can manifest in the form of the presence of trapped solar gases [1] and/or higher cosmic ray exposure (CRE) ages for the chondrules [2, 3]. For example, solar origin was suggested for higher concentration of trapped ^{36}Ar observed in chondrules of enstatite chondrite Y-790001 [1].

Excess cosmogenic noble gases (^3He , ^{21}Ne and ^{38}Ar) in a chondrule from the H6 chondrite ALH76008 [2] and larger concentrations of cosmogenic noble gases in chondrules compared to matrix of eight ordinary chondrites are reported [3]. These differences in exposure ages can be due to different precompaction exposures of chondrules, or components thereof, before final assembly of the meteorite. These evidences of precompaction irradiations support the nebular formation of chondrules, in particular X-wind or shock wave models [4, 5] for chondrule formation.

Results:

Though chondrites with low CRE ages and with low parent body alteration effects are preferable for a clear recognition of precompaction irradiation records, in the present study, we selected meteorites from UOC, UEC and CC with CRE ages in the range of 2 to 34 Ma. A total 76 individual chondrules separated from ten chondrites belong to ordinary (6), enstatite (2) and carbonaceous (2) chondrites have been investigated. For 27 chondrules, which are > 1mg in weight, splits have been taken for chemical and mineralogical characterization. Nitrogen and noble gases in these chondrules were analyzed by laser probe mass spectrometer by standard procedures [6] and here we focus on noble gas results only. Measured values of noble gases mainly consist of trapped and *in-situ* (cosmogenic and/or radiogenic) components and by employing well established standard procedures these two components were decoupled.

Cosmogenic noble gases:

Chondrules from a given meteorite show variable amounts of cosmogenic noble gases (^3He , ^{21}Ne , ^{38}Ar) compared to their respective bulk chondrite as well as among themselves. Differences in ^3He abundance can be due to diffusive loss of He, which is also supported by lower abundance of

radiogenic ^4He (compared to the expected radiogenic component, for average U, Th and complete retention, over 4.6 Ga) in these chondrules.

For some cases, we found that chondrules are depleted in cosmogenic gases while for a few cases cosmogenic gases in chondrules are higher compared to bulk. As all the chondrules and bulk sample for a given meteorite come from the same depth (~ one gram sample), only cosmic ray fluence (flux x time) and/or variation in target element composition can be reasons for the observed variation in cosmogenic noble gases in chondrules. Production rates of cosmogenic noble gases normalize the abundances of these gases according to chemical composition of chondrules. Production rates for ^3He , ^{21}Ne and ^{38}Ar have been calculated for chemically characterized chondrules. For most chondrules, these production rates yielded CRE ages similar to their bulk. However, in some chondrules excess of cosmic ray exposure is required to explain higher abundances of cosmogenic noble gases.

Table 1 Chondrules from following meteorites show evidence of precompaction irradiation either as higher cosmic ray exposure or as presence of trapped solar gases.

| Meteorite | Number chondrules analysed | | |
|-----------|----------------------------|-----------------------------|-------------|
| | Noble Gases (+ EPMA) | Those showing | |
| | | Higher CRE (ΔT Ma) | Solar Gases |
| Dhajala | 22(5) | 1 (1 Ma) | 2 |
| Bjurböle | 9(5) | 3(2 Ma) | - |
| Allende | 16(7) | 2 (3 Ma) | 1 |
| Murray | 4(1) | 1 (1 Ma) | 1 |

For example, $^{21}\text{Ne}_c$ in MRY-1 chondrule is higher by a factor of 2 compared to Murray chondrite. Despite a higher Mg content of this chondrule, its calculated CRE age ($T_{21} = 3.7$ Ma) is higher compared to bulk ($T_{21} = 2.7$ Ma) by 37% (Table I). Similarly, Chondrules DH-5 (Dhajala), BB-29, BB-18, BB-15 (Bjurböle) ALD-14 and ALD-16 (Allende) also show evidence of precompaction cosmic ray exposure compared to their bulk and the precompaction exposure duration for these chondrules ranges from 1 to 3 Ma.

Trapped noble gases:

Most chondrules do not show an excess of $^{36}\text{Ar}_t$, which is indicative of the presence of solar gases [1], but have $(^{36}\text{Ar}/^{20}\text{Ne})_t$ that can be explained by mixing between Q and HL components [7]. However, a few chondrules show solar type noble gases. DH-8 and DH-11 chondrules from Dhajala chondrite show presence of solar type noble gases, which is reflected

in their $(^{36}\text{Ar}/^{20}\text{Ne})_t$ values, Ne-compositions and presence of excess ^4He .

For other chondrules, although some evidences of high abundances in gases are observed, it cannot be unambiguously attributed to solar type noble gases.

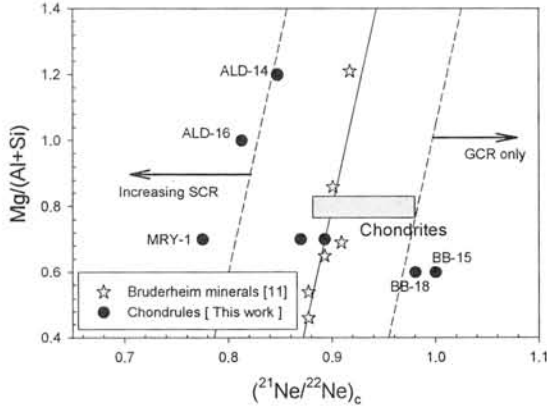


Fig. 1 $\text{Mg}/(\text{Al}+\text{Si})$ element concentration ratio against cosmogenic $(^{22}\text{Ne}/^{21}\text{Ne})_c$ for the chondrules with precompaction exposure history. The regression line represents the variation of $(^{22}\text{Ne}/^{21}\text{Ne})_c$ with $\text{Mg}/(\text{Al}+\text{Si})$ ratio as observed in mineral separates of Bruderheim meteorite [11]. The box represents the ranges of $^{21}\text{Ne}/^{22}\text{Ne}$ [12] and $\text{Mg}/(\text{Al}+\text{Si})$ [13] in chondrites. Chondrules MRY-1 and ALD-16 show possibility of SCR component acquired during precompaction exposure.

Discussion:

According to X-wind model, the formation of chondrule is suggested to have taken place near to the Sun around 0.06 AU [4]. Hence, it is expected that chondrules formed near the Sun would have signatures of solar environment. It is expected that chondrules should show evidences of exposure to solar cosmic rays in case of precompaction exposure. The cosmogenic ratio $(^{22}\text{Ne}/^{21}\text{Ne})_c$ serves as a sensitive indicator for a contribution from solar cosmic rays (SCR) [8,9].

However, this ratio is also sensitive to the target chemical composition [e.g. proportional to $\text{Mg}/(\text{Al}+\text{Si})$] of the sample [10]. We observed that chondrules with evidence of precompaction exposure, generally show higher values of $(^{22}\text{Ne}/^{21}\text{Ne})_c$. As shown in Fig. 1, $(^{22}\text{Ne}/^{21}\text{Ne})_c$ in most chondrules can be explained by variation in target chemistry and/or GCR exposure. However, chondrules ALD-16 and MRY-1 fall towards SCR exposure suggesting a two-stage exposure: a normal exposure as a meteoroid along with the chondrules from the same depth and a free space exposure prior to compaction.

From the present study, it is observed that only a few chondrules from a given meteorite show either higher CRE age or presence of solar gases or both. Such

sporadic occurrences might be better explained if the precompaction signatures are present in the chondrule precursors rather than on all phases in the chondrules. Depending on the loss or homogenization of gases, the records could have been erased in most chondrules.

References:

- [1] Okazaki et al., (2001) *Nature* 412, 795-798;
- [2] Polnau et al., (1999) *GCA* 63, 925-933;
- [3] Polnau et al., (2001) *GCA* 65, 1849-1866;
- [4] Shu et al., (1996) *Science* 271, 1545-1552;
- [5] Connolly Jr. H. C. and Love S. (1998) *Science* 280, 62-67.
- [6] Mahajan R. R. and Murty S. V. S. (2003) *Proc. Indian Acad. Sci. (EPS)* 112(1), 113-127;
- [7] Das J. P. and Murty S. V. S. (2004) *MAPS*, 39, A28.
- [8] Hohenberg et al., (1978) *Proc. Lunar Planet. Sci. Conf.* 9th 2311-2341;
- [9] Leya et al., (2000) *MAPS*, 35, 259-286.
- [10] Garrison et al., (1995) *Meteoritics*, 30, 738-747;
- [11] Bogard D. D. and Cressy P. J. (1973) *GCA* 37, 527-546;
- [12] Wieler R. (2002) *In Noble Gases in Geoche. & Cosmoche.*, pp. 844. The Min. Soc. of America, Washington;
- [13] Jarosewich E. (1990) *Meteoritics*, 25, 323-337.

Microtomographic, Petrologic and Isotopic Observations of the Accretion Histories of Chondrules. D. S. Ebel^{1,2}, N. Kita³, T. Ushikubo³, and M. K. Weisberg^{1,4}. ¹Dept. of Earth & Planetary Sci., American Museum of Natural History, Central Park West at 79th Street, New York, NY 10024 USA (debel@amnh.org), ² Lamont-Doherty Earth Observatory of Columbia University, ³Dept. of Geology & Geophysics, University of Wisconsin-Madison, 1215 W. Dayton St., Madison WI 53706-1692 (noriko@geology.wisc.edu), ⁴Dept. of Physical Sciences, Kingsborough College, City University of New York, Brooklyn, NY 11235. (mweisberg@kbcc.cuny.edu)

Introduction: The problem of chondrule and CAI origin is old [1-3], yet central to understanding the early solar system and planet formation [4-6]. Many experimental [7-10], theoretical [11-16], and observational [1,3,17-20] studies bear on this problem [21-22]. Here we summarize recent 3-dimensional (3D) tomographic observations of chondrule textures, and complementary surface (2D) chemical and isotopic measurements. These are interpreted in light of thermodynamic and magnetohydrodynamic calculations, experimental constraints, and results from observations.

Techniques: We have been systematically analyzing samples including the least equilibrated CR, CO, and CV and ordinary chondrite falls from the AMNH collection, using synchrotron x-ray computed microtomography (XR-CMT) at the Consortium for Advanced Radiation Sources beamline 13BM, Advanced Photon Source, Argonne National Lab [23]. Tomography on ~1 cm³ samples at 15-17 micron/voxel edge was followed by thick-section petrographic analysis on the AMNH Cameca SX100 electron microprobe (EMP), high-precision oxygen isotopic analysis using the CAMECA IMS 1280 at U. Wisconsin [24,25], and siderophile LA-ICPMS analysis at U. Maryland. Tomography allows location of chondrules with layered textures, and location of chondrule cores is known prior to actual slicing of the sample. Tomography allows accurate volumetric analysis of metal/silicate ratio in individual chondrules. Image analyses of x-ray intensity maps on surfaces are used to compute modes and bulk compositions in combination with 3-D data.

Results: Tomography reveals many concentric layered chondrules in all chondrite types: Multiple dusty rims (e.g., Semarkona LL3.0, Tagish Lake CI, Mokoia CV3), but particularly in the CR chondrites (e.g., Al Rais [26,27],); and concentric igneous layers (e.g., Renazzo, Acfer 139, both CR2 [23]). Chemical zoning outward from chondrule cores, observed in igneously layered Renazzo chondrules, includes increasing silica content and decreasing refractory siderophile content of metal grains [28-30]. Detailed study of O-isotopes and metal chemistry on a layered Renazzo chondrule (Ren1psA-ch3) show ¹⁶O-rich olivine and 13-17 wt% Ni metal in the core. Multiple forsterite-rich and metal-rich layers are observed in one large chondrule in Acfer139 [23-DVD-Fig.09].

Discussion: Tomographic analysis of 8 Renazzo

chondrules shows a wide range of metal/silicate ratio among chondrules. EMP data on 5 chondrules in 7 sections show Ni-, Co-rich core metal relative to rims. Modal calculations indicate different relative abundances of Si and Mg (pyroxene vs olivine) in these chondrules. Yet Renazzo has bulk solar Mg/Si, Co/Fe, Ni/Fe, and Si/Fe ratios. These facts are consistent with local formation of all the chondrules (and matrix) from a bulk material of solar composition; that is, ‘complementarity’ [31,32], consistent with chondrules “formed by relatively local events or processes in the early solar system, then accreted promptly into chondritic aggregations” [2, p. 367].

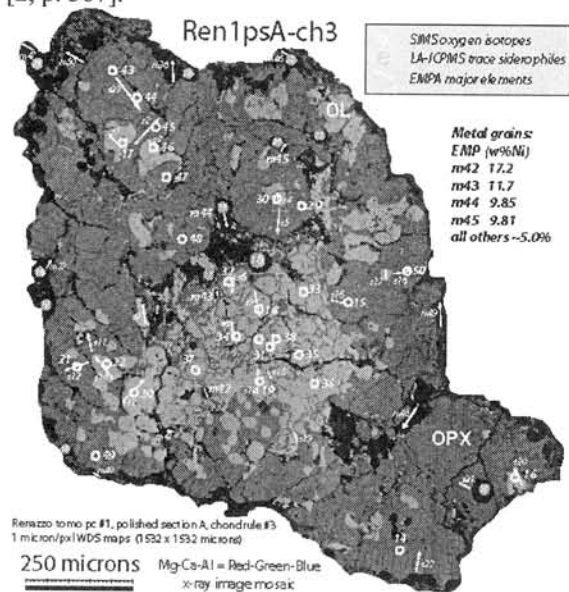


Fig 1: Data locations for chondrule 3 of study.

Sequential silicate/metal layers are present in some CR chondrules. These indicate repeated cycles of igneous rim formation, consistent with the annealing of dusty rims in multiple, short duration heating events. The presence of discrete, concentric internal metal layers is suggestive of early, high-temperature differentiation of metals from silicates in the protoplanetary disk.

Metal grains from chondrule Ren1psA-ch3 [Fig. 1] have compositions predicted for high-temperature equilibration with a near-solar composition vapor [15,33; Fig. 2], and these grains are adjacent to ¹⁶O-rich olivine in the chondrule core [Fig. 1]. Toward the rim, the olivines approach CR whole-rock oxygen isotopic compositions along a slope 1 line [Fig. 2], and metal grains become more ‘solar’ [Fig. 2]. These

systematic trends are consistent with accretion of dust or 'fluffy' CAIs and AOA's to make the core, melting and recrystallization of the core material, followed by accretion of a lower-temperature dust rim, its annealing and melting, and yet another cycle of dust accretion and melting.

These findings do not support a model for CR chondrule formation starting with FeO-rich silicates and Fe-rich sulfides, with volatilization, reduction, metal evaporation and recondensation to form observed metal grain systematics [34]. Our findings confirm that [2, p.368]: "The concentric arrangement of metal in these objects suggests that they grew, with successive layers being added by accretion or condensation."

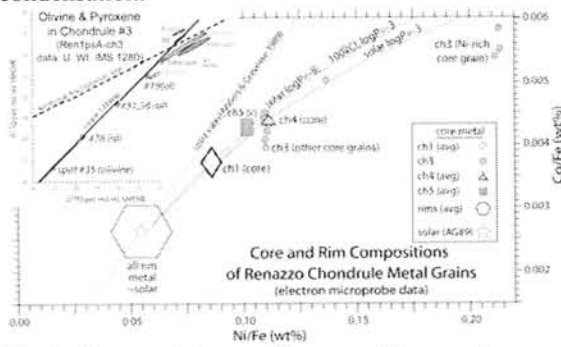


Fig 2: Core and rim metal compositions, and oxygen isotopic compositions, focus on chondrule #3 (Fig 1).

Chondrite parent bodies appear to have formed by local processes of hierarchical chondrule growth by dust accretion, annealing and melting, from bulk material of solar (chondritic) composition. Accretion of parent bodies from these local regions (e.g., annular rings in the disk) was efficient and rapid. The earliest generation of chondrules (or, the cores of eventual chondrules) was refractory-rich, and ^{16}O -rich. These chondrule cores were coated by layers of more pyroxene-normative, ^{16}O -poor dust, which records equilibration with disk gas at lower temperatures. Annealing and partial remelting affected these objects, reequilibrating cores and rim layers. Dusty and igneous layering records these processes, but imperfectly, in many chondrites. In the ordinary chondrites, the remelting and annealing process was more efficient and more completely obscures earlier events. Discrete metal and silicate layers in many CR chondrules suggests that metal and silicate fractionated, one from the other, early in the chondrule-forming period, and that layers of metal grains represent different accretionary episodes that occurred at successively lower temperatures.

The finding of refractory material in Stardust samples, and in the IDP record, indicate that protoplanetary matter was largely homogenized near the atomic scale, either in the ISM or in the disk. Although cometary material is compositionally similar to chondrite clasts, its texture appears finer. It may be that textural, rather than chemical or isotopic,

features of extraterrestrial materials are the most reliable clues to where and when they formed in the protoplanetary disk.

References: [1] Sorby H.C. (1877) *Nature* 15: 495-498. [2] Wood J.A. & McSween H.Y. Jr. (1977) In *Comets, Asteroids, Meteorites* (ed. A.H. Delsemme), 365-373. [3] Sears, D.W.G. (2004) *The Origin of Chondrules and Chondrites*. Cambridge U. Press. [4] Weidenschilling S.J. (1997) *Icarus* 127: 290-306. [5] Cuzzi J.N. & Alexander C.M.O'D. (2006) *Nature* 441: 483-485. [6] Dominik C., Blum J., Cuzzi J., Wurm G. (2007) In *Protostars and Planets V*, pp.783-800. [7] Hewins R. & Radomsky P.M. (1990) *Meteoritics* 25: 309-318. [8] Connolly H.C. Jr., Jones B.D., Hewins R.H. (1998) *Geochim. Cosmochim. Acta* 62: 2725-2735. [9] Osada Y. & Tsuchiyama A. (2001) *LPS XXXII*, #1334. [10] Wurm G. & Blum J. (2006) In *Planet Formation: Theory, Observations, and Experiments* (eds. H. Klahr & W. Brandner), Cambridge U. Press. [11] Desch S.J., and Connolly H.C. Jr. (2002) *Meteor. Planet. Sci.* 37: 183-207. [12] Jung M. K. R., Mac Low M.-M., Ebel D. S. (2004) *Astrophysical Journal*, 606, 532-541. [13] Nagahara H., Kita T.N., Ozawa K., Morishita Y. (1999) *Antarctic Meteorites XXIV*: 113-115. [14] Alexander C.M.O'D. (2004) *Geochim. Cosmochim. Acta*, 68, 3943-3969. [15] Ebel D.S. (2006) In *Meteorites and the Early Solar System II*, (D. Lauretta et al., eds.) University Arizona, Tucson. p. 253-277. [16] Ciesla F.J. (2007) arXiv:astro-ph/0702032v1 [17] Weisberg M.K., Prinz M., Clayton R.N. and Mayeda T.K. (1992) *Meteoritics* 27: 306 (abstract). [18] Huss G.R., Alexander C.M., Palme H., Bland P.A., Wasson J.T. (2005) In [22] pp. 701-731. [19] Weisberg M.K., Connolly H.C., Ebel D.S. (2004) *Meteor. Planet. Sci.*, 39, 1741-1753. [20] Wood, J.A. (1963) *Icarus* 2, 152-180. [21] Hewins R., Jones R.H., Scott E.R.D., eds. (1996) *Chondrules and the Protoplanetary Disk*. Cambridge University Press. [22] Krot A.N., Scott E. R. D., Reipurth B., eds. (2005) *Chondrites and the Protoplanetary Disk*, Astronomical Society of the Pacific Conf.Series, Vol. 341. [23] Ebel D.S. and Rivers M.L. (2007) *Meteor. Planet. Sci.* in press. [24] Kita N.T., Nagahara H., Tomomura S., Tachibana S., and Valley J.W. (2006) *LPSC XXXVII*, #1496. [25] Kita N.T., Ushikubo T., Fu B., Spicuzza M.J., Valley J.W. (2007) *LPSC XXXVIII*, #1981. [26] Weisberg, M.K., Prinz M., Clayton R.N., Mayeda T.K. (1992) *Meteoritics* 27: 306 (abs). [27] Prinz M., Weisberg M.K., Nehru C.E., Delaney J.S. (1985) *LPS XVI*, 677-678. [28] Campbell A. J., Zanda B., Perron C., Meibom A., Petaev M. I. (2005) In [22] pp. 407-431. [29] Humayun M., Campbell A.J., Zanda B. Bourot-Denise M. (2002) *Lunar Planet. Sci.* XXXIII, Abs. #1965. [30] Rubin A.E., Wasson J.T., Clayton R.N., Mayeda T.K. (1990) *Earth Planet. Sci. Lett.* 96: 247-255. [31] Bland P.A., Alard O., Benedix G.K., Kearsley A.T., Menzies O.N., Watt L.E., Rogers N.W. (2005) *Proc. National Acad. Sciences* 102: 13755-13760. [32] Palme H. (2001) *Phil. Trans. R. Soc. Lond. A.*, 259, 2061-2075. [33] Weinbruch S., Palme H., Spettel B. (2000) *Meteor. Planet. Sci.* 35: 161-171. [34] Zanda B., Bourot-Denise M., Hewins R.H., Cohen B.A., Delaney J.S., Humayun M., Campbell A.J. (2002) *Lunar Planet. Sci.* XXXIII, #1852.

This research was funded by NASA through NNG06GE42G (DSE). Use of the APS was supported by the U.S. Department of Energy, Office of Science, Office of Basic Energy Sciences, under Contract No. DE-AC02-06CH11357. We acknowledge use of NASA Astrophysics Data System Bibliographic Services.

Formation of symplectic inclusions by direct quenching of a high-FeO/(FeO+MgO) silicate liquid on the Moon. T. J. Fagan, ¹Waseda University, 1-6-1 Nishiwaseda, Shinjuku, Tokyo, Japan, fagan@waseda.jp.

Introduction:

Symplectites are fine-grained, complex intergrowths of two or more minerals sharing curved "worm-like" crystal boundaries. The intergrowths occur because of a combination of rapid breakdown of a pre-existing phase and short diffusion distances of the atoms forming the product phases [1,2]. Symplectites have been observed in terrestrial rocks and rocks returned from the Moon, as well as SNC meteorites and lunar meteorites [3-7].

Many symplectites reported from lunar and SNC meteorites and from the Apollo collection consist of intergrowths of fayalite, FeO-rich high-Ca pyroxene and a silica phase [6-9]. They are interpreted typically as the breakdown products of pyroxferroite, a metastable phase that can form during rapid cooling of a mafic silicate liquid that has evolved to compositions of high FeO/(MgO+FeO) [6-8]. Another model proposes that FeO-rich symplectites can form from exsolution and reactions among silicates and Fe-oxides [10]. In either case, the symplectites are a step removed from the true liquid compositions; thus characterization of late-stage liquids must be interpreted through intervening solid-state reactions.

Symplectites are present in lunar meteorite Northwest Africa 773 (NWA 773) and paired meteorites [9,11]. Most of these symplectites consist of intergrowths of stoichiometric fayalite, hedenbergite and silica, and I interpret them as products of breakdown of pyroxferroite (see above, and especially [8]). These formed during late stages of igneous differentiation, which resulted in the broad range of FeO/(FeO+MgO) observed in lithic clasts of the NWA 773 breccia [12]. However, some of the silica-rich symplectic phase is characterized by non-stoichiometric enrichments in K and Al. This paper proposes that this K- and Al-rich phase quenched directly from silica-rich liquid. If so, this phase allows a much more direct view of differentiated igneous liquid from the Moon (i.e., the phase quenched directly from a liquid without an intervening solid phase).

Analytical Methods:

The key observations of this study are from one polished thin section (PTS) of NWA 773 (on loan from M. Killgore of University of Arizona). An elemental map of the PTS was prepared for an earlier study [9] using a Cameca SX-50 electron microprobe at University of Hawaii. More detailed elemental and back-scattered electron (BSE) images and quantitative analyses were collected using a JEOL JXA-8900 electron microprobe at Waseda University. Quantitative analyses were collected by wavelength

dispersive spectroscopy using well-characterized oxide and silicate standards and the following beam conditions: 15 kV; 20 nA; focused (0 μ m) beam. Although the beam can be focused to diameters < 1 μ m, the activation volumes are probably on the order of one or two μ m. Thus, analyses of fine-grained, intergrown phases in the symplectite commonly yield low analytical totals.

Results and Discussion:

NWA 773 is composed of two distinct lithologies: an olivine cumulate and a breccia (Fig. 1). Several symplectite clasts are present in the breccia. One large clast is characterized by distinct relatively coarse euhedral crystals of plagioclase feldspar (An₇₀Or₀₄), and has a texturally distinct core composed of fayalite (Fa₉₈) with multiple inclusions. The fayalite core is surrounded by finely intergrown symplectite composed of homogeneously distributed hedenbergitic pyroxene, fayalitic olivine, and silica. Though analyses of these fine-grained minerals are different, they appear to be stoichiometric or nearly so. The Si-rich phase shows no evidence of significant enrichments in K or Al (Fig. 3). This symplectite is considered to be the equivalent of the pyroxferroite breakdown material of [7] and [8].

In contrast, the blebby, symplectite-like Si-rich inclusions in fayalite show significant enrichments in K and Al (Fig. 3). Obviously, this material is not silica. Moreover, quantitative analyses indicate that it does not match feldspar stoichiometry (~3.4 Si, 0.6 Al and 0.5 K atoms per 8 oxygen, respectively).

References:

- [1] Mongolip P. and Ashworth J.R. (1983) *Jour. Petrology* 24: 635-661.
- [2] Johnson C.D. and Carlson W.D. (1990) *Jour. Metamorphic Geology* 8: 697-717.
- [3] Papike J.J. et al. (1998) in *Planetary Materials* (Papike J.J., editor), *Reviews in Mineralogy* 36: p. 5-1 to 5-234.
- [4] Yanai K. and Kojima H. (1991) *Proc. NIPR Symp. Antarct. Meteorites* 4: 70-91.
- [5] Koeberl C. et al. (1993) *Proc. NIPR Symp. Antarct. Meteorites* 6: 14-34.
- [6] Aramovich C.J. et al. (2002) *Amer. Mineral.* 87: 1351-1359.
- [7] Rubin A.E. et al. (2000) *Geology* 28: 1011-1014.
- [8] Warren P.H. et al. (2004) *Meteorit. Planet. Sci.* 39: 137-156.
- [9] Fagan T.J. et al. (2003) *Meteorit. Planet. Sci.* 38: 529-554.
- [10] Xirouchakis D. et al. (2002) *Geochim. Cosmochim. Acta* 66: 1867-1880.
- [11] Zeigler R.A. et al. (2007) *Lunar Planet. Sci. Conf. XXXVIII: Abstract #2109*.
- [12] Fagan T.J. (2006) *NIPR Antarct. Meteorit.* XXX: 9-10.

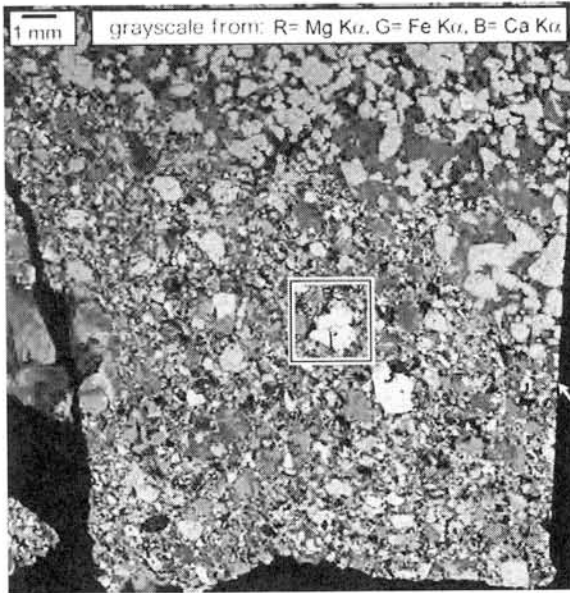


Fig. 1. NWA 773 breccia lithology shown in a grayscale image converted from R:G:B false color map with R = Mg, G = Fe and B = Ca $K\alpha$ X-ray intensities. The more Fe-rich minerals appear bright in this image. Olivine cumulate lithology is in upper right portion of image (arrow at right points to boundary between cumulate and breccia). Square highlights area shown in greater detail in Fig. 2.

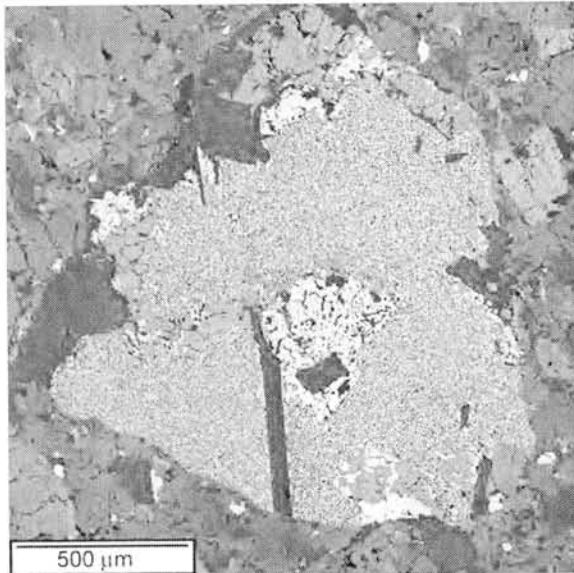


Fig. 2. Back-scattered electron (BSE) image of symplectite clast. This clast encloses a texturally distinct fayalite (Fa_{98}) with multiple inclusions (Fig. 3). Elongate, euhedral crystals with relatively dark BSE contrast are plagioclase feldspar ($An_{70}Or_{04}$).

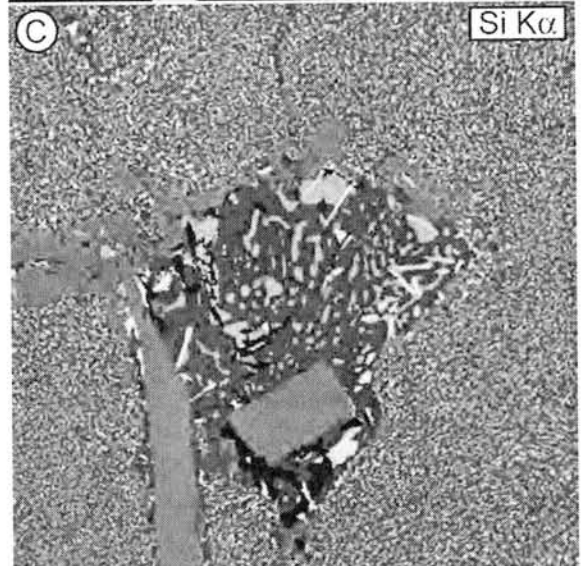
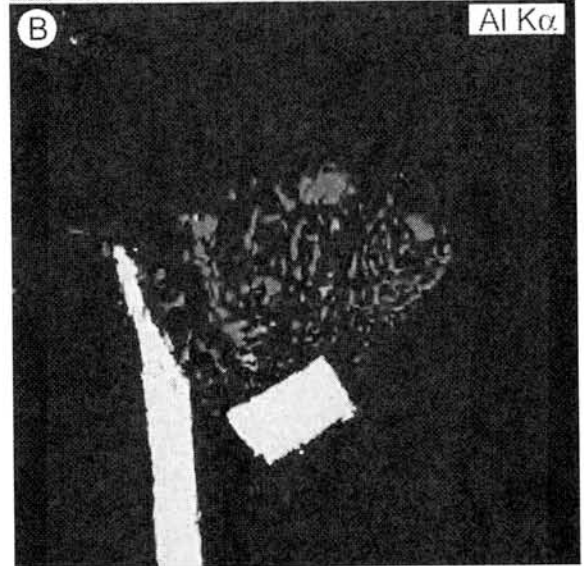
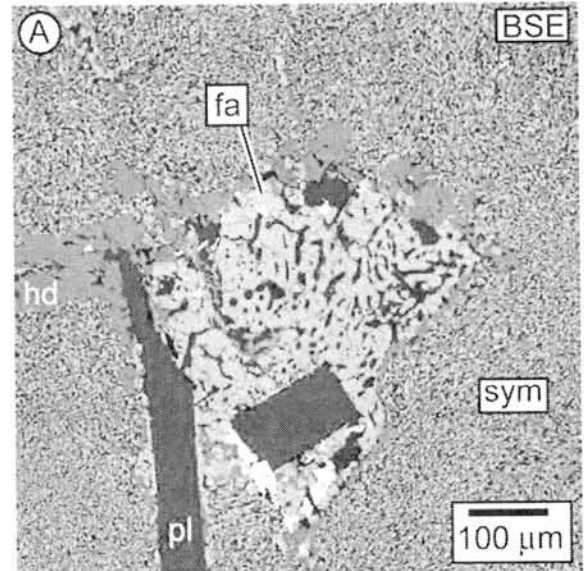


Fig. 3. Detailed views of fayalite clast with non-stoichiometric symplectitic inclusions (see Fig. 2). All images at the same scale (see A). Abbreviations: fa = fayalite; hd = hedenbergite pl = plagioclase feldspar; sym = symplectite.

Al-Mg and Fe-Ni isotope records in UOCs belonging to low petrologic grades.
J. N. Goswami, R. Mishra and N. G. Rudraswami, Physical Research Laboratory,
Ahmedabad-380 009, India. E-mail: goswami@prl.res.in

Introduction:

A combined study of Al-Mg and Fe-Ni isotope systematics in individual early solar system objects is useful to infer the solar system initial $^{60}\text{Fe}/^{56}\text{Fe}$ ratio that is not well constrained at present [1-4]. Being a stellar nucleosynthesis product, an accurate estimation of the initial abundance of ^{60}Fe will allow us to pinpoint the plausible stellar source of this nuclide and estimate the contribution from such a source to the inventory of the other short-lived nuclides present in the early solar system. This will also allow us to evaluate the possible role of ^{60}Fe as a heat source during the late evolution of meteorite parent bodies, after the exhaustion of the primary heat source, ^{26}Al . Even though CAIs have been studied extensively for Al-Mg isotope systematics, they are not ideal for studies of Fe-Ni isotope system. We have initiated a combined study of ^{26}Al and ^{60}Fe records in silicate chondrules from unequilibrated ordinary chondrites (UOCs) belonging to low petrologic grade (3.0-3.3). One expects pristine isotope records, undisturbed by thermal metamorphism, to be preserved in them. Even though troilite is a suitable phase for hosting ^{60}Fe [1, 2], the possibility of diffusion of Ni, particularly when troilite is in association with metal [2], makes silicates a better phase [3] and also facilitate study of both the Fe-Ni and Al-Mg isotope systems.

Sample description and analytical techniques:

Three thin sections of Antarctic meteorites belonging to LL group, Y-793596 (3.0), Y-791324 (3.1) and ALHA76004 (3.3), received from the National Institute of Polar Research (NIPR), have been selected for this study. In addition, we have also analyzed chondrules from Semarkona (LL3.0) and two L chondrites with petrologic grade 3.0 (LEW86134) and 3.05 (QUE97008) from the NASA collection of Antarctic meteorites. Results obtained from studies of ^{26}Al records in chondrules from ALHA76004 were reported last year [5] and data for Al-Mg isotopic systematics in the two UOCs belonging to the L group are also reported earlier [6]. We present here preliminary results obtained from the study of ^{60}Fe in chondrules from ALHA76004 and LEW86134. Initial results from studies of ^{60}Fe records in chondrules from Semarkona and QUE97008 were presented in 38th LPSC [7].

Carbon coated polished thin sections of the samples were mapped and analyzed using a scanning electron microscope equipped with energy dispersive X-ray spectrometer to identify chondrules that have Al-rich phases ($\text{Al}/\text{Mg}>20$) that are greater than ten

micron in size. Chemical compositions of these phases were also determined using a Cameca SX-100 electron microprobe. The Al-Mg isotope systematics in Al-rich phases, primarily glassy mesostasis and occasional plagioclase, were studied using a Cameca ims-4f secondary ion mass spectrometer following procedures described earlier [5, 6]. Repeated analyses were conducted on a given spot, as long as the Al/Mg ratio remained nearly constant, to improve analytical precision of the measured Mg isotopic ratios. Studies of Fe-Ni isotope systematics were done in olivine and pyroxene present in chondrules having excess ^{26}Mg from ^{26}Al decay. Intensities of $^{57}\text{Fe}^+$ and $^{60}\text{Ni}^+$ were measured initially to identify spots with high Fe/Ni ratios suitable for studies of Fe-Ni isotope systematics. The measurements were carried out at a mass resolution ($M/\Delta M$) of ~ 4000 sufficient to resolve the major interference in the masses (60,61,62) of interest (Fig.1). Contribution from hydrides is at less than per mil level. A focused primary $^{16}\text{O}^-$ beam with intensity $\geq 7\text{nA}$ was used to sputter secondary ions from the sample surface and the largest contrast aperture was used to maximize transmission. The count rates in ^{60}Ni ranged from 20 to 100 cps. We have also included mass 56.7 to monitor dynamic background during each analysis. Typical count times are: 5s($^{56.7}\text{Fe}$), 1s(^{57}Fe), 10s (^{60}Ni)

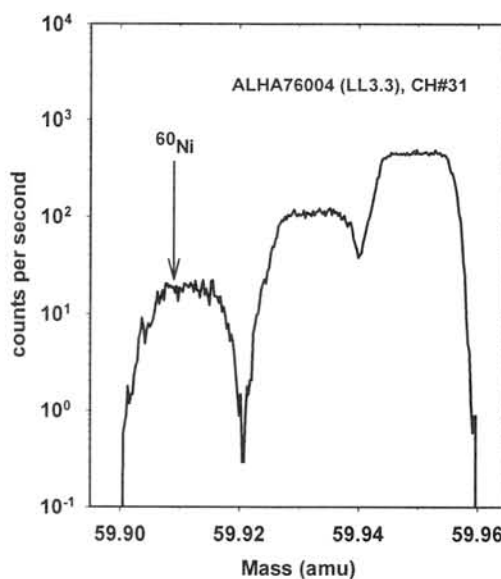


Fig.1. High-mass-resolution spectrum at mass 60 showing well-resolved ^{60}Ni peak in a chondrule from ALHA76004.

50s (^{61}Ni) and 20s (^{62}Ni). Each analysis consisted of 15 or 20 blocks of 5 cycles each through the above mass sequence. A typical analysis took about two hours (Fig. 2). Mass calibration was performed at

suitable intervals during each analysis. Repeated analyses were conducted in a given spot as long as the Fe/Ni ratio remained nearly constant. The measured $^{62}\text{Ni}/^{61}\text{Ni}$ ratio was used to infer the magnitude of instrumental mass fractionation for obtaining the true $^{60}\text{Ni}/^{61}\text{Ni}$ ratio. Reference values for Ni isotope ratios taken are 23.1004 (60/61) and 3.1759 (62/61), respectively.

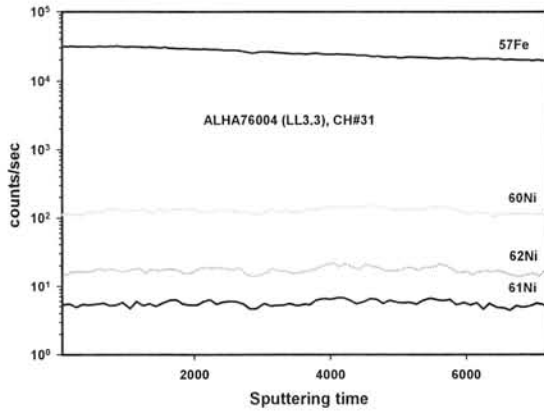


Fig. 2. Measured count rates for ^{57}Fe , ^{60}Ni , ^{61}Ni and ^{62}Ni during an analysis of a pyroxene in a chondrule from ALHA76004

Result and discussion:

Results obtained from Al-Mg isotope studies showed that two chondrules from Y-791324 (LL3.1) and four chondrules from ALHA76004 (LL3.3) have ^{26}Mg excess suggesting presence of ^{26}Al at the time of their formation. We are yet to locate suitable Al-rich phase in chondrules from Y-793596 (LL3.0) that will allow a meaningful study of ^{26}Al records. Several chondrules from Semarkona (LL3.0), LEW86134 (L3.0) and QUE97008 (L3.05) hosting radiogenic ^{26}Mg from ^{26}Al decay have also been identified. The initial $^{26}\text{Al}/^{27}\text{Al}$ values in these chondrules range from 0.5×10^{-5} to 1.9×10^{-5} [5,6,7]. Most of the chondrules hosting radiogenic ^{26}Mg are porphyritic olivine or porphyritic olivine-pyroxene in nature along with few porphyritic pyroxene chondrule and one bar-chondrule.

The study of Fe-Ni isotope systematics in chondrules hosting radiogenic ^{26}Mg was hampered by low Fe/Ni ratios (a few times 10^3) in most of the chondrule olivines except for the bar chondrule in LEW86134. A few pyroxenes in chondrules from Semarkona and ALHA76004 also have reasonable Fe/Ni ratio that allowed us to look for excess ^{60}Ni from the decay of ^{60}Fe in them. However, the derived initial $^{60}\text{Fe}/^{56}\text{Fe}$ values have low precision resulting from low count rates of ^{61}Ni and ^{62}Ni . We have reported earlier an initial $^{60}\text{Fe}/^{56}\text{Fe}$ value of $(2.31 \pm 1.8) \times 10^{-6}$ (2σ error) for a Semarkona chondrule [7]. The new results obtained from

analysis of pyroxenes in a chondrule from ALHA76004 and the barred-olivine chondrule in LEW861347, indicate presence of excess ^{60}Ni in them. The inferred initial $^{60}\text{Fe}/^{56}\text{Fe}$ ratios have large errors associated with them and encompass the range of values, $(2.2-3.7) \times 10^{-7}$ and $(9.2 \pm 2.4) \times 10^{-7}$, reported previously [2,3]. We are currently making efforts to improve the precision of our data by excluding ^{61}Ni from the analysis routine and correcting instrumental mass fractionation effect by studying Ni isotope systematics in relatively Ni-rich spots within the analyzed chondrule itself.

References:

- [1] Tachibana S. and Huss G. R (2003) *ApJL*, 588, 41-44.
- [2] Mostefaoui S. et al. (2005) *ApJ*, 625, 271-277.
- [3] Tachibana S. et al. (2006) *ApJL*, 639, 87-90.
- [4] Quitté G. et al. (2006) *MAPS*, 41, 5229.
- [5] Rudraswami N. G. and Goswami J. N. (2006) *13th Symp. Antarctic Meteorites*, 103-104.
- [6] Rudraswami N. G. and Goswami J. N. (2007) *EPSL*, 257, 231-244.
- [7] Goswami J. N. et al. (2007) *LPSC XXXVIII*, Abstract# 1943.

Advances in the characterization and classification of the least-metamorphosed chondrites.

J. N. Grossman¹, A. J. Brearley², M. Kimura³ and M. K. Weisberg⁴. ¹United States Geological Survey, 954 National Center, Reston, Virginia 20192, USA (jgrossman@usgs.gov); ²Dept. Earth and Planetary Sciences, University of New Mexico, Albuquerque, NM 87131, USA; ³Faculty of Science, Ibaraki University, Mito 310-8512, Japan; ⁴Department of Physical Sciences, Kingsborough College of the City University of New York, Brooklyn, NY 11235, USA.

Background:

In the 1960s, it was established that most chondrites had experienced secondary processing that modified their chemical, mineralogical, and petrological properties. The classification scheme of Van Schmus and Wood (VS&W) [1], now in universal use, distinguishes meteorites that were most altered from their original states from those that experienced the least alteration. Ordinary and enstatite chondrites, plus those carbonaceous chondrites classified by [2] as "type III," were placed in a metamorphic sequence from type 3 to type 6, where type 3 indicates the lowest degrees of heating and type 6 indicates the most. The other carbonaceous chondrites were all recognized to be primitive rocks in a chemical and petrological sense, and were placed in two discrete categories, types 1 and 2, again chosen to echo the roman-numeral chemical classification scheme of [2].

By 1980, it had become clear that a wide range of metamorphic effects was present just within type 3 chondrites. Accordingly, the VS&W classification scheme was modified by adding a decimal place after the 3, such that type 3.0 designated specimens that were essentially unmetamorphosed, whereas type 3.9 indicated those chondrites heated nearly to the same degree as a type 4 [3]. This scheme has been successfully applied and is widely accepted for ordinary (H, L, and LL) and CO carbonaceous chondrites, as well as for R chondrites and their clasts. It has been less successfully applied to enstatite (EH and EL) and CV chondrites because of their unusual mineralogy and complex parent-body histories, respectively.

The original meanings of types 1 and 2 in the VS&W scheme have also been modified over the last three decades. What were originally two separate categories are now widely taken to be a continuous aqueous alteration scale running backwards from type 2 (less altered) to type 1 (highly altered) [e.g., 4, 5], leading to the classification of numerous chondrites as CM1 and CM1/2 [6] and, in one case, CR1 [7]. One recent paper [8] subdivides type 2 for CM chondrites, running in the same reverse sense, from 2.9 (least altered) to 2.0 (highly altered). However, the latter scheme returns to the original VS&W concept of having type 2 as a discrete category from type 1, again confining the entire alteration scale for CMs to type 2 (and eliminating the category CM1).

Because the VS&W numbering scheme is used to represent two distinct variables, progressive heating in the sequence 3.0→3.9→4→6 and

progressive aqueous alteration in either the sequence 2→1 [4] or 2.9→2.0 [6], it does not allow for the description of metamorphic effects in chondrite groups that have experienced significant aqueous alteration or alteration effects in those that have experienced metamorphism.

In this paper, recent work is reviewed and presented, along with new data that can be used to further refine the metamorphic part of the VS&W classification scheme for the least-metamorphosed chondrites. A variety of metamorphic effects have been observed that allow the addition of a second decimal place to the VS&W scheme, running from type 3.00 to 3.15. Many of these changes are not subtle and involve major changes in the composition and mineralogy of chondritic components. This refined scale can and should be applied not just to the ordinary, CO, and CV chondrites, all of which are traditionally classified as type 3, but also to CH and CB chondrites, as well as those that have been classified as type 2 (CM and CR).

Metamorphic effects considered:

Olivine composition and zoning. All ferroan olivine (with >2 mol% Fa) in the most primitive chondrites, occurring in chondrules or as coarse isolated grains, contains a significant amount of Cr, generally >0.3 wt% expressed as Cr₂O₃. Ferroan olivine in ordinary chondrites contains ~40% more Cr than that in carbonaceous chondrites. In chondrites classified as near type 3.00, such as Semarkona and Acfer 094, as well as typical CM2 and CR2 chondrites, individual ferroan olivine grains show smooth igneous zoning profiles for Cr. New TEM studies of Semarkona show that the Cr is in solid solution in the olivine. In petrologic type 3.05 chondrites, olivine still preserves igneous zoning profiles, although the profiles show much more scatter than in type 3.00; TEM shows that very fine-scale exsolution of Cr-rich material has occurred parallel to the (001) planes in the olivine. Zoning profiles of olivine in type 3.10-3.15 chondrites show little or no preservation of igneous trends and are irregular; exsolution lamellae in these grains may be visible in the optical microscope in transmitted light. Small chromite grains and Cr-rich veinlets and rims are also common. Plots of the standard deviation vs. the mean Cr₂O₃ content in the cores of random olivine grains show systematic trends for carbonaceous and ordinary chondrites that can be used for classification purposes [9], although it is actually possible to make a reasonable classification based on the zoning found in single grains.

Matrix composition. The chemical composition of fine-grained matrix shows a dramatic change between petrologic type 3.00 and 3.05 in both ordinary and carbonaceous chondrites [9]. The sulfur content of matrix drops by at least a factor of 2 across this metamorphic range, although the physical mechanism by which this happens is not well understood. Re-evaluation of these data for CO chondrites may also allow further refinement of the metamorphic scale between types 3.00 and 3.10.

Chondrule mesostasis composition. During metamorphism from type 3.00 to 3.05, alkali elements exchange between chondrule mesostases and fine-grained matrix outside the chondrules. Glass is alkali-poor in type I chondrules in the least metamorphosed chondrites, but becomes greatly enriched during early stages of metamorphism [9]. This greatly affects the compositions of chondrules for alkalis (and other volatile elements) [10].

Metal composition and structure. Dramatic changes in the composition and structure of kamacite occur during the earliest stages of thermal metamorphism [11]. In type 3.00, chondrule kamacite is homogeneous and is probably martensite; most grains have nearly solar Co/Ni. In only slightly more metamorphosed chondrites, tiny Ni-rich domains appear, and grains are plessitic; grains may deviate greatly from solar Co/Ni, and tiny inclusions of phosphides and oxides may be present. By type 3.05, Ni-rich domains in chondrule metal grains have further coarsened, inclusions are common, and compositions scatter widely.

Amoeboid olivine inclusions (AOIs). Because AOIs were formed from very fine-grained (<10 μm) forsteritic olivine ($\text{Fa}_{0.1}$), they can also be sensitive indicators of the early stages of metamorphism in CO chondrites [12]. Between type 3.0 and 3.1, thin veins of fayalitic olivine develop in the olivine, probably during the earliest stages of the Fe-Mg exchange with surrounding fine-grained matrix [13].

State of organic matter. The organic matter in chondrites matures during thermal metamorphism and can be used to identify and classify the most primitive chondrites [14,15]. Significant changes in the Raman spectra of organic matter can be documented between type 3.00 and 3.05 in both ordinary and carbonaceous chondrites.

Applications:

The combined study of all of the above metamorphic effects is leading to an unprecedented refinement of the VS&W scale. It is now possible to place the most primitive type 3 chondrites in a metamorphic sequence, which is well calibrated across chondrite groups, e.g., Acfer 094, (CM/CO3.00), Semarkona, (LL3.01), ALH 77307 (CO3.03), QUE 97008 (LL3.05), Y-81020 (CO3.05). In addition, a more complete characterization of the metamorphic sequence of CO chondrites will now be possible, with the identification of at least three

meteorites in the previously unpopulated class, type 3.1 (A-881632, DOM 03238, NWA 2918).

A number of CM2 and CM2-like chondrites have been identified which may have experienced thermal metamorphism (e.g., [16]). Despite the relatively high temperatures previously proposed for these meteorites, studies of the Cr distribution in olivine of A-881655, PCA 91008, WIS 91600, Y-793321, and B-7904 show that none of these could have been metamorphosed beyond type 3.10, with B-7904 showing the most convincing evidence for heating to type 3.10 levels. Studies of the metal composition and structure in these meteorites are underway.

The metamorphic grades of CV chondrites have long been elusive due to complex parent-body processing. Studies of olivine and organic matter are helping to resolve this problem, as they are not highly sensitive to the alteration. No CV chondrite has yet been found that is below metamorphic grade 3.1, but work is still in the early stages.

The future of classification:

Because we are now able to discern subtle differences in the thermal histories of the least metamorphosed chondrites, a re-evaluation of the VS&W classification scheme is in order. Metamorphic effects have now been measured in some type 2 chondrites (see above), and it seems likely that other type 2 chondrites will be found which have also been heated above type 3.00 levels. Aqueous alteration effects have long been known in classical type 3 chondrites (e.g., Semarkona and some CV and CO chondrites). For this reason, The VS&W categories of type 1 and type 2 should now be considered as obsolete. An independent scale for aqueous alteration should be developed that applies to all chondrite groups. Most CM and CR chondrites are probably best described as type 3.00.

References: [1] Van Schmus W.R. and Wood J.A. (1967) GCA 31, 747-765; [2] Wiik H.B. (1956) GCA 9, 279-289; [3] Sears D.W.G. et al. (1980) Nature 287, 791-795; [4] McSween H. Y. (1979) Rev. Geophys. Space Phys. 17, 1059-1078. [5] Zolensky M.E. et al. (1997) GCA 61, 5099-5115. [6] Grady M.M. et al. (1987) Proc. 8th Symp. Ant. Met., 162-178. [7] Weisberg M.K. and Prinz M. (2000) Meteorit. Planet. Sci. 35, A168. [8] Rubin A.E. et al. (2007) GCA 71, 2361-2382. [9] Grossman J.N. and Brearley A.J. (2005) Meteorit. Planet. Sci., 40, 87-122. [10] Grossman J.N. et al. (2007) LPSC abstract #2000. [11] Kimura M., Grossman J.N. and Weisberg M. K. (2007) Meteorit. Planet. Sci., submitted. [12] Chizmadia L.J. et al. (2002) Meteorit. Planet. Sci. 37, 1781-1796. [13] Chizmadia and Bendersky (2006) LPSC abstract #2255. [14] Bonal L. et al. (2007) GCA 70, 1849-1863. [15] Bonal L. et al. (2007) GCA 71, 1605-1623. [16] Grossman et al. (2005) Meteorit. Planet. Sci. 40, 5169.

Cathodoluminescence imaging and spectral analyses of phosphates in the Martian meteorites: A review. A. Gucsik^{1*} (gucsik@mpch-mainz.mpg.de), W.J. Protheroe Jr.², J.A.R. Stirling³, K. Ninagawa⁴, H. Nishido⁵, T. Okumura⁵, N. Matsuda⁵, Sz. Bérczi⁶, Sz. Nagy⁶, A. Kereszturi⁶ and H. Hargitai⁶; ¹Max Planck Institute for Chemistry, Department of Geochemistry, Becherweg 27, D-55128, Mainz, Germany; ²AOL Inc., 8711 Beau Monde, Houston, TX 77099-1107, USA; ³Geological Survey of Canada, 601 Booth St., Ottawa, ONT, K1A 0E8, Canada; ⁴Department of Applied Physics, Okayama University of Science, 1-1 Ridai-cho, Okayama, 700-0005, Japan; ⁵Research Institute of Natural Sciences, Okayama University of Science, 1-1 Ridai-cho, Okayama, 700-0005, Japan; ⁶Eötvös Lóránd University of Budapest, H-1117 Budapest, Pázmány Péter sétány 1/c, Hungary.

Introduction: Cathodoluminescence (CL) is emission of visible light stimulated by energetic electrons. In the previous studies of CL properties of meteorites, it was demonstrated (compared to the standard optical microscopy) that its detection provides for a more complete investigation of specific minerals [1; and references therein]. The main purpose of the CL studies reported here is to provide an overview of the detailed mineralogical information the method provides on phosphates in Martian meteorites.

Samples and Experimental Procedure:

Y000593 nakhlite: We studied two polished thin sections of the Y000593 nakhlite Martian meteorite supplied from the National Institute of Polar Research (NIPR, Tokyo, Japan). SEM-CL imaging and CL spectral analyses were performed on the selected thin sections coated with a 20-nm thin film of carbon in order to avoid charge build-up. SEM-CL images were collected using a scanning electron microscope (SEM), JEOL 5410LV, equipped with a CL detector, Oxford Mono CL2, which comprises an integral 1200 grooves/mm grating monochromator attached to reflecting light guide with a retractable parabolic mirror. The operating conditions for all SEM-CL investigation as well as SEM and backscattered electron (BSE) microscopy were accelerating voltage: 15 kV, and 3.0-5.0 nA at room temperature. CL spectra were recorded in the wavelength range of 300-800 nm, with 1 nm resolution by the photon counting method using a photomultiplier detector, Hamamatsu Photonics R2228 [2].

ALH84001 sample N fragments (#3734, #3738, and #3739): CL spectra were collected with a micro-computer-based solid state multichannel analyzer, integrated with a linear CCD-array silicon detector from 200-1100 nm, interfaced to the optical chain of a MBX Cameca microprobe. The separated grains were also analyzed with a SX50 microprobe at 20kV, 10 nA and 10 second peak counting time. The small size and limited stability of the minerals do not allow for longer counting times and higher beam currents. The sample had already been damaged by previous use of high beam currents and exposure times [3].

The basics of cathodoluminescence emission: To understand the CL signal, it is useful to consider energy diagrams of the electromagnetic spectrum. According to Boggs et al. [4] the energy difference between the top of the valence band (VB) and the bottom of the conduction band (CB) in minerals corresponds to approximately 400 nm. Thus, even a small amount of energy from the electron beam causes electrons to enter the CB, from where they then fall back and move randomly through the crystal structure until they encounter a trap or recombination center. As electrons return to lower energy states via traps, they can produce photons with energies in the visible region of the spectrum, or even in the near-infrared region. If they return directly from the CB to the VB, they emit photons in the UV region of the spectrum. It is important to note that minerals are insulators or wide-band gap materials, in which the band gap between conduction and valence bands is too large for simple thermal excitation to promote electrons from lower-energy states to the higher-energy states [1].

Figure 1 shows the hypothetical energy level diagrams of the energetical transitions in an ideal mineral structure. The relationship between energy and wavelength (nm) can be expressed as follows: energy (eV) = 1239.8 wavelength (nm). The y-axis in Fig. 1 indicates the energy differences of the recombination centers or traps. The near-ultraviolet (near UV) range is located in the upper part of the band gap between the conduction and valence bands in Fig. 1. This indicates that higher energy (in eV) charge traps or recombination centers (broad bands between 200-400 nm) plot in the upper part of the band gap. The lower energy trap positions (bands between 400-800 nm) can be found in the center of the band gap or close to the valence band.

In general, CL is used in the Earth Sciences for the characterization of crystallization effects, identification of the microdeformations and 3-D mapping of trace elements in minerals.

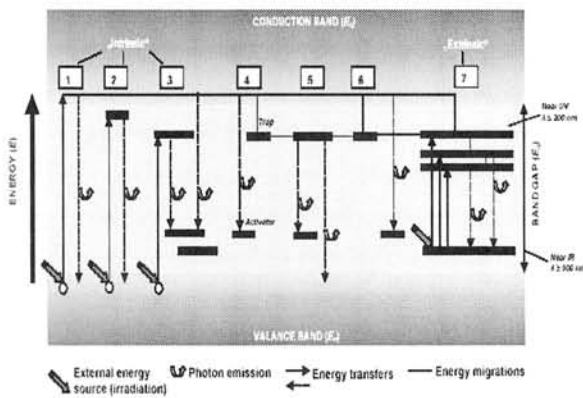


Figure 1. Idealized energy levels of CL emission centers [1, and personal communication with Lutz Nasdala, 2003].

Results and Discussion:

Y000593 nakhlite: Apatite (Ap) was found in the mesostasis of this nakhlite meteorite, which occurs in veins between mostly clinopyroxene (Cpx) and plagioclase (Pl) (Fig. 2a). A detailed mineralogical description of the Y-000593 nakhlite can be found in Imae et al [5]. In their petrological studies the apatite content (0.21 wt%) was determined by EPMA. This mineral appears as yellow CL color in the Luminoscope images and CL-bright areas in the SEM-CL images (Figs. 2b,c). CL spectral analysis and chemical composition data of apatite are shown in Figure 2c [2]. The results indicate that apatite is chloroapatite, which is an anhydrous phosphate containing unfamiliar anions F, Cl, O, OH, as well as cations of medium and large size: Mg, Cu, Zn, and Ca, Na, K, Ba, Pb [6].

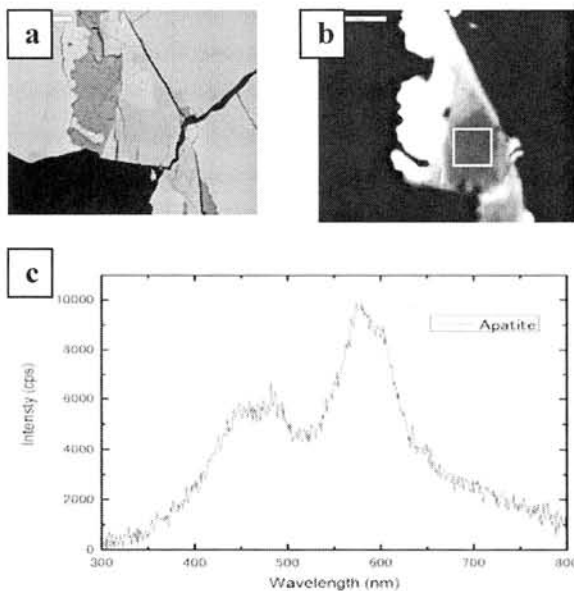


Figure 2. BSE (a), CL (b) images and CL spectrum (c) of Y000593 nakhlite sample. The width of the

images is approximately 500 μm [2].

ALH84001 sample N fragments (#3734, #3738, and #3739): The CL spectra results are very preliminary and the peaks have been labeled as indicated by the probe analysis and CL spectral analysis of standards at the Geological Survey of Canada. The results suggest the presence of the Ca-phosphates, which are often called whitlockite, which, however, are better described as β -Ca-phosphates as discussed by E. Dowty. It is important to note that the calculated formula closely matches that suggested by E. Dowty (Figs. 3a,b,c) [3,7].

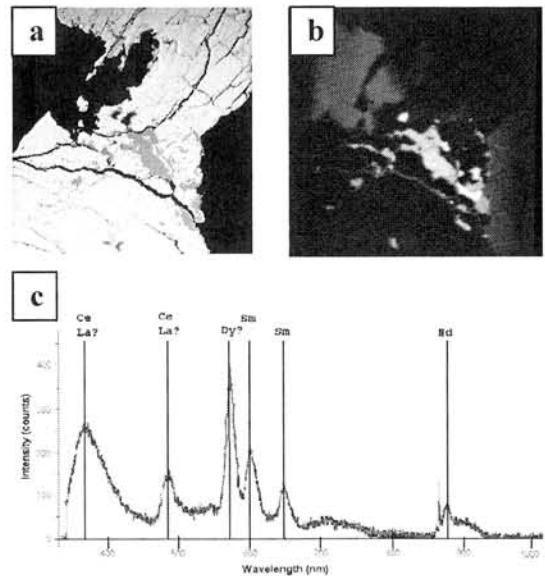


Figure 3. BSE (a), CL (b) images and CL spectrum (c) of ALH84001 (N fragments) sample. The width of the images is approximately 500 μm [3].

Conclusions: CL spectroscopy combined with SEM-CL imaging is a potentially powerful technique in the study of phosphates. As a consequence the CL technique can play a key role in in-situ investigations of records of atmospheric-fluid-rock interactions on Mars, such as formation of sulfates, carbonates, and phosphates.

Acknowledgement We are thankful to Prof. Kojima at National Institute for Polar Research (Tokyo, Japan) for offering a set of the Martian (Y-000593) meteorite.

References: [1] Marshall D.J. (1988) *Cathodoluminescence of geological materials*. Unwin Hyman, Boston, 146 pp. [2] Matsuda N., Gucsik A., Nishido H., Ninagawa K., Okumura T. and Kayama M. (2007) *LPS XXXVIII* Abstract #1061. [3] Protheroe W. J., Jr. and Stirling J. A. R. (2000) *LPS XXXI*, Abstract #2021. [4] Boggs S. et al (2001) *Meteoritics Planet. Sci.* 36, 783-797. [5] Imae N. et al. (2005) *Meteoritics Planet. Sci.*, 40, 1581-1598. [6] Barbarand J. and Pagel M. (2001) *Amer. Min.* 86, 473-484. [7] Dowty et al. (1977) *EPSL* 35, 347-351.

Introduction

Scientific concepts in Planetary Science are in large part based on theories and models. These theories are changing with new observations or models that describe reality better than previous ones. System of major theories – called paradigms [1]– are changing when new observations and better models made majority of scientists abandon an earlier system of theories. This event is called a paradigm shift.

Such systems of theory also exist in the minds of everyone. Concepts of a phenomenon – meteorites, for example – are different in the mind of a 5-year old child and a grown-up. During someone's education, "paradigm shifts" occur concerning these concepts, but these systems are not as coherent as scientific paradigms and not always fit the current scientific frames. Such change of cognitive schemes were first described by Piaget [2].

Mapping these mental concepts from kindergarten to university level reveal (1) the change in personal (more or less coherent) explanations of things (mostly in childhood), the effect of education: (2) in one part, the material the student memorized and the extent of distortion of the memorized curriculum; and (3) the impact of popular media: press, movies, books etc. From these three sources sometimes conflicting theories can be found in the concepts of students, one often not being able to erase or overwrite the other. Materials learned through formal education often results in passive knowledge that can not be used for solving real, practical problems or linking the memorized material to scenes seen at the cinema.

In formal education and also in scientific outreach – including press releases – it is essential to know the prior knowledge, concepts and misconceptions of the potential reader (in schools: student). Without having a picture of these, educational and outreach materials may be not effective.

The research of the conceptual framework (including preinstructional and informal knowledge) and misconceptions has a rich literature. Several research was made about the mental concepts and naive models of the Earth, Sun, Moon and the Day/Night cycle [3, 4, 5, 6].

Mapping concepts and misconceptions about meteorites

Large part of previous research concentrated on the ages of 3 to 12 years. The research presented here has the goal to map concepts and misconceptions from 3 to 23 years, from kindergarten to university level. The research was conducted in Budapest and Piliscsaba (the capital of Hungary and a small town 30 km North of Budapest).

In the research knowledge about meteorites was mapped. Since meteorites are part of the popular culture, children from very early age has a concept

about them. This concept is well grounded from an early age and is refined with new elements during the years of education (a good example to this refinement is the knowledge of the building material of meteorites). However, in a later stage new misconceptions may come in.

Questions

In the research we used informal discussion in kindergarten (audio recorded and typed later) and questionnaires for older students. For the older students, new questions were added.

The basic questions were the followings:

- What is a meteorite?
- What are meteorites made of?
- What is the size of meteorites?
- Where can you find meteorites?
- What happens when a meteorite reaches the surface of the Earth?
- What is the difference between meteorites and meteors?
- What is the relation of falling stars and meteorites?
- Which are the best known meteorites?
- What is the goal of the scientific research on meteorites?
- Draw the timeline of the life a meteorite.

Results

Some results from the research:

- children from a very early age have a general concept of what a meteorite is
 - at high school level even the difference of meteorites and meteors are clear to some of the students
 - there are clear age categories when a new information is built into the knowledge of meteorites
 - in several cases the answers reveal basic contradictions
 - the word "meteorite" can refer to asteroids, comets, meteoroids, meteors, meteorites or "transient" planetary bodies (Fig.1.) or even craters to many students
 - There is a confusion about where one can find a meteorite: in space or on Earth
 - At kindergarten level, falling stars and meteorites are clearly two separate phenomena. For some 15-16 years old, these two are "similar", to other 15-16 years old they have "no connection".
 - The extinction of dinosaurs are usually not linked to meteorites or and impact event at kindergarten; but they have other explanations.
 - Several students related the goal of meteorite research to avoiding large impact to Earth.
- The last result is not surprising, since the goal of real scientists of a particular field of study is often

poorly known by students, even at university level.

This and other results show the topics that should be explained or clarified and stressed in educational and outreach materials for the various ages. Visualization of such problems (like “the life of a meteorite”) is essential in this (Fig.1.).

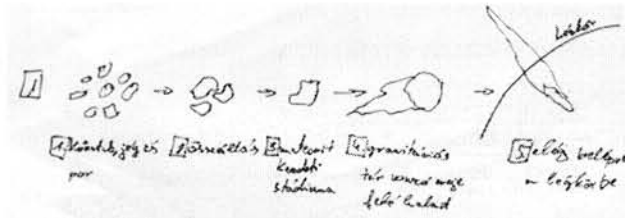


Fig 1. Life of a meteorite, drawn by a 16-year old student: explanations: “1: stone, ice and dust. 2: aggregation 3: early phase of a meteorite 4: it is moving towards the force of the gravitational field 5: it burns in the atmosphere”

Conclusion

The mental concept of meteorites is being mapped from kindergarten to university level. Several misconceptions and conflicting concepts have been found. The research reveals topics that should be clarified or that should have more emphasis in educational or outreach materials from elementary to university level. One of the most interesting result is about the goal of meteorite research in general: students have a poor understanding about what meteorite researchers are doing.

References:

- [1] Kuhn T. S. (1962) *The Structure of Scientific Revolutions*. University of Chicago Press
- [2] Piaget J. (1929) *The child's conceptions of the World*. Harcourt, Brace and Co. New York.
- [3] Nussbaum J and Novak J. D. (1976) An assessment of children's concepts of the earth utilizing structural interviews. *Science Education* 60, 535-550
- [4] Vosniadou S and Brewer W. F. (1990) A cross-cultural investigation of children's conceptions about the earth, the sun and the moon: Greek and American data. In: Mandl, H. et al. (ed.): *Learning and instruction: European research in an international context*. 605-629.
- [5] Vosniadou, S. (1994) Capturing and modeling the process of conceptual change. *Learning and instruction* 4. 1./ 45-69.
- [6] Korom E. (2005). *Fogalmi fejlődés és fogalmi váltás*. Műszaki Könyvkiadó, Budapest.

How much of the S-type asteroids are made of ordinary chondrite materials, and why are they so highly space-weathered? T. Hiroi¹, T. Nimura^{1,2,3}, Y. Ueda², S. Sasaki⁴, and C. M. Pieters¹, ¹Department of Geological Sciences, Brown University, Providence, RI 02912, USA, ²Department of Earth and Planetary Science, University of Tokyo, Tokyo 113-0033, ³JAXA Institute of Space and Aeronautical Sciences, 3-1-1 Yoshinodai, Sagami-hara, Kanagawa 229-8510, ⁴RISE Project, National Astronomical Observatory of Japan, Mizusawa-ku, Oshu City, Iwate 023-0861, Japan.

Introduction:

It has been an important question whether the high abundance of ordinary chondrites really reflects their abundance in the main asteroid belt. The abundant S-type asteroids and less abundant Q-type asteroids could contain significant amount of ordinary chondrite materials of different degrees of thermal metamorphism and space weathering [1]. On the other hand, there is a study that indicates only about 25 % of the main-belt S-type asteroids could be made of ordinary chondrite materials [2]. This issue is highly related to the nature of space weathering on pyroxene, olivine, and metallic iron.

Nature of space weathering:

According to examinations of lunar soil surfaces [3] successful simulations of space weathering [4, 5, 6] and, nanophase reduced iron (npFe⁰) particles in a vapor coating layer formed by micrometeorite bombardments or solar wind sputtering plays a significant role in the process. Because the concentration of npFe⁰ particles naturally depends of the abundance of Fe in the vapor, the bulk Fe content of the surface material is expected to affect the rate and possibly the limit of the degree of space weathering. There are unpublished experimental studies demonstrating such effect [7]. Therefore, understanding the rate of space weathering process and its compositional dependency gives us insight on asteroid surface composition.

Why are the S asteroids so space-weathered while Vesta looks fresh?

The answer to these questions could be simply that Vesta had a relatively recent large impact event which resurfaced the asteroid, and that only highly space-weathered asteroids are classified as S type. However, based on the above assumption that bulk Fe content highly dominates the rate of space weathering, another answer would be that Vesta's surface has no metallic iron if it is made of HED materials while the S asteroids have metallic iron available on the surface if they are made of either ordinary chondrite or stony-iron materials. In this context, the trend that olivine-rich asteroids look more space-weathered than pyroxene-rich ones [8] is due to the presence of metallic iron on the olivine-rich asteroids, probably because they expose core-mantle boundaries.

Are meteorites unbiased samples of asteroids?

If we are sampling the main asteroid belt materials evenly as meteorites, there should be a large amount of ordinary chondrite materials there. However, because collisional process works against physically weak and/or brittle materials, irons, stony-irons, and ordinary chondrites could have survived preferentially due to their strengths. On the other hand, asteroid surfaces also suffered heavy bombardments over 4.5 billion years, possibly losing any weak, outer crust and mantle with no metallic iron which strengthens them. In addition, the fact that iron meteorites are believed to have come from tens to hundreds of different basaltic parent bodies while there is only one intact basaltic asteroid (Vesta) still surviving to date suggests that physical strength played a major role in the collisional history of the main-belt asteroids. Furthermore, progress in understanding how small objects can be deviated from their orbits (e.g., YORP effect [9]) supports mixing of small asteroids. Therefore, it seems plausible to assume that our sampling of surface materials of the main-belt asteroids as meteorites is not so biased as a big picture. Recent discovery [10] of many more V-type asteroids which are not affiliated with Vesta also seems consistent with the discovery of some eucrites which cannot share the same parent body as the majority of HEDs [11, 12].

Conclusion:

The majority of the S asteroids may contain metallic iron. Estimating how much of them are made of ordinary chondrite materials would require high quality measurements of visible and near-IR reflectance spectra and a better method of estimating their compositions and degrees of space weathering.

References:

- [1] Binzel R. P. et al. (2004) *Icarus*, 170, 259-294.
- [2] Gaffey M. J. et al. (1993) *Icarus*, 106, 573-602.
- [3] Keller L. P. and McKay D. S. (1993) *Science*, 261, 1305-1307.
- [4] Cassidy W. and Hapke B. (1975) *Icarus*, 25, 371-383.
- [5] Yamada M. et al. (1999) *EPS*, 51, 1255-1265.
- [6] Sasaki S. et al. (2001) *Nature*, 410, 555-557.
- [7] Ueda Y. (personal communication).
- [8] Hiroi T. and Sasaki S. (2001) *Meteorit. & Planet. Sci.*, 36, 1587-1596.
- [9] Lowry S. P. (2007) *Science*, 316, 272-274.
- [10] Binzel R. P. et al. (2007) *Lunar Planet. Sci.*, 38, Abstract #1851.
- [11] Yamaguchi A. et al. (2002) *Science*, 296, 334-336.
- [12] Mittlefehldt D. W. (2005) *Meteorit. & Planet. Sci.*, 40, 665-677.

Yamato 000097 magnetic signature and comparison with other Iherzolitic shergottites: preliminary results

V. Hoffmann¹, M. Torii², M. Funaki³

¹Institute for Geosciences, University of Tübingen, Sigwartstrasse 10, 72076 Tübingen, and Department of Geosciences and Environment, University of München, Germany; Email: viktor.hoffmann@uni-tuebingen.de

² Department of Biosphere-Geosphere System Science, Okayama University of Science, Okayama, Japan.

³ National Institute of Polar Research, 9-10 Kaga 1 Itabashi, Tokyo 173-8515, Japan.

Introduction:

During the 41st JARE in 2000 3 new Martian meteorites were found and later identified as Iherzolitic shergottites Yamato (Y) 000027, Y000047 and Y000097 [1]. The 3 SNC were collected in a small area and are probably paired. A preliminary petrological description was given by [2]. Presently 8 Iherzolitic shergottites are identified (ALH77005, LEW 88516, Y793605, GRV99027 and GRV020090, from Antarctica, NWA1950 and NWA2646 from Sahara (hot desert) area, the situation of YA1075 is still unclear). In 2007 we were provided with a small chip of Y000097 by the Committee on Antarctic Meteorite Research of NIPR within the consortium study of the Y00 new Iherzolitic shergottites. Here we present preliminary results on the magnetic signature of Y000097. The data will be compared with new results from some other Iherzolitic shergottites.

Samples and experiments:

We received a 0.105gr chip of Y000097 (No. 82) for a detailed investigation of the magnetic properties. A series of investigations is conducted to study the following magnetic parameters: (1) magnetic susceptibility (MS), frequency and field dependence, anisotropy of MS, (2) NRM (natural magnetic remanence) and AF (alternating field) demagnetization for studying type and characteristics of NRM, (3) low temperature experiments of IRM (isothermal magnetic remanence) to 0.5K, (4) magnetic hysteresis and IRM at room-temperature (RT). Magnetic mineralogy and magnetic remanence carriers are characterized in detail by optical microscopy and micromagnetic observations, and will be supported later by mineralogical analyses (X-ray, EMPA, Raman spectroscopy etc.).

Results:

(1) Room temperature mass specific magnetic susceptibility was found to $695,9 \cdot 10^{-9} \text{ m}^3/\text{kg}$ (log value 2.84 ± 0.01) which fits well with the MS values of the SNC field within the stony meteorite MS diagram [3]. In comparison with MS of other Iherzolites, Y000097 represents more the lower end of the MS scale of the Iherzolitic shergottites (for example NWA 1950 3.34/3.54, NWA 2646 2.66). ALH77005 shows very scattered MS values (1784,9

– $4668,2 \cdot 10^{-9} \text{ m}^3/\text{kg}$ (log 3.25-3.67) probably reflecting its complicated history [4]. Interestingly Y000097 MS ($695,9 \cdot 10^{-9} \text{ m}^3/\text{kg}$) fits quite well with Y793605 MS ($794,9 \cdot 10^{-9} \text{ m}^3/\text{kg}$), log values are 2.84 and 2.90, respectively. Frequency (500/1000/2000/4000/8000 Hz) and magnetic field dependence (10/20/40/80/160 /320 A/m) of MS both show complicated behavior which is comparable to other Iherzolites. Anisotropy of MS is quite low ($P=1.061$) and is in the same range as most of the other Iherzolites and Y793605. Only for ALH77005 MS anisotropy is higher, in the range of 1.13-1.22 which might reflect the different shock histories of the Iherzolitic shergottites.

(2) NRM intensity of Y000097 is $4.704 \cdot 10^{-3} \text{ Am}^2/\text{kg}$, the AF demagnetization behavior does not point towards a stable remanence. However, more detailed test will have to be performed to see of which type the magnetic remanence is and to which extent it is influenced by shock.

(3) Low temperature IRM experiments were done on an MPMS to study the magneto mineralogy of Y000097. As for most of the studied SNC, a significant difference of the FC and ZFC curves is observed whereby higher IRM intensities are found for FC. Y000097 shows a transition around 80K in the FC behavior which can be attributed to ferri-chromite or titanomagnetite phases. No indication for Fe-sulfides is seen [5] report the presence of chromite, ilmenite and Ni-Fe sulfides in Y000097.

(4) Magnetic hysteresis, IRM acquisition and DC backfield curve was measured on a small fragment of our sample. Mrs/Ms was found to be 0.27 and Hcr/Hc was 2.72 which both lie in the range of the other known Iherzolites. In comparison with ALH77005 Hc and Hcr are double as high for Y000097, so the magnetic remanence is much harder. The hysteresis loop is slightly constricted which could point to two interacting magnetic phases.

(5) Optical microscopy and micromagnetic observations by using Bitter-technique gave the following results: large chromite particles (several μm to 10s of μm in size) of primary origin penetrated

by shock-induced mechanical cracks and shock melt veins, large Fe-sulfide grains (up to 10 μ m and more), also mechanically affected by shock), μ m-sized and submicron sized Fe-sulfide grains and melt droplets (spherules) found in larger Fe-S particles (partly shock-melted) and especially enriched in impact melt pockets and veins, micron-sized particles in a shock melt vein which could represent Fe/Fe-Ni rich phases. We believe that the chromites are of primary origin as are also the larger Fe-S particles. The tiny μ m- and submicron sized Fe-S particles and melt droplets (spherules) however might be a product of shock metamorphism and therefore of secondary origin. Micromagnetic experiments using Bitter technique did not show any ferri(o)magnetic phases within optical resolution limits (ca. 0.1 μ m). All chromites and Fe-sulfides analyzed in the microscope did not show any micromagnetic structures and were not covered by ferrofluid.

Summarizing our preliminary investigations, we assume that the carriers of the magnetic remanences in Y000097 might be dominated by spinel-phases, close to magnetite in chemical composition, in very small particle sizes, most likely in SD-PSD range. Proper candidates could be tiny, micron to submicron sized Fe-rich exolutions in the large chromite grains or in the olivines, for example.

Acknowledgements:

The investigations are performed within a consortium study of the Y00 new Iherzolitic shergottites organized by the Committee on Antarctic Meteorite Research of NIPR.

References:

[1] Meteorite Newsletter 14 (2006), edited by H. Kojima, NIPR. [2] Misawa K. et al., Antarctic Meteorites XXX (2006), 63-64. [3] Rochette P. et al., Quad. Geophys., 18 (2001), 31pp. [4] The Mars Meteorite Compendium (2007), compiled by C. Meyer, ARES, NASA, JSC. [5] Mikouchi T., Kurihara T.: Antarctic Meteorites 2007.

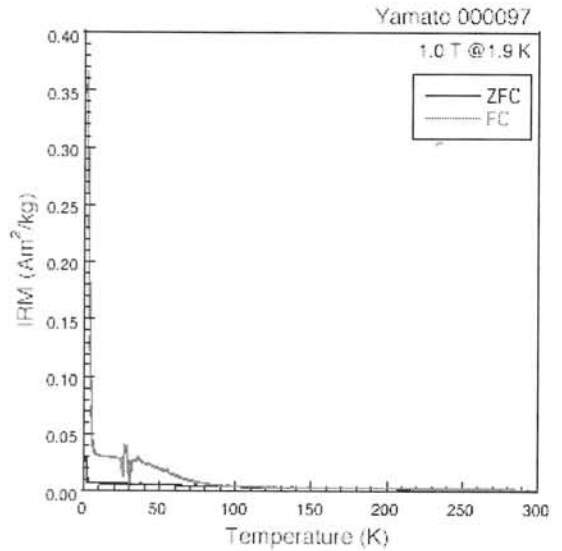


Fig. 1: Low-temperature IRM experiment as measured with MPMS: in the FC (field cooling) curve a clear transition at about 80K is seen.

Irradiation History of Gibeon Iron Meteorite

M. Honda¹, K. Nagao², and H. Nagai¹

¹Department of Chemistry, Nihon University, Setagaya, Tokyo, 156. ²Laboratory for Earthquake Chemistry, Graduate School of Science, Univ. of Tokyo, Bunkyo-ku, Tokyo 113-0033.

Introduction:

Gibeon Iron meteorite has been known to be one of the most popular large size iron meteorite. The fall was in the strewn field extending the longest distance of the long axis. The size has been estimated, from the north west to south east, to be longer than 400 km in the Republic of Namibia, the South West of Africa. The fall has been known since 1838. The total recovery has been estimated to be 21 tons in total, composing about 80 pieces of average 280 kg size fragments.

The class is IVA, and the chemical compositions have been well studied. The content of Ni, Ge, and Ga are low. The content of Phosphorus is low as about 0.04 %. The purity is relatively high and it is easy to keep fresh in a laboratory. The ductility is also high as possible bending to 180 degree.

Cosmic ray induced nuclides:

Nuclear and isotopic products have been studied in the large iron meteorite. Cosmogenic radioactive nuclides, ¹⁰Be, ³⁶Cl, and others, were determined by AMS methods. For stable light noble gases, such as He, Ne, and Ar isotopes were by a highly sensitive gas mass-spectrometry. For a non-volatile stable nuclide, Sc-45 has been determined by NAA, along with other irons. Based on the contents of radio-nuclides and light noble gases determined in the fragments, we realized the complex histories of the meteorite. By the data obtained with randomly examined about 100 species of fragment samples, we could classify the meteorite as a mixture of two sub groups, which have different irradiation histories.

The first group has a common irradiation history by cosmic rays for about 3 E8 years. On the other hand, group 2 is composed of the secondary products derived from fragments of the first group and having variable shorter exposure records of 1 – 0.1 E8 years, based on cosmogenic ¹⁰Be and the ²¹Ne. The many 2nd group members seem to be deficit of the considerable fractions of cosmogenic ³He or ³H products. All measured data have been examined comparing with some El Taco's reference samples.

Results:

The reasonable irradiation history of Gibeon can be obtained by assuming the extensive escape of the volatile products and by counting the atoms of stable non-volatile products. In this experiments we could select the number of Scandium-45 atoms as the stable product. The blank level of the natural scandium atoms can be estimated with the one of the lowest or deepest fragments of irons. Among the samples of the El Taco, the deepest, 2/5 was useful, supplying 0.002 ± 0.001 ppb Sc (and 0.09E-8 cc/g³He; also 0.001dpm/kg¹⁰Be).

References:

[1] Buchwald V. (1975) Handbook of Iron meteorite Vol.2, 584-593, [2] Noguchi et al (2004) Symposium NIPR June 3; Noguchi et al (2003) 13th Goldschmidt Symposium S.49. Sept. 11, Kurashiki, [3] Honda M. et al (1988) NIPR 1, 197-205. [4] Paneth F.A. et al (1952) 2, 300. [5] Nord R. and Zaehring J. (1972) Geochimii Analiticeskoy Chimii, Acad. Nauk 59

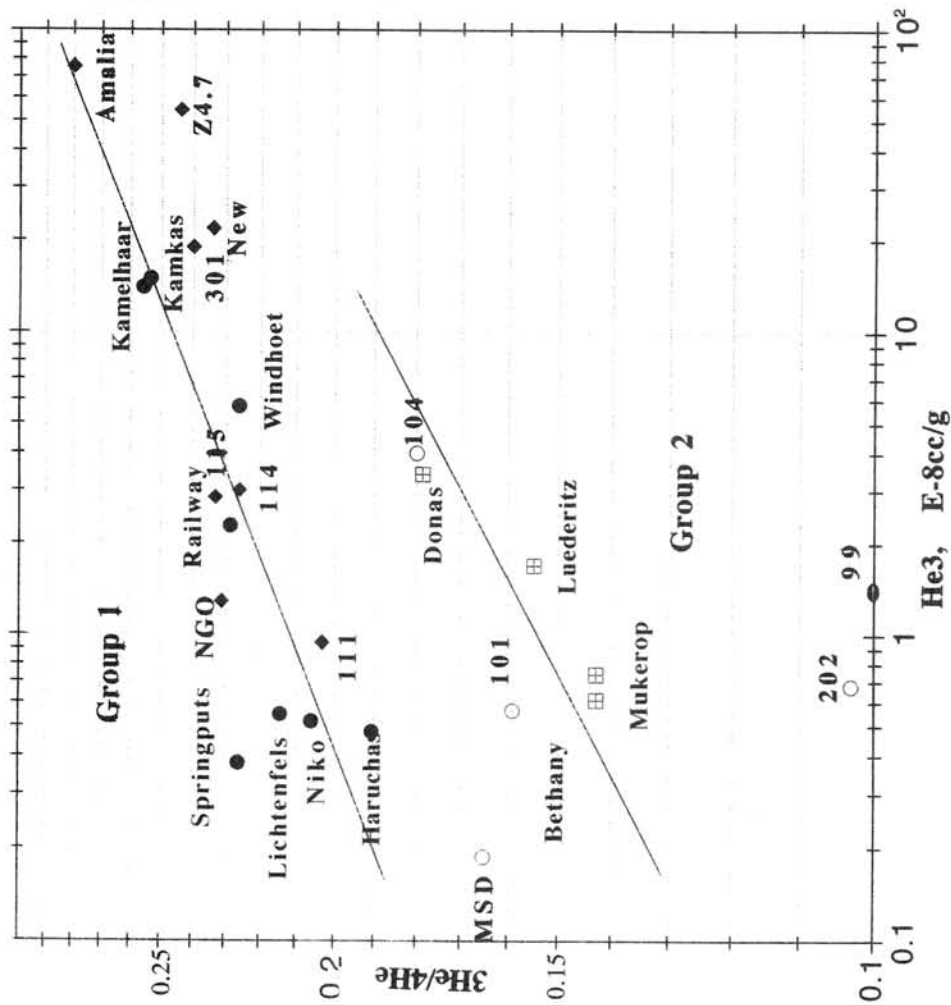


Fig. 2 Recovery sites and the He contents. by Nord and Zaehring. (Ref.5) and others.

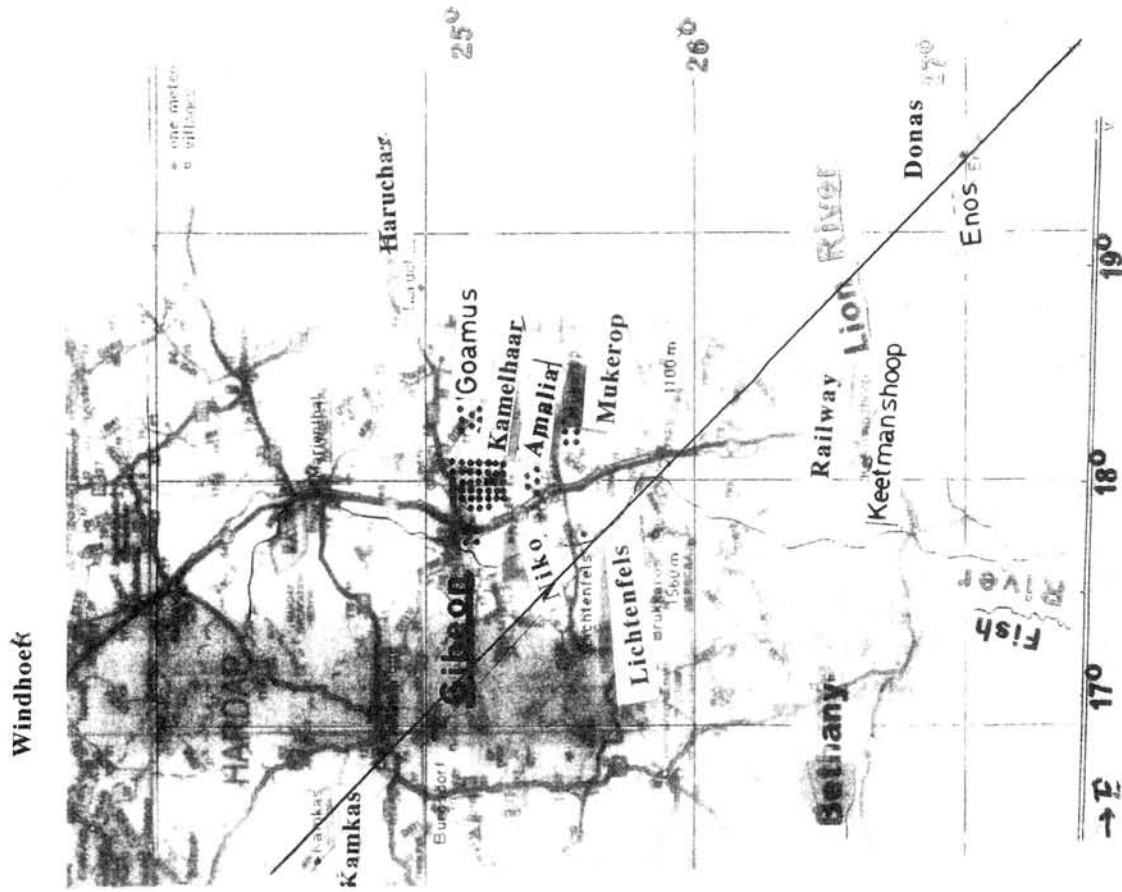


Fig.1 Strewfield of Gibeon. (Ref.1);

Magmatic inclusions in new lherzolithic shergottites, Y000027, Y000047, and Y000097.

Y. Ikeda¹ and N. Imae², ¹Department of Material and Biological Science, Ibaraki Univ. Mito 310-8512, Japan (y-ikeda@mx.ibaraki.ac.jp). ²National Institute of Polar Research, Kaga 1-9-10, Tokyo 173-8515, Japan.

Introduction:

Magmatic inclusions are common in martian meteorites [1], and the Yamato lherzolithic shergottites, Y00027, Y00047, and Y00097, contain many magmatic inclusions within minerals (Fig. 1). The magmatic inclusions always contain glass, and have crystallized from melts trapped in crystallizing host minerals. They represent the parent magma or fractionated melts of the Yamato lherzolithic shergottites.

Occurrence of magmatic inclusions:

Magmatic inclusions in the Yamato lherzolithic shergottites occur within olivine, pyroxene, chromite, and ilmenite. Their occurrence within a host mineral is different from those within other host minerals, and they are summarized in Table 1. Magmatic inclusions within olivine are common, and are rounded and large in comparison to those in other host minerals. They are always lined with pyroxene, although those within other host minerals are lacking in the rims. Those in pyroxene are rare, and they are irregular in shape and small. Those within chromite are rounded, although those in ilmenite are ellipsoidal.

Analytical methods:

Minerals and glasses in more than 50 magmatic inclusions were analyzed using an electron-probe microanalyser. Modal abundances of minerals and glasses in several large magmatic inclusions were obtained by using transparent cross-section papers which were put on back-scattered electron images of magmatic inclusions, and the bulk compositions of inclusions were estimated by the modal abundances, mineral densities, and mineral chemical compositions.

Results:

Pyroxenes in magmatic inclusions are mainly fassaitic and contain high Al₂O₃ contents from 3-15 wt%, although Al₂O₃ contents of pyroxenes in the host lithology are lower than 3 wt% (Fig. 2), and they are orthopyroxene, pigeonite, and augite. Glasses in magmatic inclusions show a wide range of chemical compositions. Compositions of glasses in magmatic inclusions within olivine are mostly Ca-Na-rich andesitic to dacitic melts, although Na-K-rich rhyolitic glasses rarely occur. Glasses in magmatic inclusions within pyroxene are Na-Ca-rich dacitic and Na-K-rich rhyolitic, but those within chromite and ilmenite are Na-K-rich rhyolitic. Silica blebs often occur in magmatic inclusions within olivine. The silica blebs are mostly

rounded or elongated ellipsoidal, and their sizes are smaller than a few tens of microns. They occur in close association with fractionated melts in magmatic inclusions, and could have formed by liquid immiscibility of fractionated melts which were enriched in silica and feldspar components. Plagioclase occurs in some magmatic inclusions within olivine, and it is very rare in martian meteorites that euhedral plagioclase crystals occur in magmatic inclusions. Phosphate occurs in magmatic inclusions within ferroan olivine and in close association with fractionated glass.

Bulk compositions of magmatic inclusions within magnesian olivine:

Bulk compositions of four large magmatic inclusions within magnesian olivine in the Yamato lherzolithic shergottites are shown in Table 2, indicating that they are andesitic in composition. Original trapped melts should be basaltic, and the trapped melts have abundantly precipitated wall olivine to have changed the melts to andesitic compositions. The andesitic melts crystallized pyroxenes and lined the inclusions with them to produce pyroxene rims surrounding the inclusions. Ferroan olivine grains may have trapped fractionated melts, and they sometimes contain phosphate crystals.

Magmatic inclusions in pyroxene, chromite, and ilmenite:

Magmatic inclusions within pyroxene, chromite, and ilmenite are lacking in rims surrounding the inclusions. They may represent fractionated melts which are poor in olivine components, and never crystallized olivine in their inclusions. Instead, trapped melts within pyroxenes have crystallized pyroxene as wall of the inclusions, and the pyroxene crystals grew in euhedral forms to result in irregular outlines of the inclusions within pyroxene. Although kaersutite occurs in magmatic inclusions within pyroxene of the ALH-77005 lherzolithic shergottite which is similar in lithology to the Yamato lherzolithic shergottite [2], no amphibole occur within pyroxene of the latter. Chromite trapped fractionated melts, and crystallized pyroxenes to produce Na-K-rich rhyolitic glass. Ilmenite grains also have trapped extremely fractionated melts, and the melts quenched as glass free from minerals.

References:

- [1] Ikeda Y. (2005) Antarctic Meteorite Research, No. 18, 170-187. [2] Ikeda Y. (1998) Petrology of magmatic silicate inclusions in the ALH 77005 lherzolithic shergottite, MAPS, 33, 803-812.

Table 1. Occurrences of magmatic inclusions within olivine (Type I), pyroxene (Type II), chromite (Type III), and ilmenite (Type IV) in the Yamato lherzolitic shergottites (Y000027, 000047, 000097) are different from each other.

| Type | Host Mineral | Shape and Size | Inclusion Rim | Mineral Assemblage | Composition of Glass |
|------|--------------|-------------------------|---------------|--|---|
| I | Olivine | Round 30-300 μ | Aug-Fas | Opx-Aug-Fas Glass, \pm Silica blebs \pm Pl, \pm Phosphate | Ca-Na-rich andesitic to dacitic, Na-K-rich dacitic to rhyolitic |
| II | Pyroxene | Irregular 5-50 μ | no | Glass \pm Pl, \pm Ilm | Na-Ca-rich dacitic and Na-K-rich rhyolitic |
| III | Chromite | Round 5-50 μ | no | Opx-Aug-Fas, Glass, \pm Silica blebs | Na-K-rich rhyolitic |
| IV | Ilmenite | Ellipse <100 μ | no | Glass | Na-K-rich rhyolitic |

Table 2. Bulk chemical compositions of four large magmatic inclusions (A, η , θ , ι) within magnesian olivine.

| | A | η | θ | ι | average |
|--------------------------------|-------|--------|----------|---------|---------|
| SiO ₂ | 59.76 | 62.65 | 61.82 | 63.13 | 61.84 |
| TiO ₂ | 1.84 | 1.35 | 1.09 | 1.11 | 1.35 |
| Al ₂ O ₃ | 15.05 | 14.38 | 12.87 | 15.95 | 14.56 |
| Cr ₂ O ₃ | 0.03 | 0.01 | 0.04 | 0.02 | 0.02 |
| FeO | 3.06 | 3.23 | 4.10 | 2.84 | 3.31 |
| MnO | 0.04 | 0.07 | 0.08 | 0.10 | 0.07 |
| MgO | 3.08 | 3.98 | 4.88 | 3.73 | 3.92 |
| CaO | 14.66 | 11.77 | 13.57 | 10.09 | 12.52 |
| Na ₂ O | 2.23 | 2.55 | 1.15 | 2.81 | 2.18 |
| K ₂ O | 0.23 | 0.03 | 0.41 | 0.22 | 0.22 |
| TOTAL | 99.98 | 100.03 | 100.00 | 99.99 | 100.00 |

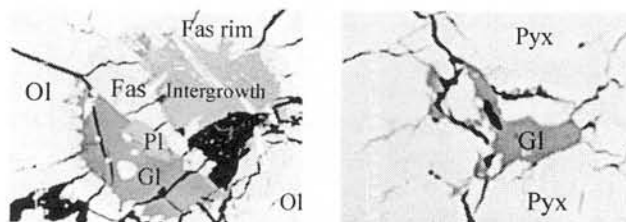
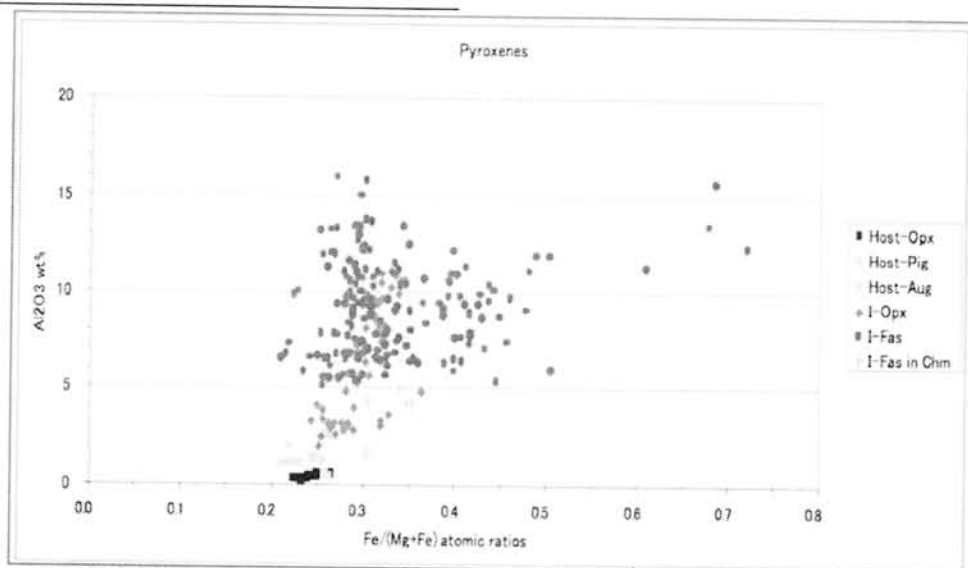


Fig. 1. Magmatic inclusions within olivine (left: rounded outline) and pyroxene (right: irregular outline). Fassaite (Fas), plagioclase (Pl), glass (Gl), intergrowth of plagioclase and silica (intergrowth), and pyroxene (Pyx).

Fig. 2. Al₂O₃ contents of pyroxenes in host lithology (Host-Pyx) and magmatic inclusions (I-Pyx) are plotted against their Mg-Fe ratios.



Petrography of new lherzolitic shergottites of Yamato (Y) 000027, Y000047, and Y000097: Main lithologies and shock veins. N. Imae¹ and Y. Ikeda², ¹National Institute of Polar Research, 9-10, Kaga 1-chome, Itabashi-ku, Tokyo 173-8515, Japan (imae@nipr.ac.jp). ²Department of Material and Biological Sciences, Ibaraki University, Mito 310-8512, Japan.

Introduction: Three paired specimens, Yamato (Y) 000027, Y000047, and Y000097, recovered from Antarctica in 2000 were recently added as sixth lherzolitic shergottites (Misawa et al. 2006). We are carrying out petrographical and mineralogical studies of these three meteorites as one of the consortium study.

Samples: Studied polished thin sections are Y000027 (41-1, made from two chips, 22 mm² of A and 16 mm² of B), Y000047 (41-1, 23 mm²), and Y000097 (51-1, 85 mm²).

Analytical methods: An electron probe microanalyzer was used for the chemical analyses of constituent phases. Defocused electron beam of 10 μm with 3 nA was used for the analyses of maskelynite and glass, and focused electron beam with 9 nA was used for other minerals. The Raman spectra for high pressure phases, pyroxenes and phosphates were obtained on polished thin sections using a Raman microspectrometer. Modes of constituent phases are obtained by counting the area using tracing papers with scale.

Results: 1. Modal abundances of constituent phases and textures. One portion (A) in the polished thin section (41-1) of Y000027 shergottite consists of poikilitic area, 34.2% [oikocrystic low Ca pyroxenes (69%) and rounded chadacrystic olivines (27%)], and interstitial area, 29.7% [pyroxenes (55.2%), olivines (34.7%), maskelynite (9.3%) and chromite (9.2%)]. The poikilitic and interstitial area are completely divided by one thick shock melt vein (36.1%), 1.8-2.2 mm in width and 5.3-5.4 mm in length. The other portion (B) consists of the poikilitic area (64.8%) and the interstitial area (35.2%). The polished thin section of Y000047 (41-1) consists entirely of poikilitic texture with thin shock veins (0.2%) and fusion crust (0.76%).

2. Constituent minerals of main two lithologies. The main constituent phases are pyroxenes (Fig. 1), olivines (Fa_{26.5-32} in poikilitic area, and Fa₃₀₋₃₅ in interstitial area), chromites (Fig. 2; V₂O₃=~0.6-1.2 in poikilitic, ~0.5-2.3 in interstitial, in wt%), and maskelynites (An₄₃₋₄₉Ab₄₀₋₅₄Or₁₋₃). Minor phases are ilmenite (with MgO of 1-1.4 wt% and V₂O₃ of 4.4-4.9 wt%), pyrrhotite (Fe₁₋₃S, δ=0.02-0.05), pentlandite, merrillite, a Cl-apatite, and a baddeleyite, occurring mainly in the interstitial area. Outlines of some maskelynites are rectangular or wedged in shape, and the compositional contrast with hour glass structure is observed under the backscattered electron image (Fig. 3).

3. Boundaries between poikilitic and interstitial areas. At the boundaries between poikilitic and interstitial areas in Y000097, a characteristic feature is observed: when the rim of an

oikocrystic pyroxene in poikilitic area faces with maskelynite, a continuous change of the single crystal of pyroxene from oikocrystic pyroxene to interstitial pyroxene is observed in the zoning from the core toward the rim (Fig. 4).

4. Shock veins. Y000027. The thick melt vein consists of abundant small euhedral magnesian olivines (38.1%), relict olivines (9%), a relict low Ca pyroxene (~0.7%), interstitial glass (48.5%), and chilled margin pyroxene (3.7%). Smaller euhedral magnesian olivines (≤8 μm) have compositions of Fa_{~18}, while larger ones (≥~8 μm) show reverse zoning with core more ferroan. Y000047. Networks of thin shock veins of ≤~60 μm are observed in Y000047 (Fig. 5). Several high pressure phases of low Ca pyroxenes are identified in them: three kinds of glasses and akimotoites (Figs. 6 and 7). The rounded aggregates of glasses in the center portion in the vein, each 2-3 μm in size, have variable compositions, including the most magnesian composition in the veins with Fe#~16 (Fig. 6). Akimotoites occur both in the periphery and in the center, and the composition of akimotoites in the center is the most ferroan in the shock vein (Fig. 6). Two kinds glasses of pyroxene in the center and the rim [2], and akimotoites in the rim have all similar Fe#s, however, there are slight differences for Al₂O₃ contents between these three phases (Fig. 6).

Discussion: 1. Poikilitic-interstitial boundaries The decrease of the Al₂O₃ content toward the surface for the rim pigeonite in Fig. 4 suggests that it co-crystallized with plagioclase, which changed maskelynite later.

2. Shock vein. Shock veins are observed only in maskelynite free areas. Several high pressure phases of low Ca magnesian-pyroxenes would have formed from an local impact melt of oikocrystic pyroxenes. The aggregates of grape-like glass are vitrified possibly from perovskite rather than majorite (Fig. 5) [3]. Although akimotoites are the subsolidus phase according to a high pressure phase diagram of MgSiO₃ [4], they would have solidified directly from impact melt, but did not formed by the solid state transformation from low Ca pyroxene, based on the occurrence and compositions (Figs. 5 and 6). The crystallization-solidification sequence was perovskite, rim-akimotoite, rim-glass, center-glass, and finally center-akimotoite in this order.

Acknowledgment: We are grateful to Prof. M Kimura for discussions.

References: [1] Misawa K. et al. (2006) *Ant. Met.*, 30, 63-64. [2] Chen M. et al. (2004) *MAPS*, 39, 1797-1808. [3] Sharp T. G. et al. (1997) *Science*, 277, 352-355. [4] Gasparik T. A. (1990) *Am. Min.*, 75, 1080-1091.

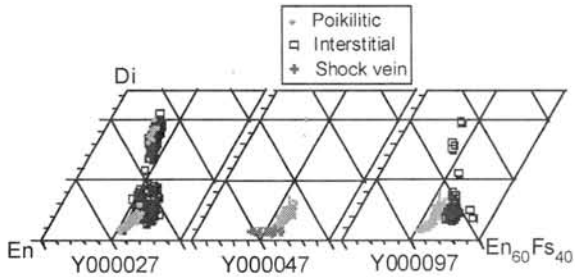


Fig. 1. Pyroxene compositions.

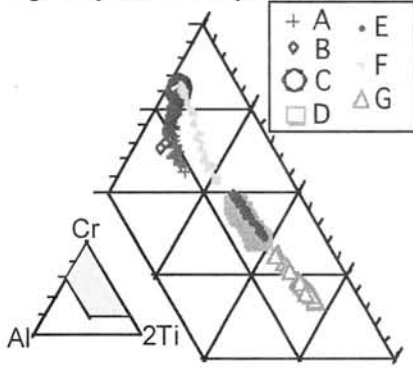


Fig. 2. Chromites in Y000027 (wt% ratio). Grain A (enclosed in pyroxene-olivine, Mg#=19-23), B (in pyroxene, 23-27), and C (in pyroxene, 25-27.5) is chromites in poikilitic area, and D (in pyroxene, 12-17), E (in olivine, 11-13), F (in maskelynite, 17-20), and G (in maskelynite-pyroxene, 11-13) in interstitial area.

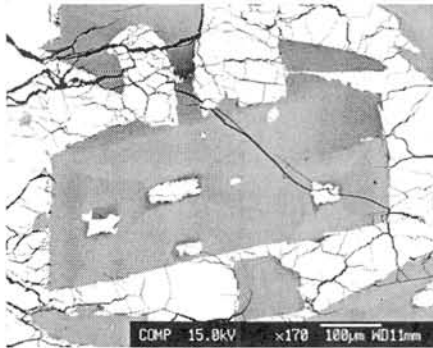


Fig. 3. Maskelynite showing hour glass structure in Y000097. Lighter portion is anorthite-component richer, and darker portion is albite-component richer.

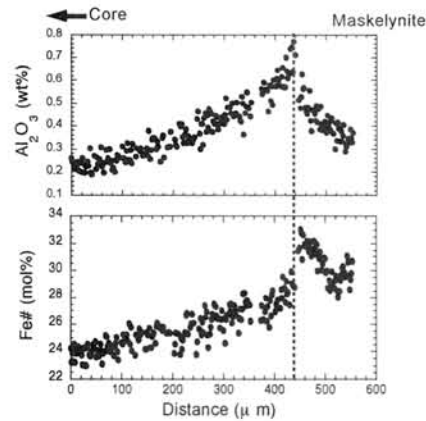


Fig. 4. Chemical zoning of an oikocrystic pyroxene in Y000097.

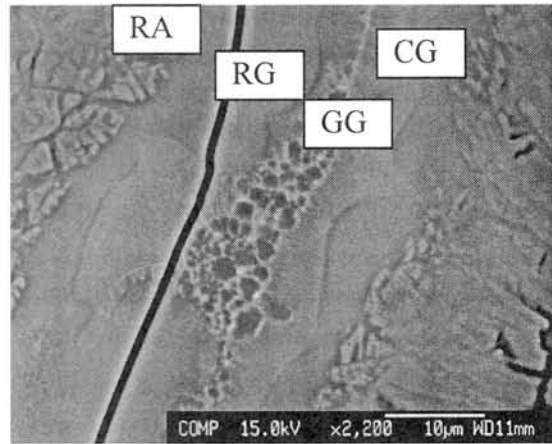


Fig. 5. High pressure phases in the shock vein in Y000047. GG: grape glass. CG: center glass. RG: rim glass. RA: rim akimotoite.

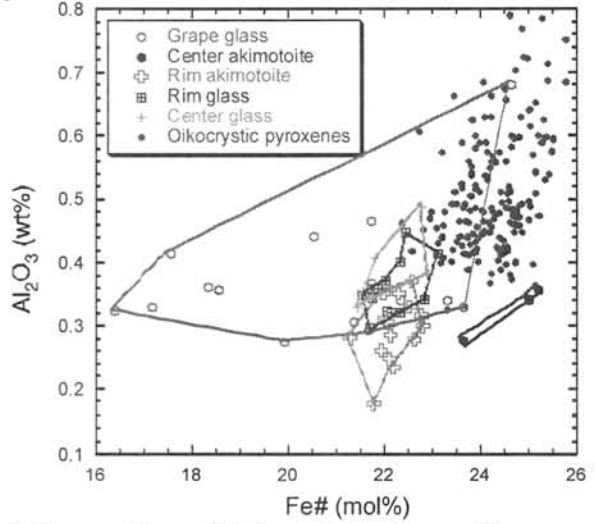


Fig. 6. Compositions of high pressure phases of low Ca pyroxene and low Ca pyroxenes in Y000047.

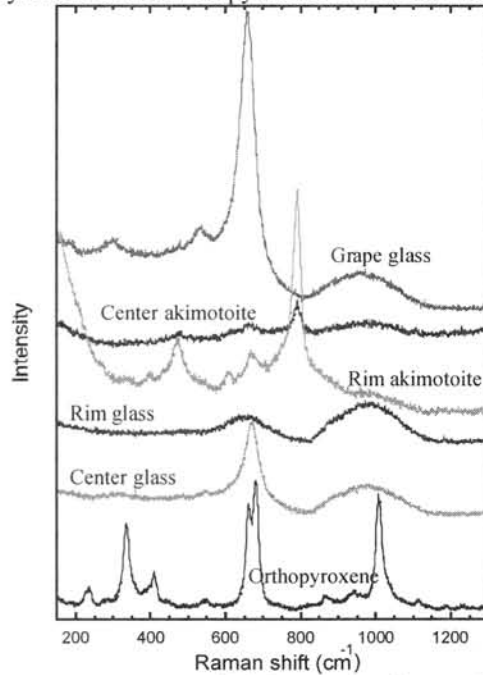


Fig. 7. Raman spectra of high pressure phases of low Ca pyroxene and a oikocrystic pyroxene in Y000047.

Cathodoluminescence spectral study of alkali feldspar and plagioclase in Yamato Martian nakhlite meteorites. M. Kayama¹, A. Gucsik², N. Matsuda¹, H. Nishido¹ and K. Ninagawa³, ¹Research Institute of Natural Sciences, Okayama University of Science 1-1 Ridai-cho, Okayama, 700-005, Japan, ²Max Planck Institute for Chemistry, Department of Geochemistry, Mainz, Germany, ³Department of Applied Physics, Okayama University of Science, Okayama, Japan.

Introduction:

Cathodoluminescence (CL) spectroscopy and microscopy provide useful information on an existence of trace element in materials as well as lattice defect. In general, the CL peak intensity and peak position are related to composition, sample temperature and crystal fields responsible for a structural configuration. This could be altered by pressure including a post-shock temperature effects. This indicates that CL might be a useful technique to evaluate the stages of shock metamorphism in the rock-forming minerals. In this study, CL properties of alkali feldspar and plagioclase in Yamato 000749 are measured to characterize shock metamorphic events of the Martian nakhlite meteorites (Yamato 000749).

Sample and Methods:

Alkali feldspar (Or₈₀) and plagioclase (An₇₀), which were not transformed into maskelynite as a high-pressure polymorph of feldspars formed by shock effects, exist in nakhlite as mesostasis. These grains were selected for CL spectral and imaging measurements and CL data obtained were compared to that of the terrestrial analogues. A cathodoluminescence scanning microscopy (SEM-CL), SEM (JEOL: JSM-5410) combined with a grating monochromator (OXFORD: Mono CL2), was used to measure CL spectra in the range from 300 to 800 nm in the visible light range of an electromagnetic spectrum, where the operating conditions: accelerating voltage:15 kV and beam current: 1.0 nA.

Result and Discussion:

CL spectra of alkali feldspar show a broad peak at 420 nm (blue), which is related to the Al-O⁻-Al defect center and a peak at 755 nm (red), which is attributed to Fe³⁺ impurity center (Fig. 1). These peak positions at 420 and 755 nm were shifted from 390 to 420 nm and 710 to 755 nm by comparing to that of terrestrial alkali feldspar. Similar peak shifts of blue and red peaks are observed in alkali feldspar shocked by impact cratering e.g. Ries Crater. This fact indicates that nakhlite might experience shocked event. Plagioclase has blue, yellow and red CL peaks, which are attributed to defect centers and transition metal element activator centers such as Mn²⁺ and Fe³⁺ (Fig. 2). Yellow and red spectral peaks show peak shifts from 560 to 575 nm and 750 to 780 nm respectively, which are also observed in plagioclase

from Ries Crater. Moreover, plagioclase in Yamato 000749 shows slight peak shift by comparing with experimentally shocked plagioclase (Ab₆₀) at 20 GPa by rail gun experiment. It implies that impact pressure shocked on nakhlite is relatively low and might be below 20 GPa derived from the correlation between shock pressure and peak positions of yellow and red peaks

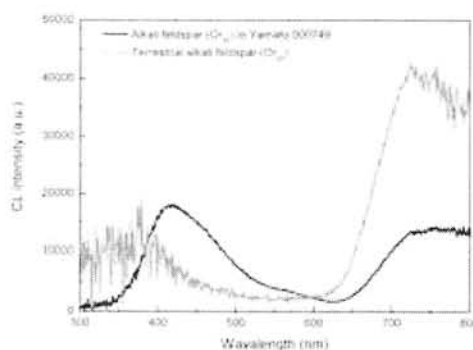


Figure 1: CL spectra of alkali feldspar

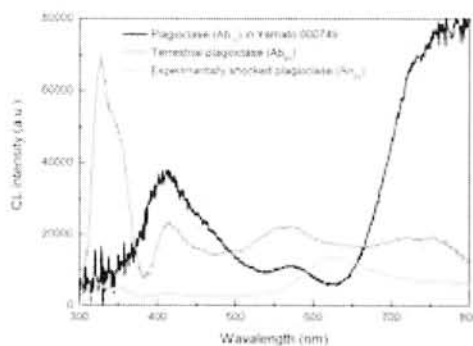


Figure 2: CL spectra of plagioclase

Amorphous Silicates in Primitive Solar System Materials. Lindsay P. Keller and Scott Messenger, Robert M Walker Laboratory for Space Science, Astromaterials Research and Exploration Science Directorate, Mail Code KR, NASA Johnson Space Center, Houston, TX 77058. Lindsay.P.Keller@nasa.gov

Introduction:

Spectroscopic studies have shown that amorphous silicate grains are ubiquitous throughout interstellar space and are major components of young stellar systems and comets. While amorphous silicates are rare in meteorites, they are abundant in anhydrous interplanetary dust particles (IDPs) and in samples of Comet Wild-2 returned by the Stardust spacecraft. Coordinated mineralogical and isotopic studies of amorphous silicates in these primitive materials show that most appear to have formed in the solar system, but some amorphous silicate grains are true 'stardust,' originating from stars that perished before the solar system formed. The study of such materials provides detailed views on the lifecycles of dust in the galaxy and of the origins of the first solar system solids.

Spectroscopic observations of interstellar silicate dust indicate that it is small (<0.5 μm dia.) and dominantly amorphous (crystallinity <~2%). The average chemical and isotopic compositions of interstellar grains are thought to be near solar composition, based on elemental depletion patterns and cosmic ray studies. Some interstellar grains may have condensed in the ISM or had their compositions partially homogenized by deposition of material destroyed by interstellar shocks.

In cometary (anhydrous) IDPs, the amorphous silicate grains are abundant and occur mostly in the form of GEMS (glass with embedded metal and sulfides). GEMS are submicrometer-sized rounded grains that consist of nanophase inclusions of FeNi metal, FeNi sulfides, and numerous trace phases in a Mg-Al-Fe-Si-rich glassy matrix. Coordinated transmission electron microscope and ion microprobe measurements show that, at most, few percent of GEMS are presolar (stardust), based on their oxygen isotopic compositions. The vast majority of GEMS however, have chemical and oxygen isotopic compositions consistent with their formation in the early solar system [1].

Amorphous silicates are also commonly observed in the samples of Comet Wild-2 returned by the Stardust spacecraft. Electron microscopy observations show that the amorphous silicates in the Wild-2 particles contain abundant nanophase FeNi metal grains and FeNi sulfides dispersed in an amorphous Mg-silicate matrix that bears some similarities to GEMS grains but differs in detail [2, 3]. The GEMS-like materials in Stardust particles appears to have been mixed to varying degrees with the silica aerogel capture medium. The mixing and heating that occurred during capture produced grains with silica-rich compositions. Some of the

amorphous material appears to have fine vesicles and some loss of sulfur, consistent with thermal alteration during capture.

Infrared Spectroscopy:

Interstellar amorphous silicates show a broad and featureless absorption band in the infrared with a maximum at 9.7 μm . The contribution of crystalline silicates such as olivine and pyroxene to this feature is estimated to be <2% [4]. GEMS grains have infrared spectral properties that, in some cases are similar to ISM amorphous silicates [5]. One expectation based on the IDP results is that GEMS-like amorphous silicates might be similarly abundant in comet Wild-2. Indeed, despite complications due to overlap with the aerogel Si-O feature, we find that the majority of Wild-2 particles are dominated by amorphous silicates whose maximum absorption feature occurs between 9.5-11.7 μm [3].

Compositions:

Bulk elemental compositions of GEMS grains have been systematically measured and show that they are sub-solar with respect to S/Si, Mg/Si, Ca/Si, and Fe/Si. For these element/Si ratios, the average GEMS compositions are ~60% of solar values, although the average Al/Si ratio in GEMS is indistinguishable from solar [1]. The elemental and isotopic data for GEMS grains suggest that most formed in the early solar nebula either as shock melts or as direct, non-equilibrium condensates.

Few data exist on the bulk elemental compositions of the amorphous grains in Wild-2 samples. We obtained quantitative x-ray maps from microtome thin sections of Stardust particles using a JEOL 2500SE STEM. Our results show that the silicate matrices of these particles are compositionally heterogeneous on the 0.1 μm scale, similar to the heterogeneities exhibited by GEMS grains in IDPs (Figures 1 and 2). However, the compositions of Wild-2 grains are systematically enriched in Si compared to GEMS because of mixing with silica aerogel. The petrography of the metal and sulfide inclusions in Wild-2 samples is also different from those in GEMS. A common opaque assemblage in Wild-2 samples are inclusions with cores of FeNi metal (either kamacite or taenite) surrounded by a rim of Ni-poor Fe sulfide, whereas the metal and sulfide inclusions in GEMS occur as isolated single crystal grains. The abundance of S in the Wild-2 particles and in GEMS grains is not consistent with the composition of interstellar silicates and therefore, they cannot be pristine samples of presolar grains.

Conclusions:

Amorphous silicates were widespread constituents of the early solar system. Rare amorphous silicate stardust grains survived intact, but most were destroyed or heavily altered by shock and irradiation processes in the interstellar medium. Current evidence indicates that amorphous silicates were also efficiently produced in the early solar nebula.

While the analysis of Stardust cometary materials is still at an early stage, it appears that amorphous silicates were common in comet Wild-2. The exact nature of these grains has not yet been

determined, and is clouded by their variable thermal modification and fine scale mixing with aerogel during the capture process. Continued coordinated chemical and isotopic studies of Wild-2 materials are essential to clarifying the relationship of amorphous silicates in this comet to those observed in anhydrous IDPs, interstellar space, and young stellar objects.

References:

- [1] Keller, L. P. and Messenger, S. (2004) LPS XXXV, #1985, [2] Chi, M. *et al.* (2007) LPS XXXVIII, [3] Keller, L. P. *et al.* (2006) *Science*, 314, 1728. [4] Kemper, F. *et al.* (2004) *ApJ*. 609, 826. [5] Bradley, J. P. *et al.* (1999) *Science* 285, 1716.

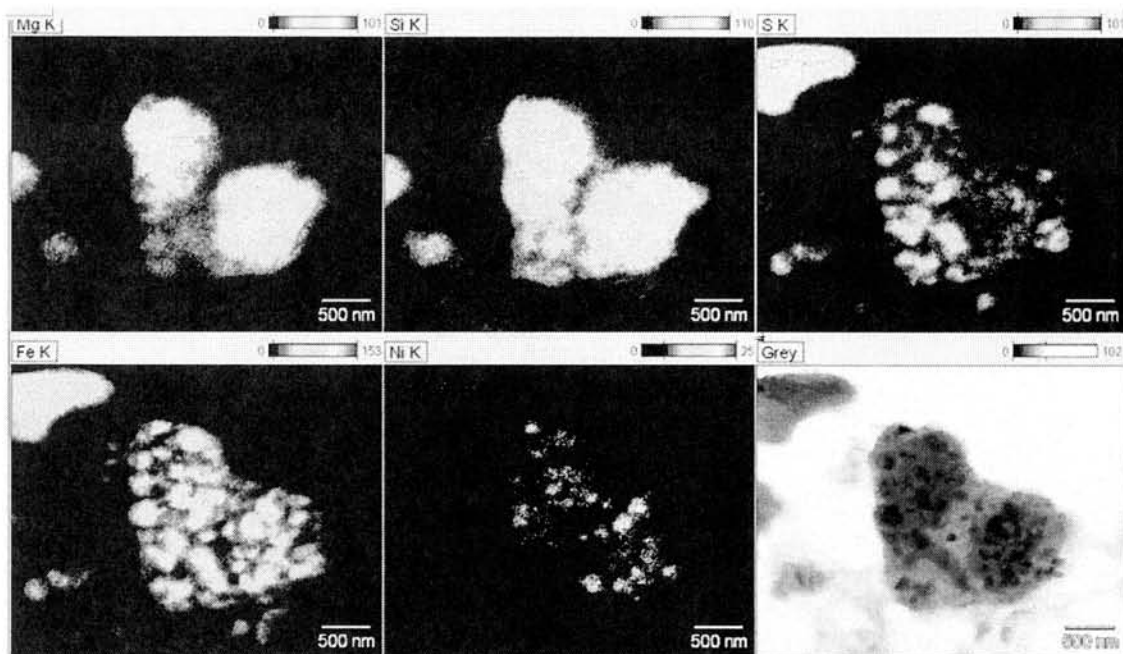


Fig. 1. X-ray maps showing the elemental distribution in a GEMS grain aggregate from IDP L2005AL5.

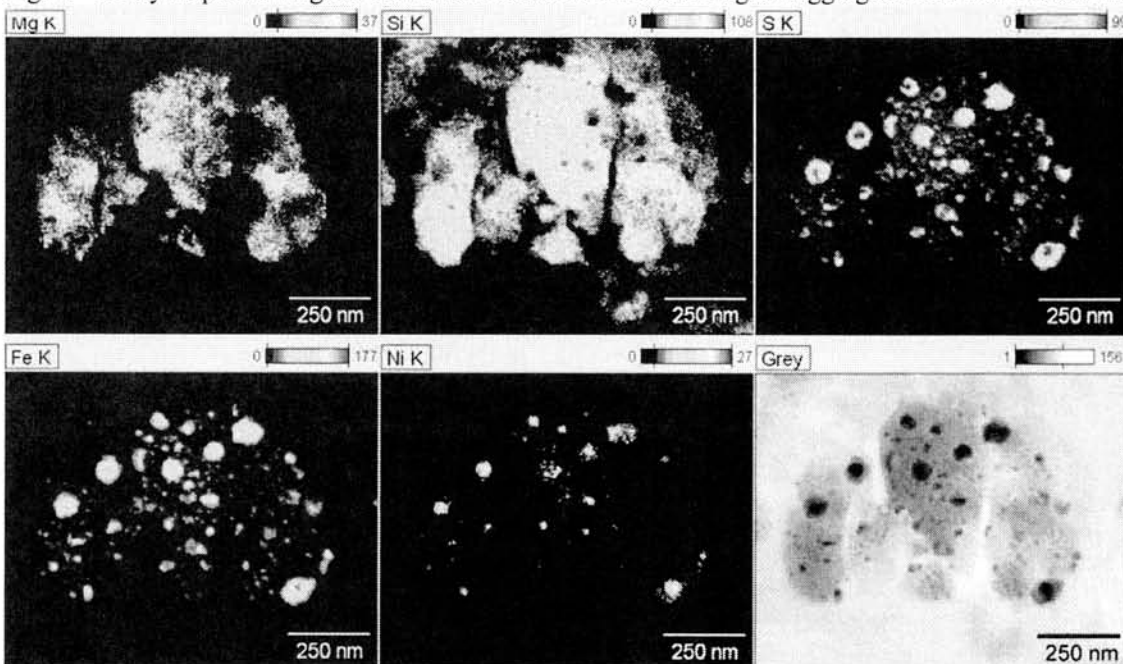


Fig. 2. X-ray maps from Stardust fragment C044, track 7 [3] Compare to Figure 1. The vertical fractures are artifacts from the sample preparation.

Distribution and occurrence of liquid water on Mars from the analysis of valley network structure. A. Kereszturi, Collegium Budapest, Eotvos Lorand University of Sciences Department of Physical Geography, Hungarian Astronomical Association, e-mail: kru@mcse.hu

Introduction: The role of liquid water has been investigated on the Martian environment by several authors, but the origin of the channels and valleys on the surface is still controversial. Models suggest formation by precipitation, groundwater sapping, melting of surface ice by hot ejecta, or all together [1,2,3,4,5]. During the last years a complex image shaping regarding the occurrence and behavior of liquid water on Mars. One important aim in the near future is to connect in time and space the different water-related structures and processes.

Unfortunately we lack all the necessary knowledge for such synthesis, but there are several pieces of information on the areal and spatial *distribution of water-related structures*:

- Selective nature of fluvial erosion [6], the inhomogeneous distribution of valleys.
- Discrete valleys show poorly graded sections, few tributaries, lack of smallest segments [7].
- Volcanic local and regional hydrothermal systems may have played a role in valley formation.
- Impact-driven local (in the crater) and regional (area of fallout) melting at craters larger than 20-30 km [8, 9] may have also been present.

The picture of the *distribution of wet periods in time* is also incomplete, but we have general views, the most important are the follows:

- Valleys are old, formed during the Noachian.
- Few valleys are Hesperian aged [10, 11].
- Based in OMEGA spectral measurements water and relative warm climate was on the planet only at the beginning (Phyllosian), later cold and wet acidic environment could be present only rarely on the surface (Theikian) [12].
- Martian meteorites (aged between 4,56 Ga and 0,16 Gy) show only limited exposure to water, like few phyllosilicates are in ALH84001 [13], few alteration minerals in Lafayette, Nakhla [14, 15].
- A northern ocean and crater lakes were present probably ephemerally for several time in Martian history [16].
- Recent gullies formed probably from brine seepage.
- Volcanic activity and related ice melting happened in the last 10-20 million years.

Drainage network analysis: on Earth the network shape of a drainage system can be used to reconstruct its origin, above all the source of the water [17]. The author has analyzed the Martian drainage networks based on morphology and morphometry from Viking, MGS (MOC), MEX (HRSC) images and MOLA topographic data [18].

The systems were classified into five groups based on appearance and physical dimensions together. The proposed main groups are the follows (with possible analogs from the Earth in brackets):

1. Weakly integrated, small, parallel valleys (centrifugal),
 2. integrated small valleys (dendritic),
 3. medium sized lonely valleys (disordered),
 4. confined outflow valleys (catastrophic flood),
 5. unconfined, braided outflow valleys (dichotomic).
- Strongly fractured network types are important because of the weak integration of valley systems. Most valleys show erosional structures, exceptions may be in the 5. group of braided patterned outflow systems. Some examples are visible in the Figure, where rows from top to bottom represents examples for the five types form 1 to 5.

Conclusion: It seems to be possible that with the analysis of valleys' network structure to get closer to the origin of water produced them. During the next years these and other data on the presence of liquid water on past Mars may be synthesized into one common picture. The possible environment of water-related mineral alterations inside the Martian meteorites may be positioned into this picture. We may get data about the time of their formation (position in planetary evolutionary history of liquid water), just like information on their spatial distribution (spatial position according to surface and subsurface environment types). Such results help reconstruct the environmental conditions on Mars were present during the formation water-related minerals in Martian meteorites.

Referelces: [1] Carr, M. H. (1999) *Fifth Int. Conf. on Mars*, #6030. [2] Craddock R. A. and Howard A. D. (2002) *JGR*, 107(E11), 5111. [3] Irwin R. P. & Howard A. D. (2002) *JGR*, 107(E7), 5056. [4] Grant J. A. (2000) *Geology*, 28, 223–226. [5] Sharp R. P. & Malin M. C. (1975) *Geol. Soc. Am. Bull.*, 86, 539–609. [6] Lee, P. (2000) 31th *LPSC* #2080, [7] Malin M. C. & Carr M. H. (1999) *Nature*, 397, 589-591. [8] Harrison, K. P. & Grimm, R. E. (1999) 30th *LPSC* #1941. [9] Mougini-Mark P. et al. (1988) *Bull Volc.* 50, 361. [10] Gulick, V. C. & Baker, V. R. (1990) *JGR*, 95, 14,325-14,344. [11] Fassett, C. I & Head, J. W. (2006) *Icarus*, submitted. [12] Bibring J.-P. et al. (2006) *Science* 21, 400-404. [13] Bearley, (1998) 29th *LPSC* #1451, [14] Treiman et al., 1993, *Meteorites* 28, 86, [15] Bridges & Grady (2001) *EPSL* 176, 267. [16] Fairén et al. (2003) *Icarus*, Volume 165, Issue 1, p. 53-67. [17] Gabris Gy. (1986) *dissertation for candidate degree*, [18] Kereszturi, S., Gabris, Gy. (2007) 38th *LPSC* #1045.

Acknowledgment: The authom thanks for the Polaris Observatory, Budapest. The ESA ECS-project No. 98004 grant is also highly acknowledged.

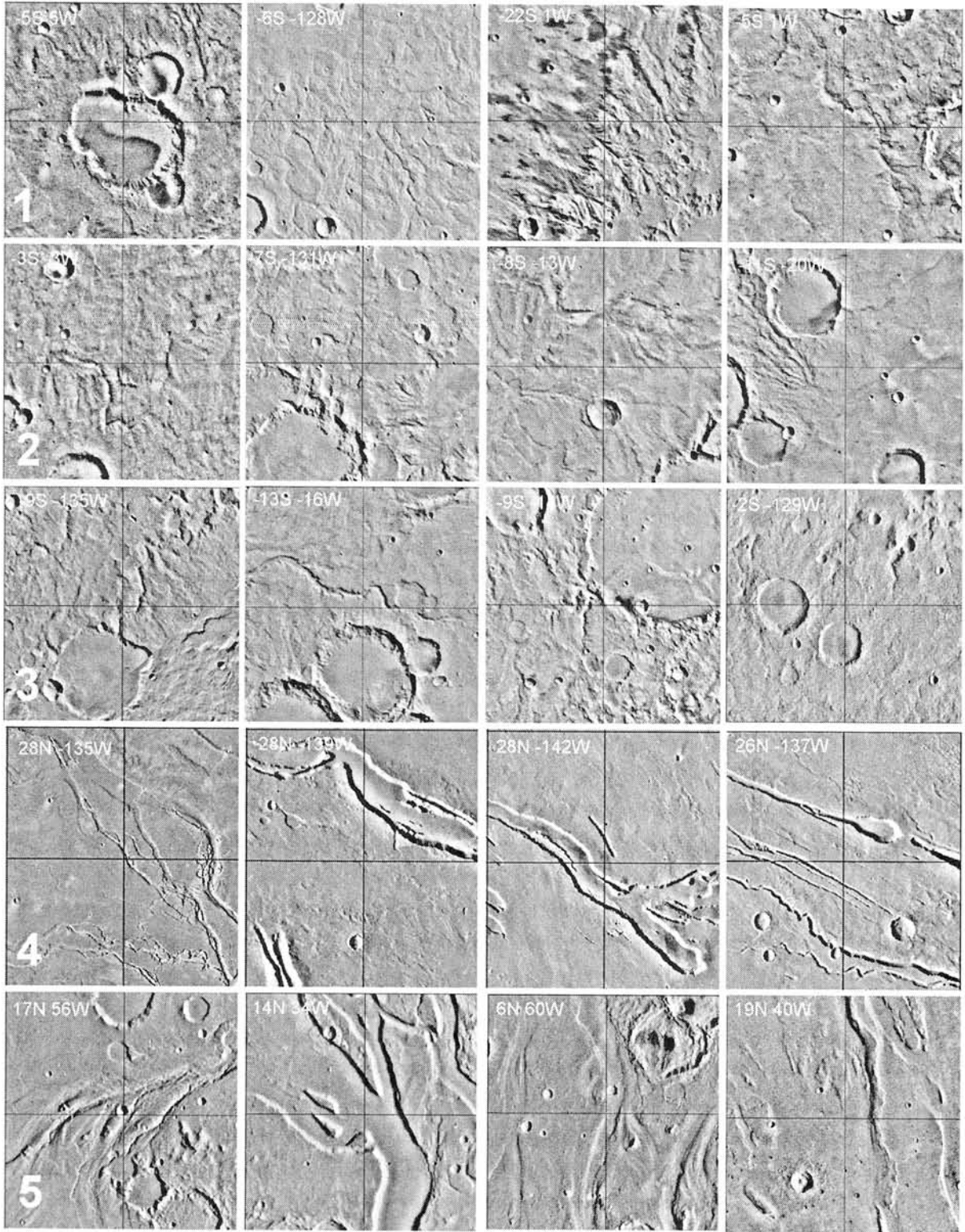


Figure: Examples for the 5 proposed valley network system types. Each row represent one type, the images are from the Viking Orbiter mosaic map and show 2x2 degree areas in mercator projection

Unique high-pressure phase assemblage in a heavily shocked L6 chondrite, NWA 4719.

M. Kimura¹, H. Fukuda¹, A. Suzuki², and E. Ohtani², ¹Ibaraki University, Japan, makotoki@mx.ibaraki.ac.jp, ²Tohoku University, Sendai, Japan.

Introduction:

High-pressure minerals, such as ringwoodite, wadsleyite, majorite-pyroxene garnet, akimotoite, (Mg,Fe)SiO₃-perovskite, lingunite and others, have been reported in shock melt veins of many L chondrites, a few H and LL chondrites, a CB chondrite, and some Martian meteorites [e.g., 1-3]. The occurrence of these high-pressure minerals indicates shock-induced melting and crystallization under the long duration of high-pressure and -temperature conditions [e.g., 2]. Especially, shock veins in L chondrites abundantly contain high-pressure minerals. Here we report unique high-pressure phase assemblage in an L6 chondrite, NWA 4719. The assemblage preserves the crystallization condition under higher pressure than the other chondrites.

Petrography of NWA 4719:

NWA 4719 is a newly approved L6 chondrite. The total mass is 812g, and covered by a fusion crust. This chondrite shows texture typical of type 6 chondrite, such as poorly defined chondrule, well recrystallized matrix, and coarse-grained plagioclase (An₁₀Ab₈₃Or₇). Olivine and low-Ca pyroxene are almost homogeneous in composition (Fo₂₅ and En₇₇Fs₂₁Wo₂). The shock stage and weathering grade are S4 and W2, respectively.

Petrology and mineralogy of shock veins:

NWA 4719 contains well developed shock veins and melt pockets (Fig. 1). The veins are 0.05 to 1.2 mm in width, and ringwoodite is abundantly recognized under optical microscope. Figure 2 shows a back-scattered electron image of a shock vein. Spherules of Fe-Ni metal and troilite are abundantly encountered in the veins. The veins mainly comprise two silicate lithologies: 1) coarse-grained rounded to irregular silicate grains (~10 to ~100 μm), and 2) fine-grained (below ~5 μm) silicate aggregate.

Coarse-grained lithology mainly consists of olivine (Fo₇₅) and low-Ca pyroxene (En₇₇Fs₂₁Wo₂) with minor amount of plagioclase (An₁₀Ab₈₁Or₉) in composition. Their chemical compositions in minor as well as major elements are identical to those in the host, respectively. Fine-grained lithology seems to be aggregate mainly comprising olivine and low-Ca pyroxene in composition.

However, by using laser micro Raman spectrometer, we identified all silicate minerals both in lithologies as high-pressure polymorphs, ringwoodite, akimotoite and lingunite. Majorite is extremely rare in NWA 4719, although majorite is one of the most common high-pressure minerals in shock veins of H and L chondrites. Wadsleyite and

jadeite are not encountered in the veins of NWA 4719.

The most striking feature of this chondrite is abundant occurrence of pyroxene glass (Fig. 3). Pyroxene in composition is mostly glass in the coarse-grained lithology. The fine-grained lithology mainly consists of ringwoodite and pyroxene glass.

Discussion:

Pyroxene glass was reported from some heavily shocked L6 chondrites [4-6]. However, these chondrites also contain abundant majorite. Although Chen et al. [4] reported the occurrence of pyroxene glass surrounded by majorite, pyroxene glass in NWA 4719 is never associated with majorite. The high abundance of pyroxene glass and extremely rare occurrence of majorite characterize NWA 4719.

The occurrence of pyroxene glass in the coarse-grained lithology and identical composition to the host pyroxene of NWA 4719 suggest that the pyroxene glass was not derived from melt. Some pyroxene glass was reported as vitrified product from silicate perovskite directly produced from precursor pyroxene under very high-pressure conditions (more than 23 GPa) [e.g., 4]. Our observations are consistent with such origin.

Silicate perovskite should form under higher-pressure conditions than majorite [e.g., 5]. Shocked L6 chondrites usually contain both perovskite and majorite. On the other hand, the veins in NWA 4719 contain almost exclusively vitrified perovskite. This suggests that after the crystallization of perovskite the shock veins cooled rapidly without crystallization of majorite. This is consistent with the absence of wadsleyite and jadeite.

On the other hand, silicate perovskite is completely vitrified at above 477°C at ambient pressure [7]. Therefore, the post-shock temperature was more than 477°C, and perovskite was completely vitrified in NWA 4719. Thus, the assemblage of high-pressure phases can give constraint on the cooling history of shock veins.

The phase assemblage of NWA 4719 indicates that the veins in it crystallized under the highest pressure conditions among chondrites. As suggested by [8], the pressure conditions of the veins vary widely in chondrites.

Acknowledgements: Dr. A. Yamaguchi helped to use Raman spectrometer in NIPR. The sample was supplied by Hori Mineralogy.

References:

- [1] Chen M. et al. (1996) *Science*, 271, 1570-1573.
- [2] Ohtani E. et al. (2004) *EPSL*, 227, 505-515.
- [3] Kimura M. et al. (2006) *Antarctic*

Meteorite XXX, 38-39. [4] Chen M. et al. (2004) *MAPS*, 39, 1797-1808. [5] Xie et al. (2006a) *GCA*, 70, 504-515. [6] Tomioka N. and Kimura M. (2003)

EPSL, 208, 271-278. [7] Durben D.J. and Wolf G. (1992) *AM*, 77, 890-893. [8] Xie et al. (2006b) *MAPS*, 41, 1883-1898.

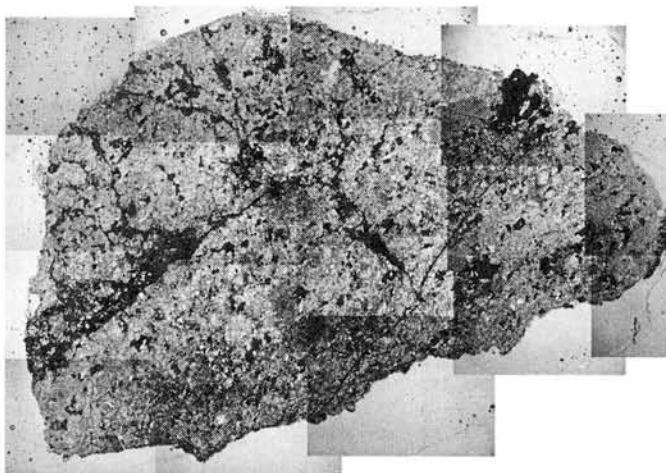


Figure 1. Optical photomicrograph of L6 chondrite NWA 4719. This chondrite contains well developed shock veins and melt pockets. Width is 1.8 cm.

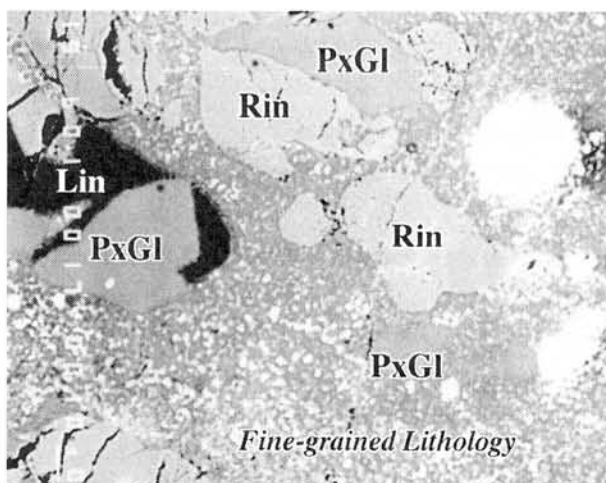


Figure 2. Back-scattered electron image of a shock vein in NWA 4719, showing high-pressure phases, such as ringwoodite (Rin), pyroxene glass (PxGl) and Lingunite (Lin). Width is 160 μm .

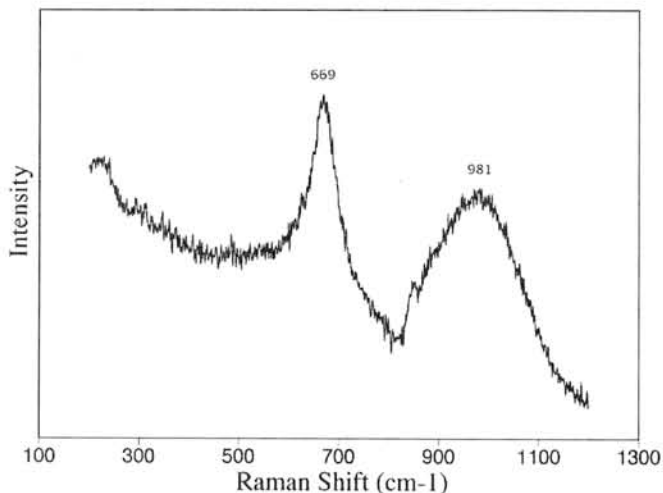


Figure 3. Raman spectrum of pyroxene glass in coarse-grained lithology.

A micro-Raman study on thermal histories of carbonaceous matter in carbonaceous chondrites. F. Kitajima and T. Nakamura, Department of Earth and Planetary Sciences, Faculty of Sciences, Kyushu University, Hakozaki, Fukuoka 812-8581, Japan. (kitajima@geo.kyushu-u.ac.jp)

Introduction:

Chondritic insoluble carbonaceous macromolecular matter converts gradually to graphitic material during thermal metamorphism in parent bodies. Raman spectroscopy is a useful tool to evaluate the degree of structural order of the graphitic matter, and it can indicate to what extent thermal metamorphism has proceeded. Typical Raman spectrum of graphitic matter shows two Raman bands in the first-order region; G-band at about 1600cm^{-1} , and D-band at about 1350cm^{-1} [1]. G-band is assigned to E_{2g} in-plane vibrational mode of polyaromatic structure. D-band is not present in a perfectly stacked graphite. This band is induced by structural defects, and becomes active by the relaxation of D_{6h} symmetry leading to the relaxation of wave-vector selection rules. The intensity of this band is commonly used for practical applications to evaluate the amount of disorder in carbon materials.

The D/G peak area ratio (or D/G peak intensity ratio) has been recognized to correspond to the lateral size (L_a) of a crystallite of the graphitic matter [1]. Beyssac et al. [2] pointed out that the D-band has substructure named D_1 - D_3 bands, and they observed the relative decrease of D_1 -band with increasing metamorphic grade, resulting in the decrease of D_1/G peak intensity ratio and $D_1/(G+D_1+D_2)$ peak area ratio, through reaching to almost infinite graphite showing only G-band. However, this relationship is highly inaccurate for poorly ordered carbonaceous matter [3]. In the range of lower maturity level, Allwood et al. [4] observed that D_1/G and $D_1/(D_1+G)$ increase with increasing thermal maturity. Bonal et al. [3] reported that D/G peak intensity ratio decreases for the coals with vitrinite reflectance (VR) $<5\%$, and increases with increasing maturity for $5\% < \text{VR}$.

In this investigation, we examined the thermal histories of several carbonaceous chondrites suffered various degrees of thermal metamorphism, using the Raman spectra of the carbonaceous matter.

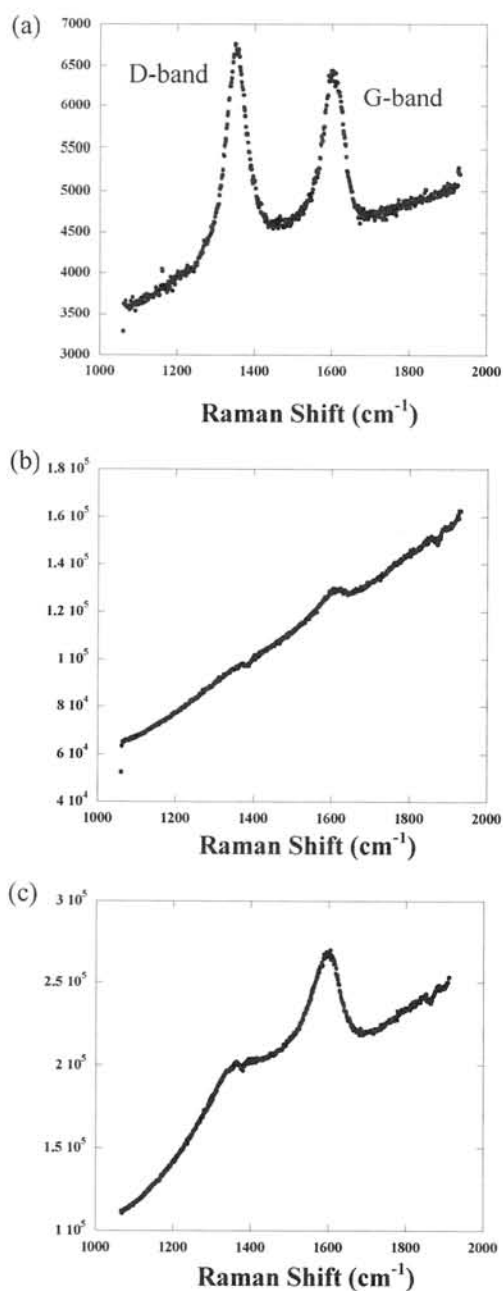
Experimental:

Raman spectra were obtained using JEOL JRS-SYSTEM 2000 Raman spectrometer. An excitation wavelength of 514.5nm was used on an argon ion laser. The laser beam was focused by a microscope equipped with a $50\times$ objective, leading to a spot diameter of $2\mu\text{m}$. The power at the sample surface was 0.1 or 1.0mW . Spectra of the first-order region were acquired for 30sec . The measurement was repeated three times and they were accumulated. Curve fitting was carried out using Pseudo-Voigt function, after subtraction of fluorescence background assuming a linear baseline. The spectra

were interpreted as they consist of 3-5 components.

Results and discussion:

Raman spectra of the chondrites that suffered thermal metamorphism show a distinguishable feature from those of the unheated chondrites (Figs.1).



Figs.1 Raman spectra of chondritic carbonaceous matter. (a) Allende (Laser power at the sample surface, 0.1mW), (b) Murchison (Laser power, 0.1mW), (c) Murchison (Laser power, 1.0mW).

The CM chondrites experienced extended thermal metamorphism (A 881334, Y 86695, Y 82054, B 7904, Y 86789), Y 793321 (CM, weakly heated), Coolidge, Allende (CV), and Ornans (CO) show well-developed G- and D-bands clearly even if laser power is reduced to 0.1mW (Fig.1a). In contrast, the unheated CM chondrites (Y 791198, Cold Bokkeveld, Sayama, Boriskino, Murray, Murchison), Tagish Lake, Ivuna (CI), and A 881458 (CM, very weakly heated) showed weak G- and D-bands on the slope of a fluorescence peak, when the laser power was 1.0mW, and reducing the laser power to 0.1mW, the D-bands disappeared (Figs.1b, 1c). This property can be non-destructive tool to distinguish strongly heated meteorites from unheated meteorites. The former group corresponds to the group showing weak absorption at 2472eV in Sulfur *K*-edge XAFS spectra, and the latter corresponds to the group showing relatively strong absorption at 2472eV. A piece of wood showing neither G- nor D-bands originally was heated in vacuo for comparison. After heating at 300°C, it showed a similar spectrum to those of the unheated meteorites (weak G- and D-bands), and after heating at 500 °C, its spectrum became similar to those of the heated meteorites showing well-developed G- and D-bands.

The G-band position (ϖ_G) of the vitrinites shifts up with increasing metamorphic grade, and the FWHM-G (Full width at half maximum of G-band) decreases. The G-band position (ϖ_G) highly correlates negatively with the FWHM-G of vitrinites. The G-band position (ϖ_G) of the meteorites in this investigation also shows weak negative correlation with its FWHM-G.

References:

- [1]Tuinstra and Koenig (1970) *J. Chem. Phys.* 53, 1126-1130. [2]Beyssac O. et al. (2002) *J. metamorphic Geol.* 20, 859-871. [3]Bonal L. et al. (2006) *Geochim. Cosmochim. Acta* 70, 1849–1863. [4]Allwood A. C. et al. (2006) *Vibrational Spectroscopy* 41, 190–197.

Determination of ^{26}Al content for Antarctic meteorites using AMS.

H. Kusuno¹, T. Fukuoka¹, H. Kojima² and H. Matsuzaki³ ¹Department of Environmental Systems, Faculty of Geo-Environmental Science, Rissho University, Kumagaya, Saitama 360-0194, Japan (tfukuoka@ris.ac.jp). ²Antarctic Meteorites Research Center, National Institute of Polar Research, Itabashi-ku, Tokyo 173-8515, Japan. ³Department of Nuclear Engineering and Management, School of Engineering, the University of Tokyo

Introduction

Determination of terrestrial ages of Antarctic meteorites supplies useful information for the frequency of meteorite fall, mechanism of accumulation of meteorites and the age of ice. ^{26}Al ($T_{1/2} = 7.17 \times 10^5 \text{y}$) is a useful tool for the dating of terrestrial age of meteorite.

There are two types of determination methods for ^{26}Al contents in small amount of meteorites. One is γ -ray counting by extremely low background γ -ray counting system (Institute of Cosmic Ray Research, the University of Tokyo), another is accelerator mass spectrometry (AMS) analysis. In this study, we developed analytical procedure for AMS analysis of ^{26}Al in meteorite samples. To check the consistency of the results obtained from these two methods, ^{26}Al contents in 2 meteorites have been determined by γ -ray counting system and AMS analysis as basic study.

Experimental

Fig. 1 shows basic analytical procedure for AMS analysis of ^{26}Al in meteorite samples developed in this study. 2~10g pieces of sample was crushed and pulverized on an agate mortar. 10mg of powdered sample was performed with HF treatment in a Teflon beaker. Heat dry up sample was dissolved in 2N HCl. Purified Al was precipitated as $\text{Al}(\text{OH})_3$ by NH_4OH . $\text{Al}(\text{OH})_3$ precipitation put in Pt crucible was dried up, then it was baked as Al_2O_3 at 900°C. ^{26}Al content was determined by AMS (MALT; Micro Analysis Laboratory, the University of Tokyo) using Al_2O_3 sample mixed with Ag metal. Recovery rate of Al was 95~100%. Concentration of impurities (Fe, Mg) was checked by atomic absorption spectrometry, Si concentration was checked by colorimetric analysis. Those concentration were less than detection limits.

Results and discussion

Table 1 shows ^{26}Al contents in 6 non-Antarctic meteorites (Tatahouine, Millbillillie, Allende, Ningqian, Dashoguz and Valera) and 3 Antarctic meteorites (Y-74097, Y-791000 and Y-791422) determined by AMS. The analytical errors of these results were less than 2%. ^{26}Al contents in Millbillillie and Allende were agree with them determined by extremely low background γ -ray counting system (Table 1). ^{26}Al contents in Ningqian, Allende, Y-74097 and Y-791000 agree with values in references within error. However, ^{26}Al contents in Tatahouine, Millbillillie and Y-791422 do not agree with the values in references. This may cause by differences in production rate of ^{26}Al between outside and inside of the meteorite bodies.

In this study, we established the analytical procedure of AMS for ^{26}Al contents in meteorite samples. However this analytical method is destructive. There are more than 1,000 of Antarctic meteorite samples of NIPR collection which the weights are less than 2g. The non-destructive analytical method is desirable for these meteorites, when the destructive analysis was used for these meteorites, precious meteorites samples will be lost. So we will determine ^{26}Al contents in Antarctic meteorites less than 2g using extremely low background γ -ray counting system, this analysis can determine ^{26}Al in meteorite samples with non-destructive. AMS analysis is suitable for more than 2g of Antarctic meteorites.

References

- [1] Welten K. C., et al. (1997) *MAPS* 32, 891
- [2] Chai C., et al. (1987) *Meteoritics* 22, 355
- [3] Cressy, et al. (1972) *J. geophys. Res.* 77, 4905-4911.

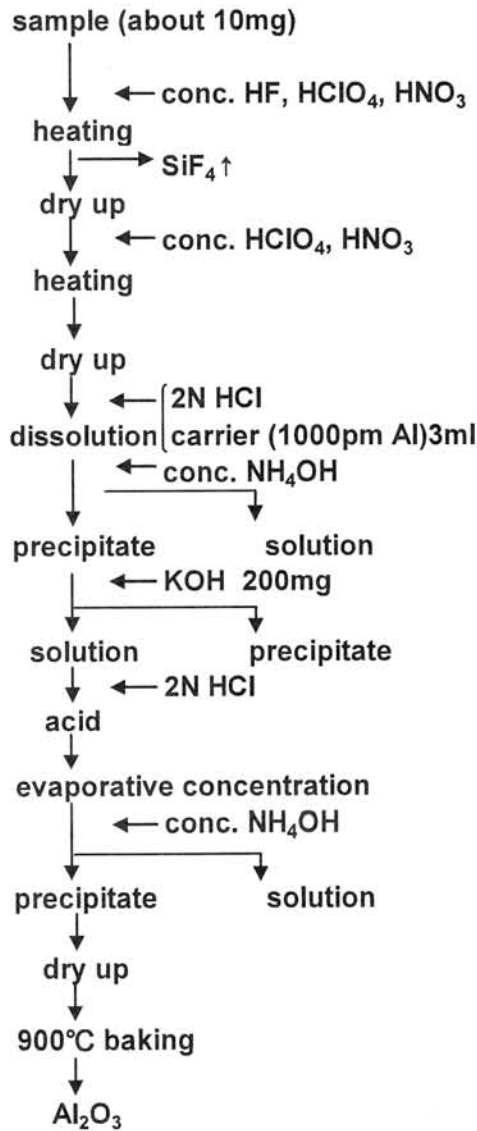


Fig. 1 Analytical procedure for AMS analysis of ^{26}Al in meteorite samples in this study

Table 1. The analytical results of ^{26}Al contents in meteorite samples, in this study

| Meteorite name | type | Original weight [kg] | ^{26}Al content [dpm/kg] | | Reference | |
|----------------|------|----------------------|--|-------------|----------------|---------------------------------|
| | | | extremery low background γ -ray counting system | AMS | | |
| Tatahouine | Dio | 12 | | 72 ± 1 | 80.3 ± 2.3 | Welten K. C., et al. (1997) [1] |
| Millbillillie | Euc | 25.4 | 109 ± 7 | 105 ± 2 | 80 ± 1 | Welten K. C., et al. (1997) [1] |
| Allende | CV3 | 2000 | 53 ± 7 | 52 ± 1 | 52 ± 5 | Cressy P. J., et al (1972) [2] |
| Ningqiang | CK3 | 4.6 | | 53 ± 1 | 54 ± 10 | Chai C., et al. (1987) [3] |
| Dashoguz | H5 | 7 | | 69 ± 1 | | |
| Valera | L5 | 50 | | 63 ± 2 | | |
| Y- 74097 | Dio | 2194 | | 76 ± 2 | 74 ± 1.9 | Welten K. C., et al. (1997) [1] |
| Y-791000 | Dio | 90.4 | | 70 ± 2 | 73.9 ± 3.6 | Welten K. C., et al. (1997) [1] |
| Y-791422 | Dio | 61.8 | | 88 ± 2 | 79.4 ± 1.7 | Welten K. C., et al. (1997) [1] |

Three Genetic Types of Ultrahigh-Pressure Minerals in Meteorites. A. A. Marakushev, N. G. Zinovieva, and L. B. Granovsky, Department of Petrology, Geological Faculty, Moscow State University, Leninskie Gory, Moscow 119992, Russia (zinov@geol.msu.ru)

Minerals that can be produced by natural processes only under very high pressures may be used as indicators of these pressures not only in rocks but also in meteorites.

Meteorites contain at least three types of such minerals, which principally differ in settings and mineral assemblages.

1. Diamond that occurs as minute grains (no larger than 10 nm) with abundant fluid inclusions is contained, in association with moissanite SiC, in the kamacite matrix of chondrites of all of their chemical groups.
2. Diamond that composes larger grains (10-10000 nm) rich in fluid inclusions composes, along with daubreelite, troilite, and moissanite, graphite-kamacite injections in ureilites (pigeonite-olivine achondrites).
3. Ringwoodite, wadsleyite, majorite, and some other minerals in association with a vitreous phase were found exclusively in brecciated chondrites.

The aforementioned ultrahigh-pressure minerals mark principal evolutionary stages of iron-stony meteoritic material in the solar system. This evolution began with the derivation and evolution of chondritic magmas, which compose the cores of giant planets, such as Jupiter [1]. Under the tremendous pressure of their fluid shells, the chondritic magmas exsolved into tiny silicate droplets (chondrules) in a Ni-Fe kamacite matrix. A trace left by this extremal pressure is minute diamond crystals in the kamacite matrix. These diamonds are so rich in fluid inclusions that their density decreases to 2.2 g/cm³ (whereas the density of diamond itself is as high as 3.5 g/cm³).

As was emphasized in our earlier publication [2], chondrites were formed within a very broad range of fluid pressure and are multi-facies rocks in this sense. A direct indication of diamond crystallization under the tremendous pressure of the parent giant planet was obtained in 1996, when the *Galileo* space probe entered the atmosphere of Jupiter and recovered evidence that the ¹³⁶Xe/¹³⁴Xe ratio in it is equal to 1.04, i.e., the same as in diamonds from carbonaceous chondrites (in contrast to this ratio equal to 0.80 in solar wind [3]).

The extremely high pressure, whose traces are left in the form of diamond crystals rich in fluid inclusions, predetermined an anomalous distribution of oxygen isotopes between chondrules and the matrix (tg α = 1), whereas the crystallization of chondrites that occurred mostly

upon the relief of the pressure was associated with a normal distribution of oxygen isotopes between minerals (tg α = 0.5) [1].

The diamond contained in chondrites (as well as moissanite in assemblage with this mineral) is much richer in fluid components (Fig. 1), including noble gases, than terrestrial diamond.

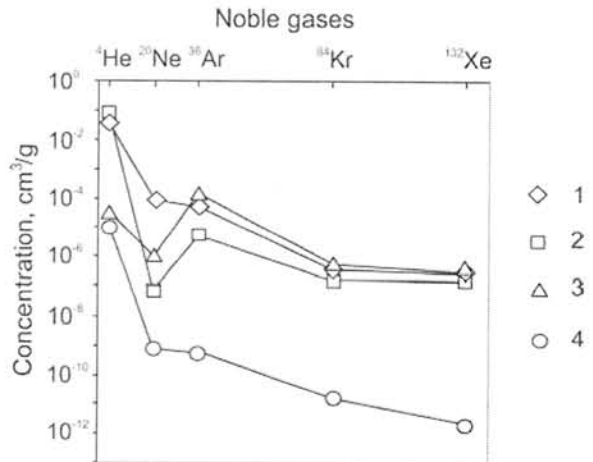


Fig. 1. Concentrations of noble gases (in cm³/g) in (1) diamond and (2) moissanite in the matrix of carbonaceous chondrites [4, 5] and (3) in ureilites [6] and terrestrial diamond [7]. The minerals are well preserved in chondrites in spite of their later recrystallization under a relatively low pressure (after the parent protoplanets had lost their giant fluid shells under the effect of the sun).

For comparison, the diagram also shows data on diamond from ureilites, which has Ar, Kr, and Xe concentrations only slightly different from those in diamond in chondrites, whereas the He and Ne concentrations in diamond from ureilites are significantly lower. The two types of diamond also differ in their setting in the matrix of meteorites: diamond of chondrites is included in a kamacite matrix, while a material analogous to this matrix in ureilites composes complicated interstitial and veinlet injections (Fig. 2) in pigeonite-olivine aggregates.

This material was injected together with hydrogen-bearing fluids, which induced the recrystallization of olivine with the development of reversed zoning in its grains, a decrease of its Fe mole fraction to almost zero, and with the release of native iron according to the reaction $Mg_{1.7}Fe_{0.3}SiO_4 + 0.3H_2 = 0.7Mg_2SiO_4 + 0.3MgSiO_3 + 0.3Fe + 0.3H_2O$. Iron liberated in this process contains no nickel and is thus different from kamacite that was emplaced

together with diamond (and that contains 3-5 wt % Ni). The relations described above reflect the evolution of chondritic magmatism, which was controlled by the exsolution of the chondritic planet into an outer silicate (ureilite) shell and an inner kamacite core. The high fluid concentrations in the latter were acquired by the core during the protoplanetary evolutionary stage of chondritic magmatism under the fluid pressure of the shells of the parent planets. This pressure eventually induced the explosive breakup of chondritic and exsolved ureilite-kamacite planets into asteroids. During the stage preceding this breakup, the planets acquired their endogenic activity, whose driving forces were fluids from the kamacite cores that affected the silicate shells.

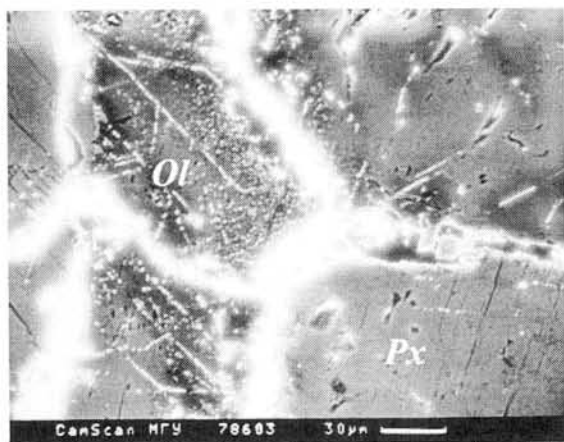


Fig. 2. Combination of interstitial and veinlet diamondiferous graphite-kamacite injections in the Yamato-74659 ureilite. It can be clearly seen that the injections weakly affect pyroxene (pigeonite) and more strongly alter olivine grains, which acquire thereby secondary zoning, with the Fe mole fraction of the olivine decreasing to zero and with the release of nickel-free native iron.

A manifestation of this processes in the ureilite shells was the intrusion of fluid-rich diamond-bearing kamacite melts, a process that predetermined their complicated injected texture (Fig. 2). Diamond nuclei that are contained in them and are typical of matrix chondritic melts served as seeds for the metastable growth of diamonds under decreasing pressure as a consequence of the migration of hydrogen and helium (the most mobile components) from the fluids. The pressure exerted by the fluid injections was high during the further growth of diamond crystals, which contain abundant hydrogen inclusions when hosted in ureilites, and the accommodation of garnet in the zones of fluid-induced recrystallization of olivine (*Ol*) and pyroxene (*Opx* and *Cpx*) (table) with the origin of glass.

The partial melting of ureilites and the crystallization of garnet in them are manifestations of the explosive transformations of the planets

under the effect of fluids, which were concentrated in the cores of the planets and led to the formation of asteroids and meteorites.

Table. Composition (wt % of oxides) of minerals in garnet-bearing recrystallization zones in ureilites.:

| Components | <i>Ol</i> | <i>Opx</i> | <i>CPx</i> | <i>Grt-1</i> | <i>Gl</i> |
|--------------------------------|-----------|------------|------------|--------------|-----------|
| SiO ₂ | 42.97 | 57.89 | 52.62 | 47.64 | 69.07 |
| TiO ₂ | - | - | 0.36 | 0.36 | - |
| Al ₂ O ₃ | - | - | 5.37 | 20.45 | 1.7 |
| Cr ₂ O ₃ | 0.2 | 0.39 | 0.7 | - | 1.4 |
| FeO | 1.67 | 1.7 | 1.06 | 5.99 | 9.02 |
| MnO | 0.31 | 0.29 | 0.38 | 0.23 | 0.47 |
| MgO | 54.67 | 39.3 | 20.46 | 21.51 | 16.54 |
| CaO | 0.18 | 0.42 | 19.05 | 3.82 | 1.81 |

Grt-1 - garnet (pyrope) from the Novo-Urei meteorite.

Their brecciation was associated with fluid-induced melting and the formation, along with garnet, of numerous high-density phases (ringwoodite, wadsleyite, majorite, etc.), which were described, for example, in [8], in the vitreous veinlets of the Dhofar L chondrite. That paper contains an interesting description of olivine fragment, which is transformed into an association of forsterite (in the central part of the fragment) and ringwoodite (in the margin of the fragment). These transformations can be represented by the schematic reaction $2Mg_{1.5}Fe_{0.5}SiO_4 = Mg_{1.1}Fe_{0.9}SiO_4$ (ringwoodite) + $Mg_{1.9}Fe_{0.1}SiO_4$ (forsterite). This olivine transformation, which is associated with the complete recrystallization of its fragment, is possible only under the effect of a fluid, which is in conflict with traditional concept that these minerals are produced during the collisions of asteroids. The resultant association⁵ of forsterite and ringwoodite corresponds to a pressure of 13 GPa and highlights the stressed character of chondritic kamacite-ureilite planets caused by high fluid concentrations in their kamacite cores and the grandiosity of their explosive breakup into asteroids and meteorites.

Acknowledgments: This work was supported by the Program "Support of Scientific Schools, grant 2849.2006.05".

References:

- [1] Marakushev A. A. et al. (2003) *Kosmicheskaya Petrologiya*, Moscow, Nauka-press, p. 387.
- [2] Marakushev A. A. et al. (2006) *Doklady Earth Sciences*, 407A, 3, 434-437.
- [3] Manuel O. and Katragada A. (2003) *Proc. ACM 2002*, 787-790.
- [4] Huss G.R. and Lewis R.S. (1994) *Meteoritics*, 29, 791-81.
- [5] Lewis R.S. et al. (1994) *GCA*, 58, 471-494.
- [6] Gobel R. et al. (1978) *JGR*, 83, 855-867.
- [7] Wada N. and Matsuda J. (1998) *GCA* 62,13, 2335-2345.
- [8] Badjukov D. D. et al. (2005) *LPS XXXVI*, 1684#.

Cathodoluminescence, micro-Raman and Infrared studies of silica minerals in Nakhlite from Antarctica. N. Matsuda¹ (non@misasa.okayama-u.ac.jp), H. Nishido², A. Gucsik³, K. Ninagawa⁴, T. Okumura² and M. Kayama², ¹Institute for Study of the Earth's Interior, Okayama University, Tottori, Japan, ²Research Institute of Natural Sciences, Okayama University of Science, Okayama, Japan, ³Max Planck Institute for Chemistry, Department of Geochemistry, Mainz, Germany, ⁴Department of Applied Physics, Okayama University of Science, Okayama, Japan.

Introduction:

This systematic spectroscopical study has been focused on mineralogy of the mesostasis of a Martian nakhlite sample from the Antarctica. A multiple technical approach including cathodoluminescence (CL), Micro-Raman and Infrared (IR) spectroscopic provides us detailed information on crystallochemical features of the mesostasis containing of the minor amount of minerals, which would be difficult in using the conventional optical microscopical observations and investigations.

Samples and methods:

Two polished thin sections of Yamato 000749 and Yamato 000593, which are possibly paired, were supplied from the National Institute of Polar Research (NIPR). CL image, which can be compared to optical image under a petrographic microscope, was obtained using a cold-cathode type "Luminoscope" operated at 15 kV with a cooled CCD camera. CL image at high magnification and CL spectra were collected on a Scanning Electron Microscope-Cathodoluminescence (SEM-CL), SEM (JEOL: 5410LV) with a grating monochromator (Oxford: Mono CL2), where EDS system can be used in combination with SEM-CL. Operation condition is at 15 kV (accelerating voltage) and 1.0~5.0 nA (a beam current). Raman spectra were obtained using a micro-Raman spectrometer (Thermo Nicolet: Almega) with a Nd:YAG-laser (20 mW at 532 nm) laser excitation system. IR spectra were collected using a micro-IR spectrometer (Thermo Nicolet: Centaurus) with ATR mode.

Results and discussion:

The analysis by EPMA identified several silica minerals in the mesostasis. CL imaging reveals that these minerals exhibit bright blue (fig. 1a) and dark blue (fig. 1b) CL emissions. They show similar CL spectral patterns with a broad peak at around 400 nm corresponding to lattice defect. But their intensities are different, whereas quartz exhibits fairly weak broad peaks at around 400 and 650 nm.

Raman spectra of these silica minerals give two spectral patterns, which can be assigned to tridymite and cristobalite by comparing with their terrestrial reference samples.

Tridymite in the mesostasis coexists with augite, olivine, plagioclase and Ti-rich magnetite. It occurs dispersively as a subhedral grain, of which longer dimension reaches up to 30 micrometers.

Zoned augite is embedded in the space among tridymite grains and has Fe-rich rim attached to tridymite. Cristobalite with 5~30 micrometers in width occurs as an anhedral interstitial form associated with plagioclase laths.

Micro-IR analysis of tridymite and cristobalite in mesostasis revealed that their IR spectra exhibit broad peaks centered at 3100~3400 cm^{-1} assigned to OH stretching vibration modes, whereas augite and olivine in nakhite and terrestrial silica minerals show no such similar peak position. This suggests that crystallization for the formation of nakhite involved H_2O in the igneous melt on the Mars.

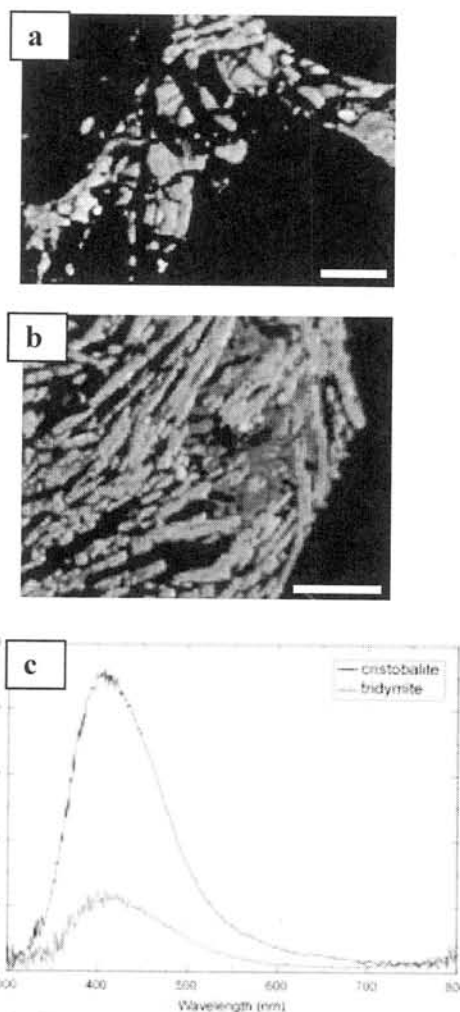


Figure 1. CL image of tridymite in Yamato 000593 (a), CL image of cristobalite in Yamato 000749 (b) and CL spectra of tridymite and cristobalite (c). Scale bars indicate 100 micrometers.

Al, Ti, and Cr: Complex zoning in synthetic and natural nakhilite pyroxenes. G. McKay¹, L. Le², and T. Mikouchi³, ¹Mail Code KR, NASA Johnson Space Center, Houston, TX 77058, ²ESC Group, NASA Johnson Space Center, ³Dept. of Earth and Planetary Science, Univ. of Tokyo, 7-3-1 Hongo, Tokyo 113-0033, Japan.

Introduction: Nakhilites are olivine-bearing clinopyroxene cumulates [e.g., 1]. The cumulus pyroxenes have cores that are relatively homogeneous in Fe, Mg, and Ca, but show complex zoning of minor elements, especially Al, Ti, and Cr. Zoning patterns contain information about crystallization history parent magma compositions. But it has proven difficult to decipher this information and translate the zoning patterns into petrogenetic processes [2-5]. This abstract reports results of high-precision EPMA analysis of synthetic nakhilite pyroxenes run at f_{O_2} from IW to QFM. It compares these with concurrent analyses of natural nakhilite MIL03346 (MIL), and with standard-precision analyses of Y000593 (Y593) collected earlier. Results suggest that (1) different processes are responsible for the zoning of MIL and other more slowly-cooled nakhilites such as Y593, and (2) changes in oxidation conditions during MIL crystallization are not responsible for the unusual Cr zoning pattern [4].

Analyses: Individual elements were counted for sufficient time to yield 1-sigma counting statistics of better than ± 0.16 wt% for Si and Ca, 0.10% for Fe, .06 for Mg, and .02 for all other elements. Analyses were performed on MIL and four synthetic samples using a single standardization. All samples were carbon-coated at the same time. These procedures result in minimum bias between samples so that all can be directly compared.

Results: Fig. 1 shows element maps of pyroxenes from Y593 and MIL. Al and Ti display patchy zoning in Y593, and show only very minor zoning of Cr. In contrast, MIL pyroxenes show almost no zoning in Al (not shown), but significant zoning of Cr. The latter tends to be depleted in the centers of the crystals and enriched in the outer portions of the homogeneous cores. Fig 2. shows a BSE image and an Al map of a

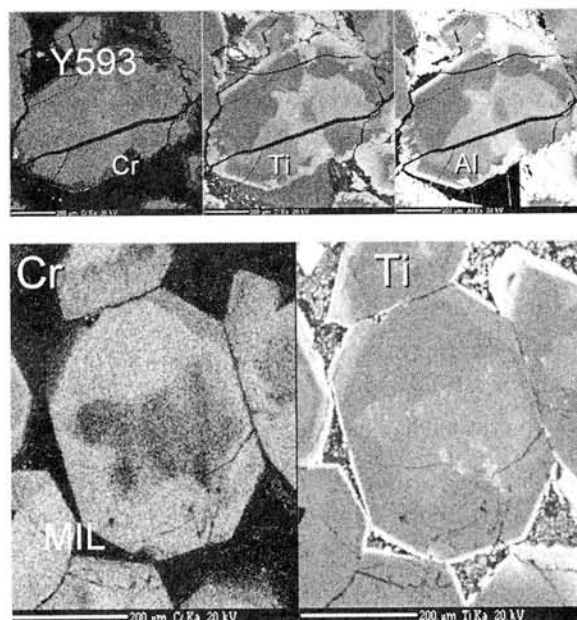


Fig. 1. Maps of Cr, Ti, and Al zoning in Nakhilite pyroxenes. Each image is $\sim 500 \mu\text{m}$ across.

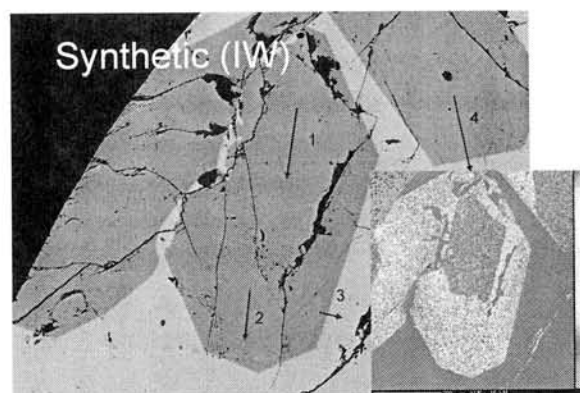


Fig. 2. BSE image and Al map (inset) of synthetic pyroxene grown at IW. Analytical traverses are marked on BSE image. Map $\sim 600 \mu\text{m}$ across.

synthetic nakhilite pyroxene that crystallized at IW. Al-poor regions in the center of the large grain and bottom of the top right grain were produced by sector zoning.

Variation of Cr with Ti is shown in Fig. 3 for synthetic pyroxenes crystallized at four oxygen fugacities, and for MIL pyroxene cores. Routine (less precise) analyses of Y593 pyroxenes are also shown. Note Cr decreases with increasing Ti for MIL, in contrast to all other samples. Fig 4 shows variation of Cr with Fe/Mg. Again, in con-

trast to all other samples, Cr in MIL decreases with increasing Fe/Mg. These trends suggest fractional crystallization played a part in MIL pyroxenes. Cr is highly compatible in pyroxene, and would be strongly depleted from the melt during fractional crystallization. However, the fact that most Cr-poor regions are in the center of grains would require that these grains initially formed as hollow skeletons, or hopper grains, and subsequently filled in as Cr was depleted from the melt. There is no suggestion of this behavior in other nakhlites, which do not show the low Cr contents displayed by the MIL central pyroxenes.

Fig 5. shows structural formula data calculated from microprobe analyses and sheds light on substitution mechanisms for alter-valent cations in these nakhlite pyroxenes. A perfect analysis in which all Al is in the tetrahedral site and is charge compensated by Ti or Cr would plot along the line of slope 1. All pyroxenes plot below that line, indicating either that some Cr or Ti is entering as reduced species, or else some of the Al is entering the octahedral sites. Lack of correlation with fO_2 for the synthetic charges renders the former unlikely. This result suggests that Al activity was higher or Si activity lower in the melt from which MIL crystallized.

Because $D(Cr)$ in our experiments is a strong function of fO_2 , we investigated the possibility that changes in redox conditions could be responsible for variations in MIL Cr. MELTS calculations indicate that the cation total calculated from EPMA analyses (Fig. 6) would increase with fO_2 . The magnitude of the expected increase is indicated by the bar at the right in Fig. 6. Although we see an increase in cation total from IW to QFM pyroxenes, there is no significant difference in cation total between Cr-rich and Cr-poor regions of MIL pyroxene. Thus it appears that redox changes are not responsible for the observed Cr variations.

References: [1] Treiman, A. (2005) *Chem Erde* 65, 203. [2] McKay & Mikouchi (2005) *MAPS* 40, A5335. [3] McKay *et al.* (2006) *Antarctic Meteorites* 30, 61. [4] McKay *et al.* (2007) *LPSC* 38, 1721. [5] Cameron & Papike (1981) *Am. Min* 66, 1.

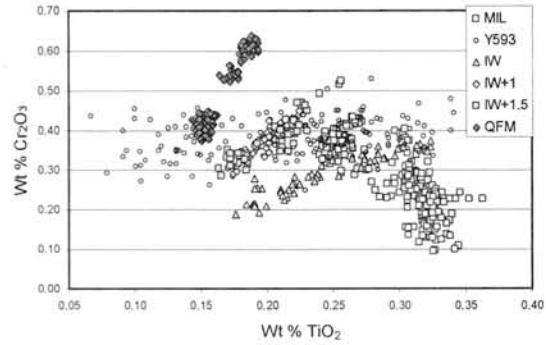


Fig. 3. Variation of Cr with Ti for synthetic pyroxenes from IW to QFM and for MIL. Less precise analyses of Y593 are also shown.

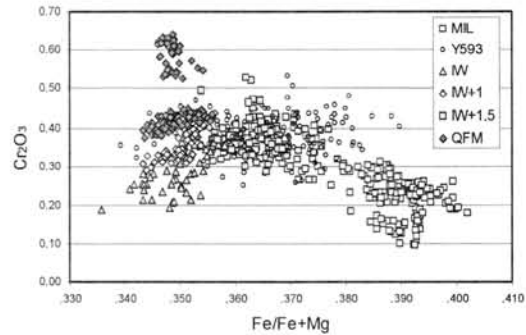


Fig 4. Variation of Cr with Fe/Mg for synthetic pyroxenes, MIL, and Y593.

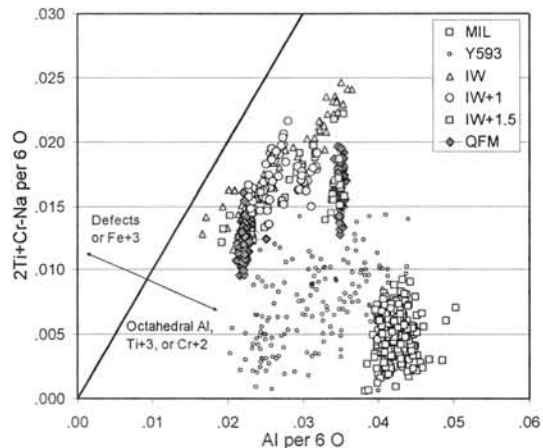


Fig. 5. Structural formula calculation indicating substitution mechanisms for Ti and Al [5].

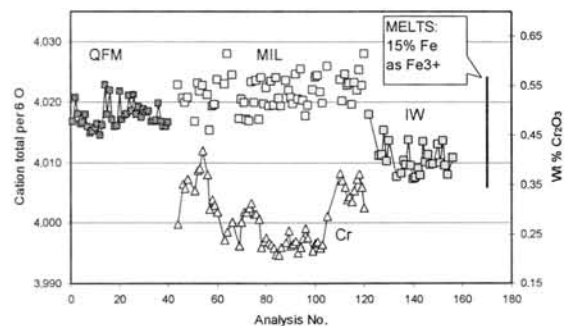


Fig. 6. Cation totals for synthetic and MIL pyroxenes. Cr profile is shown to indicate location of Cr-rich outer regions. Bar at right shows predicted change in cation total from IW (bottom) to QFM (top).

The petrology and origin of new ureilites found in Grove Mountains, Antarctica. B. Miao^{1,2*}, Y. Lin¹ and D. Wang³, ¹ Resources and Environment Engineering, Guilin University of Technology, Jiangan Road 12, Guilin 541004, P. R. China, ² State Key Laboratory of Lithospheric Evolution, Institute of Geology and Geophysics, Chinese Academy of Sciences, P.O. Box 9825, Beijing 100029, P. R. China, ³ Key Laboratory of Isotope Geochronology and Geochemistry, Guangzhou Institute of Geochemistry, Wushan, Guangzhou 510640, P. R. China. (*Email: miaobk@mail.igcas.ac.cn; miaobk@glite.edu.cn)

Introduction:

Ureilites are composed of coarse-grained olivine, pigeonite and carbon polymorphs, but lack of plagioclase [1]. They have two sets of different characteristics: “primary” features, such as high contents of carbon and similar oxygen isotope compositions to carbonaceous chondrites [2], and “evolved” features of coarse-grained igneous textures [3] and depleted lithophile elements bulk compositions. Many models have been proposed to explain their origins, e.g. magmatic accumulation and partial melting [4]. However, the origin of ureilites is an enigma, including formation of diamond and its relation with graphite. Three new ureilites were found in Grove Mountains, Antarctica [5, 6]. Here, we report their petrology and discuss their origins.

Petrology:

All three ureilites (GRV 021512, 143.4 g; GRV 022931, 1.24 g; and GRV 024516, 24.7 g) are the olivine-pigeonite type. Both GRV 021512 and 024516 are coarse-grained, consisting of predominant olivine and pigeonite, with interstitial MgO-rich silicates and graphite polymorphs. The triple junctions of 120° are very common among coarse-grained silicates (Fig.1). Olivine has reduced rims along the boundaries and/or fractures. In contrast, pigeonite shows little reduction or has a very narrow reduced rim. Graphite mainly occurs in fine-grained matrix, and some as thin plates included in pigeonite grains. The reduced “rosettes” of olivine may be reaction products of the grains with graphite. GRV022931 has a cataclastic porphyritic texture (Fig.2), different from GRV021512 and GRV024516. It is composed of coarse-grained olivine (19.1 vol%) and pigeonite (14.1 vol%) embedded in carbonaceous matrix (66.3 vol%). Both olivine and pigeonite grains are very irregular in shape with embayed outlines. But GRV022931 contains less abundant graphite than the other two ureilites. Raman spectra show coexistence of diamond and graphite (Fig.3). Diamond grains occur homogeneously in the carbonaceous veins and/or plates in these three ureilites (Fig. 4). Diamond grains are about 1-5 μm in size. The major silicate grains are slightly fractured and show undulatory extinction, suggesting their shock stages of S2/3.

Mineral chemistry:

The coarse grains of olivine have homogeneous cores with Fo contents of 79.6, 78.8 and 84.0 mol%, respectively. They usually contain minor Cr₂O₃ (0.46-2.11 wt%) and CaO (0.11-0.46 wt%). Almost all olivine grain have reduced rims with Fo >90 mol%. The coarse grains of pigeonite are also homogeneous in chemical compositions, with average compositions of En_{74.5}Wo_{8.0}Fs_{17.5} in GRV 021512, En_{71.7}Wo_{10.4}Fs_{17.9} in GRV 022931, and En_{76.0}Wo_{9.0}Fs_{15.0} in GRV 024516. In addition, all pigeonite grains also have minor Cr₂O₃ (0.92 - 1.22 wt%) and MnO (0.22 - 0.51 wt%).

Discussion and conclusions:

1. The three new ureilites share common main petrological features of olivine-pigeonite type, and they are monomict. Significant differences (e.g. compositions of olivine and pigeonite, and the modal abundances of carbonaceous matrix) between them argue that they are not paired.

2. All three meteorites contain diamond as small euhedral grains (1-5 μm) homogeneously distributed in the carbonaceous matrix. The coexistence of diamond and graphite supports a shock-induced origin of diamond.

3. The lack of other severely shocked features could be due to modification by post-shock thermal metamorphism, as indicated by the reduced rims of olivine and the triple junctions of 120° of coarse-grained silicates.

Acknowledgement:

This work is supported by the National Natural Science Foundation of China (Grant No.40473037).

References:

- [1] Goodrich C. A. (1992) *Meteorit.*, 27, 327–352.
- [2] Clayton R. N. et al. (1988) *GCA*, 52, 1313–1318.
- [3] Berkley J. L. et al. (1980) *GCA*, 44, 1579–1597.
- [4] Singletary S. J. et al. (2003) *Meteorit. Planet. Sci.*, 38, 95–108.
- [5] Russell S. S. (2005) *Meteorit. Planet. Sci.*, 40, A201–A263.
- [6] Connolly H. C. et al. (2006) *Meteorit. Planet. Sci.*, 41, 1271–1419.

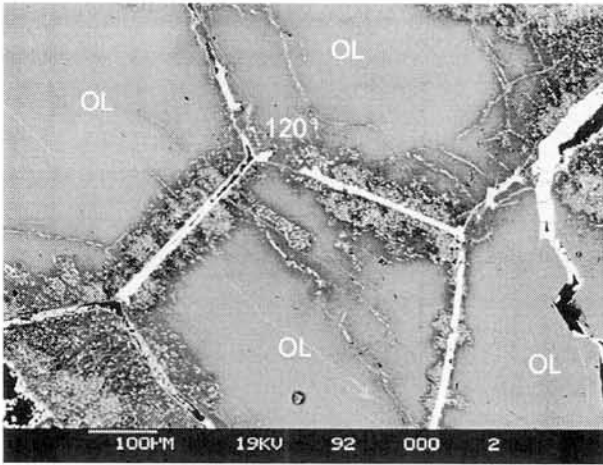


Fig.1 The 120° triple junction of olivine (OL) grains in GRV021512.

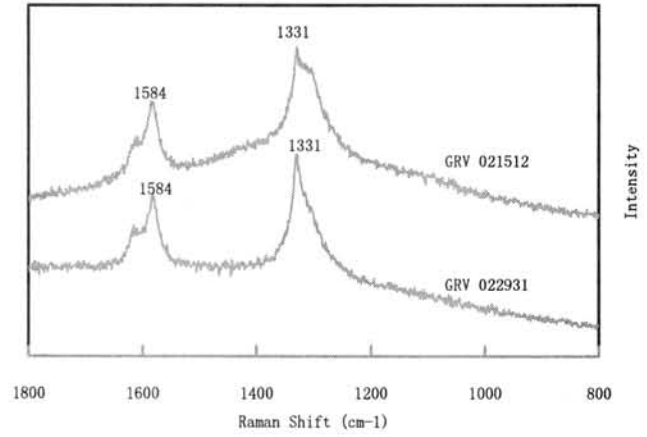


Fig.3 Raman spectra of graphite and diamond.

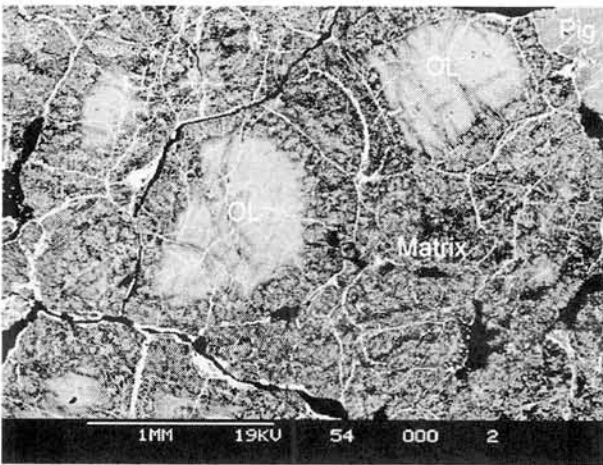


Fig.2 The cataclastic porphyritic texture of GRV022931, note that olivine (OL) and pigeonite (Pig) are isolated by carbonaceous matrix.

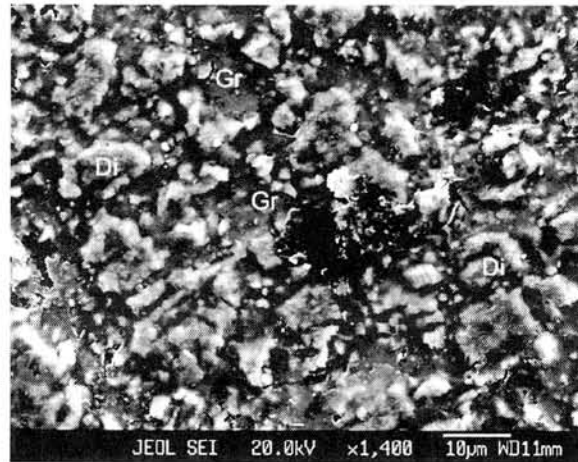


Fig.4 Coexistence of diamond (Di) and graphite (Gr).

Introduction: Lherzolitic shergottite is one of the major groups of Martian meteorites and currently consists of seven samples [1]. All the known lherzolitic shergottites show similar petrology and mineralogy [e.g., 2] and their crystallization and exposure ages are identical [e.g., 3]. Thus, they are widely considered to share the same original source on Mars and fell on the earth as separate falls [e.g., 2]. In spite of these similarities, each sample is slightly different from one another in mineral chemistry probably due to different degrees of re-equilibration [e.g., 2]. Recently, three new lherzolitic shergottites (Y000027, Y000047, and Y000097) were identified in the Yamato 00 Antarctic meteorite collection [4]. It is of great interest whether these new Y00 shergottites can fit to this story. If this is the case, it is important to know the difference of Y00 shergottites from other lherzolites to further understand petrogenesis of this Martian meteorite group. This will be also helpful to reconstruct the igneous body from which they originated. This abstract reports mineralogical and petrological study of three Y00 lherzolitic shergottites to check their possible pairing [2] and to understand crystallization history by comparing with other lherzolitic shergottites.

Petrography: The thin sections studied show two distinct textures, poikilitic and non-poikilitic in all three samples. Shock metamorphism is severe in all sections (e.g., patchy and mosaic extinction of pyroxene and olivine, maskelynitization of plagioclase, shock melting). Among three samples, the presence of a wide shock melt vein (~1.5 mm wide) in Y000027 is remarkable [4]. Except for this, all three samples show generally similar textures. The abundance of poikilitic areas is larger than that of non-poikilitic areas, and non-poikilitic areas are interstitial to pyroxene oikocrysts. In poikilitic areas, large pyroxene oikocrysts (up to 8 mm) enclose rounded olivine grains (usually ~500 μm) and euhedral chromites (~200 μm), and maskelynite is rare and small (~100 μm). Most areas of pyroxene oikocrysts are low-Ca pyroxene, and augite is usually present at edges of the oikocrysts. In non-poikilitic areas, olivine, maskelynite and pyroxene are major constituent phases with minor amounts of merrillite, Ti-rich chromite, ilmenite, and Fe(-Ni) sulfide. Olivine grains in non-poikilitic areas are usually ~1 mm, while pyroxene and maskelynite are smaller. Olivines in non-poikilitic areas are angular in shape unlike rounded grains in poikilitic areas.

Magmatic inclusions (~100 μm) are common in olivine grains in both areas and often surrounded with radial fractures.

Mineral chemistry: *Pyroxene* oikocrysts in poikilitic areas are chemically zoned from Ca-poor cores to Ca-Fe-rich rims. The zoning range is nearly identical among three Y00 samples (En₇₇Fs₂₁Wo₂-En₆₇Fs₂₂Wo₁₁) (Fig. 1). Augite in poikilitic areas is slightly zoned (En₅₄Fs₁₆Wo₃₀-En₄₈Fs₁₄Wo₃₈). Pigeonite in non-poikilitic areas is higher in Fe contents than that in poikilitic areas (En₆₇Fs₂₇Wo₆-En₆₀Fs₂₅Wo₁₅), which is also identical in three samples (Fig. 1). Augite in non-poikilitic area is compositionally similar to that in poikilitic areas (Fig. 1). Minor element contents (Al, Ti and Cr) in pyroxenes are also distinct between poikilitic and non-poikilitic areas. *Olivine* in Y00 shergottites shows a small compositional variation (Fa₂₄ to Fa₃₃). Such a variation is present among different grains, and individual grains are nearly homogeneous. The olivine grains in poikilitic areas are more Mg-rich and show wider compositional variation (Fa₂₄₋₃₁) than those in non-poikilitic areas (Fa₃₀₋₃₃) (Fig. 2) in all samples. Olivine grains located near the edges of pyroxene oikocrysts generally have more Fe-rich compositions as compared with those near centers of oikocrysts. *Maskelynite* in Y00 shergottites is weakly zoned (An₅₉Ab₄₀Or₁-An₄₇Ab₅₀Or₃). There is no significant compositional difference between two different areas. FeO decreases from the core to the rim (0.6-0.3 wt%), but then increases (0.3-0.6 wt%). Chromite in poikilitic areas is rather homogeneous (1 wt% TiO₂, 6-8 wt% Al₂O₃, 25-27 wt% FeO, 52-58 wt% Cr₂O₃), but that in non-poikilitic areas is zoned towards the rim of ulvöspinel-rich component (1-16 wt% TiO₂, 58-27 wt% Cr₂O₃). Ilmenite contains up to 6 wt% MgO. Merrillite contains 3 wt% MgO, 1 wt% FeO and 2 wt% Na₂O. A Ca, P-rich phase with low total sum is also

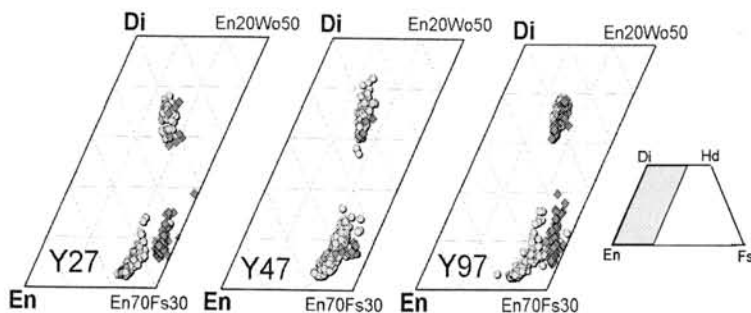


Fig. 1. Pyroxene compositions of Y000027 (Y27), Y000047 (Y47) and Y000097 (Y97) projected onto pyroxene quadrilateral. Circles are from poikilitic areas and diamonds from non-poikilitic areas.

present, which may be alteration of merrillite.

Crystallization of Y00 shergottites: The inferred crystallization sequence of minerals in Y00 shergottites is as follows. (1) Olivine and chromite crystallized from the parent magma. (2) Low-Ca pyroxene crystallized in a closed system by progressive fractional crystallization, and grew into large oikocrysts enclosing olivine and chromite. (3) The crystallizing pyroxene was replaced by augite during oikocryst growth. (4) Eventually, small interstitial melts were left between large pyroxene oikocrysts, olivine and chromite. Pigeonite and plagioclase began to crystallize from these evolved interstitial melts and formed non-poikilitic textures with cumulus olivine and chromite. (5) Small amounts of augite formed and Ti-rich spinel overgrew on cumulus chromite. Because of residence in interstitial melts, cumulus olivine in non-poikilitic areas became more Fe-rich due to re-equilibration and showed a narrower compositional distribution (Fig. 2). Chemical zoning of olivine and pyroxene suggests minor effect of re-equilibration after solidification of the whole rock. (6) Later shock event caused severe shock metamorphism including formation of a thick melt vein in Y000047. The sharp boundary between the vein and the host rock shows quenching after the shock. In fact, no compositional change is observed on the phases at the boundary.

Comparison with other lherzolitic shergottites: Because mineralogy and petrology of three Y00 shergottites are almost identical, we believe that they are paired meteorites as suggested by [4].

The mineralogy and inferred crystallization history of Y00 shergottites are generally similar to those of other lherzolitic shergottites [2]. There is little difference in pyroxene, maskelynite and chromite compositions (both in major and minor elements) between Y00 and other lherzolitic shergottites. Especially, minor elements in maskelynite show very similar zoning patterns to one another, possibly recording the same event [2]. Thus, it is evident that they experienced a very similar igneous crystallization history and supports the hypothesis that they all originated from the same igneous body on Mars.

Olivine is useful to estimate degrees of re-equilibration as well as comparison of each sample because of fast Fe-Mg diffusion rates [2]. Olivines in ALH77005 and GRV99027 show a tight compositional distribution (Fa_{24-30}), but those in LEW88516 and Y793605 have wider compositional distributions and are more Fe-rich (Fig. 3). NWA1950 (Fa_{23-32}) is intermediate between ALH77005-GRV99027 and LEW88516-Y793605 (Fig. 3). These observations show that ALH77005 and GRV99027 experienced larger degrees of re-equilibration than LEW88516 and Y793605 [2]. Y00 olivine composition is similar to NWA1950 and Y793605-LEW88516 olivines, but

different from any of them. Because of different olivine composition, Y00 samples are probably not paired with Y793605. The presence of merrillite in Y00 is also distinct from Y793605, which lacks merrillite.

Acknowledgment: We thank NIPR for organizing the Y00 shergottite consortium and providing samples.

References: [1] Meyer C. (2007) *Mars Meteorite Compendium*, NASA-JSC. [2] Mikouchi T. (2005) *MAPS*, 40, 1621-1634. [3] Nyquist L. E. et al. (2001) *Space Sci. Rev.*, 96, 105-164. [4] Misawa K. et al. (2006) *Antarct. Meteorites*, XXX, 63-64.

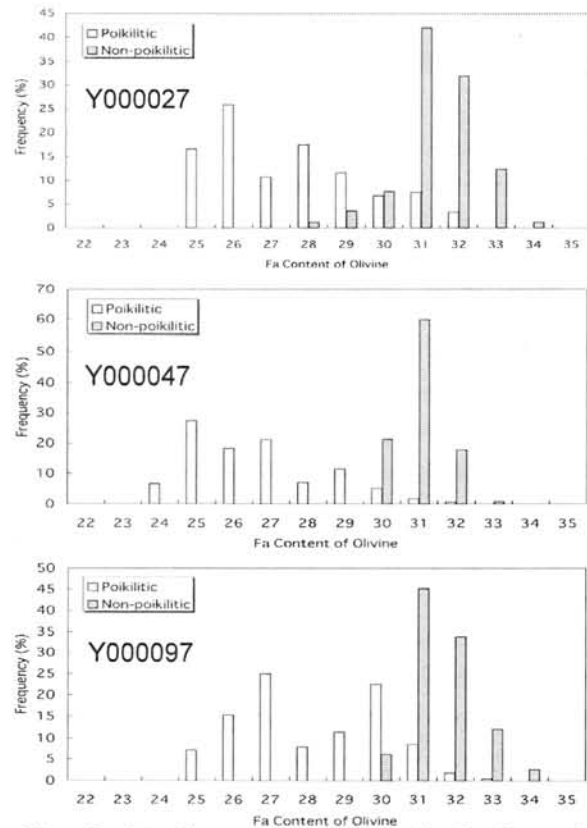


Fig. 2. Fayalite compositional distribution of olivine in Y00 lherzolitic shergottites.

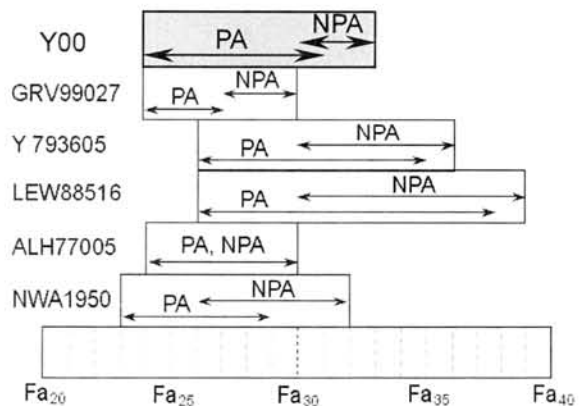


Fig. 3. Olivine compositions of lherzolitic shergottites. PA: poikilitic area. NPA: non-poikilitic area.

Rb-Sr and Sm-Nd Isotopic Studies of Lherzolitic Shergottite Yamato 000097. K. Misawa¹, C.-Y. Shih², Y. Reese³ and L. E. Nyquist⁴, ¹Antarctic Meteorite Research Center, National Institute of Polar Research, Tokyo 173-8515, Japan (misawa@nipr.ac.jp), ²ESCG/Jacobs Sverdrup, Houston, TX 77058, U.S.A., ³ESCG/Muñiz Engineering, Houston, TX 77058, U.S.A., ⁴ARES, Mail Code KR, NASA Johnson Space Center, Houston, TX 77058, U.S.A.

Introduction: Lherzolitic shergottites, Yamato (Y) 000027, Y000047 and Y000097 are composed of low-Ca pyroxene, olivine and maskelynite plagioclase with minor amounts of oxides and phosphates, and show poikilitic and non-poikilitic textures [1]. Shock effects are prevalent in these meteorites (i.e., shock-melt vein/pocket, maskelynite, mosaicism of olivine).

As a part of the consortium studies for these Martian meteorites we have undertaken Rb-Sr and Sm-Nd isotopic studies of Y000097 to precisely determine its crystallization age and to compare the isotopic signatures with those of other shergottites [2], especially lherzolitic shergottites ALH 77005 [3-5], Y-793605 [6-8] and LEW 88516 [5].

Analytical Procedures: A sample of Y000097,53, weighing 0.85 g, was processed by gently crushing to grain size <149 μm . About 25% of the crushed material was taken as whole-rock samples (WR, WR2 and reserve). Pyroxene (Px) and maskelynite plagioclase (Plag) fractions were obtained by using a Frantz isodynamic magnetic separator. We could not obtain a pure olivine separate; instead it contains some pyroxenes (Ol+Px). We also processed three whole-rock samples of Y-793605,71 for comparison.

The whole-rock and mineral concentrated samples were washed with 2N HCl in an ultrasonic bath for 10 minutes to leach out phosphates. Acid residues and leachates (WR(r), Px(r), Ol+Px(r), Plag(r), WR(l) and $\Sigma\text{Min}(l)$: combined mineral leachates) plus unleached whole-rock samples (WR1 from the homogeneous powdered sample Y000097,21 and WR2 from Y000097,53) as well as whole-rock samples from Y-793605,71 (WR1, WR2, WR(r) and WR(l)) were analyzed for Rb-Sr and Sm-Nd following the procedures of [9].

Results and Discussion: The rubidium and strontium concentrations for whole-rock and mineral samples for Y000097 are shown in Fig. 1. The near concordancy of rubidium and strontium in 2N HCl-leached and unleached whole-rock samples strongly suggests the terrestrial weathering effect on rubidium and strontium is not so significant for Y000097 and Y-793605. The strontium concentration of WR2(,53) is ~90% higher than that of WR1(,21). This is attributed to a higher abundance of mesostasis in the sub-sample Y000097,53 compared to the homogeneous sample Y000097,21. The strontium concentration of Plag(r) is 346 ppm and is ~3 times higher than those of maskelynite samples from ALH 77005 and LEW 88516 [3-5]. The rubidium concentrations of the unleached whole-rock samples, WR1(,21) and WR2(,53), are comparable to those of other lherzolitic shergottites [3-5, 7, 10, 11].

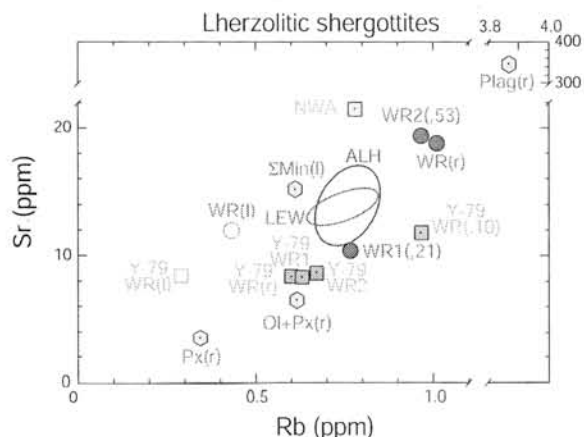


Fig. 1. Rubidium and strontium concentrations in Y000097 and other lherzolitic shergottites. Circles and hexagons are whole-rock and mineral samples, respectively, for Y000097. Ellipsoids represent variations of whole-rock samples, ALH=ALH 77005 and LEW=LEW 88516. Y-79=Yamato-793605, NWA=NWA 1950. Data are from [3-5, 7, 10, 11] and this study.

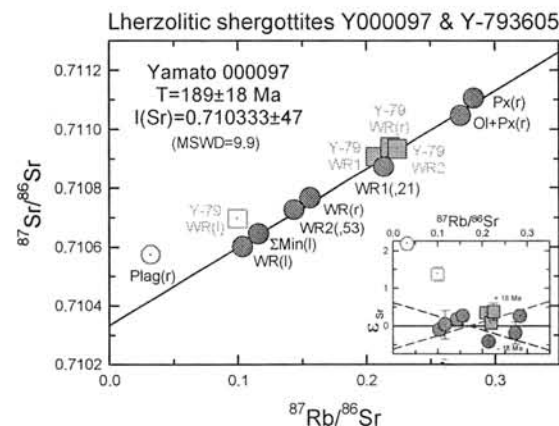


Fig. 2. Rb-Sr analytical results for Y000097 (circles) and Y-793605 (squares). A total of seven data points of Y000097 (filled circles) define a linear array corresponding to a Rb-Sr age of 189 ± 18 Ma with an initial $^{87}\text{Sr}/^{86}\text{Sr}$ of 0.710333 ± 0.000047 . The inset shows deviations of $^{87}\text{Sr}/^{86}\text{Sr}$ in parts in 10^4 (ϵ -units) relative to the 189 Ma isochron. Dotted lines on either side of the best fit line correspond to ± 18 Ma. The Plag(r) and Y-79 WR(l) points deviate upward from the isochron by 2.2 and 1.4 ϵ -units, respectively, suggesting a minor isotopic disturbance.

The Rb-Sr analytical results for Y000097 are shown in Fig. 2. A total of eight data points define a linear array corresponding to a Rb-Sr age of 152 ± 31 Ma with an initial $^{87}\text{Sr}/^{86}\text{Sr}$ of 0.710441 ± 0.000076 (mean square of weighted deviates: $\text{MSWD}=73$) for $\lambda(^{87}\text{Rb})=1.402 \times 10^{-11} \text{ yr}^{-1}$ using the Williamson regression program [12]. However, the Rb-Sr system of Y000097 is slightly disturbed. The Plag(r) point deviates upward from the isochron. Excluding the Plag(r) point, the age becomes 189 ± 18 Ma

(MSWD=9.9) with an initial $^{87}\text{Sr}/^{86}\text{Sr}=0.710333\pm 0.000047$.

The Rb-Sr data for the whole-rock samples of Y-793605 (WR1, WR2 and WR(r)), except for WR(l), plot on the Y000097 isochron (see Fig. 2, inset), suggesting that these lherzolitic shergottites may have almost identical crystallization ages of ~180 Ma. The present results are consistent with the previous isotopic studies for Y-793605 [6-8].

On the age versus initial $^{87}\text{Sr}/^{86}\text{Sr}$ diagram (Fig. 3), the error parallelogram for Y000097 overlaps that for Y-793605 but does not overlap those for ALH 77005 or LEW 88516, suggesting that Y000097 and Y-793605 were either co-magmatic or derived from very similar source regions. On the other hand, ALH 77005 and LEW 88516 may have been derived from similar but distinct source regions.

The isotopic disturbances observed in Y000097 and Y-793605 may be due to shock metamorphism, which produced impact-melt veins, or aqueous alteration on the Martian surface. Five data points (Plag(r) and four whole-rock samples from Y-793605) define a linear array corresponding to a Rb-Sr age of 136 ± 5 Ma with an initial $^{87}\text{Sr}/^{86}\text{Sr}=0.710511\pm 0.000011$. This age is older than the leachate-residue ages for LEW 88516 (~90 Ma) [5] but is comparable to those for Y-793605 (140-150 Ma) [6]. The initial $^{87}\text{Sr}/^{86}\text{Sr}$ ratio is 250 ppm higher than that obtained from the 189 Ma isochron but is almost identical to that of LEW 88516 ($^{87}\text{Sr}/^{86}\text{Sr}=0.71052\pm 0.00004$) [5].

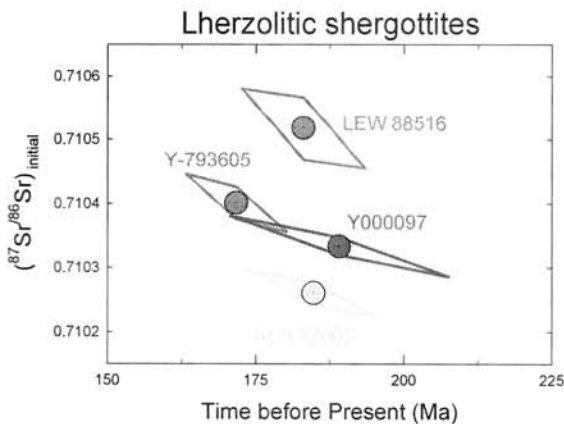


Fig. 3. Age versus initial $^{87}\text{Sr}/^{86}\text{Sr}$ diagram for lherzolitic shergottites. Data are from [5, 7] and this study. Ages and initial isotopic ratios are re-calculated using the Williamson regression program [12]. Strontium isotopic ratios are adjusted to $^{87}\text{Sr}/^{86}\text{Sr}=0.710250$ of the NBS 987 strontium standard [13]. The error parallelogram for Y000097 overlaps that for Y-793605.

The samarium concentration of the homogeneous sample WR1(21) is in good agreement with the INAA results by [14] (Fig. 4). The samarium concentration of WR2(53) is ~30% higher than that of WR1(21), suggesting again that Y000097,53 contains more abundant mesostasis. Enrichments of samarium in acid leachates, WR(l) and $\Sigma\text{Min}(l)$, are comparable (~25 x CI-chondrite).

About 80-90% of the samarium was leached out from whole-rock and mineral samples, which is consistent with a previous ion probe study for shergottite phosphates [15]. The samarium concentration of Plag(r) is comparable to those of the acid residue maskelynite from ALH 77005 and LEW 88516 [5]. This fact suggests that the Plag(r) fraction does not include impact-melt glass and/or phosphates. Additional Sm-Nd isotopic analyses are in progress.

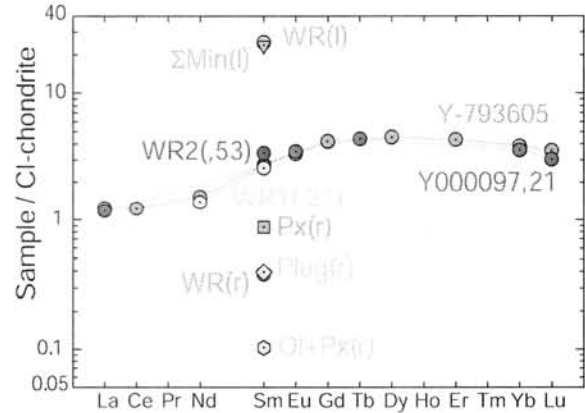


Fig. 4. CI-chondrite normalized samarium and neodymium abundances of whole-rock and mineral samples for Y000097. The REE patterns for Y000097,21 [14] and Y-793605 [8] are also shown.

References: [1] *Meteorite Newsletter* vol. 14 (2006), Misawa K. et al. (2006) *Antarct. Meteorites*, **XXX**, 63-64. [2] Nyquist L.E. et al. (2001) *Space Sci. Rev.* **96**, 105-164. [3] Shih C.-Y. et al. (1982) *Geochim. Cosmochim. Acta* **46**, 2323-2344. [4] Jagoutz E. (1989) *Geochim. Cosmochim. Acta* **46**, 2429-2441. [5] Borg L.E. et al. (2002) *Geochim. Cosmochim. Acta* **66**, 2037-2053. [6] Misawa K. et al. (1997) *Antarct. Meteorite Res.* **10**, 95-108. [7] Morikawa N. et al. (2001) *Antarct. Meteorite Res.* **14**, 47-60. [8] Misawa K. et al. (2006) *Antarct. Meteorite Res.* **19**, 45-57. [9] Shih C.-Y. et al. (1999) *Meteoritics & Planet. Sci.* **34**, 647-655. [10] Gillet P. et al. (2005) *Meteoritics & Planet. Sci.* **40**, 1175-1184. [11] Dreibus G. et al. (1992) *Meteoritics* **27**, 216-217. [12] Williamson J.H. (1968) *Can. J. Phys.* **46**, 1845-1847. [13] Nyquist L.E. et al. (1994) *Meteoritics & Planet. Sci.* **29**, 872-885. [14] Shirai N. and Ebihara M. (2007) *this volume*. [15] Lundberg L.L. et al. (1990) *Geochim. Cosmochim. Acta* **54**, 2535-2547.

Shock-Wave Heating Model for Chondrule Formation: Conditions to Reproduce Chondrule Shapes. H. Miura^{1,2}, T. Nakamoto³, and M. Doi^{3,4}, ¹Theoretical Astrophysics Group, Department of Physics, Kyoto University, Japan (miurah@tap.scphys.kyoto-u.ac.jp), ²Research Fellow of the Japan Society for the Promotion of Science, ³Earth and Planetary Science, Tokyo Institute of Technology, Japan, ⁴Pure and Applied Sciences, University of Tsukuba, Japan.

Introduction:

The data of chondrule shapes are strong clues for elucidating the chondrule formation mechanism. The three-dimensional data of chondrule shapes have been measured by using the X-ray micro-tomography [1]. The external shapes were approximated as three-axial ellipsoids with a-, b-, and c-axes (axial radii are A, B, and C ($A \geq B \geq C$), respectively). The plot of C/B vs. B/A shows that two groups can be recognized: oblate to prolate chondrules with C/B and B/A close to unity (group-A) and largely-deformed prolate chondrules with relatively small B/A of 0.7-0.8 (group-B). The oblate chondrules might be naturally explained by the rapid rotation of molten droplet [1]. However, the origin of the prolate shapes is not clear.

In the shock-wave heating model, which is one of the most plausible models for chondrule formation, [e.g., 2], it is naturally expected that the molten precursor dust particle (droplet) is exposed to the high-velocity gas flow. The strong gas ram pressure causes some hydrodynamical behaviours of the droplet: deformation and internal flow [3, 4], fragmentation [5], and stripping of the surface layer [6]. Recently, we developed the three-dimensional hydrodynamic simulation code for investigating the hydrodynamics of molten chondrule precursor dust particles in the framework of the shock-wave heating model [7]. We carried out the simulations of droplet deformation and found that the rotating viscous droplet exposed to the gas flow deforms to a prolate shape with the gas ram pressure and the angular velocity estimated from the shock-wave heating model [8]. Our results suggest that the existence of such prolate chondrules are the strong evidence of the chondrule formation by shock waves.

In this paper, we investigate how the droplet shape depends on the gas ram pressure p_{fm} and the angular velocity ω , and discuss the appropriate conditions to reproduce the external shapes seen in group-A (almost spheres) and -B (largely-deformed prolate shapes).

Methods:

We derived the analytic formula of the droplet deformation. The droplet viscosity just before solidification is very large, so the droplet deformation proceeds very slowly. If the rotation period of the droplet is much shorter than the deformation timescale, the gas flow can be approximated as to be axis-symmetrical about the rotation axis by taking a time average (see Figure 1).

Assuming the axis-symmetrical gas flow, we can obtain the analytic formula of the droplet deformation by solving the linearized hydrodynamical equations analytically, which is the same approach adopted by [3, 4, 6]. In our analytic formula, we found that the droplet shape depends only on two non-dimensional parameters: the Weber number W_e , which is the gas ram pressure normalized by the surface tension γ_s defined by $W_e \equiv p_{fm} r_0 / \gamma_s$, where r_0 is the unperturbed droplet radius, and the centrifugal force normalized by the gas ram pressure defined by $R \equiv \rho \omega^2 r_0^2 / p_{fm}$, where ρ is the mass density of the droplet. The deformed droplet radius is written by

$$r_s(\theta) = r_0 \left[1 + (W_e/12)(R_{cr} - R)P_2(\cos \theta) \right]_{\frac{1}{3}} \quad (1)$$

where θ is the angle against the rotation axis, $R_{cr} = 19/20$ is the critical value of R , and P_n is the Legendre function. Using Eq. (1), we can obtain the axial ratios C/B and B/A of the droplet for arbitrary sets of W_e and R . In the following sections, we discuss the condition to reproduce three-dimensional chondrule shapes based on our analytic formula.

Analytic Solution of Chondrule Shapes:

Figure 2 shows the axial ratios of the droplet calculated from Eq. (1) as a function of the Weber number W_e and the normalized centrifugal force R . When $R < R_{cr}$ (left side of a vertical dotted line), the centrifugal force is weaker than the effect of the gas ram pressure. In this case, the gas flow deforms the droplet to a prolate shape (see Figure 1). In this case, the axial ratio C/B is unity. The solid curves show the contours of the axis ratio B/A of 0.9, 0.8, 0.7 and 0.6 from bottom to top. The group-A chondrules have the axial ratios B/A of $\sim 0.9-1.0$, so the blue region suggests the condition to form the group-A chondrules. On the other hand, the group-B prolate chondrules have the axial ratios B/A of $\sim 0.7-0.8$, so the red region is for them.

In contrast, when $R > R_{cr}$ (right side of a vertical dotted line), the centrifugal force dominates the axis-symmetrical gas ram pressure and the droplet is deformed to be an oblate shape. In this case, the axial ratio B/A becomes unity and the solid curves turn into the indicator of the axial ratio C/B. The conditions for the group-A chondrules also appear in this rapidly-rotating case, however, the external shapes of group-B chondrules are no longer explained. In addition, the rapid rotation causes the shape instability as derived in the case of rotating droplet without the gas flow [9]. The condition corresponding to the shape instability is displayed by

the grayed region. It is found that the large part of the condition for oblate shapes is covered by the condition of the shape instability. It means that the largely-deformed oblate chondrules might be hardly reproduced by the rapid rotation.

Three-Dimensional Hydrodynamic Simulations:

We also carried out the three-dimensional hydrodynamic simulation of the rotating viscous droplet exposed to the gas flow. In the simulation, we did not assume the axis-symmetrical gas flow (see Figure 1). According to our numerical simulations, the approximation of the axis-symmetrical gas flow is valid when the rotation period is shorter than about $0.1t_{\text{def}}$, where t_{def} is the deformation timescale of the droplet. When the droplet rotates rapidly enough to satisfy the condition, our numerical simulations show a good agreement with the analytic formula (see Eq. 1), in which the axis-symmetrical gas flow was assumed (see Figure 1). The blue and red symbols in Figure 2 indicate the conditions on which the axial ratios of the final droplet shapes are similar to the group-A and -B, respectively. The symbols of pluses (+) mean the results of the other droplet shapes. Cross symbols (×) result into the shape instability.

Origin of Group-A and -B:

We discuss the origin of different two groups in chondrule shapes (group-A and -B). In the shock-wave heating model, the relative velocity between the droplet and the ambient gas decreases by the gas friction as they travel far from the shock front. If there is no heating source except the gas friction, the droplet would solidify before the relative velocity decreases significantly [10]. In this case, the group-B prolate chondrules can be formed because the gas ram pressure is sufficient to deform the droplet during solidification. In contrast, if the chondrule-forming region is too optically-thick for the dust thermal emission to escape directly, the radiation field in the chondrule-forming region becomes so strong that the dust particles cannot cool to solidify even after they stop with respect to the ambient gas [10, 11]. In this case, since the gas ram pressure does no longer affect the droplet during solidification, chondrule shapes would be close to sphere like as in the group-A. The intermediate shape corresponding to in the “gap” can be produced only when the radiation field is an intermediate strength, so they might be rare. It suggests that chondrules with such intermediate shapes might be observed by investigating more samples in the future.

Summary:

In this study, we obtained the conditions to reproduce external shapes of chondrules in the framework of the shock-wave heating scenario. The conditions are given by two non-dimensional parameters: Weber number W_e , which is the gas ram pressure normalized by the surface tension, and the centrifugal force normalized by the gas ram pressure R . The difference in shapes between the group-A (almost spheres) and -B (largely-deformed prolate

shapes) might result from the difference of the optical depth in the chondrule-forming region.

References:

- [1] Tsuchiyama A., et al. (2003) *LPS XXXIV*, 1271-1272. [2] Iida A., et al. (2001) *Icarus*, 153, 430-450. [3] Sekiya M., et al. (2003) *Prog. Theo. Phys.*, 109, 717-728. [4] Uesugi M., et al. (2003) *Eath, Planets and Space*, 55, 493-507. [5] Susa H. and Nakamoto T. (2002) *Astrophys. J.*, 564, L57-L60. [6] Kato T., et al. (2006) *Meteoritics*, 41, 49-65. [7] Miura H. and Nakamoto T. (2007) *Icarus*, 188, 246-265. [8] Miura H. et al. (2007) *LPS XXXVIII*, 1505-1506. [9] Chandrasekhar S. (1965) *Proc. Roy. Soc. London, A.*, 289, 1-26. [10] Miura H. and Nakamoto T. (2006) *Astrophys. J.*, 651, 1272. [11] Desch S. J. and Connolly H. C., Jr. (2002) *Meteorit. Planet. Sci.*, 37, 183-207.

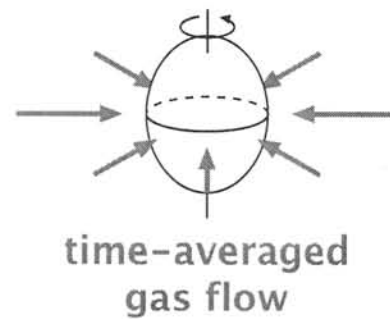


Figure 1: The schematic picture of the time-averaged gas flow around the rotating viscous droplet. If the rotation period is much shorter than the droplet deformation timescale, the gas flow can be approximated as to be axis-symmetrical like this figure.

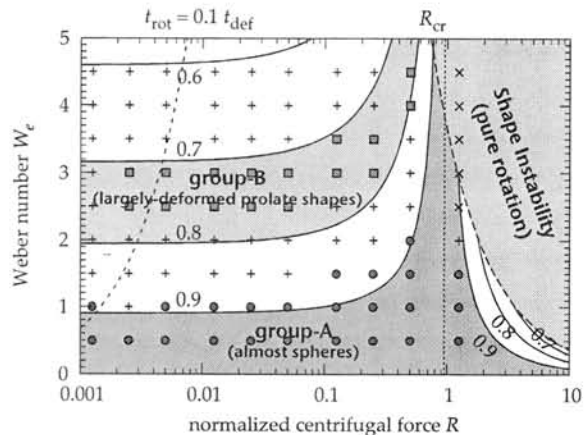


Figure 2: The axial ratios of the droplet calculated from Eq. (1) as a function of the Weber number W_e and the normalized centrifugal force R . The blue and red regions indicate the conditions to reproduce the group-A (almost spheres) and -B (largely-deformed prolate shapes). They match with the three-dimensional hydrodynamic simulations (blue and red symbols, respectively). The assumption of the axis-symmetrical gas flow (see Figure 1) is valid when the rotation period is shorter than about $0.1t_{\text{def}}$, where t_{def} is the deformation timescale of the droplet.

DETAILED ANALYTICAL SCANNING ELECTRON MICROGRAPHY OF CARBON-BEARING MATERIALS AT THE BARRINGER METEORITE CRATER IN U.S.A. Y. Miura, Inst. Earth Planet. Material Sciences, Graduate School of Science & Engineering, Yamaguchi University, Yoshida 1677-1, Yamaguchi, 753-8512, Japan, yasmiura@yamaguchi-u.ac.jp

Introduction: Carbon-bearing materials of the Barringer meteorite crater, Arizona, U.S.A. have been analyzed by X-ray diffraction (XRD) and analyzed scanning electron microscopy (ASEM) in 1993 [1]. The purpose of this paper is to elucidate source of carbon of the same samples from Field-Emission ASEM with carbon EDX detection (JEOL7000F) [2].

Large blocks of carbon without oxygen: Large blocks of carbon-bearing materials with about 10cm in width are mixed with (1) carbon (99%), (2) Fe-Ni with carbon, and (3) Calcium-rich carbonate and silica-rich oxides in the rim of large blocks (Fig.1). There are no such carbon-rich materials from carbonaceous meteorites and carbonate rocks from the deeper places of Earth. Minor elements of carbon (99%) in side the vein are Ca and Si from target rocks around the crater (but little oxygen). Ca and Si-rich grains in the rim have enough oxygen content from target rock of sandstone and limestone around the crater.

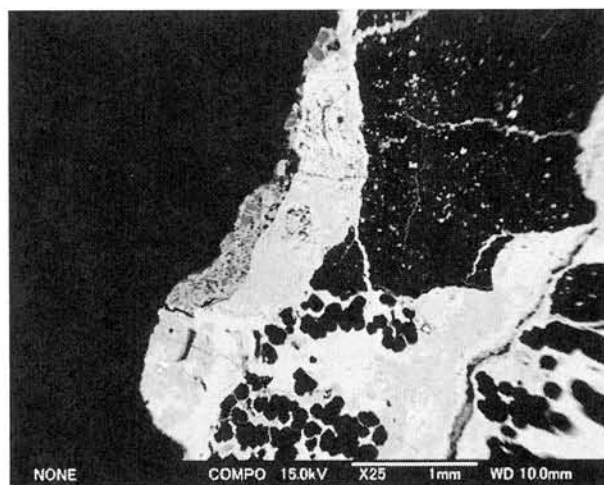


Fig.1 FE-ASEM image of carbon-rich, FeNi-rich, Si, Ca-rich grains from Barringer crater, Arizona, U.S.A. Compositional image. Bar is 1mm.

Complicated mixtures of FeNi-rich grains with and without carbon and oxygen: FeNi-rich grains of kamacite composition with the brightest images in the vein (Fig.2) contain much carbon but little oxygen. This indicates that the kamacite-like grains are formed after impact event by mixing with carbon dioxide from limestone rock. Contents of carbon and oxygen are

largely changed at FeNi-rich grains due to rapid-mixture during impact event (Fig.2). This feature cannot be found any meteorite and terrestrial rocks.

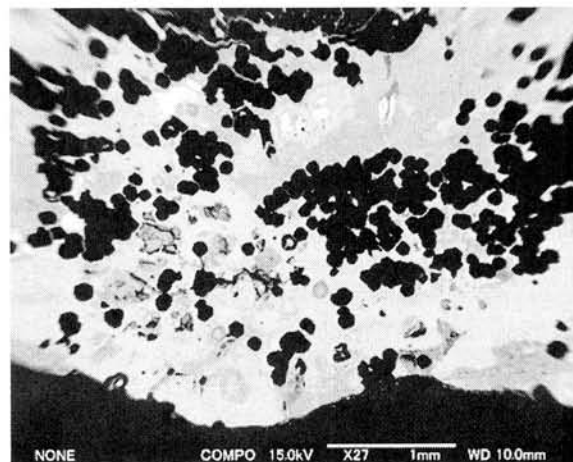


Fig.2. FE-ASEM image of FeNi-rich grains with various carbon and oxygen contents from the Barringer crater, Arizona, U.S.A. Compositional image. Bar is 1mm.

Different feature of carbon-rich grains: If carbon grains of the present sample are formed at static high pressure condition, all carbon shapes should be uniform. However, carbon-shapes of Barringer crater blocks are not uniform, from irregular to polyhedral shapes with filled or vacant core of each shape of carbon (Fig.3). This indicates that various carbon-rich grains are formed at rapid impact event. As meteorite contains Fe and Mg in their parent bodies, carbon-rich grains without Mg content can be explained at impact event of carbon and oxygen-rich target rock around the crater. As there are no much Ca-carbonate rock with carbon and oxygen in meteoroid parent bodies (as cosmic space), the carbon-rich blocks are formed in terrestrial surface with limestone rocks.

In fact, carbon-rich (99.9%) grains have trace amounts of Fe and Ni. On the other hand, curved feature of carbon-rich (91.7%) grains contains much Fe, Ni and oxygen contents. These irregular and mixed features of carbon-rich grains indicate formation of rapid reaction of huge impact event during the Barringer crater formation..

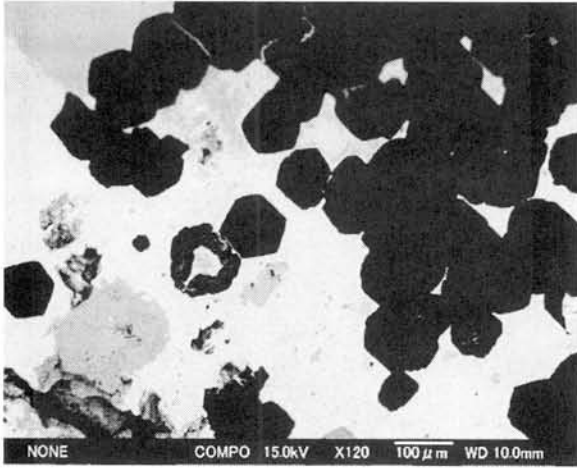


Fig.3. FE-ASEM image of various features of carbon-rich grains from Barringer crater, Arizona, U.S.A. Compositional image. Bar is 0.1mm.

Irregular texture inside the carbon-rich blocks:

In-site observation by the FE-ASEM shows detailed feature of carbon-rich grains with wormy-like texture (Fig.4). If it is formed at static high-pressure, internal texture should be regular texture. Figure 4 shows (1) irregular texture inside the carbon blocks, and (2) some multi-layer growth due to vaporization during impact.

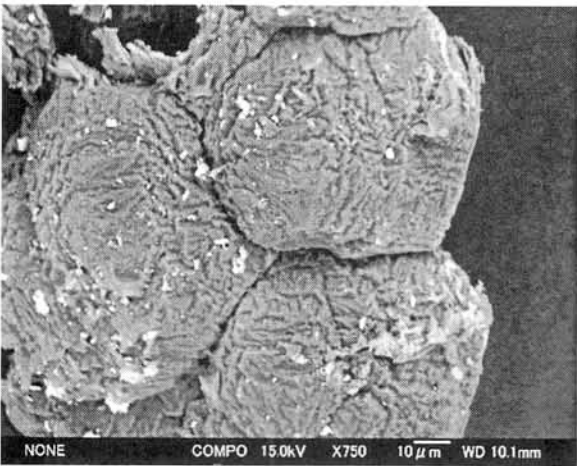


Fig.4. FE-ASEM image of FeNi-rich grains with various carbon and oxygen contents from Barringer crater, Arizona, U.S.A. Compositional image. Bar is 1mm.

Content of carbon: Carbon contents of carbon-rich grains are varied from 99.9% to 91.7%, with CaO (1.5 to 2.1%) and SiO₂ (2.2 to 2.5%) , where there are much oxygen contents in carbon-poor(91.7%)

grains (Fig.5). Calcium elements are explained from target rock of limestone around the crater.

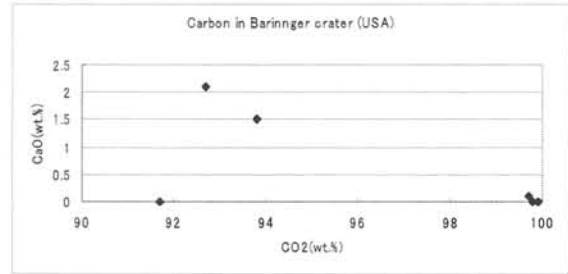


Fig.5. Relation of carbon and Ca contents shown in Figs. 3 and 4. Calcium elements are mixed from target rock.

Summary: The present results can be summarized as follows:

- (1) Rapid-mixture of carbon-rich and Fe-Ni-rich grains are found by FE-ASEM images of the Barringer crater, Arizona, U.S.A.
- (2) Content of carbon and oxygen of mixed grains can be explained as formation of impact on terrestrial surface.
- (3) Irregular and wormy texture and Ca content of carbon-rich grains indicates vapor growth of impact event.

Acknowledgements: Author thanks to operate by myself for the FE-ASEM machine in Yamaguchi, Japan in the study.

References:

[1] Miura Y., Noma Y. and Iancu G. (1993): New occurrence of shocked graphite aggregates at Barringer crater. *Meteoritics (USA)*, 28(3), 402.
 [2] Miura Y. (2007), *LPI Contribution, No.1338* (LPI/USRS, USA), abstract#1277.

FE-ASEM OBSERVATION OF IMPACT SPHERULES WITH CARBON, FE, AND NI ON KT GEOLOGICAL BOUNDARY: PROPOSED MODEL OF VARIOUS IMPACTS AMONG ROCKS, ATMOSPHERE AND OCEAN ON EARTH: Y. Miura, Inst. Earth Planet. Material Sciences, Graduate School of Science & Engineering, Yamaguchi University, Yoshida 1677-1, Yamaguchi, 753-8512, Japan, yasmiura@yamaguchi-u.ac.jp

Introduction: There are no direct observation of meteoritic elements of iron-group elements (Fe,Ni) and separated carbon (with minor calcium) elements for spherules on geological boundary. Impact history on Earth has been discussed by crater records on terrestrial surface so far. The purposes of this paper are to propose model of various impacts among rocks, atmosphere and ocean on Earth and to show impact evidences on KT (Cretaceous- Tertiary) spherules with Fe, Ni and C elements from Field-Emission analytical scanning electron microscopy (FE- ASEM) operated by author [1-4].

FE-ASEM observation of carbon with Fe, Ni, Co in spherules at Cretaceous-Tertiary (KT) boundary: Carbon-rich grains with iron-group elements (Fe, Ni) by impact on limestone rocks has been obtained at the sample of Cretaceous-Tertiary (KT) geological boundary in Spain by in-situ observation. Field-Emission analytical scanning electron microscopy (FE-ASEM) shows aggregates of spherules with Fe-Ni-Si-C (in $10 \mu\text{m}$ size) as shown in Fig.1.

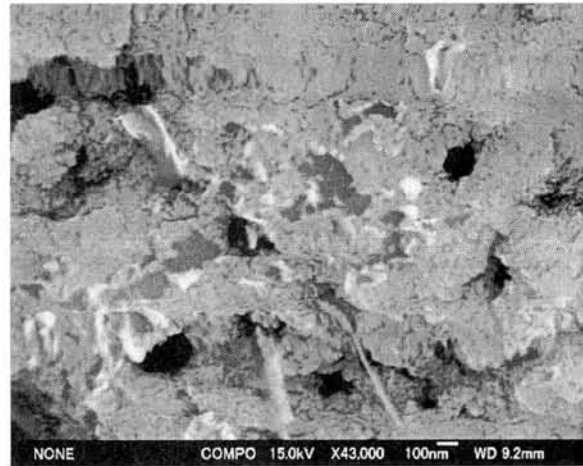


Fig.2. FE-ASEM image of impact grains with various Fe, Ni, Si and carbon from KT sample. Compositional image. Bar is 100nm. Bright grains are Fe,Ni rich parts.

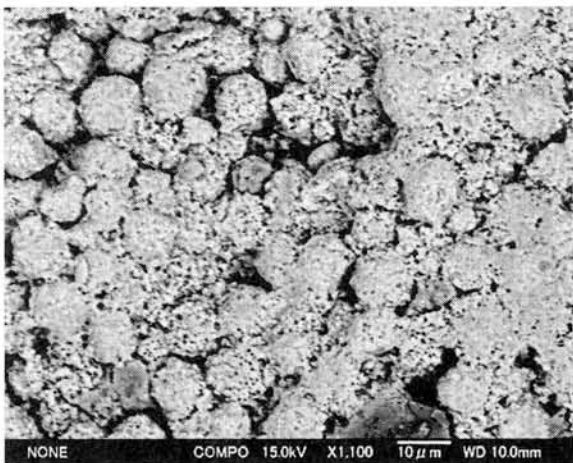


Fig.1 FE-ASEM image of spherules of Fe, S, Ni and Si from KT geological boundary. Compositional image. Bar is $10 \mu\text{m}$.

Various changes of carbon in KT spherules: KT spherules show mixtures of Fe-S-Si, Fe-Si-Ni and C-Fe-Ca systems in composition (Figs.2 and 3). Large spherules ($600 \mu\text{m}$ in size) contain smaller spherules ($10 \mu\text{m}$ in size) with minor grains ($1 \mu\text{m}$ and 100nm in size), which is direct evidences of impact vaporization from meteorite and target rocks.

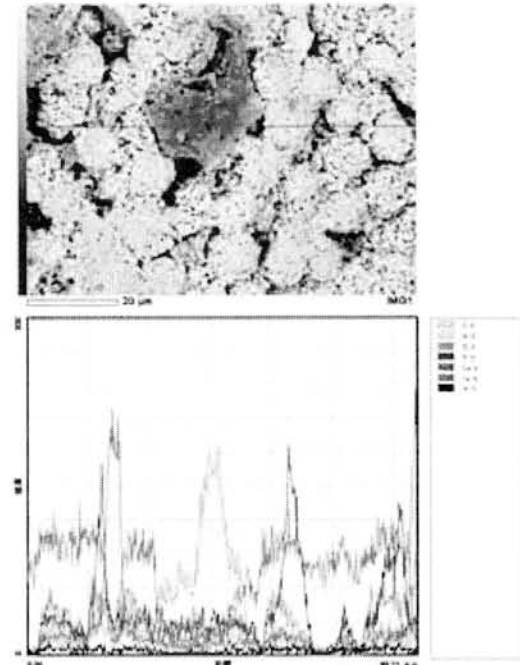


Fig.3. Line profile of carbon grain (93%CO₂) with FE-ASEM image from KT sample. Compositional image. Bar is $20 \mu\text{m}$.

Carbon and oxygen data for about 600 Ma on Earth produced by impact events: Crater records on rocks of the crust for about 600Ma are not enough for all impact history due to moving on surface by continental drift. Compositional records estimated from soil compositions are good indicator for various impacts among rocks, atmosphere and ocean on terrestrial surface. In fact, these target rocks and evaporated rocks contain meteoritic components of iron- and platinum-group elements.

Proposed model of various impacts: From compositional data of iron- and platinum-group elements of target rocks, remained geological boundary samples of carbon- and FeNi-bearing materials contains impact information among atmosphere, ocean water and crustal rocks for about 600Ma [1-4]. Proposed models for various impacts are herewith discussed on five geological boundaries of mass extinction as follows:

(1) Ordovician-Silurian boundary on Palaeozoic Era (435Ma): Major explosion in atmosphere followed to ocean impacts are proposed from carbon data.

(2) Devonian-Carboniferous geological boundary on Palaeozoic Era (360Ma): Both explosion in atmosphere and impacts on igneous rocks are proposed from data of oxygen and carbon changes.

(3) Permian-Triassic geological boundary on Palaeozoic to Mesozoic Era (250Ma): Heavy impacts on ocean-water and limestone rocks are proposed from data of oxygen and carbon changes.

(4) Triassic-Jurassic geological boundary on Mesozoic Era (205Ma): A few impacts on rocks of limestone and igneous rocks are proposed from data of oxygen changes with small carbon changes.

(5) Cretaceous-Tertiary (KT) geological boundary on Mesozoic to Cenozoic Era (65Ma): A few impacts on rocks of limestone and igneous rocks are proposed from data of oxygen and carbon changes.

As there are no reports on impact craters from 580Ma to 215Ma, probable impacts on this period are mainly at atmosphere and ocean water. This model can be explained also from largely ocean water on north hemisphere which is considered to be mainly target on Earth from 580Ma to 215Ma.

On the other hand, there are many remained impact craters from 215Ma to 5Ma which can be explained as target rocks of the crust after continental drift to north hemisphere.

Permian-Triassic (PT) geological boundary is considered to be a period between the above two ages; that is, (1) impact event changes from atmosphere-ocean water to crust rocks, and (2) Remarkable moving of crustal rock as impact target by continental drift finally.

Summary: The present results can be summarized as follows:

(1) Spherules of KT geological boundary are mixture of 3-sizes ($10\ \mu\text{m}$, $1\ \mu\text{m}$ and 100nm in sizes) which are evidences of impact vaporization between asteroid meteorite and target rock.

(2) Meteoritic components of iron-group elements and carbon from targets can be found at geological boundary to indicate the location of impact events on Earth.

(3) From compositional data and information of impact, proposed model of various impacts is shown in five geological boundaries of mass extinction from atmosphere-ocean water impacts to crust rock impacts in this study.

Acknowledgements: Author thanks to operate by myself for the FE-ASEM machine in Yamaguchi, Japan in the study.

References:

- [1] Miura Y. (2006), *LPS XXXVII*, abstract #2441 (LPI/USRS, USA).
- [2] Miura Y. (2006): *ICEM2006 Symposium Abstract Paper Volume* (Yamaguchi University, Yamaguchi, Japan), 102-103, 112-113.
- [3] Miura Y. (2007), *LPI Contribution, No.1338* (LPI/USRS, USA), abstract#1277.
- [4] Miura Y. (2006): Antarctic Meteorite XXIX (NIPR), 30, 69-74.

Noble gases of the Yamato 000027 and Yamato 000097 Iherzolitic shergottites. K. Nagao¹, J. Park² and H. Choi¹, ¹Laboratory for Earthquake Chemistry, Graduate School of Science, University of Tokyo, Bunkyo-ku, Tokyo 113-0033, Japan, ²NASA Johnson Space Center, 2101 NASA Parkway, Houston, TX 77058, USA.

Introduction:

Noble gases for two bulk samples from the Iherzolitic shergottites Yamato 000027 and Yamato 000097, and a melt vein sample from Yamato 000027 have been investigated to clarify cosmic-ray exposure history and to observe trapped noble gases of Martian origin. Most shergottites show relatively short cosmic-ray exposure histories (<5Ma) compared with other Martian meteorites, i.e., ~11 Ma for nakhlites and Chassigny, ~15 Ma for ALH 84001 orthopyroxenite. Only an exception among the shergottites is Dho 019, which has the longest exposure age of ~20 Ma. EET 79001 shergottite is supposed to contain Martian atmosphere especially in shock induced melt materials [1].

Experimental methods:

Bulk samples weighing 6.0 and 53.9 mg from Y000027 and 19.8 and 110.1 mg from Y000097 were measured for noble gases by using total melting and stepwise heating methods, respectively. A melt vein sample (30.2 mg) from Y000027 was measured by the stepwise heating method. The heating temperature for total melting was 1800°C and the stepwise heating employed temperatures of 400, 600, 800, 1000, 1200, 1400, 1600, and 1800°C. Noble gases released from the samples at each temperature step were purified with Ti-Zr getters and separated into four fractions, He-Ne, Ar, Kr, and Xe, then measured on a modified-VG5400(MS-II) noble gas mass spectrometer. Sensitivities and mass discrimination correction factors of the mass spectrometer were calibrated by measuring known amounts of atmospheric noble gases and a ³He-⁴He mixture with ³He/⁴He = 1.71x10⁻⁴. Blank corrections have been applied for the noble gas data.

Mineral separation was carried out on about 250 mg sample from the allocated Y000097 chip by J. P. at NASA. The mineral separates will be measured for noble gases in future with the same procedure noted above.

Results and discussion:

Elemental abundances and isotopic compositions of noble gases are similar among the bulk samples from Y000027 and Y000097. The results suggest pairing for these meteorites. He and Ne are predominantly cosmogenic, and low temperature fractions show terrestrial atmospheric contamination.

Cosmic-ray exposure ages are examined in Table 1, where cosmogenic ³He, ²¹Ne and ³⁸Ar concentrations, production rates for these isotopes, and calculated cosmic-ray exposure ages are summarized. The production rates P₃, P₂₁ and P₃₈ for Y000097 were calculated using the formulas by

Eugster and Michel [2] and the bulk chemical compositions of Y000097 by Shirai and Ebihara [3]. Because Y000027 seems to be paired with Y000097, the production rates for Y000097 were applied to Y000027. Exposure ages based on the ³He and ²¹Ne are longer than those from the ³⁸Ar concentrations. Same case has been reported for Y793605 Iherzolitic shergottite by Nagao et al. [4], where the exposure ages calculated with ³He and ²¹Ne were adopted as shown in Table 1. Hence, we tentatively adopt 4.9 Ma as an exposure age for Y000027 and Y000097, which are the average value of T₃ and T₂₁ for bulk and melt vein samples. The age is similar to that of Y793605 (5.4 Ma), suggesting pairing for these meteorites. Compared with the Yamato Iherzolitic shergottites, the Y980459 shergottite [5] has much younger exposure age (~2 Ma).

Table 1. Cosmogenic noble gases and cosmic-ray exposure ages of Y000027 and Y000097 shergottites.

| Sample | unit | Y000027 | | | Y000097 | | Y793605# | | Y980459* | |
|--------------------------------------|--------------------------|---------|-----------|------|---------|------|----------|------|----------|--|
| | | bulk | melt vein | | bulk | | bulk | | bulk | |
| | | TM | SH | SH | TM | SH | TM | SH | SH | |
| ³ He | | 677 | 728 | 649 | 734 | 729 | 891 | 835 | 270 | |
| ²¹ Ne | 10 ⁻¹⁰ cc/g | 151 | 147 | 176 | 151 | 139 | 126 | 112 | 72.9 | |
| ³⁸ Ar | | 21.6 | 19.2 | 29.1 | 24.9 | 20.4 | 20.9 | 17.6 | 21.7 | |
| P ₃ | | 159 | 159 | 159 | 159 | 159 | 161 | 161 | 166 | |
| P ₂₁ | 10 ⁻¹⁰ cc/gMa | 28.5 | 28.5 | 28.5 | 28.5 | 28.5 | 21.8 | 21.8 | 28.9 | |
| P ₃₈ | | 7.46 | 7.46 | 7.46 | 7.46 | 7.46 | 7.29 | 7.29 | 10.1 | |
| T ₃ | | 4.26 | 4.58 | 4.09 | 4.62 | 4.59 | 5.53 | 5.19 | 1.6 | |
| T ₂₁ | Ma | 5.30 | 5.16 | 6.18 | 5.30 | 4.88 | 5.78 | 5.14 | 2.5 | |
| T ₃₈ | | 2.90 | 2.57 | 3.90 | 3.34 | 2.74 | 2.87 | 2.41 | 2.1 | |
| Av(T ₃ ,T ₂₁) | | | | 4.90 | | | 5.4 | | 2.1 | |

TM: Total melting; SH: Step heating; #: Nagao et al. (1997); *: Okazaki and Nagao (2004)

Both Y000027 and Y000097 show maximum ⁴⁰Ar/³⁶Ar(trap) values of about 2000 at the temperatures around 1000-1400°C. It is difficult to estimate a contribution of Martian atmospheric Ar to the high ⁴⁰Ar/³⁶Ar ratios. If we assume the ⁴⁰Ar is totally in situ produced radiogenic ⁴⁰Ar, an upper limit of K-Ar age can be calculated as 1.4 Ga for Y000097 using the K₂O concentration of 0.0282 wt% [3]. The young age also supports Martian origin for the Y000027 meteorite.

Fig. 1 is a correlation diagram for ¹²⁹Xe/¹³²Xe vs. ⁸⁴Kr/¹³²Xe. Data points for Y000027 and Y000097 bulk samples plot following a typical trend observed for shergottites, i.e., data points move to EFA (elementally fractionated air [6]) from terrestrial atmosphere at low heating temperatures, then move to Martian atmosphere at higher temperatures (>1000°C). Highest ¹²⁹Xe/¹³²Xe of 1.3 was observed at 1400°C for bulk samples. Apart from the bulk samples, the melt vein sample from Y000027 shows extremely different trajectory as plotted in Fig. 1. Kr/Xe ratios are much higher than those for the bulk samples, especially at 1400°C extraction temperature, where the ⁸⁴Kr/¹³²Xe became as high as 76. The ¹²⁹Xe/¹³²Xe ratio at 1600°C is 1.6, which is higher than that for bulk samples. Though the higher ¹²⁹Xe/¹³²Xe ratio in melt vein than in bulk samples

may indicate higher abundance of Martian atmospheric noble gases in melt vein portion, mechanism for the enrichments in Martian atmospheric noble gases especially in Kr is difficult to be clarified.

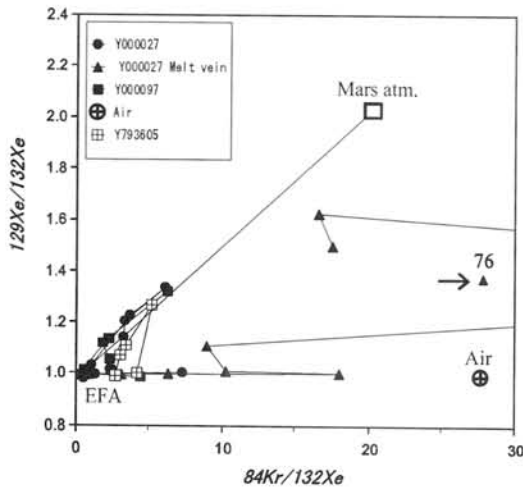


Fig. 1. $^{129}\text{Xe}/^{132}\text{Xe}$ vs. $^{84}\text{Kr}/^{132}\text{Xe}$ diagram for Yamato 000027 and Yamato 000097 lherzolitic shergottites. Yamato 793605 shergottite [4] is also shown for comparison.

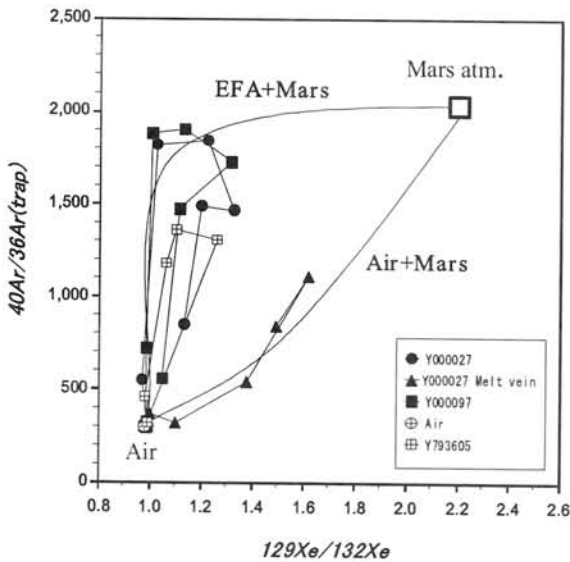


Fig. 2. Plot of $^{40}\text{Ar}/^{36}\text{Ar}$ vs. $^{129}\text{Xe}/^{132}\text{Xe}$. The lines labeled as EFA+Mars and Air+Mars represent mixing curves between elementally fractionated terrestrial air and Martian atmosphere and terrestrial and Martian atmospheres, respectively.

Fig. 2 is a plot of $^{40}\text{Ar}/^{36}\text{Ar}$ versus $^{129}\text{Xe}/^{132}\text{Xe}$, where ^{36}Ar had been corrected for cosmogenic ^{36}Ar . Bulk samples release terrestrial atmospheric Ar and Xe at the low temperatures, followed by rapid increase in $^{40}\text{Ar}/^{36}\text{Ar}$ ratios up to about 2000. Elevated $^{129}\text{Xe}/^{132}\text{Xe}$ ratio, which seems to be a Martian atmospheric signature, is observed at higher

temperatures (1.3 at 1400°C). The patterns seem to follow the mixing curve between Martian atmosphere and the EFA. Contrary to the release pattern for the bulk samples, the melt vein show rapid increase in $^{129}\text{Xe}/^{132}\text{Xe}$ up to 1.6 at 1600°C , while $^{40}\text{Ar}/^{36}\text{Ar}$ remains low (≤ 1000). The pattern may be explained by the mixing between terrestrial and Martian atmospheres. As both $^{40}\text{Ar}/^{36}\text{Ar}$ and $^{129}\text{Xe}/^{132}\text{Xe}$ in Martian atmosphere are believed to be high (>2000 and >2 , respectively), the relatively low $^{40}\text{Ar}/^{36}\text{Ar}$ in the melt vein might be heavier contamination from terrestrial atmospheric Ar.

Fig. 3 shows ^{36}Ar and ^{40}Ar release at each extraction temperature. The patterns for bulk samples from Y000027 and Y000097 are identical. On the other hand, the melt vein sample releases almost one order of magnitude larger amount of ^{36}Ar than the bulk samples. Enhanced release of ^{40}Ar at low and high temperature ranges was also observed. Because $^{129}\text{Xe}/^{132}\text{Xe}$ in the melt vein is higher than those in bulk samples, both terrestrial and Martian atmospheric heavy noble gases are enriched in the melt vein portion. Shock implantation of Martian atmosphere may responsible for the Martian component, but a trapping mechanism for the large amounts of terrestrial noble gases is not clear at present.

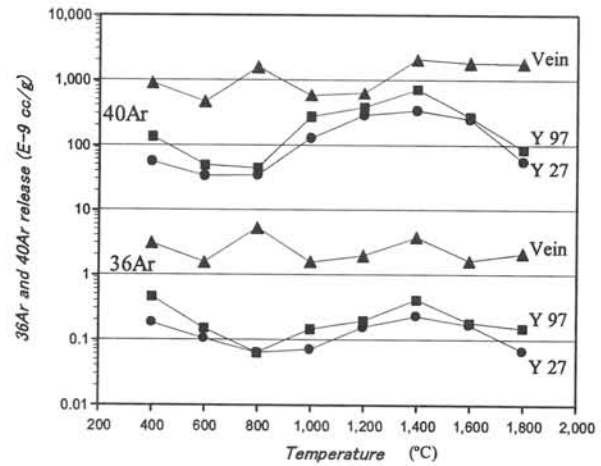


Fig. 3. Release patterns for ^{36}Ar and ^{40}Ar at the temperatures from 400 to 1800°C . Enhanced release of Ar from the melt vein at high temperatures is accompanied by high $^{129}\text{Xe}/^{132}\text{Xe}$ of Martian origin.

References:

- [1] Bogard D.D. and Johnson P. (1983) *Science* 221, 651-654.
- [2] Eugster O. and Michel Th. (1995) *G.C.A.* 59, 177-199.
- [3] Shirai N. and Ebihara M. (2007) *Antarct. Meteorites XXXI* (this volume).
- [4] Nagao K. et al. (1997) *Antarct. Meteorite Res.* 10, 125-142.
- [5] Okazaki R. and Nagao K. (2004) *Antarct. Meteorite Res.* 17, 68-83.
- [6] Mohapatra R.K. et al. (2002) *LPSC #1532*.

Planar Microstructures on the Shock-induced deformation twins in clinopyroxene from the aubrite Allan Hills 78113. Sz. Nagy¹ (ringwoodit@yahoo.com), A. Gucsik², S. Józsa¹, Sz. Bérczi¹, K. Ninagawa³, H. Nishido⁴
¹Eötvös Lóránd University of Budapest, H-1117 Budapest, Pázmány Péter sétány 1/c., Hungary; ²Max Planck Institute for Chemistry, Department of Geochemistry, Becherweg 27, D-55128, Mainz, Germany; ³Department of Applied Physics, Okayama University of Science, 1-1 Ridai-cho, Okayama, 700-0005, Japan; ⁴Research Institute of Natural Sciences, Okayama University of Science, 1-1 Ridai-cho, Okayama, 700-0005, Japan.

Introduction: Shock-induced physical and chemical changes in minerals are collectively called shock effects or shock metamorphic effects. This term is relatively broad and covers any type of shock-induced change, such as formation of lattice defects, phase transformations, decomposition reactions and resultant changes in physical and chemical properties [1]. The deformation and transformation effects largely arise during the compression phase of shock waves. The response of a mineral to shock compression largely depends on its crystal structure and composition. With the resolution of the optical microscope, two basic types of planar microstructures can be distinguished: Planar fractures (PF) and planar deformation features (PDFs). The progressive shock-pressure causes twins such as in feldspars, pyroxenes, and calcite [1,2,3,4]. The purpose of this optical microscopic study is to identify and characterize planar microdeformations especially in clinopyroxene as well as evaluate the shock stages in a ALH78113 sample (Fig. 1).

Sample: The ALH78113 sample is an aubritic type enstatite achondrite. The sample contains large enstatite grains up to 2.5 cm, and several dark clasts. The grains form a slightly brecciated texture. Olivine is also discernible in some parts of this sample. Microprobe analyses show that the pyroxene is iron free enstatite ($\text{FeO} < 0.1 \text{ wt\%}$) with minor and variable amounts of CaO (0.2-0.6 wt%, average 0.5 wt%) [5].

Results: The single enstatite grains contain relatively high density of irregular fractures, and shows straight deformation twin lamellae (Fig. 1). These twins are produced by shock wave propagation, and their have 10^0 of extinction angle relative to the host grain. The twins are 5-15 μm wide, and 10-100 μm long (Fig. 1). The planar microstructures are extending through the twin lamellae (Fig. 1). The microstructures are 1-3 μm long, and $>1 \mu\text{m}$ wide. The spacing between two neighbouring microstructures is about 2 μm . However, we did not observe the high pressure polymorph of pyroxene nor pyroxene glass. Consequently, the sample may be classified to be in the low shock pressure regime. The observed microstructures have one set on the shock-induced twin lamellae. We assume, that the twins were produced earlier during the shock process, and the microstructures were produced later, both in the

case of the planar fractures and planar deformation features.

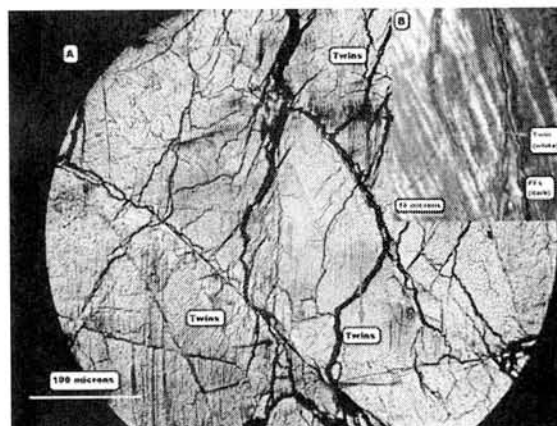


Fig. 1. A, Shock-induced twin lamellae in clinopyroxene. B, Planar microstructures on twin lamellae..

The development of distinctive shock-metamorphic features such as PDFs in denser mafic minerals including amphibole, pyroxene, and olivine apparently occurs at higher pressures and over a more limited pressure range than in case of quartz and feldspar.

The most common shock effects observed in mafic minerals shocked at 30GPa are planar fractures, mechanical twins and regular comminution features. In general, mafic minerals in naturally and experimentally shocked basalts show only extreme comminution accompanied by the melting [3] only at relatively higher pressures. Consequently, our observed planar microstructures are planar fractures (PFs). According to the above-mentioned optical microscope observations of shock-induced twins and planar elements, the clinopyroxene was shocked to about 30GPa.

Acknowledgement: The authors are very grateful to NIPR for providing the thin section for this study. This work was a part of the JSPS-HAS scientific joint project.

References: [1] Langenhorst F. (2002) Bulletin of the Czech Geological Survey, Vol.77, No. 4., 265-282. [2] Stöffler D. and Langenhorst F. (1994) Meteoritics, 29, 155-181. [3] French B. (1998) LPI Contribution No. 954, Lunar and Planetary Institute, Houston, 120pp. [4] Hornemann U. and Müller W. F. (1971) Neues Jb. Mineral.Mh.,6,247-256. [5] <http://tin.er.usgs.gov/meteor/>

Optical and Raman spectroscopical properties of the shocked olivines from ALHA 77005 sample. Sz. Nagy¹ (ringwoodit@yahoo.com), S. Józsa¹, A. Gucsik², Sz. Bérczi¹, K. Ninagawa³, H. Nishido⁴ and M. Veres⁵
¹Eötvös Lóránd University of Budapest, H-1117 Budapest, Pázmány Péter sétány 1/c., Hungary; ²Max Planck Institute for Chemistry, Department of Geochemistry, Becherweg 27, D-55128, Mainz, Germany; ³Department of Applied Physics, Okayama University of Science, 1-1 Ridai-cho, Okayama, 700-0005, Japan; ⁴Research Institute of Natural Sciences, Okayama University of Science, 1-1 Ridai-cho, Okayama, 700-0005, Japan; ⁵MTA-SZFKI, H-1121 Budapest, Konkoly-Thege M. út 29-33., Hungary.

Introduction: Petrographic classifications of shock effects in olivine at different shock pressures, (mainly based on optical analysis), have been reported in previous studies [1,3]. Raman spectral features of the shocked olivine have been described by Turner et al. [4]. In this study, we focus on the shock effects of olivine, and their micro-Raman spectroscopical properties to characterize the crystalline background of the shock-induced microdeformations.

Sample: The ALHA 77005 Martian meteorite (lherzolitic type) was found partially inbedded in the ice at the Allan Hills site during one of the first collecting expedition. A preliminary examination of this sample reported that it is ~55% olivine, ~35% pyroxene, ~8% maskelynite, and ~2% opaques. The olivine (Fa₂₈) occurs as anhedral to subhedral grains up to 2 mm in length. The olivine grains show brown color because of the hydrous magma [5]. The ALHA 77005 contains melt pockets too, which are mostly crystallized in the spinifex texture. Additionally, the interstitial regions contain two phases: pigeonite and residual glass [6].

Shock effects in olivine: The olivine in ALHA 77005 shows shock effects as follows. The olivine exhibit distinct mosaicism. Some olivine grains have reduced interference color, and undulatory extinction. The birefringence is also reduced. Near the melt pocket, olivine shows three regions (Fig. 1). The first region is the host olivine area with lower interference color (orangeyellow). The second region is a transition zone with planar microstructures and some isotropic area (Figs. 1 and 2). The third one is a recrystallized area with irregularly rounded grains. The transition zone is about 20-25 µm wide (Fig. 2). In this part the interference color is drastically reduced, and some places show isotropic areas (Figs. 1 and 3.). In the transition zone Planar Deformation Features (PDFs) occur up to two orientation, and Planar Fractures (PFs) (Fig. 2). The PDFs are slightly curved, occurring between PFs. The spacing of PFs is between 10-15 µm. These orientations are differ from the PDFs orientations. The width of PDFs is > 1 µm, and the spacing is 1-2 µm. The boundary between the transition zone and (low interference color) host grain is relatively sharp. However, the transition between the transition zone and recrystallized area is continuous (Fig. 2). As a function of the increasing shock pressure, the olivine grains have lost its intense brown color, which indicates the loss of Fe³⁺. We suggest that the Fe³⁺ is not presented in the olivine structure. It is evidently shown, that the olivine grains do not represent pleochroism effect. If the Fe³⁺ could be in the lattice, the grains must have pleochroism. The origin of the brown color in the olivine is most likely due to the hydrous magma [5]. Around the shock melt packet, the deviation of olivine is occurred slightly. Within this area the original olivine interference color is significantly reduced to colorless.

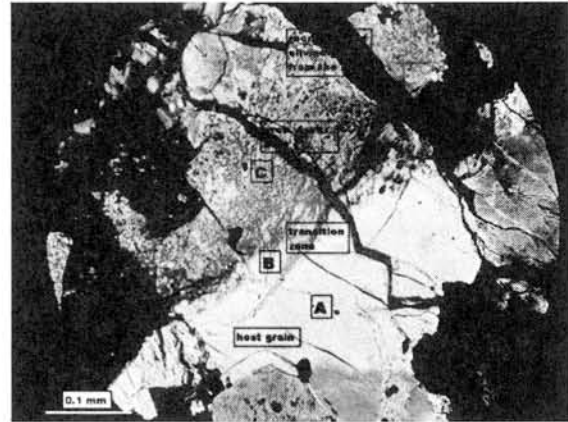


Fig. 1. Olivine grains from the ALHA 77005 sample. The figure shows three region in the olivine. A, host grain area; B, transition zone; C, recrystallized area. (D, melting pocket) (cross-polarised light)

The recrystallized area shows numerous irregular olivine grains. Near the shock melt pocket, some olivine grains have recrystallized area from the olivine melt, and these grains optically different from grains, that recrystallized between the melt pocket and the transition zone (Fig. 1, mark C). The olivine does not show shock veins, and the number of fractures is relatively small. We did not observe high pressure polymorph of olivine including spinel-like structure in neither microscopic investigation nor Raman studies. It is probably case of the grain size of olivine. We assume, that the place (Fig. 1, mark C) was isotropic between the melt pocket and the transition zone, but the recrystallization was not formed from the melt, however the material recrystallized from a short range order condition.

Raman spectroscopy of shocked olivine: In Raman spectroscopic experiments, minerals are identified by their spectral patterns and mineral compositions based on their peak positions. Olivine contains 81 optic modes, 36 of are Raman active modes [7]. Olivine spectra can be divided into 3 parts: (1) less than 400 cm⁻¹, which corresponds to the lattice modes (rotations and translations of SiO₄ units, and translations of the octahedral cations). (2) between 400-800 cm⁻¹, which is related to the SiO₄ internal bending vibrational modes. (3) 800-1100 cm⁻¹, which is attributed to SiO₄ internal stretching vibrational modes; the dominant features in this region are a doublet peaks near at 820 and 850 cm⁻¹ [7]. Doublet peak positions are changed as a function of variation of the chemical composition.

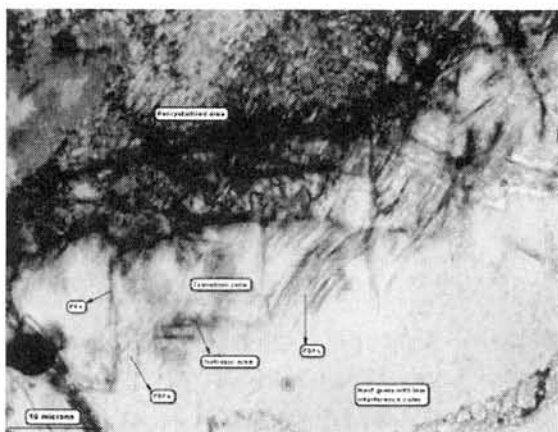


Fig. 2. The distinctive regions of the shocked olivine. The resolution is 60X. (cross-polarised light)

The A-area shows the following peaks: 595, 820, 852, and 955 cm^{-1} . The B-area contains: 580, 594, 820, 852, and 950 cm^{-1} . The peaks of the C-area are: 597, 820, 852, and 951 cm^{-1} . All of these peaks correspond to the olivine structure. The high-pressure polymorph of olivine such as ringwoodite and wadsleyite have not been identified. The epoxy related peaks are: 638, 671, 735, 916, 1014, and 1043 cm^{-1} (Fig. 4).

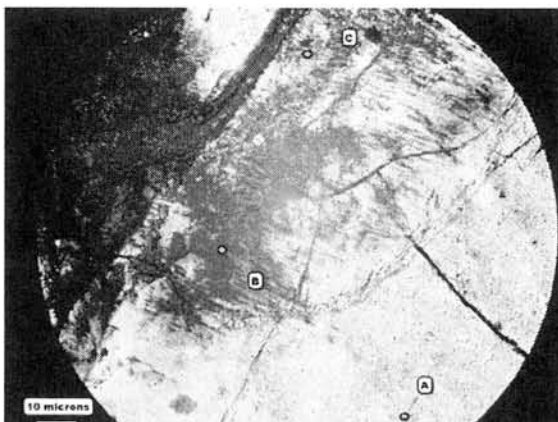


Fig. 3. The three analysing parts for the Raman investigation. Host grain (A), isotropic area (B), and recrystallized area (C). (cross-polarised light)

The doublet peak positions of the olivine structure at 820 and 852 cm^{-1} are unchanged during three measurements, which indicates that the chemical composition of olivine is also not changed (Fig. 4). We can observe a change in the B-spectra in comparison with the A and C-spectra. In the B-spectra, the 595 and 597 cm^{-1} peaks (in A and C-spectra respectively) modified to a broadening peak (Fig. 4). But this change is not significant. Therefore, we think that the olivine structure collapsed to numerous domains or crystallites during the shock wave propagation. This condition could represent to the small change in the B-spectra broadening. According to the C-spectra, the recrystallized area might be represent higher range order condition than the B-spectra of isotropic area. The A and C area have identical Raman spectra, but their appearance in the optical microscope are very different.

We suggest that the isotropic area is not a diaplectic olivine glass, because the change of the main peaks is not significant. We think that the isotropic area contains μm and/or nm -size domains, which might be too small for our optical microscopic observations. It is probable, that the irregular grains formation in the C-area, may have been due to the crystallization around the domains or crystallites.

Conclusion: The olivine grains are highly-shocked in ALHA77005 sample. We can identify/characterize three zones in these olivine grains, being near the melt pocket. In the C-area was not hot enough the temperature for the completed recrystallization as in the case of the melt. According to the Raman investigation, the nature of the isotropic area is not diaplectic olivine glass. We did not find high pressure polymorphs of olivine.

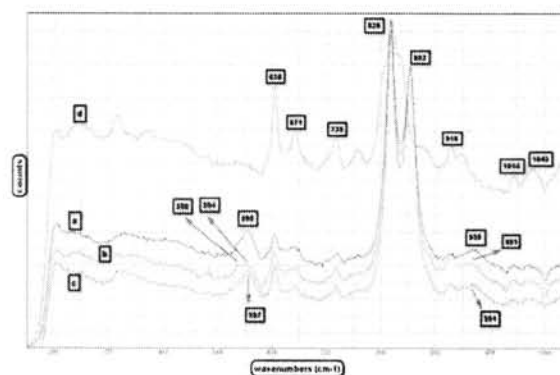


Fig. 4. Raman spectra of the three area from the Fig. 3. The D-spectra is the epoxy. The low three spectra (A-B-C) correspond to the host grain (yellow area), isotropic area (dark area), and recrystallized area from short range order condition (white-dark mixed area).

Acknowledgement: The authors are very grateful to NIPR for providing the thin section for this study. This work was a part of the JSPS-HAS scientific joint project.

References: [1] Stöffler D. (1972). Fortschr. Mineral. 49, 50-113. [2] Stöffler D. et al. (1991) Geochim. Cosmochim. Acta, 55, 3845-3867. [3] Bischoff A. and Stöffler D. (1992) Eur. J. Mineral., 4, 97-106. [4] Turner S. et al. (2004) LPS XXXV, Abstract. [5] Treiman A.H. et al. (2006) LPS XXXVII, Abstract. [6] Boctor N.Z. et al. (1999) LPS XXX, Abstract. [7] Kuebler K. et al. (2005) LPS XXXVI, Abstract.

Organic Globules in the Tagish Lake CI2 and Bells CM2 Carbonaceous Chondrites.

K. Nakamura-Messenger^{1,2}, S. Messenger¹, L. P. Keller¹, S. J. Clemett^{1,3}, and M. E. Zolensky¹

¹Robert M Walker Laboratory for Space Science, Astromaterials Research and Exploration Science Directorate, NASA Johnson Space Center, Houston, TX 77058, USA, ²ESCG/ Jacobs Sverdrup, NASA Johnson Space Center, Houston, TX 77058, USA, ³ESCG/ ERC Inc., NASA Johnson Space Center, Houston, TX 77058, USA keiko.nakamura-1@nasa.gov

Introduction:

Tagish Lake is a unique meteorite whose chemistry and mineralogy are intermediate between CI and CM2 carbonaceous chondrites [1]. It has been linked to outer belt asteroids from its orbit, reflectance spectrum, hydrated mineralogy, and abundant carbonaceous matter, possessing 2.6 wt.% organic carbon [2,3]. Tagish Lake organic matter often occurs as submicrometer, hollow globules [4,5].

We recently presented coordinated transmission electron microscopy (TEM) and isotopic measurements of organic globules in the Tagish Lake meteorite [5]. The organic globules have elevated ¹⁵N/¹⁴N ratios (1.2 to 2 times terrestrial) and D/H ratios (2.5 – 9 times terrestrial). These isotopic anomalies are indicative of mass fractionation during chemical reactions at extremely low temperatures (10 – 20 K), characteristic of cold molecular clouds and the outer protosolar disk. The globules probably originated as organic ice coatings on preexisting grains that were photochemically processed into refractory organic matter [5].

Similar objects were first observed in meteorite extracts in 1961 [6], and have recently been reported in several carbonaceous chondrites [7,8]. It is not yet known whether the organic globules found in other meteorites are also carriers of N and H isotopic anomalies. If so, organic globules will be confirmed as a common preserver of presolar matter in meteorites.

Carbonaceous chondrites have wide ranges in their bulk H and N isotopic compositions, reflecting variable degrees of alteration, dilution, and isotopic exchange of their original interstellar organic compounds. The organic globules studied in [5] had δD (1,800 to 8,000‰) and $\delta^{15}N$ (200 to 1,000‰) isotopic anomalies that were much larger than bulk Tagish Lake ($\delta^{15}N=77‰$), showing that they are a minor component of its organic matter. Several carbonaceous chondrites have significantly higher bulk H and N isotopic anomalies, suggesting that these meteorites may be rich in organic globules. According to Kerridge (1985) [9] the Bells CM2 carbonaceous chondrites reaches the highest value of bulk $\delta^{15}N$ (+335 ‰) amongst 35 different carbonaceous chondrites. The bulk δD of the Bells meteorite is also very high, reaching +990 ‰ [9].

We will present in situ studies of the globules both the Tagish Lake and Bells CM2 carbonaceous

chondrites, comparing their microstructural, chemical, isotopic, and spectroscopic properties.

Materials and Methods:

Fragments of the Tagish Lake meteorite matrix (carbonate-poor lithology) and the Bells CM2 matrix were embedded in high-purity S and sliced into 50–70 nm-thick sections with an ultramicrotome equipped with a diamond knife. The sections were floated onto ultra-pure water and transferred to amorphous C-supported Cu transmission electron microscopy (TEM) grids.

TEM measurements were obtained using a JEOL 2500SE 200kV field-emission scanning TEM (STEM) equipped with a Noran thin window energy-dispersive X-ray (EDX) spectrometer, a Gatan Tridiem imaging filter (GIF) for energy-filtered imaging (EFTEM) and EELS, and a 2K x 2K slow scan CCD camera for recording images. Image acquisition and processing were carried out using Gatan Digital Micrograph software. EFTEM images were collected with acquisition times of 20-60 s depending on element concentrations. EELS spectra were obtained in image mode with spot sizes of 10-50 nm, a dispersion of 0.3 eV, dwell times of 10-30 s at an energy resolution of 0.9 eV FWHM at the zero-loss peak. High resolution brightfield images were recorded at 500K-1M X magnification and ordering was estimated using fast Fourier transforms of selected regions within the images.

Following TEM characterization, H, C, and N isotopic compositions of the globules and surrounding matrix material were obtained with the JSC NanoSIMS 50L ion microprobe by isotopic imaging. Isotopic images were obtained by multicollection of secondary ions produced by a finely focused (50 nm) Cs⁺ primary ion beam. Each target sample was measured repeatedly, producing 10 – 20 image scans over a period of 3-4 hours. Nearby terrestrial standards (NBS graphite, 1hydroxybenzotriazole hydrate, biotite) were measured as external isotopic references.

Results:

Organic globules in Bells CM2 matrix are more abundant than the Tagish Lake meteorite. Organic globules in Bells CM2 appear to be aggregates like apple funnelcakes riddled with tiny holes (Fig.1a, also Fig.1b on the right). Single hollow globules (Fig.1b in the box) are rare in the Bells CM2, but have

similar diameters and wall thicknesses as Tagish Lake organic globules.

High-resolution TEM imaging and EELS show that the globules consist of structurally amorphous carbon that lacks long range order or development of graphite-like domains. Nitrogen K-edge structure appears for the first 2-5 seconds while acquiring an EELS spectrum, and then rapidly disappears, indicating that nitrogen component in the globules is quite beam sensitive and volatile.

The distribution of C, N, and O in the globules was obtained using EFTEM imaging (Fig.1c,d). Nitrogen was clearly below our detection limits both for EFTEM imaging and in EELS spectroscopy mode from individual spots, suggesting that the concentration of N in the globules we analyzed is less than approximately 1wt.%. With the exception of their unusual aggregate morphologies, the physical and chemical properties of organic globules in Bells CM2 are quite similar to those observed in the Tagish Lake meteorite. Isotopic measurements of the Bells organic globules are planned in the near future, and we look forward to presenting those results at the symposium.

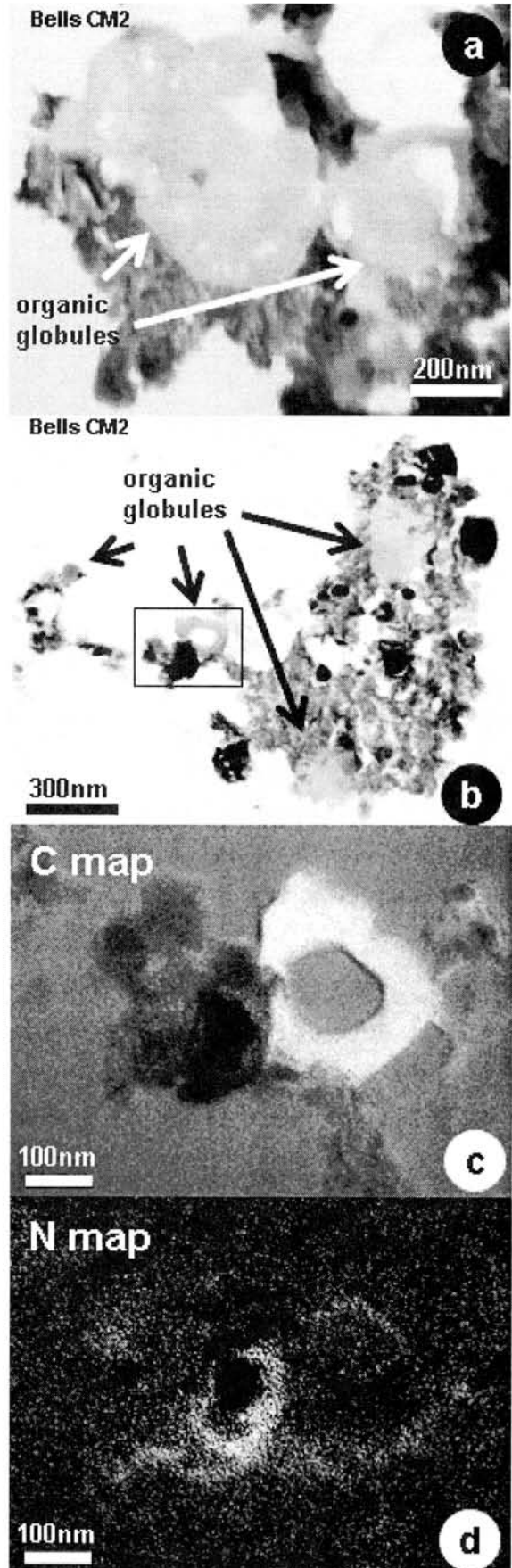
References: [1] Brown P.G. et al., (2000) *Science* **290**, 320. [2] Hiroi T., Zolensky M.E., Pieters C.M. (2001) *Science*, **293**, 2234 [3] Grady M.M et al. (2002) *Met. Planet. Sci.* **37**, 713 [4] Nakamura K. et al. (2002) *Intl. Journal of Astrobiology* **1**, 179 [5] Nakamura-Messenger K. et al. (2006) *Science* **314** 1439 [6] Claus G. & Nagy B., (1961) *Nature* **192**, 594 [7] Aoki T., Akai J., Makino K. (2003) *Intl Symp. Evolution of Solar System Materials 5* [8] Garvie L.A.J. and Buseck P.R., (2006) *Lunar Planet. Sci.* **37**, Abst# 1455. [9] Kerridge J.F. (1985) *Geochim. Cosmochim. Acta* **49**, 1707.

Fig.1a: Bright field TEM image of three organic globule aggregates from Bells CM2 meteorite embedded in saponite matrix.

Fig.1b: Bright field TEM image of three organic globule aggregates from Bells CM2 meteorite embedded in saponite matrix.

Fig.1c: Carbon K-edge EFTEM image of the boxed area shown in Fig.1b, showing carbon-containing material in high contrast.

Fig.1d: Nitrogen K-edge EFTEM image of the boxed area shown in Fig.1b.



Carbon minerals in the highly shocked Goalpara ureilite. Y. Nakamuta, Kyushu University Museum, Kyushu University, Hakozaki 6-10-1, Fukuoka 812-8581, Japan, nakamuta@museum.kyushu-u.ac.jp.

Introduction:

Ureilites are unique in containing relatively large amount of C occurring as graphite, diamond and lonsdaleite [1] and may provide important information about the formation mechanism of extra terrestrial diamond. The mode of occurrence and X-ray properties of carbon minerals in ureilites show that diamond in ureilites formed by high-pressure conversion of graphite which crystallized during igneous or metamorphic processes on an ureilite parent body or bodies [2]. Nakamuta et al. [3], [4] proposed catalytic transformation of graphite to diamond with iron as a catalyst as the transformation mechanism occurred in many ureilite meteorites and also martensitic non-catalytic transformation for some ureilites. They suggested that the catalytic transformation occurred at the conditions of temperatures exceeding eutectic temperature of carbon and iron and relatively low-pressure and non-catalytic one at the conditions of temperatures below the eutectic temperature and relatively high-pressure.

Goalpara ureilite was classified as highly shocked one due to mosaicized olivine pervasively observed in it [5]. In this study, carbon minerals in a polished thin section (PTS) were in situ observed by an optical microscope and analyzed by a laser Raman spectroscopy. X-ray powder diffraction patterns of some C-rich grains, about 50 μm in size, were also obtained after taking out from the PTS by using a Gandolfi camera.

Petrology and Experimental conditions:

Fig. 1 shows optical microphotographs of a part of Goalpara ureilite under a transmitted light with parallel nicols (A) and under a reflected light (B). Olivine crystals were pervasively and pyroxene crystals were partly darkened under a transmitted light due to tiny metals in them. Olivine crystals were mosaicized but pyroxene crystals were not and show only fractures as described by [5]. Blade-like shaped carbon minerals occur at grain boundaries of silicate crystals and also in them.

Raman spectra were recorded with a Jobin-Yvon T64000 triple-grating spectrometer equipped with confocal optics and a nitrogen-cooled CCD detector. A microscope was used to focus the 514.5 nm Ar excitation laser beam to a 1 μm spot. Accumulations lasting 60 to 300 seconds were made. The laser power on the sample was 0.6 mW.

X-ray diffraction patterns were obtained for C-rich grains removed from the PTS and mounted on glass fibers of ~ 10 μm in diameter by using a 114 mm diameter Gandolfi camera. A rotating anode X-ray generator with a Cr-anode, 0.2 x 2 mm

fine-filament, and a V-filter was used as an X-ray source. The diffraction data were recorded on IP and converted to the 2θ -intensity pattern [6].

Results:

The sizes of C-rich grains are about 1-2 mm in length and 0.1-0.5 mm in width. In each grain, diamond crystals can be observed in high relief under an optical microscope of high magnification.

Fig. 2 shows Raman spectra of carbon minerals in high relief, suggesting a hard property of them. A in Fig. 2 shows a sharp Raman spectrum at 1332 cm^{-1} assigned to F_{2g} mode of diamond. Position and FWHM of the spectrum are very near to those of terrestrial diamond. B also shows Raman spectrum at the position of diamond F_{2g} mode, but FWHM is wider than that of A and the position a little shifts toward the low wave-number side. C shows a broad band near 1600 cm^{-1} , being the position of graphite E_{2g} mode, and very broad band or bands spread over $1600\text{-}1300\text{ cm}^{-1}$. The spectrum of C as a whole is similar to that of graphite, although it is hard as being in high relief under an optical microscope.

Fig. 3 shows X-ray powder diffraction patterns of C-rich grains. A and B are those of grains containing crystals showing A and B Raman spectra in Fig. 2, respectively, and C is the pattern of the grain which shows the Raman spectrum similar to C in whole. A suggests that the grain contains well crystallized diamond similar to terrestrial diamond. B shows a little broader reflection of diamond and suggests diamond in the grain is disordered. Reflections of graphite in B and C are accompanied with those of compressed graphite. In C, reflections suggesting lonsdaleite are observed.

In some C-rich grains, crystals showing A, B and C types of Raman spectra coexist in a grain. In such a case, diamond showing a sharp Raman spectrum like A occurs only around metal veins in the grain. Such an occurrence strongly suggests that well crystallized diamond in ureilites was formed by a catalytic transformation with iron as a catalyst as suggested by [4].

References:

- [1] Goodrich C. A. (1992) *Meteoritics*, 27, 327-352.
- [2] Nakamuta Y. and Aoki Y. (2000) *Meteorit. Planet. Sci.*, 35, 487-493.
- [3] Nakamuta Y. and Aoki Y. (2001) *Meteorit. Planet. Sci.*, 36, A146.
- [4] Nakamuta Y., Aoki Y. and Kojima H. (2002) *27th Symposium on Antarctic Meteorit.* (abstract), 117-119.
- [5] Berkley et al. (1980) *Geochim. Cosmochim. Acta* 44, 1579-1597.
- [6] Nakamuta et al. (2006) *J. Mineral. Petrol. Sci.* 101, 308-318.

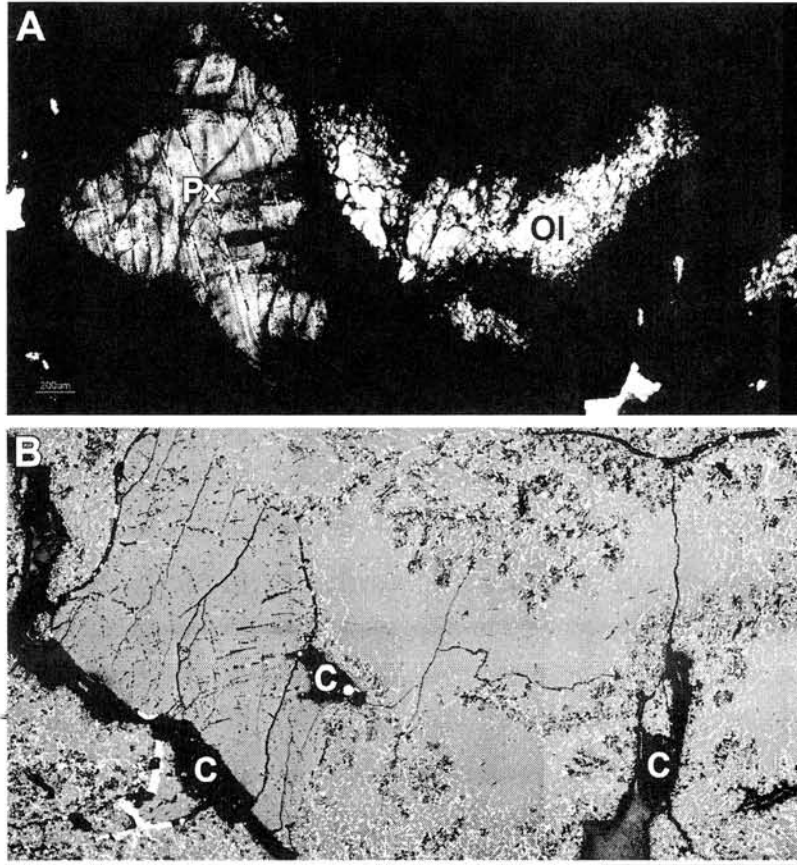


Fig. 1 Microphotographs of a part of Goalpra ureilite under a transmitted light with parallel nicols (A) and under a reflected light (B). Px, Ol and C denote pyroxene, olivine and carbon minerals, respectively. The bar at the bottom of the figure shows 1 mm in length.

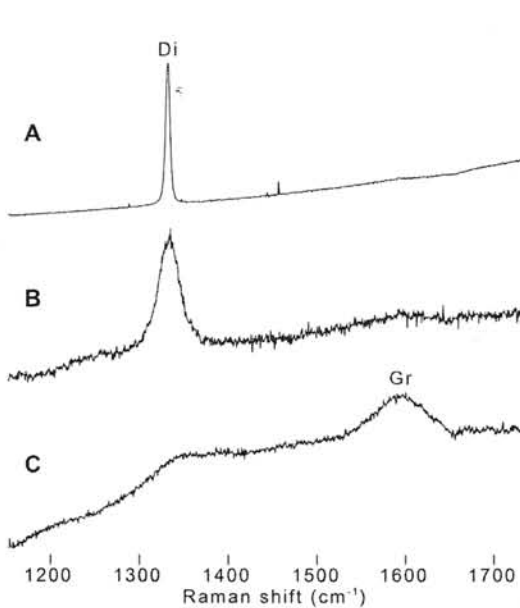


Fig. 2 Raman spectra of carbon minerals in Goalpra ureilite. Di and Gr denote Raman lines from diamond and graphite, respectively.

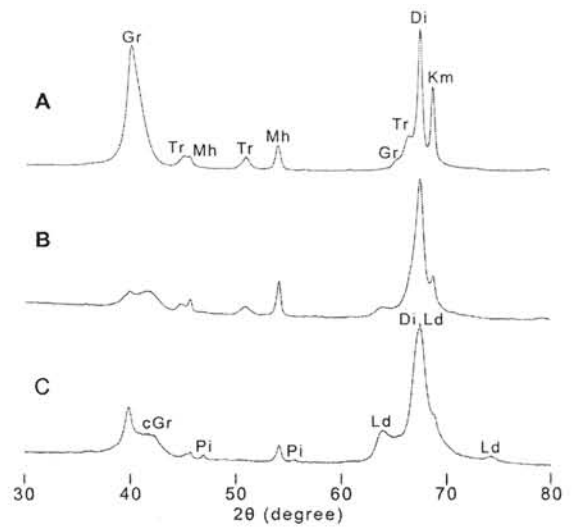


Fig. 3 X-ray powder diffraction patterns of carbon-rich grains from Goalpra ureilite. A, B and C patterns were obtained from the samples corresponding to those showing A, B and C Raman spectra in Fig. 2, respectively. Gr, Tr, Mh, Di, Km, cGr, Pi and Ld denote reflections from graphite, troilite, maghemite, diamond, kamacite, compressed graphite, pigeonite and lonsdaleite, respectively.

Search for extinct ^{36}Cl : Vigarano CAIs and the Pink Angel from Allende. D. Nakashima^{1,2}, U. Ott¹, P. Hoppe¹, and A. El Goresy³, ¹Max-Planck-Institut für Chemie, J.-J.-Becher-Weg 27, 55128 Mainz, Germany, ²Laboratory for Earthquake Chemistry, Graduate School of Science, University of Tokyo, Bunkyo-ku, Tokyo 113-0033, Japan, ³Bayerisches Geoinstitut, Universität Bayreuth, 95447 Bayreuth, Germany.

Introduction:

Radioactive ^{36}Cl ($T_{1/2} = 3 \times 10^5$ years) has been suspected to have been present in the early solar system. Its actual detection, however, has proven to be difficult [e.g., 1]. Part of the problem is that Cl-rich phases such as sodalite tend to be alteration rather than primary phases and that the decay of ^{36}Cl primarily leads to volatile ^{36}Ar (98.1%; β^- decay). There has been no clear evidence about ^{36}Ar excesses induced by ^{36}Cl decay in sodalite in Ca-Al-rich inclusions (CAIs), which may be due to ^{36}Ar loss. Although only 1.9% of decays lead to ^{36}S (β^+ decay and electron capture), it was found that ^{36}S excesses correlate with Cl/S in sodalites from a CAI in the Ningqiang meteorite, corresponding to $^{36}\text{Cl}/^{35}\text{Cl} \sim 5 \times 10^{-6}$ at the time of sodalite formation [2]. A similar ratio was found in sodalite in the Pink Angel CAI from the Allende meteorite [3]. On the other hand, there was no evidence for extinct ^{36}Cl in our study of another fine-grained Allende CAI [4]. We continued Cl- and S-isotopic analyses of sodalite in CAIs from the Vigarano meteorite and the Pink Angel CAI so as to confirm the results of [3] and to enlarge the ^{36}Cl database.

Experimental:

Two thick sections were prepared from the Vigarano meteorite, and two thin sections of the Pink Angel were kindly supplied by G. J. Wasserburg. The four sections were coated with carbon and searched for the occurrence of sodalite in the CAIs using FE-SEMs at Bayreuth University and at Max-Planck-Institute for Chemistry in Mainz. Back-scattered electron (BSE) imaging was used for SEM studies. Elemental compositions of constituent minerals of the CAIs were subsequently measured with an EPMA equipped with WDS at Mainz University. WDS quantitative analyses were performed at 15kV accelerating voltage and 10nA beam current with a focused beam 1 μm in diameter. Isotopic analysis of Cl and S in sodalite was done with the NanoSIMS at Max-Planck-Institute for Chemistry in Mainz. Sulfur isotopes 32, 34, and 36 as well as ^{37}Cl were measured in multicollection ion counting as negative ions produced by a Cs^+ primary beam of $\sim 25\text{pA}$ and $\sim 1\mu\text{m}$ in diameter. The ^{36}S count rate was corrected for background measured at 14 millimasses below the ^{36}S peak. Obtained $^{37}\text{Cl}/^{34}\text{S}$ ratios were converted into $^{35}\text{Cl}/^{34}\text{S}$ ratios using a ratio of 3.13 for $^{35}\text{Cl}/^{37}\text{Cl}$ [5]. In addition, $^{35}\text{Cl}/^{34}\text{S}$ ratios were corrected with a relative sensitivity factor of 0.83 (favoring Cl) as determined

by [3]. For the measurements of Vigarano sodalite, Mundrabilla troilite and FeS grains close to the CAIs were used as standards. For the measurements of Pink Angel sodalite, Mundrabilla troilite, matrix around the Pink Angel, and terrestrial sodalite were used.

Results and discussion:

In the Vigarano thick sections, we found two sodalite-bearing CAIs (VI-1 and VI-2), $\sim 2\text{mm}$ and $\sim 1.2\text{mm}$ in size. The CAIs are irregularly shaped and partly surrounded by Wark-Lovering rims [6]. The interior of the CAIs consists mainly of coarse-grained gehlenitic melilite (20-500 μm ; Åk 2-21) and small spinel grains (5-20 μm). It is considered that the CAIs are fluffy Type As [7]. Small CAI fragments having the same mineral compositions occur close to the two CAIs.

Sodalite and nepheline grains (5-20 μm) occur as mixtures along cracks of melilite, suggesting replacement of melilite by sodalite and nepheline via reaction with nebular gases bearing Na, Cl, and K. Most of the spinel grains in the CAIs are rich in Mg and almost free of Fe (Mg#95-99), whereas spinel grains near the altered regions are more Fe-rich (Mg#63-90). It is considered that Fe was also incorporated into the CAIs during the alteration.

Sodalite and nepheline occur in the main CAIs, but are absent from the small CAI fragments. If alteration occurred after fragmentation, we would expect also the CAI fragments to contain sodalite and nepheline. Hence it is likely that the alteration occurred before fragmentation. Since fragmentation should have occurred on the parent body, sodalite and nepheline in the main CAIs may have formed before accretion to the parent body (i.e. in the solar nebula).

The Pink Angel CAI is composed of a pinkish fine-grained interior surrounded by a whitish compact rim (cf. [8]). The interior is rich in sodalite (30 vol%), whereas the rim contains only 2 vol% of sodalite. Hsu et al. [3] concluded from the lack of sodalite in Allende matrix surrounding the Pink Angel CAI that alteration in the nebula was more likely. However, we found numerous sodalite grains in Allende matrix (and also [4]), which would argue for parent body alteration instead. Thus, the possibility of multiple alteration episodes should be considered.

Figure 1 shows $^{36}\text{S}/^{34}\text{S}$ - $^{35}\text{Cl}/^{34}\text{S}$ plots for sodalite in the Vigarano CAIs and in the Pink Angel (PA-1

and PA-2). In the case of Vigarano CAIs, most of the data show no ^{36}S excess and are distributed along the baseline ($^{36}\text{S}/^{34}\text{S} \sim 0.00346$). Only two data points are indicative of ^{36}S excesses, however, with large errors. If taking 2σ errors, the excesses have no statistical significance. Thus, sodalite of the Vigarano CAIs shows no clear ^{36}S excess. It is possible that the ^{36}Cl - ^{36}S system in sodalite was disturbed by later parent body processes. However, it is inferred from abundances of presolar grains and from Raman spectroscopy of organic material that Vigarano is less altered than Allende [9], which contains CAI-sodalite showing clear ^{36}S excesses [3]. Therefore, it is unlikely that the absence of ^{36}S excess from the Vigarano CAIs is due to later disturbance by parent body processes.

A weighted fit gives no positive correlation between $^{36}\text{S}/^{34}\text{S}$ and $^{35}\text{Cl}/^{34}\text{S}$ of sodalite in the Vigarano CAIs. An upper limit of $^{36}\text{Cl}/^{35}\text{Cl}$ ratio is estimated to be 1.9×10^{-6} from the 2σ uncertainty of the slope of the regression line, which is clearly lower than the previous results [2, 3].

Sodalites in Pink Angel sample PA-1 show ^{36}S excesses. The $^{36}\text{Cl}/^{35}\text{Cl}$ ratio derived from a weighted fit line is compatible with the results of [3]. On the other hand, PA-2 shows smaller ^{36}S excesses than PA-1, and the inferred $^{36}\text{Cl}/^{35}\text{Cl}$ ratio is lower than that of PA-1 and that of [3]. The different $^{36}\text{Cl}/^{35}\text{Cl}$ ratios may be due to later disturbance by parent body processes or may suggest heterogeneous ^{36}Cl distribution in a single CAI.

Lin et al. [2] and Hsu et al. [3] estimated initial $^{36}\text{Cl}/^{35}\text{Cl}$ (i.e. at CAI formation) at $>10^{-4}$. This can be explained by spallation reactions only [3], similar to the case of ^{10}Be [10]. However, ^{10}Be appears to be present in roughly equal abundance in all studied CAIs [e.g., 11], whereas our results (and also those of [12]) indicate ^{36}Cl to be variable. There seems to be no simple relationship between ^{10}Be and ^{36}Cl . A larger database of ^{36}Cl is required to establish its relation to other radionuclides.

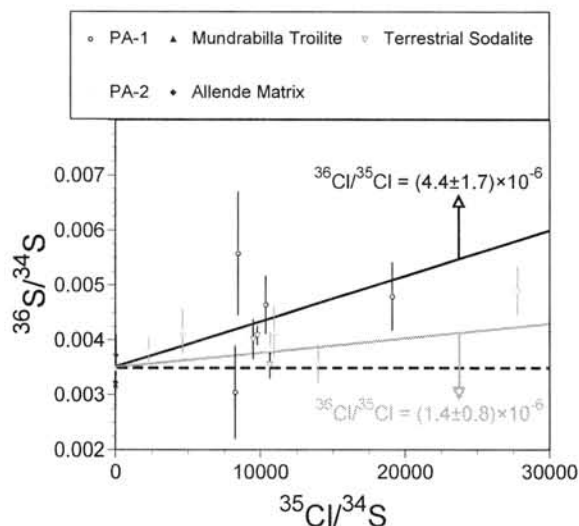
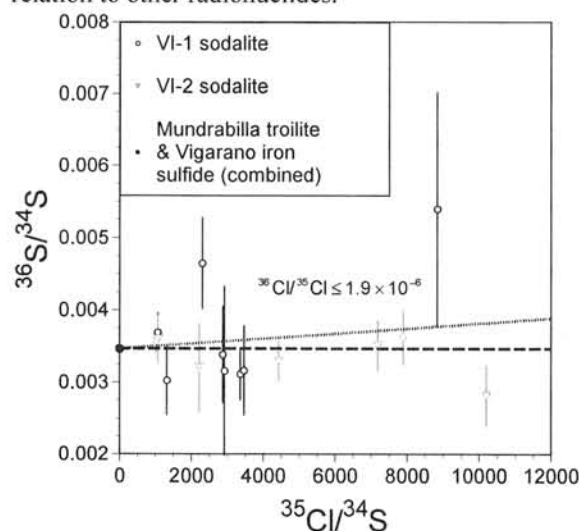


Fig. 1: (a) $^{36}\text{S}/^{34}\text{S}$ vs. $^{35}\text{Cl}/^{34}\text{S}$ plot for sodalite in the Vigarano CAIs, VI-1 and VI-2 (a) and in the Pink Angel CAI, PA-1 and PA-2 (b). Error bars are 1σ and based on Poisson statistics only. The horizontal line corresponds to normal $^{36}\text{S}/^{34}\text{S}$ as deduced from standards ($^{35}\text{Cl}/^{34}\text{S} \sim 0$). A weighted fit line yields a 2σ upper limit of 1.9×10^{-6} for the $^{36}\text{Cl}/^{35}\text{Cl}$ of sodalite in the Vigarano CAIs. From the weighted fit lines in panel b, the inferred $^{36}\text{Cl}/^{35}\text{Cl}$ ratios are $(4.4 \pm 1.7) \times 10^{-6}$ for PA-1 and $(1.4 \pm 0.8) \times 10^{-6}$ for PA-2.

References:

- [1] Wasserburg G. J. et al. (2006) *Nuclear Physics A*, 777, 5-69.
- [2] Lin Y. et al. (2005) *PNAS*, 102, 1306-1311.
- [3] Hsu W. et al. (2006) *ApJ*, 640, 525-529.
- [4] Plagge M. et al. (2006) *LPS XXXVII*, Abstract #1287.
- [5] Shields W. R. (1962) *J. Am. Chem. Soc.*, 84, 1519-1522.
- [6] Wark D. A. and Lovering J. F. (1977) *Proc. Lunar Sci. Conf. 8th*, 95-112.
- [7] MacPherson G. J. and Grossman L. (1984) *GCA*, 48, 29-46.
- [8] Armstrong J. T. and Wasserburg G. J. (1981) *LPSXII*, 25-27.
- [9] Huss G. R. et al. (2006) In *Meteorites and the Early Solar System II* (eds. D. S. Lauretta and H. Y. McSween Jr.), pp. 567-586.
- [10] McKeegan K. D. et al. (2000) *Science*, 289, 1334-1337.
- [11] Marhas K. K. and Goswami J. N. (2004) *New Ast. Rev.*, 48, 139-144.
- [12] Ushikubo T. et al. (2006) *LPS XXXVII*, Abstract #2082.

Acknowledgements:

We thank G. J. Wasserburg for providing the thin sections of the Pink Angel CAI, M. Biegler for preparation of the Vigarano sections, N. Groschopf for technical support in electron microprobe analysis, and J. Huth for technical support in SEM observation.

Petrography of Yamato-791088, a heavily shocked H chondrite. T. Niihara¹, N. Imae^{1,2} and H. Kojima^{1,2}. ¹ Department of Polar Science, The Graduate University for Advanced Studies, 9-10, Kaga 1-chome, Itabashi-ku, Tokyo 173-8515, Japan (niihara@nipr.ac.jp), ²Antarctic Meteorite Research Center, National Institute of Polar Research, 9-10, Kaga 1-chome, Itabashi-ku, Tokyo 173-8515, Japan.

Introduction:

More than 90% in chondritic meteorite collections are ordinary chondrites [1]. All of the ordinary chondrites have experienced shock event(s) on their parent bodies, and the shock degrees are different among chondrites. The shock stage of ordinary chondrites has been divided into seven types, S1-S6 and “melted”, based on their petrologic features [2]. Most ordinary chondrites are weakly shocked, and heavily shocked ordinary chondrites which are classified into “melted” are very rare.

In the collection of National Institute of Polar Research, fifteen ordinary chondrites classified into “melted” have been recognized so far. These are eleven from the LL chondrites, three from L chondrites and one from the H chondrites. Among these heavily shocked ordinary chondrites, those of the L and LL chondrites have been studied in detail [3]. However, that of the H chondrite, Yamato(Y)-791088, has not been studied in detail. Y-791088 is a partial melted rock by shock [4], and the age when the Y-791088 H chondrite has experienced impact has been estimated to be 1024 Ma using the Rb-Sr method [5].

In the present study, we petrographically describe the heavily shocked Y-791088 H chondrite in detail, and discuss its thermal history during the shock melting.

Analytical Methods:

A polished thin section (PTS) of Y-791088 (subnumber, 91-1 with the surface of 78 mm²) was used for the present study. It was observed under an optical microscope with transmitted light for transparent phases and reflected light for opaque phases. Constituent minerals and glassy phases were analyzed using JEOL JXA-8200 electron probe micro analyzer (EPMA) operated at accelerating voltage of 15 keV and the electron beam current of 9 nA with focused beam for minerals and 3 nA with defocused beam of 10 μm for glassy phase.

Results:

Y-791088, which is a partially-melted chondrite originated from some impact shock heating of the precursor H6 chondrite, mainly consists of olivines, pyroxenes, Fe-Ni metals, sulfides, glassy phases, spinels, and phosphates. The modal abundances of main constituent minerals are olivines 39.4%, pyroxenes 27.6%, opaque minerals 23.4%, and glassy phases 7.8%. Two chondrules, whose outlines are not destroyed, occur, however the interiors of these have been completely recrystallized from a shock melt, consisting of the fine grained minerals

and glassy phases. Olivines, pyroxenes, and opaque minerals can be divided into two groups based on their grain sizes; coarse and fine grained.

Olivines

Coarse grained olivines (~200 μm - 1 mm) show undulatory extinction and planar fractures. They contain abundant μm-sized Fe-Ni metals along fractures. They are irregular in shape with the compositional range of Fa₁₆₋₂₁ (C.V. = 3.7%). On the other hand, fine grained olivines (submicron-10 μm) consist of euhedral crystals surrounded by glassy phases, with compositional range of Fa₁₇₋₂₃ (C.V. = 5.2%). Therefore, the ranges of the Fa content for coarse grained olivines are narrower than that of fine grained olivines.

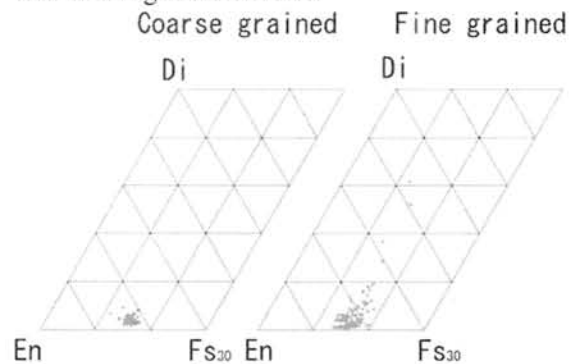


Fig. 1. Composition of pyroxenes. Coarse grained pyroxenes have a homogeneous composition. Contents of fine grained pyroxenes continuously increase from the core toward the rim.

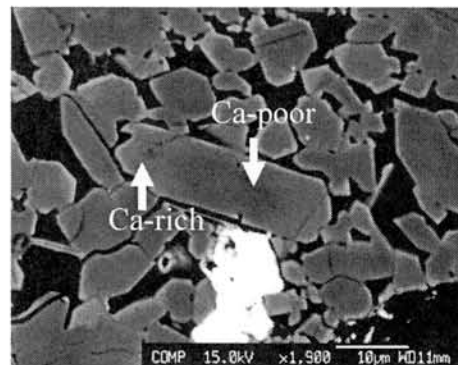


Fig. 2. Chemically zoned fine grained pyroxenes.

Pyroxenes

Coarse grained pyroxenes (~180-460 μm) show undulatory extinction and contain many fractures. They contain abundant μm-sized Fe-Ni metals along fractures. Compositions of coarse grained pyroxenes are Ca-poor (Fig. 1). While, abundant fine grained

pyroxenes (submicron-30 μm) are observed embedded in glassy phases showing compositional zoning, and the Wo contents continuously increase from the core toward the rim (Figs. 1 and 2).

Fe-Ni Metals

Coarse grained Fe-Ni metals (~180-460 μm) are irregular in shape and heterogeneous in textures, consisting of kamacite, taenite, and plessite. Ni component of coarse grained kamacite, taenite and plessite are 5-7 wt%, 29-31 wt%, and 14-18 wt%, respectively (Fig. 3). Most Fe-Ni metals are surrounded by sulfides (~30-100 μm in width). An isolated coarse grained plessite occurs.

Fine grained metals (submicron-20 μm) are rounded in shape. They are mostly plessite, the Ni content in Fe-Ni metals ranging in 7-30 wt% (Fig. 3), and are also surrounded by sulfides (~1-10 μm in width).

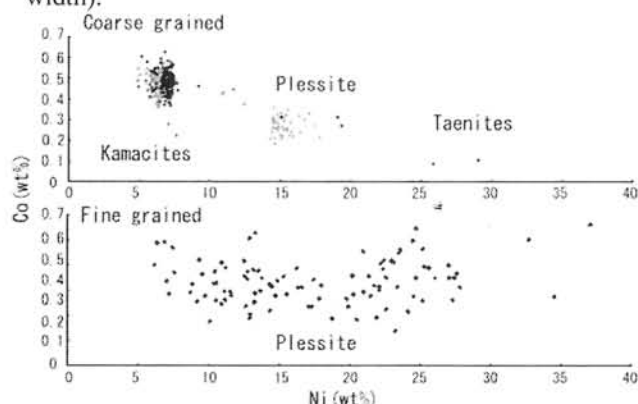


Fig. 3. Composition of coarse and fine grained Fe-Ni metals. Coarse grained Fe-Ni metals are kamacites, taenites, and plessites. Fine grained Fe-Ni metals are mostly plessites.

Sulfides

Most sulfides occur as surroundings of coarse and fine grained Fe-Ni metals. Only a few isolated sulfide grains occur with rectangular shape. The phase of sulfides is troilite.

Glassy phase

Glassy phase with albitic composition exists in interstices of mineral grains (Figs. 4 and 5). Glassy phases are divided into two types; K-rich and K-poor (Fig. 5). K-rich phases show clear texture, while K-poor phases show dusty texture under an optical microscope.

Discussion:

Compositions of coarse grained olivines and pyroxenes are homogeneous, and are identical with those of usual H6 chondrites. Therefore, coarse grained olivines and pyroxenes are not minerals crystallized from melt produced at the impact event, but are relict minerals of a H6 chondrite, which escaped the shock melting.

Fine grained olivines and pyroxenes are euhedral, surrounded by glassy phases, and have more heterogeneous composition than those of coarse

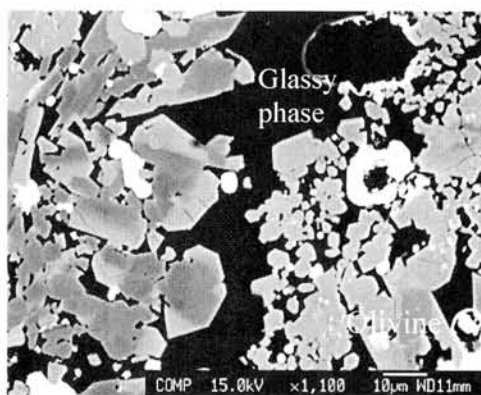


Fig. 4. Back scattered electron image of glassy phase. Glassy phase exist in interstices of mineral grains.

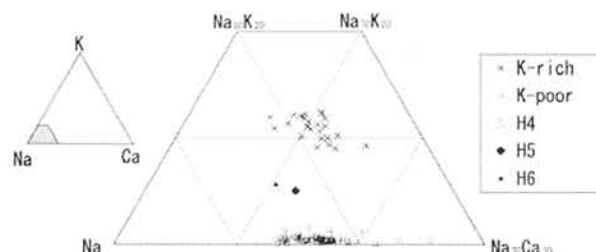


Fig. 5. Glassy phase composition. Glassy phase is divide into K-rich and K-poor phases. Compositions of plagioclases for H4, 5, and 6 were referred from [6].

grained minerals. These grains crystallized from the melt produced at impact event.

The relict olivines and pyroxenes, and isolated sulfides suggest that the temperature of the impact heating was less than 900 $^{\circ}\text{C}$. Contrastively, fine grained olivines suggest that the temperature of the shock heating is more than about ~1600 $^{\circ}\text{C}$, which is the melting temperature of magnesian olivine. Therefore there is a large difference for grains among the shock heating temperatures, and it is more than 700 $^{\circ}\text{C}$, suggesting that the duration of the shock heating was very transient. The existence of glassy phases and fine grained minerals also suggests that the cooling after heating was very rapid.

Two shock-melted chondrules seem to have been a barred olivine chondrule, and a pyroxene chondrule before the shock melting based on the textures. This evidence suggests that the mechanical deformation was not severe in spite of the strong heating at the time of the shock event.

References:

- [1] Grady M. M. (2000) Catalogue of Meteorites, 689p. [2] Stöffler D., Keil K., and Scott E. R. D. (1991) GCA, 55, 3845-3867. [3] Yamaguchi A., Scott E. R. D., and Keil K. (1998) AMR, 11, 18-31. [4] Yanai K. and Kojima H. (1995) *Catalog of the Antarctic Meteorite*, 230p. [5] Fujimaki H., Ishikawa K., Kojima H., Yanai K., and Aoki K. (1993) Proc. NIPR symp., 6, 364-373. [6] Brearley A. J. and Jones R. (1998) In: *Reviews in Mineralogy*, 36, 3, 398p.

THERMOLUMINESCENCE STUDY OF JAPANESE ANTARCTIC METEORITES X

K. Ninagawa¹, T. Kuyama¹, N. Imae², and H. Kojima²

¹Okayama University of Science, ²National Institute of Polar Research

Natural TL (thermoluminescence), the luminescence of a sample that has received no irradiation in the laboratory, reflects the thermal history of the meteorite in space and on Earth. Natural TL data thus provide insights into such topics as the orbits of meteoroids, the effects of shock heating, and the terrestrial history of meteorites. Induced TL, the response of a luminescent phosphor to a laboratory dose of radiation, reflects the mineralogy and structure of the phosphor, and provides valuable information on the metamorphic and thermal history of meteorites. The sensitivity of the induced TL is used to determine petrologic type of type 3 ordinary chondrites.

As a reliable pairing approach, TL properties within large chondrites were analyzed, taking advantage of the fact that serial samples from these meteorites is known to be paired [1]. Then a set of TL pairing criteria: 1) the natural TL peak height ratios, LT/HT, should be within 20%; 2) that ratios of raw natural TL signal to induced TL signal should be within 50%; 3) the TL peak temperatures should be within 20°C and peak widths within 10°C was proposed. This set of TL pairing criteria is less restrictive than previously used [1].

We have measured TLs of 82 Yamato and 127 Asuka unequilibrated ordinary chondrites so far [1-5]. This time we measured TL of additional 10 Yamato and 9 Asuka chondrites for determining 1) subtype and 2) pairing.

The TL data of them are listed in Table 1 and 2. The petrologic subtype was determined from their TL sensitivity. Three chondrites, A-881972 (H3), A-881981 (LL3), and Y-001041 (L3) were primitive below subtype 3.4 as shown in Fig. 1 and 2.

Above pairing criteria were also applied to the 10 and 9 samples, respectively. We found two TL potential paired fragments, Y-000708 (H3) and Y-000782 (H3), Y-000777 (H3) and Y-001035 (H3), as shown in Fig. 3.

References: [1] Ninagawa et al. (1998): Antarctic Meteorite Res., 11, 1-17. [2] Ninagawa et al. (2000): Antarctic Meteorite Res., 13, 112-120. [3] Ninagawa et al. (2002): Antarctic Meteorite Res., 15, 114-121. [4] Ninagawa et al. (2005): Antarctic

Meteorite Res., 18, 1-16. [5] Ninagawa et al. (2006): 30th Symp. Antarctic Meteorites, Tokyo, p.85-86

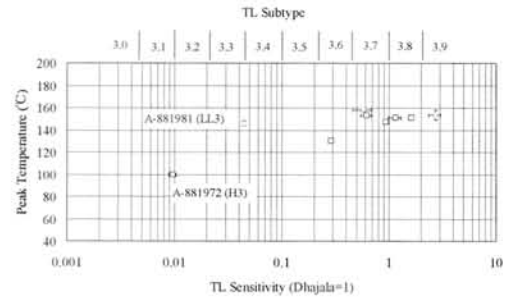


Fig.1. Correlation between TL sensitivity and peak temperature of nine Asuka chondrites

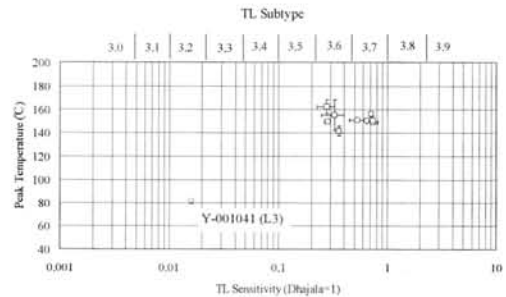


Fig.2. Correlation between TL sensitivity and peak temperature of ten Yamato chondrites.

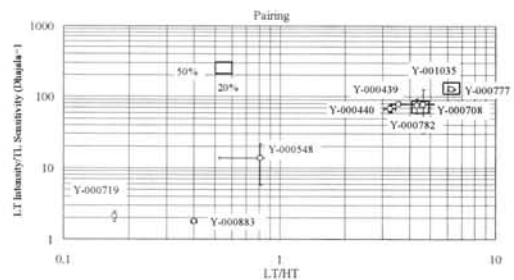


Fig.3. Ratio of LT to TL Sensitivity vs. LT/HT ratio to search fragments satisfying the pairing criteria 1) and 2).

Table1 Thermoluminescence data of nine Asuka unequilibrated ordinary chondrites

| Meteorite | Class | Natural TL | | | Induced TL | | | | LT /TL Sens. ($\times 10^3$) |
|-----------|-------|-----------------|---------------------|----------------------------|----------------------------|-----------------------|------------|-------------|--------------------------------|
| | | LT/HT | LT (10^3 counts) | TL Sensitivity (Dhajala=1) | Peak Temp. ($^{\circ}$ C) | Width ($^{\circ}$ C) | TL Subtype | | |
| A-881961 | H3 | 1.57 \pm 0.04 | 25.2 \pm 3.8 | 1.16 \pm 0.16 | 151 \pm 0 | 115 \pm 2 | 3.7-3.8 | 22 \pm 4 | |
| A-881967 | L3 | 0.74 \pm 0.01 | 10.8 \pm 4.2 | 0.58 \pm 0.11 | 158 \pm 1 | 136 \pm 2 | 3.6-3.7 | 19 \pm 8 | |
| A-881972 | H3 | | | 0.01 \pm 0.00 | 100 \pm 1 | 138 \pm 2 | 3.1-3.2 | | |
| A-881981 | LL3 | 0.66 \pm 0.05 | 0.2 \pm 0.0 | 0.04 \pm 0.00 | 146 \pm 2 | 137 \pm 0 | 3.3-3.4 | 5 \pm 1 | |
| A-881997 | LL3 | 2.48 \pm 0.10 | 174.4 \pm 25.8 | 2.71 \pm 0.34 | 154 \pm 5 | 125 \pm 1 | 3.9 | 64 \pm 13 | |
| A-882004 | H3 | 0.79 | 27.8 | 0.95 \pm 0.01 | 147 \pm 1 | 117 \pm 0 | 3.7 | 29 \pm | |
| A-882011 | H3 | 0.58 \pm 0.14 | 4.4 \pm 1.0 | 0.62 \pm 0.07 | 153 \pm 1 | 117 \pm 2 | 3.7 | 7 \pm 2 | |
| A-882053 | H3 | 1.02 \pm 0.02 | 4.1 \pm 0.5 | 0.29 \pm 0.01 | 130 \pm 1 | 146 \pm 2 | 3.6 | 14 \pm 2 | |
| A-882061 | H3 | 0.07 \pm 0.00 | 1.8 \pm 0.2 | 1.64 \pm 0.01 | 151 \pm 1 | 117 \pm 1 | 3.8 | 1 \pm 0 | |

Table2 Thermoluminescence data of ten Yamato unequilibrated ordinary chondrites

| Meteorite | Class | Natural TL | | | Induced TL | | | | LT /TL Sens. ($\times 10^3$) |
|-----------|-------|-----------------|---------------------|----------------------------|----------------------------|-----------------------|------------|-------------|--------------------------------|
| | | LT/HT | LT (10^3 counts) | TL Sensitivity (Dhajala=1) | Peak Temp. ($^{\circ}$ C) | Width ($^{\circ}$ C) | TL Subtype | | |
| Y-000439 | H3 | 3.57 \pm 0.00 | 58.0 \pm 0.8 | 0.74 \pm 0.03 | 150 \pm 1 | 133 \pm 3 | 3.7 | 79 \pm 3 | |
| Y-000440 | H3 | 3.25 \pm 0.20 | 50.5 \pm 0.3 | 0.74 \pm 0.08 | 149 \pm 2 | 116 \pm 1 | 3.7-3.8 | 69 \pm 8 | |
| Y-000548 | H3 | 0.81 \pm 0.28 | 7.2 \pm 4.1 | 0.53 \pm 0.08 | 151 \pm 0 | 113 \pm 1 | 3.6-3.8 | 14 \pm 8 | |
| Y-000708 | H3 | 4.62 \pm 1.36 | 21.5 \pm 12.6 | 0.28 \pm 0.05 | 162 \pm 6 | 133 \pm 5 | 3.6 | 78 \pm 48 | |
| Y-000719 | H3 | 0.17 \pm 0.00 | 1.4 \pm 0.2 | 0.65 \pm 0.02 | 150 \pm 0 | 116 \pm 1 | 3.7-3.8 | 2 \pm 0 | |
| Y-000777 | H3 | 6.26 \pm 0.23 | 45.0 \pm 1.6 | 0.36 \pm 0.00 | 141 \pm 4 | 124 \pm 1 | 3.6-3.7 | 125 \pm 5 | |
| Y-000782 | H3 | 4.32 \pm 0.05 | 24.7 \pm 0.0 | 0.33 \pm 0.08 | 155 \pm 13 | 134 \pm 11 | 3.5-3.7 | 76 \pm 18 | |
| Y-000883 | H3 | 0.40 \pm 0.01 | 1.3 \pm 0.0 | 0.72 \pm 0.03 | 156 \pm 2 | 123 \pm 0 | 3.7-3.8 | 2 \pm 0 | |
| Y-001035 | H3 | 6.17 \pm 0.00 | 36.3 \pm 0.0 | 0.28 \pm 0.02 | 149 \pm 1 | 126 \pm 2 | 3.6-3.7 | 128 \pm 9 | |
| Y-001041 | L3 | | 0.2 \pm 0.1 | 0.02 \pm 0.00 | 81 \pm 2 | 64 \pm 8 | 3.2-3.3 | 10 \pm 3 | |

PALEOMAGNETIC STUDY OF BASALTS FROM LONAR IMPACT CRATER.

I. Nishioka¹, M. Funaki² and K. Venkata Rao³, ¹The Graduate University for Advanced Studies, Kanagawa 240-0193, Japan (nishioka@nipr.ac.jp), ²National Institute of Polar Research, Tokyo 173-8515, Japan, ³Geological Survey of India, Nagpur 440006, India.

Introduction:

Magnetic anomaly studies of Martian and lunar surfaces demonstrated the presences of demagnetized areas around the large impact structures [1-2]. Strong stress waves generated by meteorite impact were estimated to be responsible for parts of the demagnetization. Shock experiments suggested that transient stress of less than 1GPa is enough to partially demagnetize and remagnetize basalts [3]. There are, however, only a few paleomagnetic studies of terrestrial impact structures with proof of de/re-magnetization induced by meteorite impact [4].

Lonar crater is located in Maharashtra State, India. The crater was entirely formed in Deccan basalt. A rim-to-rim diameter is 1.8 km. Fission track ages of impact glasses were determined as 50 ka or later [5]. Earlier paleomagnetic studies revealed presence of two directional components of natural remanence [6-7]. Purpose of the present study is to clarify the origin of these components and to detect any changes in natural remanence related to the impact event.

Samples and Experiments:

At least five lava flows can be recognized on the innerwall of the crater. Basalt samples were collected from the uppermost flows at eight sites and from the lower flows at ten sites. Samples were also collected outside of the rim at seven sites for comparison. Eight to ten samples were collected at each sites. Thermomagnetic and hysteresis measurements as well as microscopic observations revealed that Ti-poor titanomagnetite or cation-deficient titanomagnetite of pseudo-single domain size is the main magnetic minerals in these samples.

Paleomagnetic measurements were performed using a SQUID magnetometer with an in-line static three-axis demagnetizer. Least-square method was used to estimate direction of the isolated paleomagnetic component. To constrain the timing of the magnetization, these directions were corrected for the outward tilting of the lava flows due to the uplifted rim.

Results:

As previous studies have demonstrated [6], two paleomagnetic components were isolated for basalts from the inner wall of the rim. The soft component was erased below the peak alternating field of 10 – 25 mT. The residual hard component decayed linearly to the origin of orthogonal plot.

The directions of the soft component are near parallel to the present earth field in this area, whereas

the direction of the hard component is close to the characteristic directions of Deccan basalts [8]. Fisher's precision parameter of the soft component decreased after the tilt correction. This decrease yields the negative fold test of McFadden [9] at the 95 percent confidence level for both upper and lower flows. The negative fold test indicates that the soft component was acquired after the uplift of the rim. In contrast, the hard component isolated from the uppermost flow passed the positive fold test at 99 percent confidence level. The overall mean direction after the tilt correction ($D=125^\circ$, $I=41^\circ$, $a_{95}=4^\circ$) could not be distinguished with that of the outer rim sites ($D=126^\circ$, $I=38^\circ$, $a_{95}=3^\circ$). Site-mean directions of the lower flows have larger declinations than those of the uppermost flow ($D=120^\circ$ - 180°). The precision parameter was not significantly improved by the tilt correction.

Discussion:

The hard paleomagnetic component of the uppermost flows was successfully restored to the pre-impact direction by the tilt-correction. The directions of the preexisting magnetization were unchanged by the impact event. The more scattered paleomagnetic directions of the lower flows can be explained by the large secular variation of the geomagnetic field at that time [8].

The earlier study [6] suggested that the soft component of the lower flows is shock remanence (SRM). In our study, their negative fold test indicated its acquisition after the uplift of the rim. In contrast, SRM is expected to be acquired in the early stage of impact cratering process before any tectonic movements [7]. The soft component is, thus, expected to be viscous or chemical remanent magnetization.

References:

- [1] Mohit, P.S. and Arkani-Hamed, J. (2004) *Icarus*, 168, 305-317. [2] Halekas, J.S. et al. (2002) *GRL*, 29, 1645 [3] Pohl, J. et al. (1975) *J. Geophys.*, 41, 23-41. [4] Halls, H.C. (1979) *Geophys. Jour. R. astr. Soc.*, 59, 553-591. [5] Storzer, D. and Koeberl, C. (2004) *LPS, XXXV*, 1309-1310. [6] Poornachandra Rao, G.V.S and Bhalla, M.S. (1984) *Geophys. J. R. astr. Soc.*, 77, 847-862. [7] Cisowski, S.M. and Fuller, M. (1978) *J.G.R.*, 83, 3441-3458. [8] Vandamme, D. et al., (1991) *Reviews Geophys.* 29, 159-190. [9] McFadden, P.L. (1990) *Geophys. J. Int.* 103, 163-169.

Discovery of a Chondritic Porous Interplanetary Dust Particle among Antarctic Micrometeorites. Takaaki Noguchi¹, Tomoki Nakamura², Tomoaki Aoki², Shoichi Toh³, Naoya Imae⁴, Naoyoshi Iwata⁵, and Tottuki Micrometeorite Curation Team¹. ¹Department of Materials and Biological Sciences, Ibaraki University, ²Department of Earth and Planetary Sciences, Faculty of Science, Kyushu University, ³HVEM Laboratory, Kyushu University, ⁴National Institute of Polar Research, ⁵Department of Earth Sciences, Yamagata University.

Introduction:

Antarctic micrometeorites (AMMs) have been collected from blue ice fields in Antarctica. Recently, collection of micrometeorites from surface snow (snow MMs) has started by European and Japanese researchers [e. g. 1, 2, 3]. Vast majority of AMMs recovered from blue ice field (hereafter blue-ice field MMs [1]) are similar to heavily hydrated carbonaceous chondrites, which were probably derived from asteroids [e. g., 4, 5, 6]. On the other hand, about a half of interplanetary dust particles (IDPs) collected in the stratosphere has anhydrous mineralogy [e. g. 7]. Most of the anhydrous IDPs are quite porous and fragile and at least a part of them were probably derived from comets [7]. Such chondritic porous IDPs (hereafter CP IDPs) are characterized by the presence of abundant GEMS (glass with embedded metal and sulfides), enstatite whisker, and carbonaceous material that connect the other components [7]. We have found that snow MMs contain primarily anhydrous ones, whose population is much higher than that among blue-ice field MMs [3] and that some blue-ice field MMs having anhydrous mineralogy with a high abundance of presolar silicates [8]. However, we have not yet discovered MMs that are indistinguishable with CP IDPs among both blue-ice field MMs and snow MMs. Discovery of MMs indistinguishable with CP IDPs are important to testify that probable cometary material could have reached the earth's surface in the past because some researchers pointed out that cometary dust might have been one of the important sources of organic matter in the early Earth [e. g. 9]. In this paper, we would like to report the first discovery of a blue-ice field MM that has features indistinguishable from CP IDPs.

Sample and methods:

We used fine-grained particles collected from 2 sites at the Tottuki Point by melting blue-ice and filtering water [10]. We collected > 3500 blue-ice field MMs and classified them into several types based on their morphology and chemical composition obtained by scanning electron microscope equipped with energy dispersive spectrometer (JEOL JSM-5600LV SEM with Oxford ISIS EDS) at Ibaraki University. We selected some typical MMs of each type for synchrotron radiation X-ray diffraction (SR-XRD) at Photon Factory, High Accelerator Research Organization to investigate

bulk mineralogy of each MM. A MM was selected for transmission electron microscope (TEM) observation and EDS analysis. A Focused ion beam system for TEM sample preparation (Hitachi FB-2000K FIB at Kyushu University) was used to make of pyroxene crystals. To make ultrathin sections for detailed observation of the interior of the MM, we used the sulfur embedding method because electron energy loss spectra (EELS) analysis of light elements was also planned. Sections were made by ultramicrotome at Ibaraki University. JEOL JEM-2000FX equipped with EDAX DX4 EDS was used for conventional TEM observation at Ibaraki University. For observation of a sample made by FIB and EELS analysis of carbonaceous material in the MM was performed by an energy-filter field-emission TEM JEOL JEM-3200FSK at Kyushu University.

Results:

From fine-grained particles obtained at the Tottuki No. 5 site, we collected more than 3200 MMs larger than 10 μm across and investigated relative population of each type of MMs among all the size ranges. We recognized two types of primarily anhydrous MMs: highly carbonaceous anhydrous MMs and porous anhydrous ones. Both of them occupy less than 1 % of the total MMs collected. We could not find porous anhydrous MMs containing rod-shaped or narrow ribbon-shaped objects that are candidates for real enstatite whiskers based on SEM/EDS observation among them. However, we found a highly porous anhydrous MM showing many rod-shaped or narrow ribbon-shaped objects on its surface from among MMs collected at No. 4 site, only a few tens of meters away from No. 5 site. SR-XRD of the MM shows that it is composed mainly of olivine, low-Ca pyroxene, magnetite, and magnesiowustite.

High magnification SEM observation revealed that typical sizes of the elongated small objects are 0.1 to 0.5 μm wide x 2 to 5 μm long. We selected two such objects for FIB sample preparation. We could obtain one good section suitable for TEM observation. TEM observation of the rod-shaped object revealed that it is a unit-scale mixture of ortho- and clino-enstatite with many stacking disorders that are parallel to (100) of them. Its elongated direction is parallel to a-direction of the crystal. No screw dislocations along a-direction of the pyroxene were observed.

TEM observation of the MM revealed that about

a half of the surface of the MM are composed of equigranular olivine and Fe oxides (both magnetite and magnesiowustite) with a small amount of glass that fills the interstices of these minerals. The grain sizes of these minerals are around 100 nm. The rim has about 10- μ m thick from the surface of the MM. EDS analysis of olivine in the rim is iron-rich (Fo₆₅ to Fo₃₀). The other area of the MMs has a quite different texture. It is composed of a loose aggregate of abundant low-Ca pyroxene and a small amount of olivine as well as amorphous to poorly crystalline interstitial material, 100- to 200-nm across spheroidal objects, small amounts of Fe-Ni metal and Fe-bearing sulfide, and carbonaceous material that connects these constituents. Most of the ferromagnesian silicates in the interior are sub- μ m in size, and Fe-Ni metal and sulfide are less than 200 nm across.

In the interior of the MM, there are many low-Ca pyroxene crystals with crystallographic features common to those of enstatite whisker in CP IDPs. Chemical compositions of enstatite whiskers, low-Ca pyroxene crystals other than the whiskers, and olivine in the interior of the MM were obtained by EDS. Most of them contain less than 3 wt % FeO, 0.2-1.2 wt % MnO, and 0.6-1.3 wt % Cr₂O₃. Although they are not so enrich in MnO relative to FeO, many of them are plotted among the chemical compositions of olivine and low-Ca pyroxene in IDPs [12]. No solar flare tracks were observed in these ferromagnesian silicates. Spheroidal objects are composed of Mg-rich but Fe-bearing amorphous silicate containing less than 20-nm Fe-Ni metal and Fe-sulfide based on elemental mapping and selected area electron diffraction (SAED) patterns of these objects. In the objects near the rim above described, they contain small amounts of olivine and magnetite based on SAED patterns. Relative elemental abundances between Si-S-Fe and Ca/Si vs. Al/Si of these spheroidal objects are plotted in the area of GEMS in anhydrous IDPs [13, 14, 15] and the most primitive materials in Acfer 094, ALH 77307, and Y791198 [15].

Discussion and conclusions:

Because crystallography of fine-grained rod- and narrow ribbon-shaped low-Ca pyroxene in this MM is the same as that of enstatite whisker in CP IDPs, these low-Ca pyroxene crystals are real enstatite whiskers. Mineralogy of the "spheroidal objects" in the MM is also basically common to GEMS in CP IDPs [7]. Presence of Fe-rich olivine and magnetite in some spheroidal objects are different from typical GEMS. However, such spheroidal objects tend to exist near the rim of the MM whose texture is quite similar to run products of heating experiments of carbonaceous chondrites [17, 18, 19]. Because there is no compositional difference between spheroidal objects in the interior of the MM and those near the rim, the latter was

transformed by heating probably during atmospheric entry. Comparison of the latter objects and run products of the heating experiments of GEMS [21], the objects would have experienced around 700 °C. We think that both of these spheroidal objects are real GEMS. Because solar flare tracks in olivine in IDPs are erased by heating higher than 600 °C [20], and because no olivine and pyroxene in this MM contain solar flare tracks, even the interior of this MM experienced heating higher than 600 °C during atmospheric entry. Based on the heating experiments of carbonaceous chondrites [17, 18, 19], a part of the surface of this MM would have experienced around 1000 °C. That part would have been the "ram" face during atmospheric entry. These lines of evidences strongly suggest that this blue-ice field MM is a real CP IDP that fell on earth's surface in the past.

Acknowledgement: We thank Dr. Y. Nakamura for allowance to join Mr. T. Aoki with this investigation.

References:

- [1] Duprat J. *et al.* (2005) *LPSC XXXVI* #1678.
- [2] Duprat J. *et al.* (2005) *In: Dome C Astronomy and Astrophysics Meeting* (M. Giard, F. Casoli and F. Paletou, eds) EAS Publications Series **14**, pp. 51-56.
- [3] Noguchi T. *et al.* (2006) Paper presented to the 30th Symp. Antarct. Meteorites, June 6-8, 2006, Tokyo.
- [4] Kurat G. *et al.* (1994) *Geochim. Cosmochim. Acta*, **58**, 3879-3904.
- [5] Noguchi T. *et al.* (2003) *Earth Planet. Sci. Lett.*, **212**, 321-336.
- [6] Gounelle M. *et al.* (2005) *Meteoritics Planet. Sci.*, **40**, 917-932.
- [7] Bradley J. P. (2003) *In: Astromineralogy* (T. K. Henning ed.) Lecture Notes in Physics **609**, Berlin, pp. 217-236.
- [8] Yada T. *et al.* (2006) *LPSC XXXVII*, # 1470.
- [9] Chyba C. F. *et al.* (1990) *Science*, **249**, 366 - 373.
- [10] Iwata N. and Imae N. (2002) *Antarctic Meteorite Res.*, **15**, 25-37.
- [11] Bradley J. P. *et al.* (1983) *Nature*, **301**, 473-477.
- [12] Klöck W. *et al.* (1989) *Nature*, **339**, 126 - 128.
- [13] Keller L. P. and Messenger S. (2004) *LPSC XXXV*, # 1985.
- [14] Keller L. P. and Messenger S. (2005) *LPSC XXXVI*, # 2088.
- [15] Chizmadia L. J. (2005) *LPSC XXXVI*, # 2229.
- [16] Keller L. P. and Messenger S. (2005) *In: Chondrites and the Protoplanetary Disk* (A. N. Krot *et al.*, eds.) Astron. Soc. Pacific Conf. Ser. **341**, pp. 657-667.
- [17] Greshake A. *et al.* (1998) *Meteoritic Planet. Sci.*, **33**, 267-290.
- [18] Toppani A. *et al.* (2001) *Meteoritic Planet. Sci.*, **36**, 1377-1396.
- [19] Nozaki W. *et al.* (2006) *Meteoritic Planet. Sci.*, **41**, 1095-1114.
- [20] Fraundorf P. *et al.* (1982) *Proc. 13th LPSC*, A409-412.
- [21] Brownlee D. E. *et al.* (2005) *LPSC XXXVI*, #2391. Tottuki Micrometeorite Curation Team is comprised of undergraduate students of Noguchi's laboratory: S. Chikazawa, H. Fushimi, A. Iose, M. Kogo, Y. Maezawa, J. Mikada, A. Nakazawa, S. Nishida, N. Ohashi, M. Osonoi, Y. Suenaga, Y. Sugawara, Y. Takemasa.

Lunar Crust/Mantle Formation Intervals. L. E. Nyquist¹, C.- Y. Shih², and Y. D. Reese³,
¹Mail Code KR, NASA Johnson Space Center, Houston, TX 77058-3696, USA, laurence.nyquist@nasa.gov, ²Mail Code JE-23, ESCG/Jacobs Sverdrup, P.O. Box 58477, Houston, TX 77258-8477, USA, ³Mail Code JE-23, ESCG/Muniz Engineering, Houston, TX 77058, USA.

Introduction:

Study of the Yamato-86032 lunar meteorite showed that the Nd-isotopic composition of its anorthositic clasts were compatible with derivation from a lunar magma ocean (LMO) if the LMO had the higher initial ¹⁴³Nd/¹⁴⁴Nd ratio of the HED Parent Body [1], rather than of the Chondritic Uniform Reservoir (CHUR) [2]. We report additional Nd isotopic analyses of the Y-86032 clasts including ¹⁴²Nd/¹⁴⁴Nd measurements, and compare the results to earlier measurements of ¹⁴²Nd/¹⁴⁴Nd for lunar basalts [3] and the Yamato 980318 cumulate eucrite, which has a conventional Sm-Nd age of 4567±24 Ma [4,5]. These data place constraints on the formation intervals of the lunar crust and mantle.

Y-86032 Data:

A conventional Sm-Nd isochron giving an age of 4430±30 Ma was determined previously for subsample Y-86032,28 of the light gray clast in Y-86032 [1], referred to as 28LG here. ¹⁴²Nd/¹⁴⁴Nd analyses were made of a 26 mg bulk sample of the clast containing ~30 ng Nd. The analyses were done on the same thermal ionization mass spectrometer as used for the lunar sample data reported by [3], but with improved chemical purification techniques. No enriched isotope “spikes” were added to the sample. Isotopic analyses were of NdO⁺ because of the limited amount of Nd available for analysis. ¹⁴²Nd/¹⁴⁴Nd expressed as ε¹⁴²Nd deviations in parts in 10⁴ from ¹⁴²Nd/¹⁴⁴Nd in a terrestrial standard are shown in Fig. 1, plotted at the ¹⁴⁷Sm/¹⁴⁴Nd value previously determined for the bulk clast [1].

Y-980318 [4,5], ε¹⁴²Nd for bulk lunar basalts [3], and chondritic ε¹⁴²Nd as reported by [6]. All ε¹⁴²Nd data are plotted at ¹⁴⁷Sm/¹⁴⁴Nd values measured for the samples in question. For the lunar samples this choice is not best for chronologic interpretations, because time-integrated ingrowth of ¹⁴²Nd due to decay of ¹⁴⁶Sm occurs *prior* to basalt genesis. Nevertheless, because the Sm/Nd ratio is little fractionated during petrogenetic processes, this representation allows comparisons between lunar rocks having similar Sm/Nd ratios. Thus, for example, ε¹⁴²Nd for 28LG is slightly less but within error of ε¹⁴²Nd = 0 in the terrestrial isotopic standard, in agreement with the values for KREEP basalts (yellow triangles in figure) of similarly low Sm/Nd. Most low-Ti lunar basalts have Sm/Nd ratios near the chondritic Sm/Nd value, and have ε¹⁴²Nd values very close to those of the terrestrial standard. All high-Ti basalts in this dataset, plus Apollo 12 ilmenite basalt 12056 and “YAMM” basalt Asuka 881757, have ε¹⁴²Nd values higher than the terrestrial standard, but lower than the whole rock sample of Y980318 of similar ¹⁴⁷Sm/¹⁴⁴Nd ratio. Thus, either most of the live ¹⁴⁶Sm initially present in the early solar system had decayed prior to formation of the basalt source regions, or the Nd isotopic composition of the lunar mantle was rehomogenized after their formation.

Discussion:

Assuming homogeneous distribution of ¹⁴⁶Sm in the early solar system that is characterized by (¹⁴⁶Sm/¹⁴⁴Sm)₀ = 0.0076±0.0009 in the 4558 Ma old LEW 86010 angrite [7,8], the lunar mantle formation interval (i.e., time to isotopic closure) must have extended to significantly later times than T_{LEW} = 4523±8 Ma given by the Y980318 isochron. Alternatively, taking the initial solar system (¹⁴⁶Sm/¹⁴⁴Sm)₀ = 0.0060±0.0003 as found for Y980318, ¹⁴⁶Sm/¹⁴⁴Sm = 0.0020±0.0006 from the lunar basalt “isochron” provides a lower limit ΔT_{Y98} = 162 (+50, - 38) Ma for the period to Nd-isotopic closure in the basalt source regions. This is a lower limit both because of the lower choice for (¹⁴⁶Sm/¹⁴⁴Sm)₀ and because the slope of the “isochron” is most determined by the basalts of high Sm/Nd ratio. The Sm/Nd ratios of the basalts should have decreased as a result of element partitioning during partial melting of the mantle leading to basalt genesis. As discussed by [3], iteration of source region ¹⁴⁷Sm/¹⁴⁴Nd ratios calculated instead from the determined ε¹⁴³Nd values results in a self-consistent set of (ε¹⁴²Nd, ¹⁴⁷Sm/¹⁴⁴Nd)_{source} data shown in Fig. 2. This mantle isochron gives a “mantle formation interval” ΔT_{LEW} = 238 (+56, -40) Ma, or an age T_{LEW}

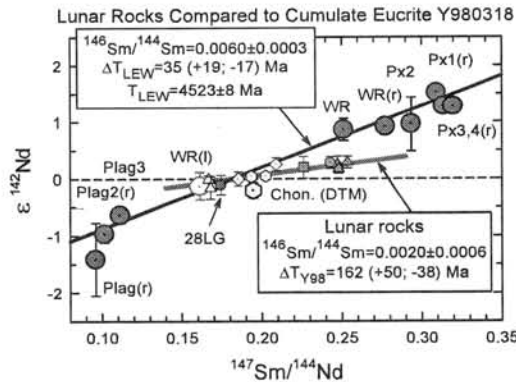


Figure 1. ε¹⁴²Nd in Y-86032,28 LG (small red circle) compared to the internal ¹⁴⁶Sm-¹⁴²Nd isochron for cumulate eucrite Y980318 [4,5] and ε¹⁴²Nd in other lunar samples measured with the same instrument [3].

Also shown in Fig. 1 are the previously determined internal ¹⁴⁶Sm-¹⁴²Nd internal isochron for

= 4320 (-56, +40) Ma for the time of Nd-isotopic closure of lunar mantle source regions. Using a similar approach for a different set of basalts, [9] derived a formation interval of 215 (+23, -21) Ma.

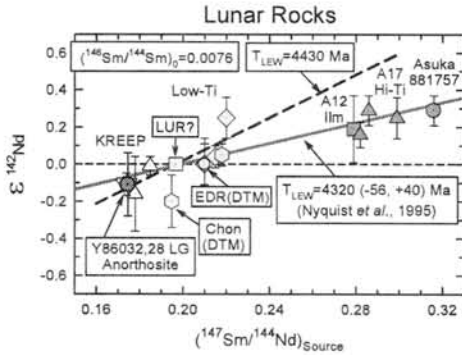


Figure 2. Mantle isochron for lunar basalts [3].

In an LMO model, initial crystallization of plagioclase occurs at ~78-86 PCS (Per Cent Solid by volume) whereas ilmenite crystallization begins only after ~95 PCS [10]. Thus, some difference in formation times of the crust and ilmenite-bearing cumulates parental to the high-Ti basalts might be expected. However, the source regions for the Apollo 12 ilmenite basalts and low-Ti A881757 would have formed earlier in the sequence. So, in this model it is reasonable to assume the crust and mantle source regions formed approximately contemporaneously. Thus, the difference between a crust formation interval of ~135 Ma, as implied by the crystallization age of 28LG, and the ~200-250 Ma mantle solidification age requires explanation. One possibility is that ^{146}Sm was heterogeneously distributed in the solar nebula, and that a lower value of $(^{146}\text{Sm}/^{144}\text{Sm})_0$ should be used to calculate lunar formation intervals. A comparison of the ^{147}Sm - ^{143}Nd and ^{146}Sm - ^{142}Nd ages of the LEW86010 angrite [7] and the Y980318 cumulate eucrite [4,5] in fact hints at this possibility. In that case the slope of the ~4430 Ma reference isochron in Fig. 2 might decrease to become coincident with the mantle isochron to give a (recalculated) age near ~4430 Ma for both crust and mantle formation. This case would be permitted by the extreme lower limit of ~124 Ma for ΔT_{Y98} for the dataset shown in Fig. 1, but additionally requires the unlikely circumstance that the Sm/Nd ratios of the basalts were not fractionated during petrogenesis. Another possibility is that the mantle Nd-isotopic system was kept open due to mantle processes such as overturn or convection [3].

The isochrons for both the cumulate eucrite data and our lunar data pass above the chondrite datum from [6], but well within error of their terrestrial EDR (Early Depleted Reservoir) datum. However, the significance of these observations is unclear since [6] did not determine isochron relationships for their meteorite data. Lower $\epsilon^{142}\text{Nd}$ values for lunar basalts than those considered here [9] are probably due to differences in analytical instruments and techniques.

Fig. 3 shows that the ^{143}Nd and ^{142}Nd data considered here for lunar samples are consistent in requiring higher abundances of the radiogenic ^{142}Nd and ^{143}Nd isotopes than present in chondrites. Our analyses of 28LG, a non-FAN "An93 anorthosite" [1] shows this relationship is not simply due to regional variation in rock types. Initial $^{142}\text{Nd}/^{144}\text{Nd}$ and $^{143}\text{Nd}/^{144}\text{Nd}$ may have varied among planetary objects due to incomplete homogenization of the early solar system.

Conclusions:

The combined ^{147}Sm - ^{143}Nd and ^{146}Sm - ^{142}Nd isotopic systems promise to yield a self-consistent chronology for lunar crust and mantle formation as more high precision Nd-isotopic data are obtained, especially for lunar crustal rocks. Although the present data are no longer in conflict with Hf-W data calling for lunar differentiation as early as ~40 Ma after formation of the solar system [11], Lu-Hf data require a closure age for the KREEP source region no later than 4.4 Ga ago, and are most consistent with closure within ~60 Ma of solar system formation [12]. Interpreting the isotopic data may require a distinction between initial elemental differentiation and isotopic closure. Fig. 3, for example, suggests early (>~4.5 Ga ago) fractionation of the Sm/Nd ratio from the chondritic value in lunar crustal rocks, but internal Sm-Nd isochrons for the rocks show that Nd isotopic closure occurred later.

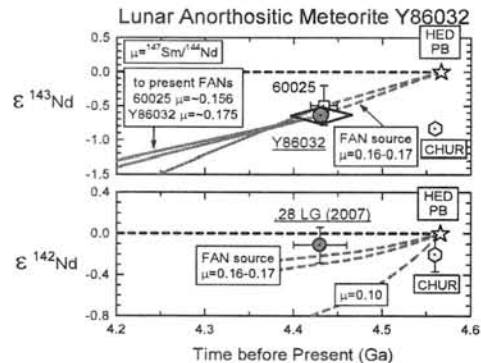


Figure 3. $\epsilon^{143}\text{Nd}$ and $\epsilon^{142}\text{Nd}$ for An93 anorthosite Y86032, 28LG and FAN 60025. The reference $\epsilon = 0$ lines are calculated for chondritic $^{147}\text{Sm}/^{144}\text{Nd} = 0.1967$ as for CHUR [2], but with the the Nd isotopic composition of eucrites [5].

References:

- [1] Nyquist L. et al. (2006) *GCA* 70, 5990-6015.
- [2] Jacobsen S. B. and Wasserburg G. J. (1984) *EPSL*, 67, 137-150.
- [3] Nyquist L. E. et al. (1995) *GCA* 59, 2817-2837.
- [4] Nyquist L. E. et al. (2004) *LPS XXXV*, #1330.
- [5] Nyquist L. E. et al. (2004) *Pap. 28th Symp. Ant. Met.*, 66-67.
- [6] Boyet M. and Carlson R. W. (2005) *Science* 309, 576-581.
- [7] Nyquist L. E. (1994) *Meteoritics* 29, 872-885.
- [8] Lugmair G. W. and Galer S. J. G. (1992) *GCA* 56, 1673-1694.
- [9] Rankenburg K. et al. (2006) *Science* 312, 1369-1372.
- [10] Snyder G. A. and Taylor L. A. (1993) *Proc. NIPR Symp. Antarct. Met.* 6, 246-267.
- [11] Touboul M. et al. (2007) *LPS XXXVIII* #2385.
- [12] Taylor D. J. et al. (2007) *XXXVIII* #2130.

Isotopic variations of macromolecular organic matter from CM chondrites during hydrous pyrolysis.

Yasuhiro Oba and Hiroshi Naraoka, Dept. of Earth Sciences, Okayama Univ. Okayama, Japan

Introduction:

A solvent-insoluble and high-molecular organic matter is a major component within organic matters in carbonaceous chondrites. This macromolecular organic matter is consisted mainly of aromatic structure with minor aliphatic carbon as well as heteroelements(N, O, S)-linked carbon. We have investigated elemental and isotopic compositions and as well as chemical structures of the macromolecules purified from several CM chondrites including Antarctic and Murchison meteorites [1, 2, 3], which revealed various degrees of thermal and/or aqueous alteration on the meteorite parent bodies. In addition, macromolecular organic matter of the Murchison meteorite yielded abundant acetic acid (~400 ppm) during hydrous pyrolysis, possibly being an important process to generate acetic acid under prebiotic conditions [4]. In this study, we report carbon and hydrogen isotopic changes of the macromolecular organic matter during hydrous pyrolysis to discuss $\delta^{13}\text{C}$ and δD distribution of several CM macromolecules with respect to their alteration processes.

Samples and methods:

Carbon and hydrogen isotopic compositions of the purified macromolecule from seven CM chondrites (Y-791198, Y-793321, B-7904, A-881280, A-881334, A-881458, and Murchison) and macromolecule residues of Murchison after hydrous pyrolysis (270°C, 300°C and 330°C for 72h; $\delta\text{D}_{\text{water}} = -75\text{‰}$) were determined using an isotope ratio mass spectrometer in on-line mode coupled with an elemental analyzer and a high-temperature pyrolyzer, respectively. Site-specific carbon isotope analysis of carboxyl groups in macromolecules was also performed [5]. The $\delta^{13}\text{C}$ and δD values were calibrated using standard gases relative to PDB and SMOW, respectively.

Results and discussion:

Hydrogen to carbon ratio (H/C, by atomic) of the Murchison macromolecule decreases from 0.62 (original) to 0.31 (330°C) with increasing temperature of hydrous pyrolysis, indicating preferential loss of H to C. Although the Murchison macromolecule become depleted in ^{13}C by up to ~3‰ during the hydrous pyrolysis, the δD value decreases significantly from +986‰ (original) to +25‰ (330°C). This δD change indicates that the macromolecular hydrogen is readily exchangeable with environmental water under hydrothermal condition on the meteorite parent body, because the δD value of water used in this study (-75‰) is similar to that of H_2O in Murchison (~ -88‰) [6].

The $\delta^{13}\text{C}$ and δD change of the Murchison macromolecule during hydrous pyrolysis is plotted in Fig. 1 with $\delta^{13}\text{C}$ and δD of Antarctic CM macromolecules. The $\delta^{13}\text{C}$ - δD change during hydrous pyrolysis is projected as a dashed arrow. The thermally altered CM chondrites such as B-7904 and A-881280 are plotted along the dashed line, suggesting a potential isotope evolution of macromolecule during hydrothermal activity on the meteorite parent body. On the other hand, $\delta^{13}\text{C}$ - δD signature of Y-793321 and A-881334 is distinctive, possibly due to different origins.

The amount of carboxyl group ranges from 2.2 to 3.5% of total macromolecular carbon, in which the carboxyl group is more enriched in ^{13}C (-7.6 to +2.3‰) by 8-10‰ relative to the corresponding bulk macromolecular carbon. The carboxyl group of Murchison residue after hydrous pyrolysis become more ^{13}C -depleted by ~6‰ relative to the original macromolecule. The Murchison residue has the similar isotopic composition to macromolecules of B-7904 and A-881280.

These isotope changes by hydrous pyrolysis are consistent with carbon and hydrogen isotopic compositions of macromolecule in the altered CM chondrites

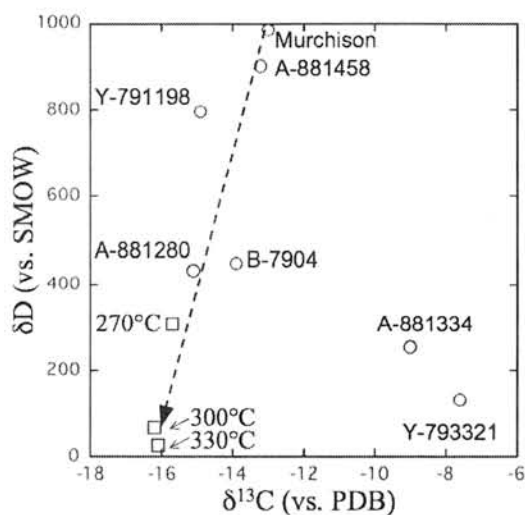


Fig.1 $\delta^{13}\text{C}$ - δD relationship of CM macromolecules with the Murchison residues of hydrous pyrolysis.

References:

- [1] Naraoka H. et al. (2004) *Meteorit. Planet. Sci.*, 39, 401-406.
- [2] Yabuta H. et al. (2005) *Meteorit. Planet. Sci.*, 40, 779-787.
- [3] Naraoka H. and Oba Y. (2006) *Antarctic Meteorites XXX*, 84.
- [4] Oba Y. and Naraoka H. (2006) *Meteorit. Planet. Sci.*, 39, 401-406.
- [5] Oba Y. and Naraoka H. (2006) *Rapid Commun. Mass Spectrom.* 20, 3649-3653.
- [6] Robert F. (2002) *Planet. Space Sci.*, 50, 1227-1234.

Noble-gas and oxygen isotopes and REE abundances of Antarctic micrometeorites.

R. Okazaki and T. Nakamura. Department of Earth and Planetary Sciences, Faculty of Science, Kyushu University, Hakozaki, Higashiku-ku, Fukuoka 812-8581, Japan (okazaki@geo.kyushu-u.ac.jp).

Introduction:

Micrometeorites (MMs) are the main fraction of extraterrestrial material falling on the Earth. Unmelted MMs include fine-grained MMs (fgMMs) and coarse-grained MMs (cgMMs). Compositional, textural and mineralogical affinities of fgMMs to the matrices of CM, CR and CI chondrites suggest that fgMMs originate as dust-size debris from main belt asteroids [1-3]. Origin of cgMMs has been discussed in [3-5]: cometary or chondrule fragments. Recently [5] suggests that cgMMs are chondrule fragments based on their textures, chemical compositions, and occurrences. In order to discuss the origin of cgMMs further, their isotopic compositions are necessary. Here we present oxygen and noble gas isotope data, in addition to textural and chemical compositions. Also REE abundances were obtained.

Analytical method:

Fourteen AMMs were picked out from the NIPR collection (50-100 μ m diameter fraction) recovered from Tottuki Point. After SEM observations, individual AMMs were embedded in acetone-soluble resin on a 6 mm diameter glass plate. Quantitative elemental analysis was performed by EPMA. Oxygen isotopes and REE abundances were determined with a Cameca 6f ion microprobe at Kyushu Univ. according to the procedure stated in [6, 7]. Applied ion beam diameters are 10 and 20 μ m for oxygen and REE analyses, respectively. After these analyses, each AMM was separated from the resin with acetone, and washed with ethanol and de-ionized water. After weighing, noble gas compositions were determined with a noble gas mass spectrometer at Kyushu Univ. Samples wrapped with Ni and Al foils were pre-heated at \sim 100 $^{\circ}$ C and heated stepwise at 200, 800, 1300 and 1800 $^{\circ}$ C. The gas extraction was performed with a new W-heater designed for stepped heating of small samples, such as individual MMs and chondrules. The noble gas analysis is now in progress. For the present, analyzed are 7 AMMs including 3 coarse-grained MMs.

Results and Discussion:

Three (T6L7, T6N8 and T7C6) of 14 AMMs analyzed were a cgMMs. The others are 5 fgMMs and 6 scoriaceous MMs. Here we make mention only of the 3 cgMMs.

The appearance of T6L7 is irregular and rough (Fig. 1). This MM consists of olivine and mesostasis glass. The olivine composition is

FeO=16, MnO=0.5 and Cr₂O₃=0.1 wt%. The mesostasis composition is SiO₂=55, Al₂O₃=5, CaO=3 and FeO=14 wt%. Though oxygen compositions of twice analyses are a little bit scattered, they are plotted on along the CCAM line (Fig. 2). These suggest that this MM is a fragment of a C-chondrite chondrule.

T6N8 consists of a quasi-spherical olivine grain coated with igneous rim (Fig. 1). Opaque grains (probably Fe-Ni metal and FeS) are present within the olivine. The olivine composition is within the range of those of chondrule olivines in carbonaceous chondrites: FeO, MnO and Cr₂O₃ are 2.7, 0.2 and 0.7 wt%, respectively. The chemical composition and the presence of opaque minerals indicate that the heating event producing the olivine grain has occurred under low oxygen fugacity. In contrast, the texture of igneous rim resembles to that reported in [5] and could be resulted from heating during atmospheric entry. The oxygen isotope composition of T6N8 is plotted on the CCAM line and essentially identical to those of C-chondrite chondrules (Fig. 2). Hence it is plausible that this MM is also fragment of a C-chondrite chondrule.

T7C6 appears to be a single olivine grain. The chemical composition (FeO=35, MnO=0.6 and Cr₂O₃<0.1 wt%) is similar to those of ordinary chondrite chondrules. Also, oxygen composition is plotted above the TF line (Fig. 2). These features are consistent with that T7C6 originated from the O-chondrite parent body.

Our noble gas analyses revealed that these 3 cgMMs contain solar He and Ne. This confirms that these particles are extraterrestrial and were exposed to solar wind as small bodies (< a few mm) after ejection from their parent bodies. Isotopic ratios of ²¹Ne/²²Ne for T6N8 and T7C6 show no excess of cosmogenic ²¹Ne (0.030 and 0.032, respectively). T6L7 shows slightly higher ²¹Ne/²²Ne of 0.036 compared to SEPs (0.032 [8]), but the excess ²¹Ne content corresponds to <1 Ma exposure with assumption of GCR+SCR exposure at 1AU [9]. Hence, the 3 cgMMs studied in this study are possibly asteroidal origin. Oxygen isotopes and mineral chemistries suggest that T7C6 comes from a parent body similar to those of O-chondrites, while the others come from the C-chondrite parent body (bodies).

REE abundance of T6L7 is basically solar, i.e. similar to those of CI-chondrites. This is reasonable because the REEs come from both of olivine and mesostasis due to larger O' beam diameter relative to the grain size of T6L7. For T6N8 and T7C6 we could obtain REE abundances of a single olivine

phase. T7C6 contains less amount of REEs than T6N8. The pattern of T7C6 is heavy-REE enriched, whereas that of T6N8 is not clearly enriched in heavy REEs. These differences might be due to prolonged heating on the parent body of T7C6.

References:

[1] Kurat G. et al. (1994) *GCA*, 58, 3879–3904. [2] Genge M. J. et al. (1997) *GCA*, 61, 5149–5162. [3] Engrand C. and Maurette M. (1998) *Meteorit. Planet. Sci.* 33, 773–786. [4] Kurat G. et al. (1996) *Meteorit. Planet. Sci.* 31, A75. [5] Genge M. J. et al. (2005) *Meteorit. Planet. Sci.* 40, 225–238. [6] Okazaki R. and Nakamura T. (2006) *LPS XXXVII*, #1510. [7] Okazaki R. and Nakamura T. (2005) *Antarct. Meteorit.*, XXIX, 63–64. [8] Benkert J. -P. et al. (1993) *JGR*, 98, 13147–13162. [9] Olinger C. T. et al. (1990) *EPSL*, 100, 77–93. [10] Engrand C. et al. (1999) *GCA*, 63, 2623–2636. [11] Gounelle M. et al. (2005) *Meteorit. Planet. Sci.* 40, 917–932. [12] Rowe M. W. et al. (1994) *GCA*, 58, 5341–6347. [13] Clayton R. N. and Mayeda T. K. (1984) *EPSL*, 67, 151–161. [14] Clayton R. N. (1993) *Ann. Rev. Earth Sci.*, 21, 115–149.

Acknowledgment:

We thank NIPR for providing AMMs, and K. Shimada for assistance with the electron microprobe analysis. This work is supported by “Grant-in-Aid for Young Scientists (B) (#17740359)” of Japan Society for the Promotion of Science to RO.

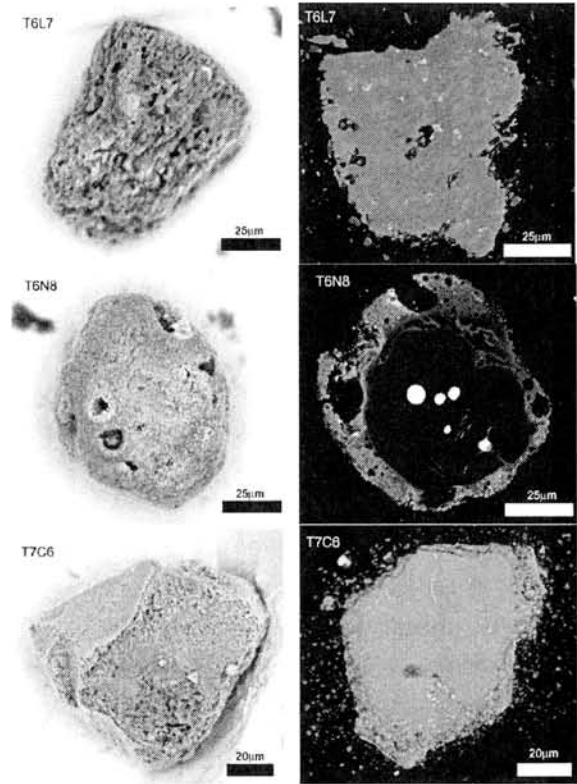


Fig. 1. BSE images of coarse-grained AMMs.

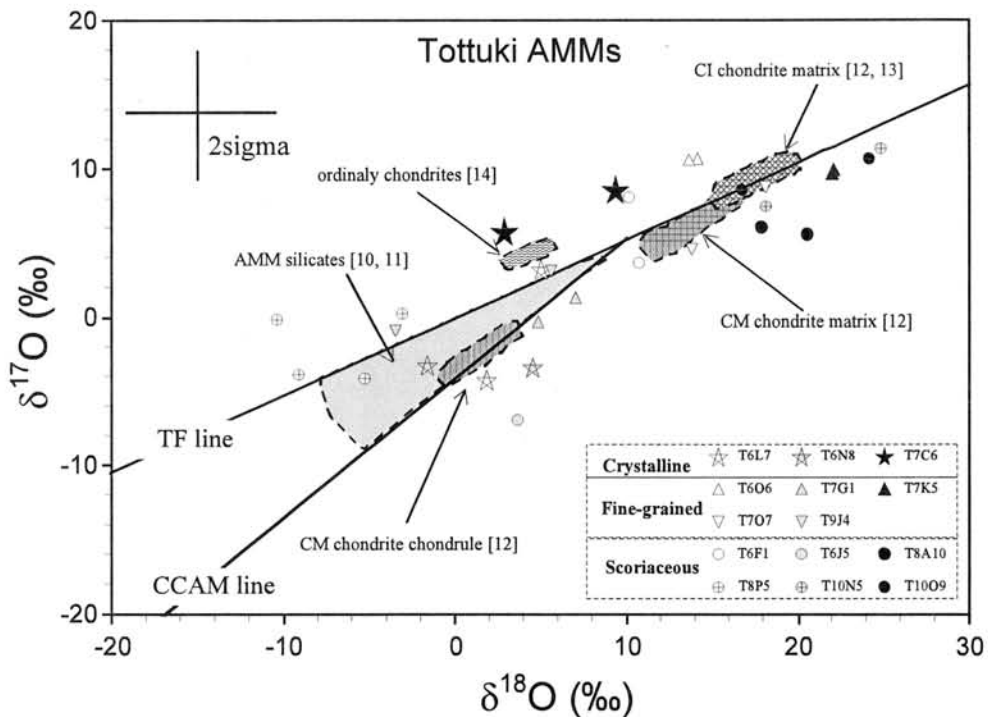


Fig. 2. Oxygen isotopic compositions of AMMs.

Cathodoluminescence and micro-Raman analyses of planar deformation features in shocked quartz from impact craters.

T. Okumura¹(okumura@rins.ous.ac.jp), A. Gucsik², H. Nishido¹, K. Ninagawa³ and M. Sakamoto⁴, ¹Research Institute of Natural Sciences, Okayama University of Science, Okayama, Japan; ²Max Planck Institute for Chemistry, Department of Geochemistry, Mainz, Germany; ³Department of Applied Physics, Okayama University of Science, Okayama, Japan; ⁴Shimohisakata Elementary School, Nagano, Japan.

Introduction:

Cathodoluminescence (CL) analysis provides us useful information on an existence of trace elements in minerals as well as lattice defects. Micro-Raman analysis is a technique that provides vibrational information on crystal structure for microscopic area. To characterize shock-induced planar microstructures such as Planar Deformation Features (PDFs) and Planar Fractures (PF) in quartz from various impact craters, we used a combination of CL and micro-Raman spectroscopy with high sensitivity and high spatial resolution.

Samples and methods:

Quartz grains from Ries Crater, Germany, Barringer Meteor Crater, USA and Oikeyama structure, Japan are used for micro-Raman and CL measurements. They were prepared as polished thin sections using a non-luminescent epoxy resin. PDFs are observed in several quartz grains from these sampling sites under a petrographic microscope. CL imaging and spectral measurements were carried out on a SEM-CL (Scanning Electron Microscope combined with a grating monochromator) with an accelerating voltage of 15 kV. Raman spectra were acquired with a confocal micro-Raman spectrometer at 20 mW using a Nd:YAG laser (532 nm) excitation system.

Results and discussion:

SEM-CL imaging of quartz grains from each crater shows non-luminescent or CL-dark lines related to PDFs, which can be clearly observed under a polarized microscope (Fig. 1). Boggs et al. [1] revealed striped CL images in shocked quartz from the Ries Crater. CL spectra of quartz grains exhibit two broad peaks at around 450 and 630 nm, which are attributed to lattice defect or self-trapped excitons (STE) and non-bridging oxygen hole centers (NBOHC), respectively. Their CL intensities are relatively weak by comparison with unshocked quartz.

Raman spectra of shocked quartz from the Ries Crater exhibit a pronounced peak at around 459 cm^{-1} , which can be assigned to Si-O-Si stretching vibration, whereas unshocked quartz has a sharp and intense peak at 464 cm^{-1} . This frequency shift may arise from a distortion of the structural configuration (i.e., formation of high density silica) caused by shock-metamorphism. The Raman imaging of shocked quartz from each impact crater shows a

stripe pattern suggesting layers comprised of high and low crystalline parts corresponding to the optical image of PDFs.

The results show that shock metamorphism might result in an alteration of electronic transition processes in defect centers that are correlated to CL emission.

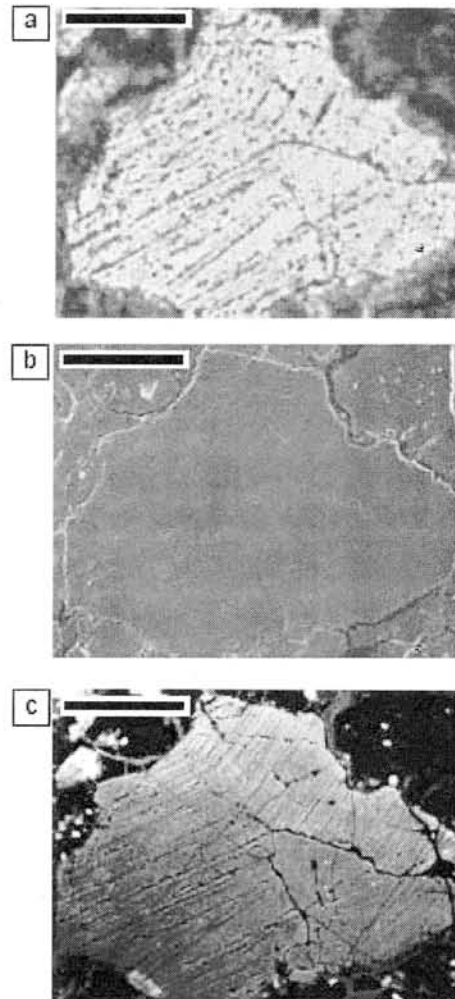


Figure. 1. Optical image of shocked quartz grain from the Ries Crater displaying multiple sets of PDFs and PF (a). Secondary electron image (b) and SEM-CL image (c) of the same grain. Scale bars indicate 100 micrometers.

Reference:

[1] Boggs Jr. S. et al. (2001) *Meteorit. Planet. Sci.*, 36, 783-791.

COMPARATIVE STUDY OF NEAR- AND FAR-SIDE LUNAR SOILS: TOWARD THE UNDERSTANDING EARLY EVOLUTION OF THE EARTH. Minoru Ozima¹, Qing-zhu Yin², Frank Podosek³, and Yayoi Miura⁴. ¹Graduate School of Earth and Planetary Science, University of Tokyo, Tokyo 113-0033, Japan (EZZ03651@nifty.ne.jp), ²Department of Geology, University of California, Davis, One Shields Avenue, Davis, CA 95616, USA, ³Department of Earth and Planetary Sciences, Washington University, St. Louis, MO 63130. USA, Earthquake Research Institute, University of Tokyo, 113-0032, Tokyo .

Introduction: Because of the almost total lack of geological record on the Earth for the time before 4 Ga, the history of the Earth during this period is still enigmatic. We propose that a comparative study of far- and near-side lunar soil would shed new light on this dark age of the Earth history.

Due to a strong dynamic coupling between the Earth and the Moon, theoretical studies of Earth-Moon dynamics have concluded that the Earth has been facing only to the near-side of the Moon since the formation of the Earth-Moon system about 4.5 billion year ago [e.g.1]. Also, theories have suggested that due to tidal energy dissipation, the Moon has been receding from the Earth. Recent theoretical studies concluded that the distance between the Earth and the Moon was about a half of the present distance about 4 Ga ago [2]. From these studies we infer that there may have been substantial interaction between the Earth through the atmosphere and the near-side lunar surface, especially in ancient time, whereas the far-side has remained essentially intact to the terrestrial atmospheric influence. Therefore, we suggest that the comparison of the far-side and near-side surface samples may impose unparalleled constraints on the evolution of the Earth such as the onset of the geomagnetic field, the evolution of a biotic oxygen atmosphere, and above all the dynamic evolution of the Earth-Moon system, a long standing fundamental problem, which has been strongly suggested by theoretical

studies, but still requires observational confirmation.

Objectives: By analyzing isotopic ratios and elemental abundances of volatile elements (O, N, light noble gases) implanted on lunar mineral grains (preferably ilmenite grains and metallic particles for higher retentivity of these elements), we may tackle the following fundamental problems.

When did the geomagnetic field (GMF) first appear? Heber et al. [3] observed anomalous noble gas and nitrogen isotopic compositions in Apollo lunar ilmenites, which are quite different from the generally assumed solar components. Heber et al. [3] concluded that the anomalous isotopic composition could not be attributed to nuclear processes in the Sun, but was likely to be due to some fractionation during implantation process. However, Ozima et al. [4] showed that the isotopic compositions were attributable to the mixing of the Solar components with terrestrial atmospheric components. They suggested that the terrestrial components have been transported from the Earth and implanted on lunar soils during the period when the Earth had not fully developed the GMF (a non-magnetic Earth). Therefore, if their interpretation were correct, the youngest age of ilmenite grains which show terrestrial isotopic signature in N and light noble gases would impose a crucial constraint on the onset time of the GMF.

When did the biotic oxygen atmosphere form?

Recently, Ireland et al.[5] reported oxygen implanted in lunar metal particles, which were mass-independently positively fractionated relative to the mean terrestrial oxygen. Since the isotopic ratio of this exotic oxygen is very close to oxygen in the terrestrial ozone layer, Ozima et al.[6] raised the possibility that oxygen fractionated in the Earth's upper atmosphere was transported to the Moon. The speculation is based on the observation that the oxygen flux escaping from the Earth can account for the amount of the mass-independently fractionated oxygen implanted in the lunar metal particles [7]. Therefore, if the ozone-layer like oxygen (mass independently and positively fractionated) are shown to constitute the major oxygen in the Earth Wind (EW), the oldest record of this exotic oxygen would constrain the initiation of the biotic Earth atmosphere. Currently observations are limited only to minor components such as O₃ and CO₂ in the middle atmosphere [8, 9], and hence the direct observation of oxygen isotopic composition in the EW is crucial in testing our proposal. This issue is also directly relevant to the problem of the origin of life in the Earth.

Have the day length and the Moon-Earth distance changed in geological time?

If the Moon has been receding from the Earth due to tidal energy dissipation as concluded by an Earth-Moon dynamic theory, we expect that the day length of the Earth should also have increased accordingly. To confirm the day length change in geological time has been a quest of Earth scientists over centuries, but a large number of studies of potential geological records such as the number of growth lines in coral has not so far been conclusive.

We propose that a firm constraint can be imposed on this intriguing problems from the following studies. (a) We can identify the time when identical periods of rotation (Earth) and revolution (Moon) had taken place from the last appearance of terrestrial components in far-side soils. (b) We would expect a systematic decrease of terrestrial volatile components on the near-side soils, if the Earth-Moon distance has been increasing. Answers to these questions would add observational confirmation to the theory on the Earth-Moon dynamic system for the first time.

Methods: To tackle the above objectives, we need (i) systematic sampling of lunar soils both in the near- and far-side of the Moon, (ii) precise isotopic and elemental analyses of volatile elements such as N, O, light noble gases implanted in lunar soil minerals, and (iii) determination of surface exposure age of an individual mineral grain. We will discuss each issue below.

- (i) Sampling: Sampling of lunar soils in a continuous vertical section of a few meter depths both from far- and near-side sites is required.
- (ii) Elemental and isotopic analyses: The currently available experimental facility such as SIMS, ultra-high vacuum noble gas MS are quite satisfactory to carry out this requirement.
- (iii) Surface exposure age of grains: We have a good reason [4] to believe that the surface exposure time of individual mineral grain is reasonably approximated by the time when a grain was first disintegrated from a bulk host rock. The latter event is very likely to have been caused by major impact event near the sampling site [10], and the disintegration time of an ilmenite grain from a host rock may reasonably be assigned to the age of impact melt minerals at the site. Therefore, by ⁴⁰Ar-³⁹Ar dating of impact melt minerals at or

near a sampling site, we may infer the surface exposure time of an ilmenite grain.

In addition to this method, the direct application of ^{40}Ar - ^{39}Ar dating to an ilmenite grain with a very carefully controlled step-heating procedure may enable us to resolve the disintegration time of ilmenite grains from their host rock.

Conclusions: Comparative study of lunar soils from near- and far-side of the moon will yield new insight on some of the most fundamental problems in Earth and planetary sciences such as the first appearance of the geomagnetic field, the evolution of oxygen in the atmosphere, and the dynamical evolution of the Earth-Moon system. Apart from the sampling from the far-side, all the objectives can be carried out with currently available experimental techniques.

References: [1] Murray C.D. and Dermott S.F. (1999) *Solar System Dynamics*, Cambridge Univ. Press, Cambridge. [2] Abe M. and Ooe M. (2001) *J. Geodetic Soc. Japan*, 47, 514-520. Bills B.G. and Ray R.D. (1999) *Geophysical Res. Lett.* 26, 3045-3048. [3] Heber V. et al. (2003) *Astrophys. J.* 597, 602-614. [4] Ozima M. et al. (2005), *Nature* 436, 655-659. [5] Ireland T.R. et al. (2006) *Nature* 440, 775-778. [6] Ozima M. et al (2007) LPSC XXXII (submitted). [7] Seki H. et al. (2001) *Science* 291, 1939-1941. [8] Boering et al. (2004), *Geophysical Res. Letters*, 31, LO3109. [9] Thiemens M.H. (2006), *Ann. Rev. Earth Planet. Sci.*, 34, 217-262. [10] Dalrymple B. and Ryder G. (1996) *J. Geophys. Res.* 101, 26069-26084.

Early differentiation of Mars: constraints from siderophile elements and oxygen fugacity. K. Righter¹, ¹NASA Johnson Space Center, Mailcode KT, 2101 NASA Parkway, Houston, TX, USA 77058.

Introduction:

Siderophile element concentrations in planetary mantles can provide important constraints on the conditions of core formation and differentiation in terrestrial planets [1]. Martian meteorites (>40 now) and spacecraft data (e.g., MER) are used to reconstruct mantle siderophile element concentrations for Mars. Results are used to re-assess the conditions of metal-silicate equilibrium in Mars, especially in light of geophysical modeling [6,7]. The conditions under which these concentrations can be set are then compared to the range of conditions proposed for the martian mantle subsequent to the formation of Mars.

Elements considered:

Compatible: Ni, Co, and to a lesser extent V are all compatible in olivine and chromite and thus are affected by magmatic fractionation. As a result, concentrations of Ni and Co in the mantle are strongly correlated with MgO and FeO [8,9]. Concentrations of V are correlated with Ti or Al, the former being preferred for Mars due to uncertainties with Al regarding garnet fractionation [9]. New data from shergottites as well as MER rovers define a Ni depletion (relative to chondrites) of approximately 150-200 depending upon the mantle composition (Fig. 1). Similar trends for Co and MgO+FeO define a Co depletion of 50; V and Ti trends define a V depletion of ~1 [9].

Incompatible: Many elements are incompatible during melting of a metal-free mantle, and when coupled with a refractory lithophile element of equal incompatibility, can be used to estimate mantle concentrations. Previous studies have shown similar incompatibility for the following siderophile – refractory lithophile element pairs: Mo-Pr, W-La, P-Ti, and Ga-Al. New data for shergottites define depletions for Mo of ~20, for P of ~3, and for Ga and W of ~5 (Fig. 2).

Results of metal-silicate modelling:

Metal-silicate partition coefficients for all of these elements have been parameterized using existing experimental data (see summary of [10]), and equations of the form:

$$\ln D = a \ln fO_2 + b/T + cP/T + d(nbo/t) + e \ln(1-X_S) + f.$$

Although there are some questions still about the magnitude of temperature effects (e.g., for Ni; [11]) or the valence of W ([12]), these expressions provide useful constraints on the conditions prevailing during core formation. For Mars, a few of the variables can be fixed with some certainty [4], such as core size (21 %), silicate melt composition ($nbo/t = 2.7$ for peridotite), core sulfur content ($X_S = 0.07$), and

oxygen fugacity ($\Delta IW = -1$), leaving pressure (P) and temperature (T) as the remaining variables. Varying P and T results in fits to the estimated depletions for Ni, Co, V, Mo, W, P, and Ga, at 8.0 GPa and 1625 °C (Fig. 3). This relatively low PT result is similar to previous assessments [2,3,4], indicating a much shallower and cooler magma ocean on early Mars. This is consistent with data that suggest the preservation of geochemical anomalies in the martian mantle [13], but at odds with some modelling assumptions of a completely molten early martian mantle [6, 14]. The depletion of Ni in Earth and Mars are different by a factor of 10. High Ni contents in the terrestrial mantle have been ascribed to an early hot magma ocean. If thermal modelling and assessments point towards a hot early Mars, we must explain why Earth and Mars have totally different siderophile element signatures (esp. Ni).

Oxygen fugacity in the martian mantle:

Calculations of fO_2 in the martian meteorites result in a 5 log fO_2 unit range in values relative to the FMQ buffer (Fig. 4). If graphite is present in a planetary mantle, the effect of pressure on C-CO-CO₂-CH₄ equilibria is such that oxygen fugacity would become very high as pressure increases. Given the range of fO_2 estimates for martian meteorites demonstrated in Figure 4, it is worthwhile considering whether this could be achieved by polybaric C-CO-CO₂-CH₄ equilibria in the martian mantle. Only 40-80 ppm C is required to keep peridotite mantle buffered at the C-O surface [25]. Indeed, studies of martian meteorites have shown that Mars is a volatile-rich planet, and C may be an important constituent of the volatile budget [26-28]. If C buffering at variable pressure is controlling oxygen fugacity in the martian mantle, it would require formation of ALH84001 at lowest pressures, shergottites at intermediate pressures, and nakhlite and Chassigny parent melt formation at high pressures, all of which is consistent with what we know.

Carbon buffering is thus a simpler explanation for oxygen fugacity variations in the martian mantle and crust, than by hydrous reservoirs [29] or by crustal assimilation [30]. Furthermore, a small activity of CH₄ would be associated with a C-CO-CO₂-CH₄ gas in the martian mantle, and degassing of this species could account for the small amount of methane detected recently at the surface of Mars [31-33].

References: [1] Wanke, H. (1981) *Phil. Trans. Roy. Soc. Lon. Ser. A*, 303, 287-302. [2] Treiman, A.H. et

al. (1987) *Proc. 17th LPSC*, pt. 2, *JGR* 92, E627-E632. [3] Dreibus, G. and Wanke, H. (1985) *Meteoritics* 20, 367-381. [4] Righter, K. et al. (1998) *GCA* 62, 2167-2177. [5] Mars Meteorite Compendium,

<http://curator.jsc.nasa.gov/antmet/mmc/index.cfm>;

compiled by C. Meyer. [6] Elkins-Tanton, L.T. et al. (2005) *EPSL* 236, 1-12. [7] Reese, C.C. and Solomatov, V.S. (2006) *Icarus* 184, 102-120. [8] Wanke, H. and Dreibus, G. (1986) in *Origin of the Moon* (Hartmann, Phillips, and Taylor, eds.), LPI, Houston, 649-672. [9] Righter, K. et al. (2006) *Amer. Mineral.* 91, 1643-56. [10] Righter, K. (2003) *AREPS* 31, 135-174 [11] Chabot, N.L. et al. (2004) *GCA* 69, 2141-2151. [12] Danielson, L.R. et al. (2007) *LPSC XXXVIII*, 2113. [13] Jones, J.H. et al. (2003) *MAPS* 38, 1807-1814. [14] Draper, D. and Borg, L.E. (2003) *MAPS* 38, 1713-1731. [15] Basaltic Volcanism Study Project (1981) Pergamon Press. [16] Newsom, H.E. (1995) AGU Geophysical Handbook Series. [17] Rieder, R. et al. (2004) *Science* 306, 1746-1748. [18] Gellert, R. et al. (2004) *Science* 305, 829-832. [19] Newsom et al. (1996) *GCA* 60, 1155-1168. [20] Jagoutz, E. et al. (1979) *PLPSC 10th*, 2031-2050. [21] Boctor, N. Z. et al. (1976) *EPSL* 32, 69-76. [22] Bunch, T.E. and Reid, A.M. (1975) *Meteoritics* 10, 303-311. [23] Wadhwa, M. (2001) *Science* 291, 1527-1531. [24] McCanta, M.C. et al. (2004) *GCA* 68, 1943-1952. [25] Holloway, J.R. (1998) *Chem. Geol.* 147, 89-97. [26] Dreibus, G. and Wanke, H. (1985) *Meteoritics* 20, 367-381. [27] Wright, I.P. et al. (1986) *GCA* 50, 983-991. [28] Grady, M.M. et al. (2004) *Int. Jour. Astrobiology* 3, 117-124. [29] Herd, C.D.K. et al. (2002) *GCA* 66, 2025-2036. [30] Jones, J.H. (2003) *MAPS* 38, 1807-1814. [31] Formisano, V. et al. (2004) *Science* 306, 1758-1761. [32] Krasnopolsky, V.A. et al. (2004) *Div. Planet. Sci.* #26.03. [33] Mumma, M.J. et al. (2004) *Div. Planet. Sci.* #26.02. [34] Szymanski, A. et al. (2003) *LPS XXXIV*, #1922. [35] Delaney, J.S. and Dyar, M.D. (2001) *MAPS* 36, A48.

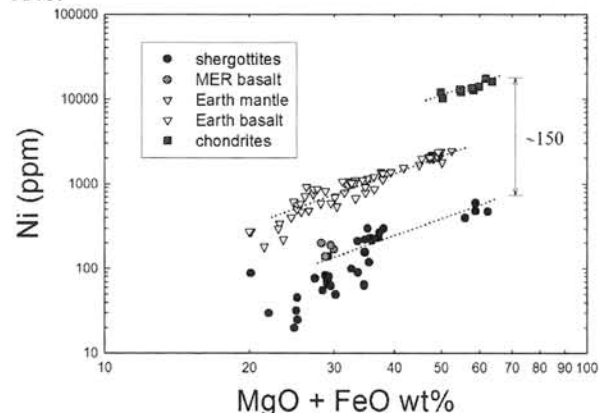


Figure 1: Ni-(MgO+FeO) trends defining depletions for the martian mantle. Data are from [15-18] and references compiled by [5].

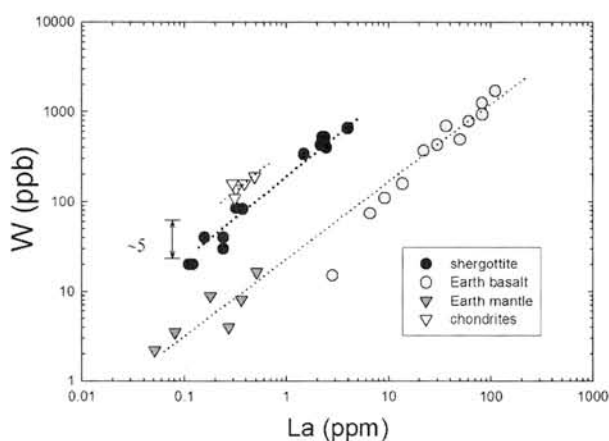


Figure 2: W-La trends defining a small depletion of W in the martian mantle, relative to chondrites. Note the small depletion compared to that defined by terrestrial samples. Data are from [16, 19, 20] and references compiled by [5].

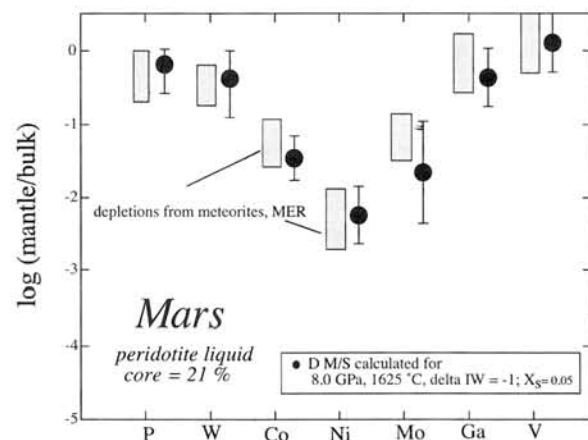


Figure 3: Comparison of calculated (shaded boxes) vs. observed depletions for Mars showing the best fit to all elements at conditions of 8 GPa and 1625 °C.

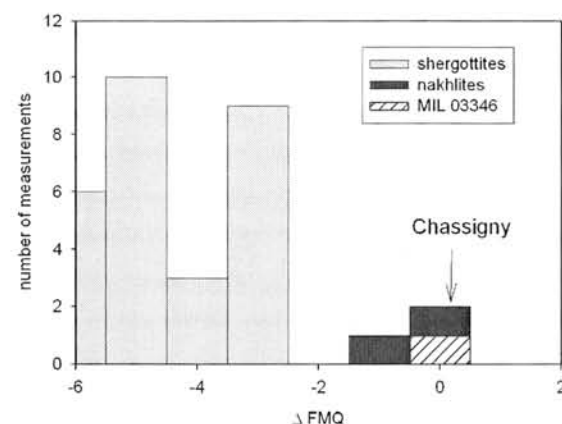


Figure 4: Summary of fO_2 determinations for martian meteorites, relative to the fayalite-magnetite-quartz (FMQ) oxygen buffer. Shergottite values from 23, 24, 26, 29, and nakhlite and Chassigny values from 21, 22, 34, 35, and this study.

Chemical composition of lherzolithic shergottites Yamato 000097. N. Shirai¹ and M. Ebihara^{1, 2}, ¹Department of Chemistry, Tokyo Metropolitan University, Hachioji, Tokyo 193-0397, Japan (shirai@comp.metro-u.ac.jp). ²National Institute of Polar Research, Tokyo 173-8515, Japan.

Introduction:

Recently, a lot of Martian meteorites were found in cold and hot deserts. Most of the Martian meteorites found in cold and hot deserts are classified to be shergottites. Among them, lherzolithic shergottites are the least abundant, followed by basaltic shergottites and olivine-phyric shergottites. According to petrographic features and oxygen isotopic compositions, Yamato (Y) 000097 (and its pairs, Y 000027 and Y 000047) is classified as the eighth lherzolithic shergottites [1], to which ALHA 77005, LEW 88516, Y 793605, GRV 99027, Grove Mountains 020090, NWA 1950 and NWA 2646 also belong. Because lherzolithic shergottites are mostly composed of two textures (poikilitic and non-poikilitic), lherzolithic shergottites have large variations in modal abundances of constituent minerals and bulk chemical compositions [2]. As a part of consortium study, we analyzed an aliquant of the 2g Y 000097 powder.

Analytical Methods:

A total of 195mg of the powdered specimen of Y 000097 (numbered as Y 000097,21-1) was allocated to us from the National Institute of Polar Research (NIPR). This sample was taken from a 1.985g powder of Y 000097,21-0, which was prepared by grinding its chunks in an agate mortar at NIPR. The sample was first analyzed by prompt gamma-ray analysis (PGA), which was followed by instrumental neutron activation analysis (INAA) and instrumental photon activation analysis (IPAA).

Results:

Differentiated planetary bodies have undergone their own differentiation histories and thereby have characteristic chemical compositions in their silicate layers. Ratios of FeO/MnO (39.3), Ni/Mg (0.00186), Cr/Mg (0.0397), Co/(MgO + FeO) (0.000145), Na₂O/Al₂O₃ (0.182), TiO₂/Al₂O₃ (0.169), Na₂O/TiO₂ (1.07) and K/La (784) for Y 000097 are all fall within their corresponding ranges for Martian meteorites. This confirms that Y 000097 is a new Martian meteorite, being consistent with the result of oxygen isotopic compositions [1].

Major element abundances are utilized for classifying Martian meteorites into different subgroups. Among them, Al, Mg and Ca abundances are found to characteristically vary among Martian meteorites. Ca/Si and Mg/Si ratios for Martian meteorites are shown in Fig. 1. Apparently, Y 000097 fall within the area of lherzolithic shergottites, which is consistent with the petrographical

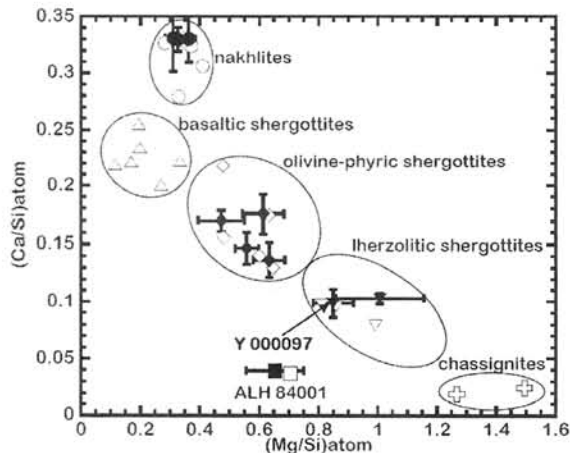


Fig. 1. (Mg/Si)atom vs. (Ca/Si)atom diagram for Martian meteorites. Solid and open symbols represent our data (unpublished values) and literature values, respectively.

observations [1].

The Mg number (molar Mg/(Mg+Fe) ratios) for basaltic shergottites, lherzolithic shergottites and olivine-phyric shergottites are 0.23-0.55, 0.67-0.73 and 0.55-0.68, respectively. It is observed that lherzolithic shergottites have a smaller range of the Mg number than those for basaltic shergottites and lherzolithic shergottites. Based on the Mg number, basaltic shergottites and olivine-phyric shergottites are divided into several subgroups. The Mg number of Y 000097 is 0.70, which is essentially the same as those of ALHA 77005 (0.69-0.73), LEW 88516 (0.67-0.71) and Y 793605 (0.69-0.73) [2].

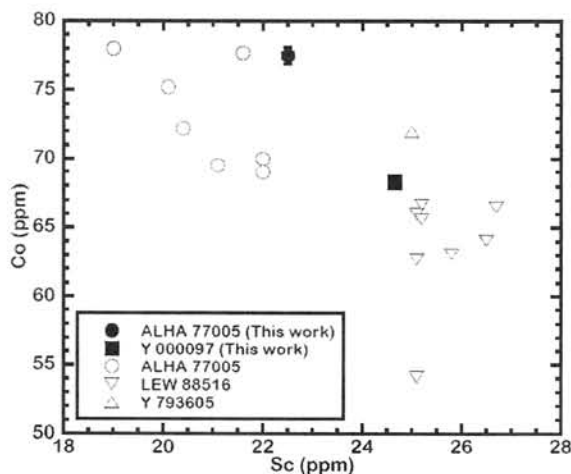


Fig. 2. Sc vs. Co abundances for lherzolithic shergottites. Solid and open symbols are the same as those in Fig. 1.

Sc and Co abundances for lherzolithic shergottites are plotted in Fig. 2. From this figure, lherzolithic shergottites can be divided into two

groups of ALHA 77005, and LEW 88516, Y 793605 and Y 000097. The differences among ALHA 77005, LEW 88516 and Y 793605 can be attributed to modal abundances of olivine and pyroxene, considering that Co is mostly hosted by olivine, while Sc is partitioned in pyroxene. In fact, a olivine/pyroxene ratio of ALHA 77005 is higher than those of LEW 88516 and Y 793605 [3, 4]. Y 000097 is similar to LEW 88516 and Y 793605 rather than ALHA 77005 in Co and Sc abundances.

As lherzolitic shergottites are heterogeneous in chemical compositions, mean values for individual meteorites [e.g. 5] must be informative for scientific discussions. It is well known that lithophile element abundances for lherzolitic shergottites largely vary due to heterogeneous distribution of non-poikilitic. For Y 793605, we calculated the average lithophile element values using literature data [6, 7, 8, 9]. CI-normalized lithophile element abundances for lherzolitic shergottites are showed in Fig. 3, where Y 000097 falls within the range for lherzolitic shergottites. Lherzolitic shergottites have essentially the same CI-normalized abundances except for Na, Al, Sr, Y, Zr and Hf. Na, Al and Sr abundances of Y 000097 are similar to those of Y 793605 and are lower than those of the other lherzolitic shergottites (ALHA 77005, LEW 88516 and NWA 1950). Although lherzolitic shergottites have large variations of Zr and Hf abundances, their ratios are constant. A Zr/Hf ratio of Y 000097 (26.5 ± 2.0) is subchondritic, which is in agreement with that of our unpublished value of ALHA 77005 (24.8 ± 1.8). Our Zr/Hf ratios of ALHA 77005 and Y 000097 are similar to those of olivine-phyric shergottites (Y 980459, DaG 476, SaU 005 and EETA 79001A), which have the lowest Zr/Hf ratios among shergottites [10].

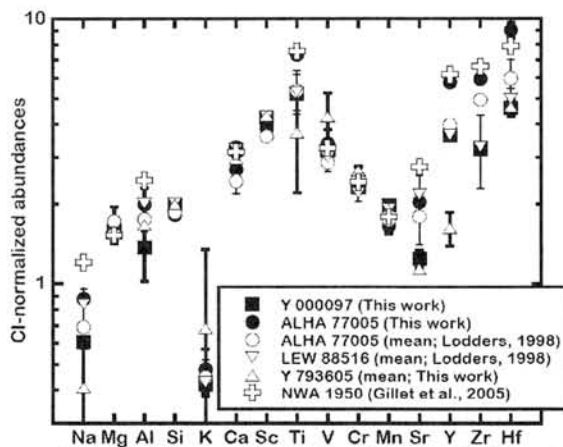


Fig. 3. CI-normalized abundances of lithophile elements for lherzolitic shergottites. Lithophile element abundances of Y 793605 are calculated from literature values [6, 7, 8, 9]. Thick and thin error bar correspond to our data and literature values, respectively.

CI chondrite-normalized abundances of rare earth elements (REEs) for lherzolitic shergottites are illustrated in Fig. 4. Light-REEs (LREEs) of Y 000097 are considerably depleted. Their REEs abundances are steeply increased towards the middle-REEs (MREEs) with a peak at Tb and are decreased towards the heavy-REEs (HREEs). The degree of depletion of LREEs in Y 000097 is different from those of basaltic shergottites and olivine-phyric shergottites, while the degree of depletion from MREEs to HREEs is similar to those of basaltic shergottites and olivine-phyric shergottites [2]. Although REE abundances significantly vary in lherzolitic shergottites, their REE abundance patterns are very similar, suggesting a close genetic linkage among lherzolitic shergottites.

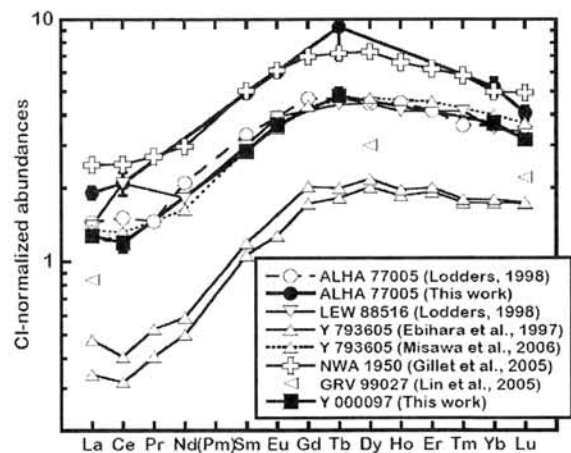


Fig. 4. CI chondrite-normalized REE abundances for lherzolitic shergottites.

References:

- [1] Meteorite Newsletter 14, No. 1 (2006).
- [2] Meyer C. (2006) Mars Meteorite Compendium.
- [3] Treiman A. H. et al. (1994) *Geochim. Cosmochim. Acta*, 29, 581-592.
- [4] Kojima H. et al. (1997) *Antarct. Meteorite Res.*, 10, 3-12.
- [5] Lodders K. (1998) *Meteorit. Planet. Sci.*, 33, A183-A190.
- [6] Ebihara M. et al. (1997) *Antarct. Meteorite Res.*, 10, 83-94.
- [7] Nishiizumi K. and Caffee M.W. (1997) *Antarct. Meteorites XXII*. Tokyo, Natl Inst. Polar Res., 149-151.
- [8] Warren P. H. and Kallemeyn G. W. (1997) *Antarct. Meteorite Res.*, 10, 61-81.
- [9] Misawa K. et al. (2006) *Antarct. Meteorite Res.*, 19, 45-57.
- [10] Shirai N. and Ebihara M. (2006) *LPSC XXXVII*, 1917.

Infrared and Raman spectroscopy of Antarctic micrometeorites.

A. Suzuki¹, S. Nakashima¹ and T. Nakamura²

¹ Department of Earth and Space Science, Osaka University, 1-1 Machikaneyama, Toyonaka Osaka, 560-0043, Japan, (akiko.s@ess.sci.osaka-u.ac.jp),

² Department of Earth and Planetary Science, Kyushu University, Hakozaki, Fukuoka, 812-8581, Japan.

Introduction:

Micrometeorites are expected to be the major source of the C flux from extraterrestrial materials delivered to the earth and might represent a major contribution to the pre-biotic organic matter on the early earth [1]. On the other hand, organics from carbaceous chondrites have been characterized non-destructively by means of Raman [2,3] and Fourier Transform Infra Red (FTIR) [3] microspectroscopies

In this study, we measured Raman and IR spectra of unmelted Antarctic micrometeorites (AMMs) for characterizing organic and hydrous components.

Samples:

The AMMs were collected at Kuwagata point around Yamato mountain, near the Japanese Showa station [4]. We chose unmelted AMMs which are the least heated fractions. These particles were already picked up from particles recovered from glacier ice. After SEM-EDX analyses, micrometeorites were removed from the copper plate and were slightly pressed between two Al-foils for both Raman and IR spectroscopies.

Methods:

We analyzed Raman and IR spectra of 11 Antarctic micrometeorite (AMM) particles.

Raman microspectroscopy: 73 points in 11 particles were analyzed. Peak positions, full widths at half maximum (FWHM), band intensity ratios (I_D/I_G) and band area ratios ($A_D/A_{(D+G)}$ (%)) for D (diamond: $\sim 1360\text{ cm}^{-1}$) and G (graphite: $\sim 1600\text{ cm}^{-1}$) bands were determined for the AMMs and compared with the literature data on carbonaceous chondrites and other cosmic materials.

IR microspectroscopy: Absorption spectra in the $4000 - 700\text{ cm}^{-1}$ range were collected on 11 grains at room temperature with a $400 \times 400\ \mu\text{m}$ aperture.

Results and Discussion:

Raman microspectroscopy:

The G band features: The peak position and FWHM of G band of the AMMs are ranging from 1581 to 1593 cm^{-1} and from 87 to 133 cm^{-1} , respectively (Fig. 1). These value ranges are almost the same as those for CM2 carbonaceous chondrites (Fig. 1).

The D band features: The peak position and FWHM of D band for the AMMs are from 1357 to

1379 cm^{-1} and from 166 to 271 cm^{-1} , respectively. This region for the AMMs mostly overlaps with the region for CIIIs. The D peak position range of the AMMs is similar to those for CM2 and CR2 chondrites.

The intensity and area ratios: The I_D/I_G and $A_D/A_{(D+G)}$ (%) are ranging from 1.1 to 1.7 and from 65 to 78, respectively. These distributions of the AMMs are close to Orgueil carbonaceous chondrite (CII). $A_D/A_{(D+G)}$ band area ratios (%) of the AMMs are in the similar range to those for CR2 and Tagish Lake carbonaceous chondrites.

These Raman features of macromolecular carbonaceous materials in the AMMs are similar to those in C1 and C2 chondrites. The AMMs studied here might have the aqueous alteration level higher than 2.

IR microspectroscopy: The IR spectra of these AMMs showed IR absorption peaks of molecular water (H_2O) at 3400 cm^{-1} , aliphatic carbonaceous components at 2960 cm^{-1} for CH_3 and 2925 cm^{-1} for CH_2 , and Si-O of silicates at 1050 cm^{-1} . By using peak height ratios of $\text{CH}_2/\text{Si-O}$ ($2925\text{ cm}^{-1}/1050\text{ cm}^{-1}$), $\text{H}_2\text{O}/\text{Si-O}$ ($3400\text{ cm}^{-1}/1050\text{ cm}^{-1}$) and CH_3/CH_2 ($2960\text{ cm}^{-1}/2925\text{ cm}^{-1}$), aliphatic and hydrous component characters of AMMs can be quantitatively investigated. The $\text{CH}_2/\text{Si-O}$, $\text{H}_2\text{O}/\text{Si-O}$ and CH_3/CH_2 ratios of AMMs are ranging $0.06 \sim 0.19$, $0.13 \sim 0.3$ and $0.5 \sim 1.2$, respectively (Fig. 2 and 3).

CH_2 and H_2O : The broad absorption band at 3400 cm^{-1} is mainly due to liquid-like molecular water [5]. The relative intensity of this band to Si-O is plotted against the $\text{CH}_2/\text{Si-O}$ in Fig. 2. AMMs show a positive relation in this diagram. Aliphatic CH_2 rich ones are richer in water.

CH_3/CH_2 vs H_2O : The CH_3/CH_2 ratio of AMMs is plotted against $\text{H}_2\text{O}/\text{Si-O}$ ratio in Fig. 3. The CH_3/CH_2 ratio showed a wide variation from 0.5 to 1.2. This ratio is smaller for longer straight chain aliphatic hydrocarbons (0.63 for C_{18} , 0.18 for C_{40}) (Fig. 3). Therefore, various types of aliphatics are present in AMMs with varying water contents.

Conclusions:

Raman features of carbonaceous components in the AMMs are similar to those in C1 and C2 chondrites, suggesting the aqueous alteration level higher than 2.

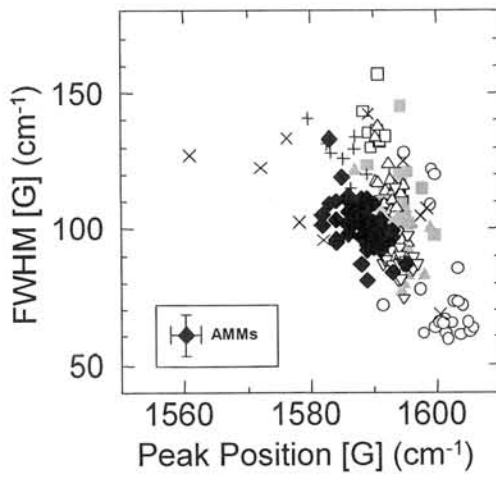
IR absorption peak height ratios of AMMs ($\text{CH}_2/\text{Si-O}$, $\text{H}_2\text{O}/\text{Si-O}$ and CH_3/CH_2 ratios) indicate that various types of aliphatics are present and

aliphatic CH₂ is richer for higher water contents.

These Raman and IR features can be used as indicators for organic evolution during the aqueous alteration.

References:

[1] Maurette M. (2006) *Micrometeorites and the Mysteries of Our Origins*. (Springer) [2] Raynal P. I. (2003) *Ph. D. Thesis, Université Peirre et Marie Curie, Paris, France* [3] Matrajt G. et al. (2004) *A&A*, 416, 983-990. [4] Yada T. and Kojima H. (2000) *Antarct. Meteorite Res.*, 13, 9-18. [5] Ito Y. and Nakashima S. (2002) *Chem. Geol*, 189, 1-18. [6] Quirico E. et al. (2005) *Planet. Space Sci*, 53, 1443-1448. [7] Sandford S. A. et al. (2006) *Science*, 314, 1720-1724.



- ◆ AMMs
- CI1s
- Orgueil
- △ CM2s
- ▲ CR2
- ▽ Tagish Lake
- CV3s
- × Stardust
- + IDPs

Fig. 1: The correlation diagrams of Raman parameters for G bands. FWHM vs. peak position of G band of the Antarctic micrometeorites (AMMs), carbonaceous chondrites, IDPs and Stardust samples. Data of carbonaceous chondrites from [2, 3], IDPs from [6] and Stardust from [7].

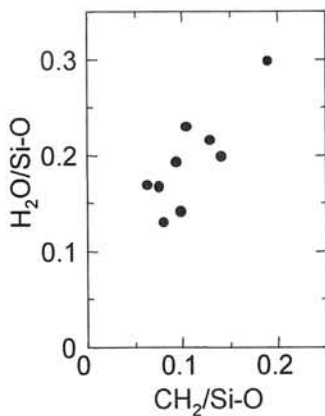


Fig. 2: The relation between CH₂ (2925 cm⁻¹) and H₂O (3400 cm⁻¹) IR peak heights relative to Si-O peak (1050 cm⁻¹) of AMMs.

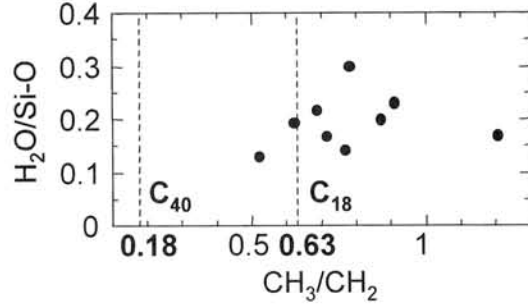


Fig. 3: The relation between CH₃ (2960 cm⁻¹)/CH₂ (2925 cm⁻¹) ratio and H₂O (3400 cm⁻¹)/Si-O (1050 cm⁻¹) ratio of AMMs. The CH₃/CH₂ ratios for C₁₈ and C₄₀ alkanes are also shown as dotted lines.

Feldspathic lunar meteorites from the farside and production of their lunar simulants.

H. Takeda¹, Y. Yazawa², T. Arai³, A. Yamaguchi³, M. Saito², T. Ishii⁴, M. Otsuki⁴ and H. Kanamori⁵, ¹Dept. of Earth and Planet. Sci., Univ. of Tokyo and Gendai GP, Chiba Inst. of Tech. (CIT), 2-17-1 Tsudanuma, Narashino, Chiba 275-0016, takeda.hiroshi@it-chiba.ac.jp, ²Dept. of Life and Envir. Sci., CIT, *Ibid*, ³Antarctic Meteorite Res. Center, National Inst. of Polar Res., ⁴Ocean Res. Inst., Univ. of Tokyo, and ⁵Inst. of Tech., Shimizu Corp., Japan.

Introduction:

We have tried to make lunar simulants for our future landing sites from some terrestrial rocks and mineral samples. Assuming that the site may be near the south-pole in the farside highland, we examined several lunar meteorites of the possible farside origin, to estimate compositional and mineralogical data of such area. Of the fifteen feldspathic lunar meteorite stones from Oman, Dhofar 489 [1], 309[2], 307, 908 [3] were selected for our preliminary mineralogical examinations. We also rely on published data for some of these stones [3] and other related stones of the farside origin, such as Y-86032 [4].

Samples and Experimental Methods:

One polished thin section 1.5 × 1.5 cm in size of a gabbro from Koyama, Yamaguchi Pref. has been prepared and was employed for mineralogical and petrographic studies. Elemental distribution maps of Si, Mg, Fe, Al, Ca, Ti and Cr were obtained by electron probe microanalysis (EPMA) at the Ocean Res. Inst. (ORI) of Univ. of Tokyo. Chemical compositions of minerals were analyzed by JEOL 733 EPMA at ORI.

Ca-rich plagioclase from Crystal Bay, Minn., and the Koyama gabbro were used for lunar stimulant productions. The gabbro samples were crushed and sieved. The powders between 250–500 microns were separated by heavy liquid with density 2.8 at ORI. The heavy liquid was prepared by dissolving sodium polytungstate Na₆(H₂W₁₂O₄₀)H₂O into water. A fraction lighter than density 2.8 was used as plagioclase, and that of heavier than 2.8 is enriched in mafic silicates, mainly olivine. The separates and bulk samples were analysed by X-ray fluorescent method. Dissolution of plagioclase has been performed at CIT by M. Saito et al. [5] under the guidance of Y. Yazawa.

Results:

Dhofar 489, the first lunar meteorite from the farside [1], contains magnesian anorthosites with An₉₆. The An contents of Dhofar 307, 309 and 908 distribute around the same range. Angular and subrounded clasts of troctolitic anorthosites and magnesian anorthosites are embedded in fine grained recrystallized, or devitrified impact melt glassy matrices. The clast types are different from one sample to others. We recognized two major clasts in Dhofar 309. One is magnesian anorthosite.

One common clast type in Dhofar 309 is a

reddish orange colored, angular fragment of crystalline rock with small angular fragments of twinned plagioclase [2]. The lithic texture of this clast, rounded small olivine crystals probably due to metamorphism, resembles those of some granulites, but elongated lath-shaped plagioclase crystals have more eucrite-like subophitic igneous texture.

The plagioclase laths show minor zonings (An 95.0-96.6). The mineral assemblage of this clast is similar to that of the spinel troctolite clast in Dhofar 489 [1]. Some clasts in Dhofar 307 are more like common granulites, but one clast is more coarse grained than common granulites and the texture is similar to the spinel troctolite in Dhofar 489 [1]. The Fo contents of olivine (Fo₈₃₋₈₈) in these troctolitic anorthosite clasts in Dhofar 307, 309 and 908 are similar to those of the Dhofar 489 spinel troctolite, but Fos of some olivine grains go up to 88. Minor pyroxene grains in the clasts (Ca₃Mg₈₆Fe₁₁ – Ca₉Mg₇₈Fe₁₁) are found with olivine grains and as isolated crystals.

The magnesian anorthosite clast, as was found in Dhofar 489 was found so far only in Dhofar 309. The largest clast includes several rounded olivine crystals and minor pyroxenes in large twinned grains of plagioclase. The An (96.0-96.6) and the Fo contents (76-79) are similar to those of Dhofar 489.

The modal abundances in volume % of the minerals of the Koyama gabbro obtained from the mineral distribution map (Fig. 1) are: plagioclase 60.9 vol.%, olivine 15.5, orthopyroxene (Opx) 10.4, augite (Cpx) 8.0, magnetite, ilmenite 0.3, and others: 4.8. The presence of magnetite in plagioclase is a problem in separating plagioclase by magnetic method. The presence of amphibole is another problem. Chemical compositions of the bulk rock and major minerals are given in Table 1. We found that the fulvic and other organic acids decomposed plagioclase and release Ca ion [5].

Discussion:

Lunar highland materials are characterized by magnesian and ferroan anorthosites with high An values. Earth minerals are quite complex because of the presence of water, ocean and atmosphere. Because of the repeated igneous activities, many terrestrial plagioclases are enriched in Na and K. The high Na abundance in such plagioclase is a problem, when we try to make simulants for lunar highland materials. It has been difficult to find

high-Ca plagioclase in large quantities on Earth, particularly in Japan. The Koyama gabbro is one candidate found in Japan, but further searches are required to obtain more Ca-rich plagioclase of other localities.

Remote sensing data indicate that the nearside and the farside of the Moon are substantially different in terms of inferred chemical compositions and rock lithologies [6]. Our discovery of magnesian anorthosites in Dhofar 489 from the lunar farside [1, 2], supports an idea that the major rock type of the northern farside is magnesian anorthosite. Korotev [3] studied lunar meteorites other than Dhofar 489 in relation to this problem. Our mineralogical investigations of some of their samples [7], suggest that varieties of impact melted or modified troctolitic anorthosites may contribute to high Mg numbers of the farside highland anorthosites.

One candidate site for construction of a lunar base in a proposed future manned lunar mission, is rims of craters at the south pole area, where permanent sunshine is available to warm up the base. Korotev [3] pointed out that together the Dhofar 489 group stones are unique among the feldspathic lunar meteorites for the geochemical reasons. Information of the Dhofar 489 group will be useful for the stimulant production of the proposed lunar base site.

Dhofar magnesian anorthosite cannot be composed mainly of ferroan anorthosite such as that typical of the Apollo missions. It is a breccia composed in large part of some type of magnesian anorthosite that is not well represented by samples in the Apollo collection. The returned samples, particularly the Apollo samples, give a very biased image of what the moon is really like. The data of Y-86032 will also contribute to the simulant productions. Korotev [3] also mentioned that Dhofar 489, is indistinguishable in composition from the others. Our mineralogical studies of some of their samples showed that the matrix texture of Dhofar 489 is different from others.

If space agriculture is planned in the base, we have to produce soil simulants. Biologists assume that the presence of organic materials and microorganisms is essential in the terrestrial soil, but it is not recommended for bacteria to go out of the base on the moon. The fossil sea water called brine water in the Chiba Kazusa formation, contains fulvic acid, which show biological stimulation effect. Since we found that the fulvic acid decomposed plagioclase, such organic materials are better than living organism to help growing plants.

Acknowledgements:

This work was carried out as a part of "Lunar simulant project" (PI: Kanamori) supported by Shimizu Corp. and JAXA and partly supported by NIPR, Research Project Fund, P-8 (Evolution of the early Solar System Materials). We thank Prof. T.

Yamaguchi of CIT for supporting our research on lunar simulants at CIT in 2006.

References:

- [1] Takeda H. *et al.* (2006) *Earth Planet. Sci. Lett.*, **247**, 171-184. [2] Takeda H. *et al.* (2007) *LPS XXXVII*, #1607. [3] Korotev R. L. *et al.* (2006) *GCA*, **70**, 5935-5956; Korotev R. L. (2006) *LPS XXVII*, #1402. [4] Nyquist L. *et al.* (2006) *GCA*, **70**, 5990-6015. [5] Saito M. (2007) *BSci. Dissertation*, Chiba Inst. of Tech. [6] Jolliff B. L. *et al.* (2000) *JGR*, **105**, No.E2, 4197-4216. [7] Arai T. *et al.* (2007) *Antarctic Meteorites XXXI*, this volume, NIPR.

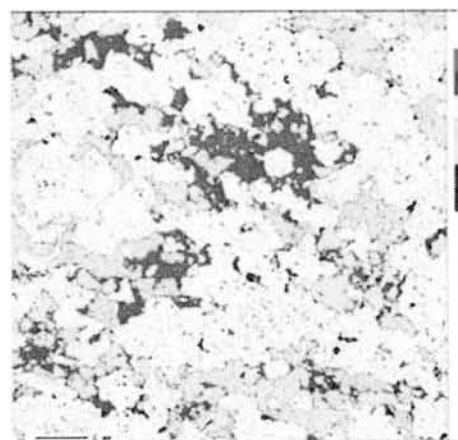


Fig. 1. Mineral distribution map of the Koyama gabbro. Yellow: plagioclase, blue: olivine, red: Opx, green: Cpx, white: magnetite, Ilmenite, black: others, cracks. Scale bar: 2 mm.

Table 1. Chemical compositions of minerals in the Koyama gabbro.

| Miner. | EPMA | | | X-ray F | |
|----------------------------------|-------|-------|-------|---------|-------|
| | Plag | Oliv | Opx | Plag* | Bulk* |
| SiO ₂ | 46.8 | 37.5 | 53.8 | 57.4 | 55.8 |
| TiO ₂ | 0.03 | 0.02 | 0.26 | 0.09 | 0.71 |
| Al ₂ O ₃ | 31.73 | 0.03 | 1.42 | 22.9 | 17.01 |
| FeO | 1.38 | 25.5 | 15.34 | | |
| Fe ₂ O ₃ * | | | | 1.45 | 8.80 |
| MnO | 0.02 | 0.45 | 0.4 | 0.02 | 0.14 |
| MgO | 1.35 | 36.7 | 26.9 | 0.41 | 3.07 |
| CaO | 15.77 | 0.05 | 1.76 | 10.36 | 8.93 |
| Na ₂ O | 2.08 | 0.01 | 0.02 | 3.03 | 2.28 |
| K ₂ O | 0.09 | 0.08 | 0.03 | 0.74 | 0.93 |
| Cr ₂ O ₃ | 0.01 | 0.01 | 0.09 | | |
| V ₂ O ₃ | 0.01 | 0.01 | 0.03 | | |
| NiO | 0.02 | 0.08 | 0.04 | | |
| P ₂ O ₅ | 0.00 | 0.02 | 0.01 | 0.08 | 0.09 |
| Total | 99.26 | 100.4 | 100.2 | 96.45 | 97.73 |

* incomplete mineral separates and bulk.

U-Pb systematics of phosphates in lunar basaltic regolith breccia, MET 01210

K. Terada^{1,2,3}, Y. Sasaki¹, M. Anand^{3,4}, K. H. Joy^{4,5,6}, and Y. Sano⁷, ¹Department of Earth and Planetary Systems Science, Hiroshima University (terada@sci.hiroshima-u.ac.jp), ²Project Center of Multi-Isotope Research for Astro- and Geochemical Evolution (MIRAGE), Hiroshima University, ³Department of Earth Sciences, The Open University, ⁴Department of Mineralogy, The Natural History Museum, ⁵UCL/Birkbeck Research School of Earth Sciences, University College London, ⁶The Rutherford Appleton Laboratory, ⁷Ocean Research Institute, The University of Tokyo

Introduction:

Lunar meteorites are valuable samples for understanding the origin and evolution of the Moon's crust, as they potentially provide a new insight into the thermal history of unexplored regions of the Moon. In spite of their scientific value, chronological studies of lunar meteorites have been difficult, since most of them are brecciated and consist of mixtures of materials, potentially of different origins. Therefore, the age determination using bulk-rock material is prohibitive. Here, we report Sensitive High-Resolution Ion MicroProbe (SHRIMP) U-Pb isotopic analyses of phosphate grains in the newly found lunar basaltic regolith breccia, Meteorite Hills 01210 ([1-2] hereafter abbreviated as MET 01210).

MET 01210 is a 22.8 g lunar meteorite collected in 2001 from the Meteorite Hills [1] and has been identified as a regolith breccia consisting of low-Ti mare basalt materials with a minor anorthositic component [3-11]. In order to understand the petrogenetic history of this meteorite, we have carried out the *in-situ* U-Pb age dating of phosphates grains in MET 01210 using the SHRIMP, installed at Hiroshima University. The primary objective of the present work is to investigate the U-Pb systematics of phosphates in MET 01210, whose radiometric age has previously not been determined. The second objective was to compare the thermal, i.e., crystallization history of the basaltic component in this meteorite with those of other low-Ti mare basalt meteorites and to provide a chronological constraint and discussion on the nature of the source region.

Sample, Analytical Methods and Results:

Two standard polished thin sections of MET 01210 (MET 01210-21 and MET 01210-31) were allocated by the Meteorite Working Group. These thin sections contained samples with a vesicular fusion crust and were composed of an immature breccia sample with rock (<4 mm) and mineral fragments (<1 mm) fused in a fine grained crystalline and glass matrix, which are dominated by low-Ti mare basalt material with a minor anorthositic component [10].

Initially, back-scattered electron (BSE) images were obtained, followed by measurements of mineral compositions by an Electron Probe Micro Analyzer (EPMA; JEOL JCMA-733II), in order to identify the

location and mineralogy of phosphates. As about half of the grains were too small for the 10 μm spot analysis by SHRIMP, four grains from MET 01210-21 and three grains from MET 01210-31, which were large enough and free from inclusion and cracks, were selected for this study.

After EPMA analysis, about 1 nA O_2^- primary beam with acceleration voltage of 10kV was focused to sputter an area $\sim 10 \mu\text{m}$ in diameter on the phosphates and positive secondary ions were extracted at 10 kV and were detected on a single electron multiplier by peak switching. The mass resolution was set to 5800 at ^{208}Pb for U-Pb analyses. The magnet was cyclically peak-stepped from mass 159 ($^{40}\text{Ca}_2^{31}\text{P}^{16}\text{O}_3^+$) to mass 254 ($^{238}\text{U}^{16}\text{O}^+$), including background, all Pb isotopes, and masses 238 for ^{238}U . No significant isobaric interferences were detected in this mass range for the phosphates. The abundance ratio of ^{238}U to ^{206}Pb was obtained from the observed $^{238}\text{U}^+ / ^{206}\text{Pb}^+$ ratio using an empirical relationship between the $^{206}\text{Pb}^+ / ^{238}\text{U}^+$ and $^{238}\text{U}^{16}\text{O}^+ / ^{238}\text{U}^+$ ratios of the standard apatite (PRAP) derived from an alkaline rock of the Prairie Lake circular complex in the Canadian Shield ($1156 \pm 45 \text{ Ma}$ (2σ)) [12]. An *in-situ* analyses of four whitlockite and four apatite grains in MET 01210, which are resistant to secondary events, resulted in a total Pb/U isochron age of $3904 \pm 86 \text{ Ma}$ in the $^{238}\text{U} / ^{206}\text{Pb} - ^{207}\text{Pb} / ^{206}\text{Pb} - ^{204}\text{Pb} / ^{206}\text{Pb}$ 3-D space (95% confidence limit).

Discussion and Remarks:

Chronological studies of numerous samples of mare basalt and related pyroclastic deposits collected by Apollo and Luna missions have been well documented (for summary, see [13-14]). In general, the high-Ti basalts (> 6wt.% TiO_2) from the Apollo11 and Apollo17 sites are relatively old, generally from 3.5 to 3.9 Ga. In contrast, low-Ti (1.5 - 6wt.% TiO_2) mare basalt samples are generally younger in the range of 3.1 to 3.4 Ga, although some exceptions exist (the aluminous low-Ti mare basalts have ages of 3.9 to 4.2 Ga [15], and the very-low Ti basalts (< 1.5 wt.% TiO_2) are much younger (3.2-3.3 Ga for LUNA 24). The observed age of about 3.9 Ga for MET01210 phosphates in this study is much older than the reported ages for low-Ti mare basalt (3.1-3.4 Ga for Apollo 15 and 3.1-3.3 Ga for Apollo 12). Thus, our result clearly demonstrates that the thermal

activity recorded in MET 01210 is quite different from those of the explored regions of the Moon by the Apollo missions, indicating protracted low-Ti basalt volcanism on the Moon (about 800 Ma from 3.1 Ga to 3.9 Ga); if age data for other low-Ti mare basalt meteorites (LAP02205 [16]) are considered then the low-Ti basalt volcanism on the Moon seems to have spanned for more than a billion year (3.9 Ga to 2.9 Ga).

Recently, Day et al. [11] reported the detailed petrographical and mineralogical descriptions of basaltic clasts in MET 01210, and discussed its association with evolved (e.g. LaPaz Icefield 02205; Northwest Africa 032) and ferroan (e.g. Asuka 881757; Yamato 793169) low-Ti basaltic lunar meteorites and suggested a possibility of similar mare source regions for these meteorites. Especially for the ferroan basaltic lunar meteorites, Arai et al [4] and Righter and Bussey [9] also pointed out the similarities of bulk composition, texture, and pyroxene composition among MET 01210 and Asuka 881757 and Yamato 793169. Furthermore, Arai et al. [4] concluded that MET 01210 is launch paired with Asuka 881757 and Yamato 793169. Recent studies on the cosmic ray exposure history of these meteorites also support this scenario, because the ^{10}Be and ^{36}Cl 4π exposure ages of 0.95 ± 0.13 and 0.90 ± 0.18 Myr for MET 01210 are quite similar to those of the ^{10}Be ejection ages of Asuka 881757 (0.8 ± 0.2 Myr) and Yamato 793169 (0.9 ± 0.2 Myr) [17-18]. From the point of view of chronological studies, the association with evolved non-brecciated basaltic meteorites are ruled out, because the phosphate formation age of LAP 02205 (2.9 Ga [16]) and the bulk Ar-Ar age of NWA 032 (2.8Ga, [19-20]) are significantly different from that of MET 01210. For Asuka 881757 and Yamato 793169, various radiometric ages have been reported based on the bulk sample analyses. Misawa et al. [21] reported a Pb-Pb age of 3940 ± 28 Ma, a U-Pb age of 3850 ± 150 Ma, a Th-Pb age of 3820 ± 290 Ma, a Rb-Sr age of 3840 ± 32 Ma, a Sm-Nd age of 3871 ± 57 Ma and a Ar-Ar age of 3798 ± 12 Ma for Asuka-881757. Thalmann et al. [22] also reported a K-Ar gas retention age of 3100 ± 600 Ma and ^{244}Pu - ^{136}Xe fission age of 4240 ± 170 Ma, also indicating old formation age. Torigoe-Kita et al. [23] investigated the U-Th-Pb, Sm-Nd and Ar-Ar isotopic systematics of Yamato-793169, and suggested that the nearly concordant U-Pb age of 3.8 Ga indicates the original formation age of 3.9 Ga and that the young Sm-Nd age of 3.4 Ga might be caused by secondary events. The phosphate formation age of 3904 ± 86 Ma for MET 01210 in this study is consistent with old crystallization age of 3.8-3.9 Ga reported for Asuka 881757 and Yamato 793169 meteorites by other investigators, indicating that these meteorites have the oldest formation ages among the known low-Ti mare basalts except for aluminous low-Ti mare basalt. The coincidence of the ages of these three meteorites

(Asuka, Yamato and MET) indicates that there is no chronological impediment to the hypothesis that all these meteorites originates from the same locality on the Moon and were launched by a single impact.

In general, the investigation of U-Pb systematics provides not only the radiometric ages of basalts, but also the μ -values ($= {}^{238}\text{U}/{}^{204}\text{Pb}$) of parent magma sources, which have important implications for the evolution of lunar magma source regions. In particular, the μ value could be used for assessing the fractionation between refractory and volatile elements and could be an important indicator when considering large-scale planetary differentiation scenarios. Our result of low inclination in a Pb-Pb isochron diagram implies that the μ -values of the source magma of MET 01210 is much lower than previous studies of low-Ti mare basalts from Apollo samples (100 to 300 [24]) and appears to be consistent with those of the Asuka 881757 (10 ± 3 [21]) and Yamato 793169 (21.6 ± 3.5 [23]). Thus, the rough estimation of the μ -values of MET 01210 also supports the hypothesis that all these meteorites originated from the same magma source and were launched by a single impact event, although investigation of U-Pb systematics of not only radiogenic phosphates but also other minerals in MET 01210 would be required to further confirm this interpretation.

References:

- [1] *Antarctic Meteorite Newsletters* 27 (2004) 1. [2] Russell S. S. et al. (2004) *M&PS* 39, A215-A272. [3] Patchen A. D. et al. (2005) *LPS XXXVI*, #1411. [4] Arai T. et al. (2005) *LPS XXXVI*, #2361. [5] Korotev R. L. and Irving A. J. (2005) *LPS XXXVI*, #1220. [6] Zeigler R. A. et al. (2005) *LPS XXXVI*, #2385. [7] Huber H. and Warren P. H. (2005) *LPS XXXVI*, #2401. [8] Joy K. H. et al. (2006) *LPS XXXVII*, #1274. [9] Righter K. and Bussey B. (2006) *M&PS* 41, A5364. [10] Joy K. H. et al. (2006) *M&PS* 41, A5221. [11] Day J. M. D. et al. (2006) *GCA* 70, 5957-5989. [12] Sano Y. et al. (1999) *Chem. Geol.* 153, 249-258. [13] Nyquist L. E. and Shih C. -Y. (1992) *GCA* 56, 2213-2234. [14] Nyquist L. E. et al. (2001) in "The Century of Space Science", 1325-1376. [15] Taylor L. A. et al. (1983) *EPSL* 66, 33-47. [16] Anand M, et al. (2006) *GCA* 70, 246-264. [17] Nishiizumi K. et al. (2006) *LPS XXXVII*, #2369. [18] Nishiizumi K. et al. (1992) *Proc. NIPR Symp. Antarct. Abstract* 17, 129-132. [19] Fernandes V. A. et al. (2003) *M&PS* 38, 555-564. [20] Fagan T. J. et al. (2002) *M&PS* 37, 371-394. [21] Misawa K. et al. (1993) *GCA* 57, 4687-4702. [22] Thalmann C. et al. (1996) *Meteorit.* 31, 857-868. [23] Kita N. T. et al. (1995) *GCA* 59, 2621-2632. [24] Premo W. R. et al. (1999) *International Geology Review* 4, 95-128.

^{26}Mg DEFICIT DATING FOR DIFFERENTIATION IN PALLASITE PARENT BODIES. T. Tomiyama^{1,3}, M. Bizzarro², G. R. Huss³, and A. N. Krot³, ¹National Institute of Polar Research, 1-9-10 Kaga, Itabashi, Tokyo 173-8515 JAPAN (Current affiliation). ²Geological Institute, University of Copenhagen, DK-1350, Denmark. ³Hawai'i Institute of Geophysics and Planetology, University of Hawai'i at Manoa, 1680 East-West Rd. POST 504, Honolulu, HI 96822, USA. (tomi@nipr.ac.jp)

Introduction:

Pallasites are stony-iron meteorites that consist of roughly equal volumes of olivine and Fe-Ni metal. It is widely believed that pallasites were mechanically mixed at the interface of the metallic core and peridotitic mantle in differentiated asteroid(s) [e.g. 1,2]. Pallasites have several (sub)groups based on differences in chemistry, mineralogy and O-isotopic compositions [3-6]. We can study evolution histories of deep interior of different asteroids, using pallasite samples.

Dating of early events in the Solar System has been one of the issues of fundamental interest in planetary science. However, time resolution of chronology with long lived radio-nuclides tend to be insufficient for dating early solar materials, because most planetary objects were developed within ~ 10 Myr.

It is known that ^{26}Al widely existed and decayed into the daughter nuclides ^{26}Mg in the early Solar System [e.g., 7]. ^{26}Al - ^{26}Mg chronology is a powerful tool for dating early Solar System events, because its half life ($t_{1/2} = 0.73$ Myr) is comparable to timescales of planetary evolution. If the isotopic system was closed during the lifespan of ^{26}Al in the early Solar System, the isotopic system will show shift in radiogenic ^{26}Mg ($^{26}\text{Mg}^*$) as $\delta^{26}\text{Mg}^* \equiv 1000 \times \{(^{26}\text{Mg} / ^{24}\text{Mg})_{\text{unknown}} / (^{26}\text{Mg} / ^{24}\text{Mg})_{\text{terrestrial}} - 1\}$, depending on the Al/Mg ratio. This would result in a small deficit in $^{26}\text{Mg}^*$ for planetary materials with very low Al/Mg ratios [8]. We can utilize high-precision analyses of Mg isotopes for $^{26}\text{Mg}^*$ deficit dating of the pallasite olivines.

For a better understanding of pallasite formation history, we have selected pallasite samples from different (sub)groups and carried out the precise analysis of Mg isotopes [9].

Experiments:

Micro-drilled powders and chipped fragments of olivines in Omolon, Imilac, Huckitta, Springwater, Vermillion and Zinder were dissolved with HF-HNO₃ acid, and Mg was purified by cation exchange chemistry. Mg isotopic ratios were measured using Multi-Collector ICP-MS (MC-ICPMS) at the University of Copenhagen. Obtained Mg isotopic ratios were corrected for instrumental mass bias with bracketing analyses of DSM3 standard solution or J-11 terrestrial mantle olivine. Al/Mg ratios were checked by MC-ICPMS

for some samples, and these were ~ 0 for pallasite olivine.

Results:

Obtained data were summarized in Table 1. Analysis of the J-11 olivine against the DSM3 during the course of this study yielded $\delta^{26}\text{Mg}^* = -0.002 \pm 0.011$ ‰, which is in good agreement with the terrestrial value. Omolon and Imilac are typical main group pallasites (PMGs), but only Omolon showed a resolvable deficit in $\delta^{26}\text{Mg}^*$. Two anomalous PMGs, Huckitta with Ge- and Ga-enriched metal [4] and Springwater with Fe enriched olivines (Fa₁₈, whereas Fa₁₂ for majority of PMGs) also exhibit $\delta^{26}\text{Mg}^*$ deficits. Zinder and Vermillion are ungrouped pyroxene-bearing pallasites (PPXs) with different oxygen isotopic compositions [5, 10]. Zinder olivine seem to have slight deficits in $\delta^{26}\text{Mg}^*$. The data from Vermillion was statistically indistinguishable from the terrestrial value.

Table 1: $\delta^{26}\text{Mg}^*$ deficits in pallasite olivines.

| sample | group ^{*1} | $\delta^{26}\text{Mg}^*$ (‰) | error ($2\sigma_{\text{mean}}$) | n |
|-------------|---------------------|---------------------------------|--------------------------------------|----|
| J-11 | terrestrial | 0.002 | 0.011 | 15 |
| Omolon | PMG | -0.025 | 0.009 | 7 |
| Imilac | PMG | -0.003 | 0.014 | 7 |
| Huckitta | PMG-am | -0.021 | 0.006 | 7 |
| Springwater | PMG-as | -0.028 | 0.012 | 9 |
| Vermillion | PPX | -0.008 | 0.010 | 14 |
| Zinder | PPX | -0.010 | 0.007 | 20 |

^{*1}PMG = main group pallasite, PMG-am/-as = PMG with anomalous metal/silicate composition [3], PPX = Ungrouped pyroxene-bearing pallasite [4].

Discussion:

If we assume that the Solar System had an initial $^{26}\text{Al}/^{27}\text{Al}$ ratio of $\sim 5.85 \times 10^{-5}$ as observed in bulk CAIs, and the bulk Solar System kept the composition corresponding to $^{27}\text{Al}/^{24}\text{Mg}$ ratio of ~ 0.1 , the initial solar $\delta^{26}\text{Mg}^*$ is given as ~ -0.042 [11,12]. The present solar $^{26}\text{Mg}/^{24}\text{Mg}$ ratio represents addition of $^{26}\text{Mg}^*$ from the ^{26}Al decay to the initial solar $^{26}\text{Mg}/^{24}\text{Mg}$ ratio. Deficits in $^{26}\text{Mg}^*$ for materials with Al/Mg ~ 0 are indicative of the early chemical fractionation which reduce the Al/Mg ratio relative to the solar composition. Because bulk composition of pallasite parent bodies was most likely similar to that of the bulk Solar System, this chemical fractionation probably occurred after the accretion of parent bodies. Pallasite parent bodies definitely experienced

extensive differentiation driven by heat sources such as ^{26}Al and ^{60}Fe decay. The silicate mantle should have fractionated by residual partial melting and/or cumulative crystallization during the magmatism, both of which would have resulted in a concentric structure with Al-rich exterior and Al-poor interior. ^{26}Al - ^{26}Mg system in the pallasite olivines should have closed at this stage, because this isotopic system should not have been disturbed by mechanical mixing of core-mantle materials nor by subsequent duration.

PMG is a dominant group of pallasites. PMGs share the same oxygen isotopic compositions [3], but it is unclear whether PMGs came from a single parent body or multiple parent bodies. Some PMGs have anomalous metal or silicate compositions to form a couple of subgroups. These variation within PMGs may indicate that PMGs possibly originated from a heterogeneous parent body or different parent bodies. Resolvable $\delta^{26}\text{Mg}^*$ deficits observed in Omolon (PMG), Huckitta (PMG-am), and Springwater (PMG-as) suggest that differentiation of the PMG parent body(ies) started when ^{26}Al was alive in the Solar System. For the simple calculation for differentiation ages, we suppose that bulk PMG parent body(ies) had the same chemical and isotopic composition as the bulk Solar System before differentiation. If the Al-Mg system was fractionated by a single differentiation event, observed $\delta^{26}\text{Mg}^*$ deficits of $-0.028 \sim -0.021$ are corresponding to ages of $0.4 \sim 0.7$ Myr after the CAI formation. Although calculated ages have considerable uncertainties, differentiation ages of these pallasite olivines seem to be comparable with chondrule formation ages [15]. This suggest that parent body(ies) for those PMGs accreted and differentiated at the very early stage of the Solar System. This result is consistent with previous studies of high-precision ^{26}Al - ^{26}Mg chronology for the differentiation age of several achondrites [8,13,14]. Recent analysis for ^{182}Hf - ^{182}W systematics ($t_{1/2} = 8.9$ Myr) also showed that metals in some pallasites are depleted in radiogenic $^{182}\text{W}^*$, which indicate that the segregation of the metal in the pallasite parent bodies started shortly after the start of the Solar System [16]. Metal segregation and Al/Mg fractionation in the mantle may have occurred simultaneously. Another PMG, Imilac did not show deficit in $\delta^{26}\text{Mg}^*$. If there are variations between the timing of differentiation of PMGs, it might indicate that PMGs evolved heterogeneously in a single parent body, or that PMGs might have originated from different parent bodies. However, we could not push these implications too far, because the Mg isotopic difference between Imilac and other three PMG samples are not clearly resolved.

PPXs are pallasites with pyroxenes with variety of textures such as individual large grains, inclusions in silicates and grains along the edges of olivines,

whereas pyroxenes in PMGs occur as symplectic intergrowths at margins of olivine grains [5]. Two PPX samples, Vermillion and Zinder should have originated from different bodies which were distinct from PMG parent body(ies), because they have distinct oxygen isotopic compositions, and because the modal abundance of pyroxenes in these pallasites are considerably different [5,10]. Observed deficits in $\delta^{26}\text{Mg}^*$ values of olivines were very small in Zinder and statistically insignificant in Vermillion. Again, the difference between those PPXs and PMGs with $\delta^{26}\text{Mg}^*$ deficits is not clear. However, it is worth while to consider the possible difference in $\delta^{26}\text{Mg}^*$ deficits between PPXs and PMGs. If PPXs have smaller $\delta^{26}\text{Mg}^*$ deficits than PMGs, the simplest explanation would be that PPX parent bodies were differentiated after the differentiation of PMG parent body(ies). Accretion rates and/or sizes of parent bodies would be responsible for a range in times of differentiation, although significant difference of thermal histories between PPXs and PMGs has not been reported. There may be another explanation. The presence of crystalline pyroxenes indicate that PPX silicates crystallized in the silica-rich melt which may have been produced by cumulative crystallization of predominant olivines. The residual melt should have also been enriched in Al and result in Mg isotopic composition richer in $^{26}\text{Mg}^*$ than that of bulk Solar System. Such an effect could be important for PPXs which contain pyroxenes as a dominant phase, such as Zinder and NWA 1911.

References: [1] Scott E.R.D.(1977) *GCA* 41, 349-360. [2] Buseck P.R. (1977) *GCA* 41, 711-740. [3] Clayton R. N. and Mayeda T. K. (1996) *GCA* 60, 1999-2017. [4] Wasson J. T. and Choi B.-G. (2003). *GCA* 67, 3079-3096. [5] Bosenberg J. S. et al. (2000) *MAPS* 35, 757-769. [6] Jones R. H. et al. (2003). *LPSC XXXIV*, #1683. [7] Lee T. et al. (1976) *GRL* 3, 109. [8] Baker J. & Bizzarro M. (2005) *Protostars & Planetes V* #8612 [9] Tomiyama T. et al. (2006) *MAPS* 41, A174. [10] Bunch T.E. et al. (2005) *MAPS* 40, A26. [11] Bizzarro M. et al. (2004) *Nature* 431, 275-278. [12] Thrane K. et al. (2006) *APJ* 646, L159-L162. [13] Baker et al. (2005) *Nature* 436, 1127-1131. [14] Bizzarro M. et al. (2005) *APJ* 632, L41-L44. [15] Kita N.T. et al. (2000) *GCA* 64, 3913-3922. [16] Quitté G. et al. (2005) *GCA* 69, 1321-1332. Supported by NASA grant #NNG05GG48G.

Observation of the radius of compound chondrules in meteorite chips. M. Uesugi and K. Uesugi, ^{*1}Department of Earth and Space Science Osaka University 1-1 Machikaneyama, Toyonaka Osaka Japan, ^{*3}Japan Synchrotron Radiation Research Institute (JASRI) 1-1-1 Kouto, Sayo-cho, Sayo-gun, Hyogo Japan.

Introduction:

Formation process of compound chondrules in the early solar nebula is one of the most important issues of the study of chondrule formation. If the compound chondrules were formed by mutual collisions between the chondrules which already solidified and still molten, their existence indicates that there was considerable difference of melting degree between the chondrules at the time of chondrule formation in a very close distance [1]. And also, the collisional formation indicates that the number density of chondrules in the chondrule formation region would be very high [2]. Thus, the structure of compound chondrules indicates several constraints on the formation of chondrules.

There are three possibilities for the origin of the difference of the melting degree between the chondrules; (1) difference of liquidus temperature, (2) difference of cooling rate (difference of radius) and (3) difference of formation region. If the difference of liquidus temperature is responsible for the difference of the melting degree, the secondary chondrule, which loses its spherical shape due to the sticking, should have lower liquidus temperature than that of primary chondrule, which retain its spherical surface. However, previous study indicates that around 50% of the compound chondrules show that the secondary chondrules have higher liquidus temperature [3]. Thus, difference of liquidus temperature would not be responsible for the difference of melting degree.

In this study, we investigated the second possibility, the difference of radius between the constituent chondrules of compound chondrule. If the difference of radius is responsible for the difference of the melting degree, the radius of the secondary chondrule should be larger than that of the primary in order to remain melting after the resolidification of the primary chondrule.

We observed the compound chondrules inside the meteorite chips by X-ray CT scanner and try to obtain the three dimensional structure of compound chondrules. We also make thin sections of the compound samples to compare the CT images and backscattered electron (BSE) images of them. Our purpose of this study is to establish the manner of observation for the radius of compound chondrules in the meteorite chips using X-ray CT scan, for further statistical study of the compound chondrules.

Method:

Two meteorite chips of Y-791717 (CO3) and Y-790448 (LL 3.1) with ϕ 5mm were measured by SP- μ CT, at BL20B2 of Spring-8, Hyogo, Japan.

X-ray energy is 35 keV, and Number of projection is 5000 for Y-791717 and 3600 for Y-790448. The exposure time is 3 seconds for Y-791717 and 2 seconds for Y-790448 for a projection from each rotational angle. Format of the CT data is 1344x1344x1024. Pixel size of all directions is 3.14 μ m. Obtained projection images are reconstructed into CT images by Convolution-BackProjection (CBP) method.

Compound chondrules are manually selected from the CT images, and separated from the CT images as three dimensional objects by "Slice" programs developed at SPring-8. After three dimensional shape for all sets of compound in the meteorite chips is identified, we made thin sections for the observation of optical microscope and secondary electron microscope. It is impossible to make thin section samples for all compound chondrules in a meteorite chip, because the thickness of diamond cutter is partially larger than the distance of compound chondrules in the meteorite chips. And also, most of the cutting planes of compound samples are not parallel. Under these restrictions, we made two thin sections for each meteorite chip.

Results and discussion:

Figure 1 shows the comparison of the BSE image of the thin section and one slice of a reconstructed slice image taken by X-ray CT of Y-791717.

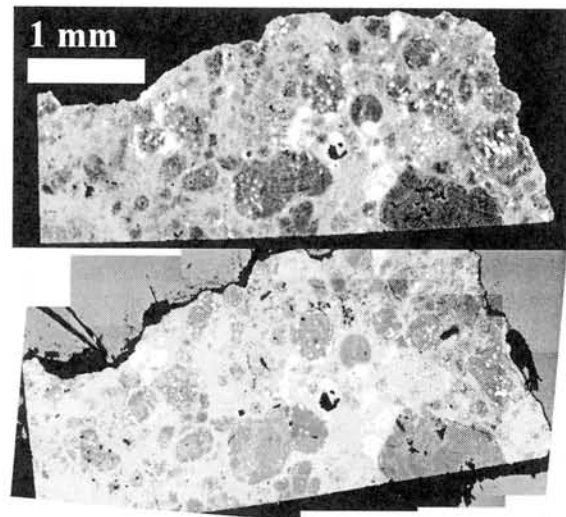


Fig. 1 A slice image (upper) and BSE image (lower) of Y-791717 (CO3) meteorite chip. White globules in the figure are metallic iron grains, and most of large dark objects would be chondrules.

Though the contrast and spatial resolution of CT

image is not sufficient for the precise observation of internal structure of chondrules, it is enough to identify the chondrule shape. Figure 2 shows the images of a compound chondrule in the center of Fig.1. At first, the three dimensional shape of the compound chondrule (Fig. 2a) shows that the large irregular shaped chondrule stuck on the surface of the smaller primary chondrule.

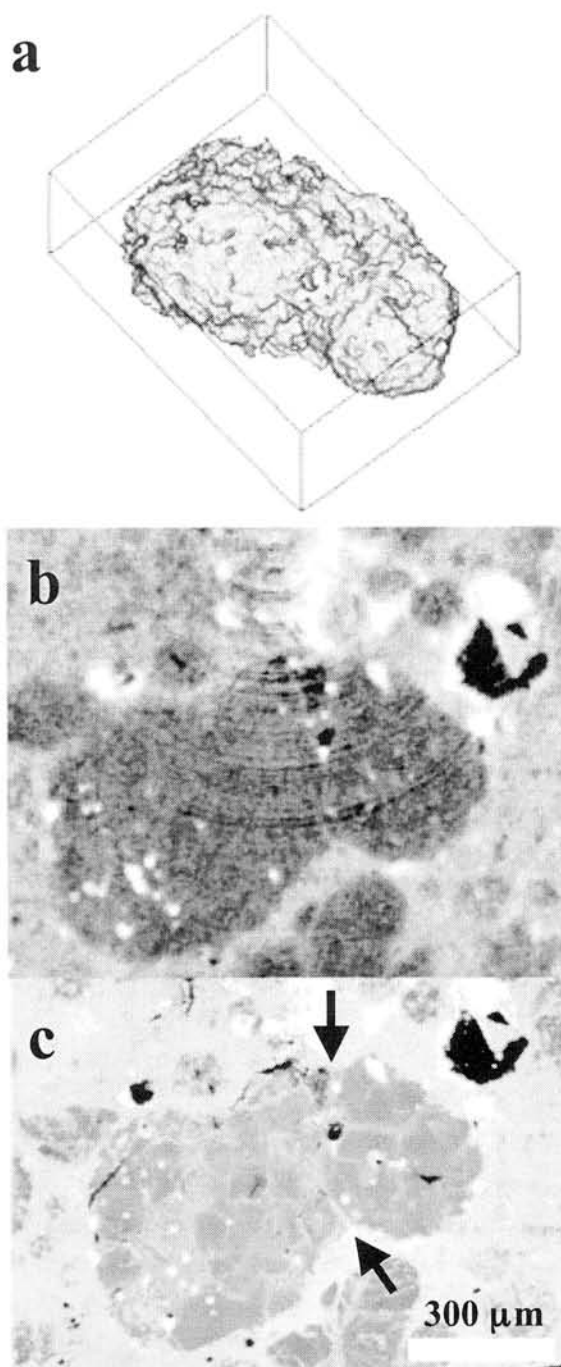


Fig. 2 A bird-eye view of a compound chondrule in Y-791717 (a) and slice image (b) and BSE image (c). The BSE image appears that a irregular shaped chondrule (left-hand side) sticks on the surface of a smaller primary chondrule (right-hand side). Black arrows in (c) show the boundary of chondrules

However, the boundary of those chondrules could not be identified from the CT image (Fig. 2b). The BSE image of the compound chondrule clearly shows the boundary between the primary and secondary chondrules (Fig 2c). The radius ratio of primary : secondary is around 1:2.

We succeed to determine the boundary and radius of chondrules for some compound chondrules from CT images (Fig.3). These chondrules would have different Fe wt%, and so the X-ray Linear Absorption Coefficient (LAC) is clearly changed at the boundary of the chondrules. In such case, the boundary of chondrules could be identified by the image processing by Slice programs, and then the radius ratio could be obtained. However, the boundary and radii of most compound chondrules could not be obtained from CT images. And also, we could not prepare thin sections of the compounds because of the limitation of cross sections. From these reasons, statistical data of the radius could not be obtained by this method. In order to increase the sample number, we should develop the high contrast CT method which enables to distinguish the primary and secondary chondrules. We are now planning the application of a new X-ray CT method on the observation of meteorite chip, called "phase contrast imaging", which would have 10^3 times higher contrast than general CT method [4].

References:

- [1] Gooding and Keil (1981) *Meteoritics*, 16, 17-43, 1981. [2] Sekiya M. and Nakamura T., (1996) *AMR.*, 9, 208-217. [3] Uesugi M. et al., (2005) *Antarctic Meteorites XXIX*, 90-91. [4] Momose A. (1995) *Nucl. Instrum. Methods. Phys. Res. A*, 352, 622-628

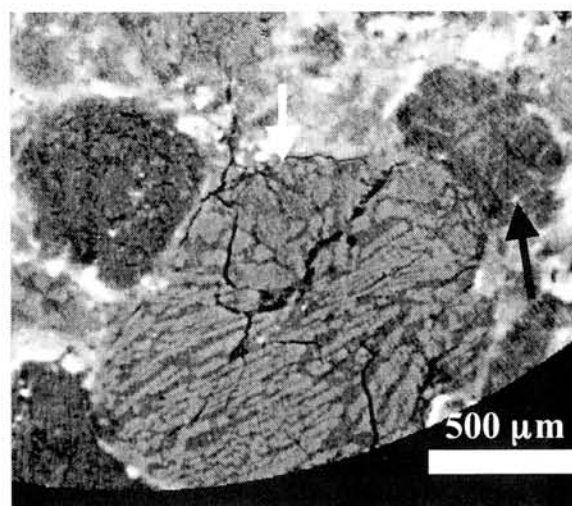


Fig. 3 A compound chondrule which shows clear boundary in Y-790448 (LL3.1) chondrite. A smaller dark object (black arrow) sticks on a large light-gray object (white arrow). The radius ratio of secondary to primary is ~ 0.5 . Dark portion in the lower part of the image is outer boundary of the CT data

Suggestions of Multiple Meteoroid Impact In Antarctica: How Do We Sort It Out?

J. G. Weihaupt¹ and A. Rice², ¹Department of Geology, University of Colorado at Denver, Denver, CO, USA, ²Department of Earth and Planetary Sciences, American Museum of Natural History, New York, NY, USA

Gravity surveys undertaken in the 1950's across Antarctica revealed a singularly strong negative free air anomaly ((to -158.3 mgal) over a large area of Wilkes Land. Its form suggested a possible meteor impact site. The gravity profiles were similar to those of known impact sites (apparent rim structures, circular basins, central peaks or rings), possessing appropriate aspect ratios (e.g., crater diameter vs crater depth), anomalously steep negative free air gravity anomaly gradients (to 4.71 mgal/km) characteristic of impact craters (and uncharacteristic of solely mantle-related or geologic crustal variations), etc. The condition of the ice covering the anomaly (heavily crevassed), the efficacy of glacial flow in bulldozing such features away, known rates of rebound and the apparent lack of isostatic compensation with surrounding environs, etc suggested the possible impact was geologically recent and that perhaps tektite strewn fields might be associated with it [1], [2].

This early suggestion has recently seen potential support by work on cores taken from the Ross Sea which has revealed the presence of material of high magnetic susceptibility (often taken as an indicator of meteor impact), impact glass and tektites. Other workers report that cores taken off Wilkes Land reveal

thick layers of impactites and ejecta (3m of pulverized Neogene shale, diatoms trapped in vesicular pores, etc) which has rendered a call for multiple craters across regions of complex geology: both terrestrial and marine. Such material is not confined to cores. Marine microfossils (Pliocene/Pleistocene) are reported in the dry valleys of Antarctica and in glacial sediments. Farther reaching are reports of *Antarctic* radiolaria, foraminifera and diatoms found as far afield as Europe, Asia. Investigators also report petrological indicators of possible impact (see [3],[4], [5] for instance).

The earlier suggestion of a single impact needs to be modified to fit the recent detection of a dominant cluster of negative free air gravity anomalies crossing the continental-oceanic boundary, and the East and West Antarctic structural boundary (i.e., Transantarctic Mountains). These anomalies are coincident with complex subglacial craterform topographic features inferred from radiosounding (to -500m below MSL). The major interior positive free air gravity anomalies are associated with subglacial topographic highs. The elliptical distribution of the negative gravity anomalies resemble known multiple impact distributions (scatter ellipses with the larger

anomalies downrange and the lesser ones uprange). This favors expanding the original suggestion to that of a multiple meteoroid impact. The multiple impact hypotheses would explain aeromagnetic surveys revealing ring-shaped structures in the subglacial rock surface much like those regarded as impact structures (the magnetic anomalies are unusual in magnitude themselves: amplitudes to 3600nT for sensors at 3.5 km elevation). Deviations from fresh impact topography can be attributed to glacial scour and ice sheet surging that should certainly accompany impact as well.

The distribution of the apparent impact structures extends well beyond the original discovery and on the basis of negative free air anomalies, into the Wilkes Subglacial Basin to the south, athwart the Transantarctic Mountains and into the Ross Embayment to the east [6]. This scenario of geologic disruption across several distinct and separate geologic provinces would fit the call to explain the detritus found elsewhere as coming from multiple sources.

It seems certain that something unusual has had a recent occurrence in

Antarctica. Several lines of research pointing to a possible multiple impact scenario sustain sufficient coherency to hopefully mount multi-disciplinary efforts to established what really occurred. The speculations entertained here have importance if they are sustained.

References (partial)

- [1] Weihaupt, J.G. (1960) *Arctic* 13, 2.
- [2] Weihaupt, J. G. (1976) , J. G. R., 81, 32, pp5651-5663. [3] Gerard-Little, P., D. Abott, D. Breger and L. Burckle (2006) Lunar and Planetary Sciences XXXVII, 1399.pdf. [4] Kellogg, T.B., Burckle, L.H., Kellogg, D.E., Fastook, J.L (1997), *Antarctic Journal of the U.S.*, 19(5), 44-45. [5] Courty, M-A., Abbott,D.H, Cortese, G., Crisci, A.Crosta, X De Wever, P Fedoroff, M France Greenwood, P., Grice, K., Mermoux, M., Scharer, U., Smith, D C Thiemens, M H (2006) *Eos Trans. AGU Fall Mtg.* Abstract GC41B-1055. [6] Weihaupt, J. W., Rice, A.; van der Hoeven, F. (2006) *Eos Trans. AGU Fall Mtg 2006*, abstract P51A-1181

THE STANNERN TREND EUCRITES: CONTAMINATION OF MAIN GROUP EUCRITIC MAGMAS BY CRUSTAL PARTIAL MELTS. A. Yamaguchi^{1,2}, J. A. Barrat¹, R.C. Greenwood³, M. Bohn¹, J. Cotten¹, M. Benoit¹ and I.A. Franchi³, ¹UBO-IUEM, CNRS-UMR 6538, Place Nicolas Copernic, F-29280 Plouzané Cedex, ²National Institute of Polar Research, Tokyo 173-8515, Japan. ³PSSRI, Open University, Walton Hall, Milton Keynes MK7 6AA, UK.

Introduction:

Eucrites are the oldest basalts in the solar system formed ~4.6 Ga ago. They are basaltic or gabbroic rocks that originated from the outer crust of the asteroid 4 Vesta [e.g., 1,2]. Most basaltic (noncumulate) eucrites are metamorphosed rocks, and are classified into six metamorphic grades [3]. They were metamorphosed under the solidus (~800-1000 °C) [4]. Some eucrites were metamorphosed near or above the solidus temperatures (~1060 °C) and experienced partial melting [5,6].

Basaltic eucrites have been subdivided into two chemical types on the basis of their Mg²⁺ (=Mg/(Fe+Mg)), Ti and incompatible trace element abundances: the main group-Nuevo Laredo (MG-NL) trend eucrites and the Stannern trend eucrites. Stannern trend eucrites are very similar to MG eucrites for major elements but are significantly richer in incompatible trace elements. The MG-NL trend eucrites can be explained by fractional crystallization [e.g., 7,8]. However, the origin of the Stannern trend eucrites is more problematic. Stannern trend eucrites could be generated from the same mantle source as MG eucrites but at smaller degrees of melting, and possibly at slightly differing oxygen fugacities. Hence, the diversity of the eucritic melts could simply reflect part of the diversity of the primary melts from the parent body mantle [e.g., 1,7,9]. Alternatively, to explain the decoupling of major elements from incompatible trace elements requires a complex scenario involving interaction between eucritic and highly residual melts [10,11]. We propose that this feature can be explained satisfactorily by contamination of normal eucrites by liquids formed through partial melting of preexisting eucritic crust.

Results and Discussion:

Fig. 1 presents REE patterns of two Stannern-trend eucrites, NWA4523 and Bouvante, and MG-NL trend eucrites, Juvinas and Nuevo Laredo. The data were obtained by ICP-AES and ICP-MS in Brest. The patterns of NL eucrites exhibit higher incompatible element concentrations, and Sr and Eu negative anomalies, in agreement with their more evolved compositions. The Stannern trend eucrites are not only richer in incompatible trace element than the other eucrites, but their trace element patterns are clearly distinctive, with pronounced negative Be, Sr and Eu anomalies.

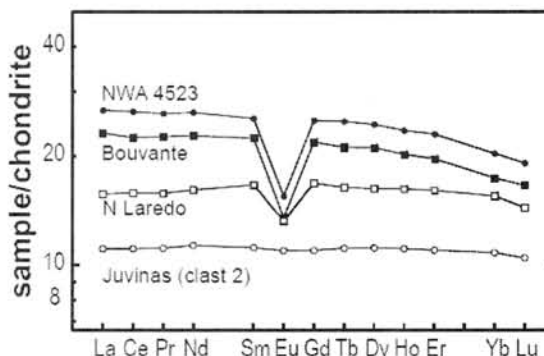


Fig. 1. Chondrite-normalized REE patterns of Stannern-trend eucrites and other eucrites.

As an alternative model to previous models, we propose that Stannern-trend eucrites were produced by contamination of MG eucrites by crustal partial melts. The composition of melts generated by the partial melting of eucritic crust can be calculated theoretically (Fig. 2). The first partial melts would certainly not be acidic, but rather intermediate to basic in composition, depending on the amount of silica and proportion of mesostasis contained in the rocks before melting. We have calculated the trace element abundances of melts produced by partial melting of an equilibrated eucrite (60% pyroxene, 40% plagioclase) using literature partition coefficients, and the composition of our reference eucrite Juvinas. In reality, the melting of a eucrite would be more complex than is considered by our model, in particular because of the involvement of accessory phases, which would be important at very low degrees of melting. However, these calculations should give a relatively realistic picture of the trace element abundances in the melts produced when the accessory phases such phosphates are no longer present in the residue. The calculated magmas produced by partial melting of a MG eucrite are rich in incompatible trace elements and display pronounced negative anomalies in K, Ba, Be, Sr, Eu and Ti relative to MG eucrites.

Contamination of a MG magma by a crustal partial melt should have little effect on its major element concentration, but a huge impact on the incompatible trace element abundance, which is exactly the variation displayed by Stannern trend eucrites. For the purposes of discussion we have calculated the melts obtained by simple mixing between a MG eucrite and a crustal partial melt

produced by 5-15 % melting (Fig. 2). The trace element abundances are strikingly well reproduced by this model. The trace element concentrations of Stannern and Bouvante are explained by a combination of about 85 % Juvinas and 15 % crustal partial melt. The calculated proportions are obviously dependent to the compositions of the end members. For example, very different proportions are obtained using the partial melts calculated for 5 % or 15 % of melting of the eucritic crust.

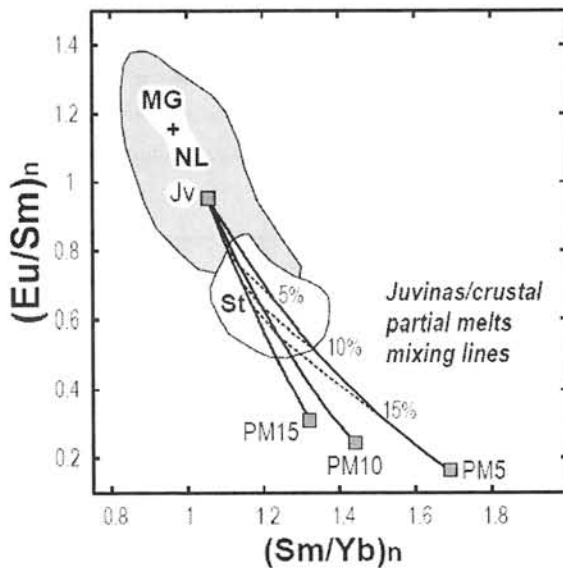


Fig. 2. (Eu/Sm)_n vs. (Sm/Yb)_n plot for noncumulate eucrites. The mixing curves between Juvinas and eucritic partial melts are calculated for three different compositions

The crustal partial melting model is consistent with the presence of partially melted eucrites. Mineralogical and geochemical evidence suggests that at least two noncumulate eucrites experienced high temperature metamorphism causing partial melting [5,6]. These eucrites have homogenized pyroxene (i.e., type 5 eucrite) [3], remnant basaltic textures, but lack mesostasis areas. The remnant basaltic textures and Fe/Mg ratios in pyroxenes confirm that EET 90020 and Y-86763 are basaltic eucrites. However, these eucrites have features that are not observed in other basaltic eucrites. EET 90020 and Y-86763 contain large crystals of tridymite and Cr-ulvöspinel. Ca-phosphates have lower REE abundances than those of other eucrites and plagioclase are enriched in LREE. Also, bulk LREE compositions are largely depleted [9]. Thus, the occurrence of partially melted eucrites on one hand, and thermal modeling on the other, indicates that at least locally, partial melts may have been generated in the Vesta's crust.

During the growth of the eucritic crust, its base was warmed up by the heat from interior where basalts were generated (i.e., magma ocean) (Fig. 3).

At depth, the early basalts (primitive or main group) were strongly metamorphosed to form type 5-6 eucrites and granulites. The eucrites would have been locally heated up close to the solidus (~1100°C) and partially melted. Later batches of basalt ascending through such high temperature zones would have been contaminated by crustal partial melts. The relative rarity of Stannern-trend eucrites implies that crustal contamination may have been a fairly local event, perhaps triggered by impact metamorphism and intrusions. Impact would raise the temperatures and cause fractures, which could be favorable paths of basalts. Despite the limited size of 4-Vesta, its crustal history has been multifaceted, involving magmatic fractionation, accumulation of basalts, remelting events, and crustal contamination of the magmas.

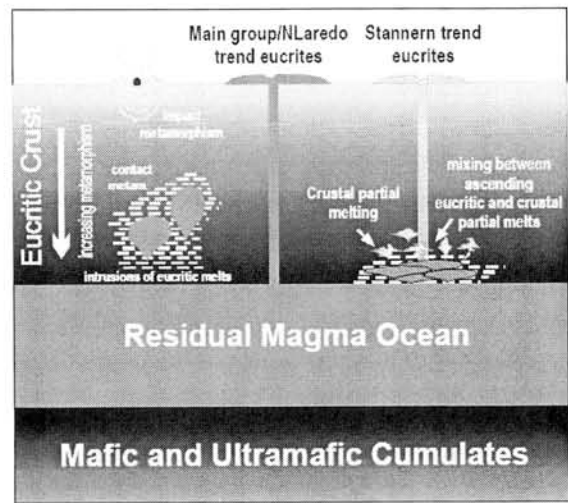


Fig. 3. Model for the origin of the Stannern trend eucrites.

References:

- [1] Consolmagno G.J. and Drake M.J. (1977) GCA 41, 1271-1282. [2] Binzel R.P. and Xu S. (1993) Science 260, 186-191. [3] Takeda H. and Graham A.L. (1991) Meteoritics 26, 129-134. [4] Yamaguchi A. et al. (1996) Icarus 124, 97-112. [5] Floss C. et al. (2000) AMR 13, 222-237. [6] Yamaguchi A. et al. (2001) GCA 65, 3577-3599. [7] Stolper E. (1977) GCA 41, 587-611. [8] Warren P.H. and Jerde E. (1987) GGA 51, 713-725. [9] Mittlefehldt D.W. and Lindstrom M.M. (2003) GCA 67, 1911-1935. [10] Barrat J.A. et al. (2000) MAPS 35, 1087-1100. [11] Warren P.H. and Kallemeyn G.W. (2001) LPS 32, 2114.

Measurements of ^{14}C , ^{10}Be and ^{129}I in meteorites and applications. A. J. T. Jull¹, D. L. Biddulph¹, L. R. McHargue^{1,2}, D. Zahn¹, G. S. Burr¹, K. J. Kim^{1,3} and P. A. Bland⁴. ¹NSF-Arizona AMS Laboratory, University of Arizona, Tucson, AZ 85721, USA. E-mail: jull@email.arizona.edu. ²Scottish Universities Environmental Research Centre, East Kilbride, UK G75 0QU, 3. Korea Institute of Geoscience and Mineral Resources, 30 Gajeon-dong, Yuseong-gu, Daejeon 305-350, Korea. 4. Imperial College, Dept. of Earth Science and Engineering, Prince Consort Road, London SW7 2AZ, United Kingdom.

Introduction:

The radionuclides produced by galactic cosmic radiation are useful for understanding the exposure age [1] and terrestrial residence age [2] of meteorites. The terrestrial age, or the terrestrial residence time of a meteorite, together with its exposure history provides us with useful insight into the history of the meteorite. Although one expects that meteorites might weather quickly in humid environments, we find that large numbers of meteorites found in semi-arid and arid environments can survive for much longer times. Meteorites in arid and semi-arid environments can survive for at least 50,000 yr, and there are some meteorites over 250,000 yr old from these locations. We will show the wide range of terrestrial ages from different environments. The terrestrial age also gives us information which can be applied to studies of infall rates, meteorite distributions, weathering of meteorites and meteorite concentration mechanisms. We would expect that weathering of meteorites and their eventual destruction would be a function of the terrestrial age. In addition, weathering would affect trace-element composition, as shown by Al-Kathiri et al. [3]. A direct connection of weathering rates to the terrestrial survival times of meteorites was initially shown by Wlotzka et al. [4] and later by Bland et al. [5,6], who were able to correlate degrees of weathering with terrestrial age for chondrites collected in the same area.

Trends in terrestrial ages:

Terrestrial ages of meteorites have been determined by the concentration of ^{36}Cl , ^{14}C or ^{41}C , measured independently or also in combination by accelerator mass spectrometry (AMS). With measurement of more than one radionuclide, then we can correct for shielding effects [1,7,8]. At our laboratory, we make measurements of ^{14}C and $^{14}\text{C}/^{10}\text{Be}$. The ratio of $^{14}\text{C}/^{10}\text{Be}$ can be used to get better precision on terrestrial ages.

Recently, we have also revised our assumption of undertaken some modeling calculations [9] to determine if we can assume a constant production rate of ^{14}C and ^{10}Be . We have expanded our studies to the ^{14}C and in some cases ^{10}Be composition of a series of iron meteorites of different expected terrestrial ages. Our estimate of the terrestrial age of Canyon Diablo from ^{14}C is about 17 ± 1 ka. It is interesting that the terrestrial ages appear to disagree with other age estimates of craters. However, this

may also indicate that our understanding of ^{14}C production in iron meteorites needs further study.

Iodine-129 measurements:

We have expanded our study of ^{129}I using AMS, to meteorites [10,11]. The use of ^{14}C and $^{14}\text{C}/^{10}\text{Be}$ for terrestrial-age measurements can be extended to iron meteorites. Initial studies of ^{129}I in chondrites indicate that this radionuclide may be useful for estimates of exposure ages [12], when coupled with accurate measurements of Te.

We will discuss the application of terrestrial-age measurements to meteorites from desert environments, including polar regions, and their significance for understanding of climatic effects in the region of collection.

References:

- [1] A. J. T. Jull 2006. Terrestrial ages of meteorites. In *Meteorites and the early solar system II* (eds. D. Lauretta and H. McSween, Tucson: University of Arizona Press, pp. 889-905.
- [2] O. Eugster et al. 2006. Irradiation records, cosmic-ray exposure ages and transfer times of meteorites. In *Meteorites and the early solar system II* (eds. D. Lauretta and H. McSween, Tucson: University of Arizona Press, pp. 829-851.
- [3] A. Al-Kathiri et al. 2005. *Meteoritics and Planetary Science* 40: 1215.
- [4] F. Wlotzka et al., 1995. Lunar & Planetary Institute Technical Report 95-02: 72.
- [5] P. A. Bland et al., 1996. *Monthly Notices, Royal Astronomical Society* 238: 551.
- [6] P. A. Bland et al. 2000, *Quaternary Research* 53: 131.
- [7] A. J. T. Jull et al., 1998. *Geological Society of London Special Publication* 140: 75.
- [8] K. C. Welten et al., 2003. *Meteoritics & Planetary Science* 38:499
- [9] K. J. Kim et al. 2003, *Lunar and Planetary Science*, 35: 1191.
- [10] K. Nishiizumi, et al. 1983 *Meteoritics* 18: 363.
- [11] C. Schnabel, et al. 2004. *Meteoritics and Planetary Science* 39: 453-466.
- [12] K. Marti et al. *Meteoritics and Planetary Science* 39: abs #5052.

AUTHOR INDEX

- Anand M.97
Aoki T.1, 78
Arai T.3, 95
Barrat J. A.105
Benoit M.105
Bérczi Sz.5, 7, 21, 64, 65
Biddulph D. L.107
Bizzarro M.99
Bland P. A.107
Bohn M.105
Brearley A. J.19
Burr G. S.107
Choi B.-G.9
Choi H.62
Clemett S. J.67
Cotten J.105
Das J. P.11
Doi M.56
Ebel D. S.13
Ebihara M.91
El Goresy A.71
Fagan T. J.15
Franchi I. A.105
Fukuda H.39
Fukuoka T.43
Funaki M.26, 77
Gánti T.7
Garrod S.9
Goswami J. N.17
Granovsky L. B.45
Greenwood R. C.105
Grossman J. N.19
Gucsik A.5, 21, 34, 47, 64, 65, 85
Hargitai H. I.5, 21, 23
Hiroi T.25
Hoffmann V.26
Honda M.28
Hoppe P.71
Horváth A.7
Huss G. R.99
Ikeda Y.30, 32
Imae N.30, 32, 73, 75, 78
Ishii T.95
Iwata N.78
Jang N.9
Joy K. H.97
Józsa S.64, 65
Jull A.J.T.107
Kanamori H.95
Kayama M.34, 47
Keller L. P.35, 67
Kereszturi A.5, 7, 21, 37
Kim K. J.107
Kim O. J.9
Kimura M.19, 39
Kita N.13
Kitajima F.41
Kojima H.43, 73, 75
Krot A. N.99
Kurihara T.52
Kusuno H.43
Kuyama T.75
Le L.48
Lee J. I.9
Lin Y.50
Marakushev A. A.45
Matsuda N.21, 34, 47
Matsuzaki H.43
McHargue L. R.107
McKay G.48
Messenger S.35, 67
Miao B.50
Mikouchi T.48, 52
Misawa K.54
Mishra R.17
Miura H.56
Miura Yasunori58, 60
Miura Yayoi86
Murty S.V.S.11
Nagai H.28
Nagao K.28, 62
Nagy Sz.5, 21, 64, 65
Nakamoto T.56
Nakamura T.41, 78, 83, 93

| | | | |
|----------------------------|----------------------------|---|------------|
| Nakamura-Messenger K. | 67 | Sasaki S. | 25 |
| Nakamuta Y. | 1, 69 | Sasaki Y. | 97 |
| Nakashima D. | 71 | Shih C.-Y. | 54, 80 |
| Nakashima S. | 93 | Shirai N. | 91 |
| Naraoka H. | 82 | Sik A. | 7 |
| Niihara T. | 73 | Stirling J. A.R. | 21 |
| Nimura T. | 25 | Suzuki A. | 39, 93 |
| Ninagawa K. ... | 21, 34, 47, 64, 65, 75, 85 | Szathmary E. | 7 |
| Nishido H. | 21, 34, 47, 64, 65, 85 | Takeda H. | 3, 95 |
| Nishioka I. | 77 | Terada K. | 97 |
| Noguchi T. | 78 | Toh S. | 1, 78 |
| Nyquist L. E. | 54, 80 | Tomiyama T. | 99 |
| Oba Y. | 82 | Torii M. | 26 |
| Ohtake M. | 3 | Tottuki Micrometeorite Curation Team | 78 |
| Ohtani E. | 39 | Ueda Y. | 25 |
| Okazaki R. | 83 | Uesugi K. | 101 |
| Okumura T. | 21, 47, 85 | Uesugi M. | 101 |
| Otsuki M. | 95 | Ushikubo T. | 13 |
| Ott U. | 71 | Venkata Rao K. | 77 |
| Ozima M. | 86 | Veres M. | 65 |
| Park J. | 9, 62 | Wang D. | 50 |
| Pieters C. M. | 25 | Weihaupt J. G. | 103 |
| Pocs T. | 7 | Weisberg M. K. | 13, 19 |
| Podosek F. | 86 | Yamaguchi A. | 3, 95, 105 |
| Protheroe Jr. W. J. | 21 | Yazawa Y. | 95 |
| Reese Y. D. | 54, 80 | Yin Q.-Z. | 86 |
| Rice A. | 103 | Yoo H. | 9 |
| Righter K. | 89 | Zahn D. | 107 |
| Rudraswami N. G. | 17 | Zinovieva N. G. | 45 |
| Saito M. | 95 | Zolensky M. E. | 67 |
| Sakamoto M. | 85 | | |
| Sano Y. | 97 | | |

